The Effect of Nitrogen, Niobium and Temperature on the High Temperature Oxidation of Titanium Aluminide Alloys

by

Julia Carmel Duncan

B.S. in Metallurgical Engineering
South Dakota School of Mines and Technology (1985)

B.S. in Chemistry
South Dakota School of Mines and Technology (1987)

S.M. in Materials Science and Engineering
Massachusetts Institute of Technology (1994)

Submitted to the Department of Materials Science and Engineering
in Partial Fulfillment of the Requirements for the Degree of

Doctor of Science
in Polymers

at the
Massachusetts Institute of Technology
September 1998

Signature of Author _____
Department of Materials Science and Engineering

Certified by _____
Linn W. Hobbs
John F. Elliott Professor of Materials
Thesis Supervisor

Accepted by _____
Linn W. Hobbs
John F. Elliott Professor of Materials
Chair, Departmental Committee on Graduate Students

The Effect of Nitrogen, Niobium and Temperature on the High Temperature Oxidation of Titanium Aluminide Alloys

by
Julia Carmel Duncan

Submitted to the Department of Materials Science and Engineering on August 7, 1998 in partial fulfillment of the requirements for the degree of Doctor of Science in Polymers in the Department of Materials Science and Engineering.

Abstract

The titanium aluminide family was selected as a promising material for the next generation of aircraft engines as well as other high temperature applications. The density of these intermetallics is approximately one half of conventional superalloy densities. This is especially attractive for reducing the engine weight and increasing the thrust/weight ratio. Increasing the operating temperature and thereby the engine efficiency has approached the maximum possible operating temperature for currently used materials.

A model set of three intermetallics -- unalloyed γ-TiAl, unalloyed α_2-Ti_3Al and a nearly stoichiometric Ti_2NbAl (an orthorhombic intermetallic structure) -- was chosen and investigated under a variety of experimental conditions. Gas mixtures of varying oxygen concentrations in both argon and nitrogen allowed the effect of oxygen concentration on oxidation kinetics to be investigated. The Ti_2NbAl-alloy was specifically chosen to examine the effect of Nb in a intermetallic compound (with Nb substituting for one Ti in the Ti_3Al intermetallic structure). This is in contrast to Nb as a simple alloy addition to γ-TiAl or α_2-Ti_3Al. Exposures at temperatures of 700°C and 800°C for 20 and 100 hours were studied (compared to temperatures of 900°C or higher used by other investigators), since these temperatures promoted a more protective scale. Additionally, the scale composition is sensitive to temperature and restricts the conventional practice of corrosion study acceleration by raising the experimental temperature.

The resulting corrosion scales were analyzed using electron microscopy (scanning and transmission), x-ray diffraction and thermogravimetric analysis. The effect of nitrogen in the gaseous environment was explored. The impact of Nb on the oxidation of the intermetallics was found to be more protective than what might be expected from examining the thermodynamics and kinetics of the Ti-Al-Nb-O-N system. At times an alternating layered scale structure resulted and the effect of N, Nb and the lower temperatures used in this study is summarized.

The oxidation rate of the Ti_2NbAl-alloy fell between the rates for γ-TiAl and α_2-Ti_3Al, with the scale on γ-TiAl growing at the slowest rate of the three compositions. However, the superior mechanical properties of Ti_2NbAl-alloy combined with the acceptable corrosion resistance promote its consideration for replacing those portions of the engine operating at intermediate temperatures that would result in significant weight and cost savings.

Thesis Supervisor: Linn W. Hobbs
Title: John F. Elliott Professor of Materials

List of Figures

List of Tables

List of Abbreviations

SAMPLE DESIGNATIONS:	
SA2-07-05N-1XX-1	sample designation with 5 sections indicating sample composition, temperature of exposure, exposure gas composition, length of oxidation and number of sample at that set of conditions
1st section	G, A2 or SA2, indicating the composition of the intermetallic alloys used in this study
2nd section	2 numerals, indicating temperature in 100's °C; 07 = 700°C, 08 = 800°C
3rd section	gas abbreviation for oxidation studies. format of ##X. First two numerals indicate the percentage of oxygen in the gas mixture (by volume). The final letter denotes the gas making up the balance of the mixture (A = argon and N = nitrogen). OO or XX denoted 100% oxygen
4th section	2 or 3 characters indicating experiment length. 3 time lengths used - 2, 20 and 100 hr, indicated by 02, 20 and 1XX.
5th section	one numeral indicating sample number run at the same conditions. Some experiments were repeated up to 7 times to repeat questionable data and to obtain reproducible results
05A	5% oxygen - balance argon
05N	5% oxygen - balance nitrogen
20A	20% oxygen - balance argon
20N	20% oxygen - balance nitrogen
OO-	100% oxygen (no third letter to indicate the gas making up the balance of the mixture); XX also used to avoid confusion with ohs looking like zeros
NN-	100% nitrogen (no third letter to indicate the gas making up the balance of the mixture)

XX	100% oxygen (no third letter to indicate the gas making up the balance of the mixture); Used to avoid confusion with ohs looking like zeros - OO vs 00.
~	approximately equal; tolerance depends on the circumstances or equipment used.
###X	Symbol for magnification, especially in light microscopy. Three possible magnifications possible in this study: 165 times, 330 times and 660 times, denoted 165X, 330X and 660X, respectively.
???	used when further information is needed. To be replaced later with the correct information
!!	used when some calculation or verification is needed. To be replaced later..
ΔG°_f	Gibbs free energy of formation (relative to a standard state)
μm	microns or micrometer, 10^{-6} meter; unit of measure
μs	microsecond or 10^{-6} second; unit of time
Å	Angstrom, unit of length, 10^{-10} meter
°C	degrees Celcius or Centrigrade (metric unit of temperature)
a%	atomic percent (compare to weight percent - wt.%)
at.%	atomic percent, preferred notation in this text
A2	Ti-25a%Al intermetallic; specific titanium aluminide alloy used in this study; based on α_2-Ti_3Al
Al	aluminum, metal element
Al oxynitride	a compound of Al containing both oxygen and nitrogen; generally refers to the specific aluminum oxide nitride of the formula $Al_{27}O_{39}N$, with the PDF card of 26-33
ALP	α_2-Ti_3Al
atm	atmosphere; a unit of pressure

Au	gold, metal element; used for making sample electrically conducting prior to electroplating
BA	breakaway oxidation, usually exhibiting linear parabolic kinetic rates; term used in the Experimental Summary (Appendix A)
B2	high temperature titanium phase, usually achieved by adding β stabilizers such as Nb, V or Mo.
Cahn	Cahn microbalance; electronic equipment for measuring thermogravimetric data
Cb	alternative abbreviation for niobium, based on the alternative name for the element, Columbium. See Nb
cm	centimeter; unit of measure
Cr	Cr, an alloying element used in titanium aluminides and also an element connected with the "Cr effect" of stabilizing alternative phases in titanium aluminides
d or d spacing	an interplanar spacing used in x-ray crystallography as defined by the equation: $n\lambda = 2d \sin \theta$; d denotes spacing between atomic planes
DuPont	DuPont microbalance: a thermal analyzer coupled with a thermogravimetric analysis plug-in
DP	DuPont microbalance abbreviation used for identifying samples run in this microbalance
EDS	energy dispersive spectroscopy
EDM	electrodischarge machine or machining (also called spark cutting)
EDXA	energy dispersive x-ray analysis
EELS	electron energy loss spectroscopy
EPMA	Electron probe microanalysis; analytical technique for composition determination
ESEM	environmental scanning electron microscope or microscopy; ElectroScan Model E-3 model used in these studies

Fe	iron, metal element
FEG	field emission gun, typically referring to the illumination source of a electron microscope
FIB	Focussed Ion Beam (microscope, machine...) method used in electronic materials to deposit or etch material away. Sometimes also accomplished with the electron beam of a conventional SEM or Environmental SEM.
FOM	Figure of Merit - quantity used in X-ray diffraction to determine closeness of match of spectra to a specific PDF card.
G	Ti-47.9a%Al; specific titanium aluminide alloy used in this study; based on γ-TiAl
GAM	γ-TiAl; specific stoichiometric intermetallic
GAXRD	glancing angle X-ray diffraction
GE Alloy	commercial alloy produced by GE, based on γ-TiAl, composition Ti-48Al-2Cr-2Nb
h	hour, unit of time (alternative to hr)
hr	hour, unit of time
hrs	hours, units of time
HT	high or elevated temperature
ImagePro	Software available at the Electron Microscopy CMSE Common Facility
Plus	used for image analysis, such as areas, distances,
IMs	intermetallics
in-situ	also in situ; in the natural or original position
JANAF	Joint Army-Navy-Air Force; reference for thermodynamic data. Third Edition used in this thesis, 1985. From the Journal of Physical and Chemical Reference Data. Vol 14, 1985. Supplement No. 1.

JCPDS	Joint Committee on Powder Diffraction Standards
K	Kelvin (absolute unit of temperature)
K	Equilibirium constants
kcal	kilocalorie, 1000 calories; unit of energy; 1 calorie = 4.186 Joules
K_g	thermogravimetric oxidation rate; obtained from weight gain of the oxidant update during experiment
kJ	kilojoule, 1000 Joules; - unit of energy
K_p	parabolic oxidation rate; obtained from weight gain of the total scale grown during experiment. Value obtained from K_g and appropriate stoichiometry
Ksi	kilogram per square inch, unit of pressure
l	liter; unit of volume
ln	natural log, defined as logarithm of base e; e 2.718; mathematical convention
LOM	light optical microscope or microscopy
LVHREM	Low Voltage High Resolution Electron Microscopy or Microscope (JEOL 6320)
m	meter, unit of length
M/A	mass per area; normalized weight gain per area used for comparing oxidation experiments
M/O	metal/oxide interface; roughly initial substrate surface, unless internal oxidation has shifted the metal interface inwards
mg	milligram, unit of weight
micron	micrometer, 10^{-6} meter; unit of length
MIT	Massachusetts Institute of Technology; a higher learning institution

mixed oxide	generally refers to the specific titanium and aluminum oxide of the formula
	$TiAl_2O_5$, with the PDF card of 41-258
Mo	molybdenum, metallic element.
ms	millisecond, unit of time
N	nitrogen, gaseous element
Nb	niobium, metallic element. Historically also called Columbium with abbreviation Cb
NCP	new cubic phase - a recent discovery of a subsurface compound in titanium aluminides consisting of a titanium aluminide with a formula between A2 and G (Ti3Al2 or Ti2Al) and with possible oxygen incorporation (as Ti5Al3O2). Also called X or Z phase by different researchers.
Ni	nickel, metal element; electroplated onto oxidized specimens in an effort to reduce the spallation of the scale.
nm	nanometer, unit of length equal to 10^{-9} meter
NP	Nikolai P., operator of some of the microbalance experiments
O	oxygen, gaseous element
O/G	oxide/gas interface; roughly equivalent to the outer surface of the oxide in contact with the environment
O/M	oxide/metal interface; alternative notation for M/O interface;
O_2	molecular oxygen species most commonly found at temperatures dealt with in this thesis
OM	optical or light microscopy (microscope)
ORT	orthorhombic Ti_2NbAl; specific ternary stoichiometric intermetallic
PDF	Powder Diffraction File - from JCPDF databases

PEELS	Parallel electron energy loss spectroscopy (compare to SEELS)
Photoshop	Adobe Photoshop™, Version 2.5.1 LE (Limited Edition); image processing software used on both IBM and MAC operating systems
ppm	parts per million, typically a volume fraction used for gas impurities
RMS	root mean square, "goodness" of fit in linear regression algorithms
RT	room temperature (approximately 25°C or 298 Kelvin)
S	sulfur or sulphur; gaseous element. Molecular formula S_2, among others
S_2	molecular sulfur commonly found at temperatures 700-900°C, used in this work
SA2	Ti-25at.%Al-23.5at.%Nb; specific titanium aluminide alloy used in this study; based on orthorhombic Ti_2NbAl, a Nb-substituted α_2-Ti_3Al
sec	second, unit of time
SEELS	Serial electron energy loss spectroscopy; (compare to PEELS)
SEM	scanning electron microscope or microscopy
S.M.	Master of Science degree, this notation used at MIT, rather than M.S.
STEM	scanning transmission electron microscope or microscopy; for this study, the analytical STEM, model VG603 was used
'super' -α_2 also Super Alpha-2	a commercial titanium aluminide alloy typically of composition Ti-25a%Al-10-15)Nb-3V-1Mo. Nb, V and Mo added as β-stablizers; Mo also added for creep resistance. If annealed, precipitates of orthorhombic Ti_2NbAl may be formed. Typically the microstructure is fine α_2 particles in a Nb-rich matrix (B2).

Ta	tantalum, a refractory metal
TGA	thermogravimetric analysis; weight gain/time data
Ti	Titanium, a metal element
theta or θ	X-ray diffraction term for the incident x-ray beam
T_m	melting temperature
two-theta or 2θ	X-ray diffraction term for the exiting x-ray beam or signal
UHP	Ultra High Purity, purity grade used for gas cylinders
V	vanadium, metallic element
VG	Vacuum Generators, manufacturer of the STEM used in this study
WAXS	Wide Angle X-Ray Spectroscopy
WG	weight gain, abbreviation used in Experimental Summary (Appendix A)
WL	weight loss, abbreviation used in Experimental Summary (Appendix A)
WPAFB	Wright-Patterson Air Force Base contact: (Dennis Dimiduk, supplier of titanium aluminide alloy samples)
X	a cubic subsurface corrosion product. See entry under NCP.
XX	used as 2 numeral designation for 100% oxygen in the DuPont microbalance experiments, rather than 00, as used in the Cahn microbalance
XEDS	X-ray Energy Dispersive Spectroscopy
XRD	X-ray diffraction
Z	a cubic subsurface corrosion zone or product. See entry under NCP.

Acknowledgments

Listen as your day unfolds,
Challenge what the future holds,
Try to keep your head up to the sky

Some may have more cash than you
Others take a different view
Try to solve the puzzles in your own sweet time

You gotta be bad, you gotta be bold, you gotta be wiser,
Your gotta be hard, you gotta be tough, you gotta be stronger
You gotta be cool, you gotta be calm, you gotta stay together...

"You Gotta Be" - Des'ree

As independent as I like to be, I do not dare to think that I accomplished this milestone on my own. The following people have been instrumental in this event and I hope to be forgiven for any omissions, as the list is quite long.

I wish to acknowledge the help of my committee:
Professor Edwin L. Thomas, who gave me some great advice on organizing the thesis and for his encouragement in writing and submitting manuscripts. He also graciously allowed me to use some of his equipment and I felt a part of his group, for which I am immensely grateful.
Professor Ronald M. Latanision, for agreeing to step in as a committee member at the last moment. His support for this "kid" was much appreciated.
Professor John B. Vander Sande, for making this document much better than it would have been otherwise. I valued his comments, his willingness to go out of his way to help me with this thesis and professionally, and for wrangling up funding so gravely needed at the end.
Professor Linn W. Hobbs, my advisor, for the financial support and for thesis corrections.

Fred Wilson for friendliness and helpfulness when I didn't know who to ask. Joe Adario and Peter Kloumann for X-ray help. Mike Frongillo for tolerance while learning and relearning Electron Microscopy. Dr. Tony Garratt-Reed for help with STEM and aid on the ESEM.
Brian Gally for help on the EDM and the great chats.
Rob Calhoun, for helping me with last-minute machining, when I know you had better things to do. I still owe you that coffee!
Len Radzilowski, whose "miniscule" help I appreciated and who always put me in a good mood, perhaps because I couldn't believe that he actually talked and could tolerate my blabbering on and on about everything and nothing.

In addition, Ned Thomas' group often felt like home away from home, just a short trip away. Thanks to MaryJane O'Rourke, Bruce Carvalho, Benita Dair for filling out my sense of a research group. I will really miss it.

Many of the people moving through the Hobbs research group have been helpful:
Phyllis King - the "good egg" holding the group together! Thanks for being so thoughtful and pleasant all the time.
Nick Pokrovskiy, who helped with *in-situ* studies and served as good company, especially when experiments were perplexing. It was hard to remain frustrated when I had to face your grinning all the time - "Excellence in all you do."
Valarie Benezra, for being a good groupmate to angst with, and putting up with my attachments to the same CDs and songs, over and over. Thanks for helping and sharing the experience with me.
Meri Treska, for help with anything x-ray related and for making me feel useful.
Former members who often were willing to lend a hand or an ear: A.N. Sreeram, Lu-Chang Qin, Chuxin Zhou, and Mike Shin.
Anabela Afonso for amusement when I so badly needed it.
Doris, for all the understanding and chats, despite the culture differences and the miles.

In my long journey here, I look back and treasure those links that somehow still remain:
Bo-Yin Yang, who I could always count on, even with our differences.
Mark Buonanno, for convincing me I could do it.
My time at Ashdown will always be filled with nice memories.
My recent roommates have had a large motivating influence, and I appreciate that, especially now - YOYO.
Ushi and Kuma for tolerating my long absences and still acting so happy to see me.
Kitsune, for having the knack of acting cute, just when I wonder if you wouldn't be happier somewhere else...
All of my "team" for always pulling through when I needed it.
Special thanks to my great former housemates Daniel and Lisa and now little Evan Bryce Moore for making me feel like family.

And finally, some people who have been with me through thick and thin and beyond.
Kim Ducheneaux who has always listened and seems to understand even when I wonder myself. I value the length of our connection beyond measure, but wish it didn't have to remind me of how quickly time flies.
Christian Honeker, for keeping at me and always having the positive spin, even when I didn't quite buy it. Thanks for making things comfortable, be it research related or just getting away from it all. It's too easy to let that go in the crunch times.
Ralph Mason, glad we are not keeping score, because it might be a toss-up over the long run, but in the last year, I am feeling decidedly behind. I won't even begin to list all the help you've given me.
My sister Lisa Duncan Brocar who always seemed to understand me even when I couldn't explain myself. To my little nephew Asa, for so patiently waiting to meet me!

To all the people who wondered why I was keeping at it - THANKS, that just made me more determined to do it anyway. (A little tenacity goes a long, long way).

Dennis Dimidik of Wright Paterson Air Force Base is thanked for providing all of the intermetallic alloys used in this study.

The majority of this work was supported by the AFOSR, under Contract No. F49620-93-1-0291DEF. Additional support came from Castle Technology, the John F. Elliott chair and the Lord Foundation.

Dedicated to:

My pit crew and support team,
especially Ralph,
Lisa (and Asa),
Kim, Christian and Bo-Yin.

... and of course, my cow-boys

Chapter 1

Introduction

Materials capable of performing at high temperatures are needed in aerospace, automotive, and energy conversion applications. Since no material is completely corrosion resistant, high temperature oxidation and scale formation are unavoidable. Through alloy selection, corrosion engineers can limit the extent of corrosion and promote corrosion scales that offer the most protection against structural damage. To this end, an understanding of the mechanism of high temperature corrosion is necessary.

Engine efficiency is an important engineering concern in the aircraft industry. Increased efficiency can be achieved in two ways:

1) increasing the engine operating temperatures or

2) lowering the engine weight and thereby increasing the thrust/weight ratio.

Nickel- and cobalt-based superalloys and conventional titanium alloys currently being used in the aircraft gas turbine technologies are near their maximum use temperatures. Advances in processing techniques including directional solidification, rapid solidification and the use of single crystal materials have enhanced favorable materials properties but had little effect on increasing their use temperature. The current operating temperature is approaching 1100°C, which yields an engine efficiency of 60%. An engine material that could operate at 1375°C would increase the efficiency to 80%.

There are few practical materials that are capable of attaining this temperature. Ceramics would require coatings to protect against corrosion and would cause concern about brittleness under load. Nickel aluminides could increase the engine temperature but have very little weight benefit. Additionally, NiAl is targeted for coatings, rather than structural components, due to its extreme brittleness. Iron aluminides have more room-temperature ductility but are heavier and possess questionable oxidation resistance.

Reduction of the engine weight has the most potential for significant improvements to the thrust/weight ratio. Titanium aluminides have densities of roughly half that of conventional superalloys currently being employed. With the proper chemical and mechanical conditions, by alloy additions and microstructural processing, they exhibit favorable oxidation resistance and comparable strengths. Table 1.1 shows density, mechanical and oxidation properties for titanium alloys, titanium aluminides and superalloys.

This research study introduces three unique aspects to the study of titanium aluminides as a potential high temperature material:

1) A decrease in the experimental temperature over that in previous studies
2) An oxidation study of the Ti_2NbAl intermetallic, which incorporates the alloying element Nb directly into the intermetallic order, rather than in a solid solution.
3) An electron microscopical investigation of the oxidation occurring under the conditions chosen, to enhance the understanding of the corrosion mechanisms occurring in the titanium aluminide system.

1.1 Oxidation at Lower Temperature

Earlier researchers had dismissed titanium aluminide intermetallics as having insufficient oxidation resistance at temperatures of 900°C or 1000°C and higher. A

unique feature in the Ti-Al system is the similarity in thermodynamic stabilities between the titanium oxide and the aluminum oxide. A typical corrosion resistant alloy contains one component that is significantly more noble that preferentially oxidizes to form a single (protective) scale composition over a temperature range of several hundred degrees. This is not the case in titanium aluminides, as a result the corrosion scale is often a mixture of two or more oxides and the scale composition is more sensitive to temperature.

As the temperature in the titanium aluminide system is decreased from 1000°C, the difference between the oxides' standard free energies of formation is increased. This difference was explored and exploited to preferentially form the more protective aluminum oxide at lower temperatures. The weight savings that titanium aluminides could achieve by replacing heavier alloys in components that operate at intermediate temperatures would be significant. Possible engine applications include blades, vanes and stators in the low pressure turbine section and exhaust (thrust) deflectors.

1.2 Niobium Incorporation

A common alloy addition for ductilizing the titanium aluminide system is niobium. A popular theory is that Nb is a β-stabilizer, and that the β phase has more available slip systems than the low temperature hexagonal structure of titanium. The oxidation resistance of titanium aluminides was also found to improve with small Nb additions.

One advantage of an intermetallic is the slower diffusion through the compound due to the ordering and bonding. The reduction typically improves the corrosion resistance of an intermetallic over that of a non-intermetallic. An intermetallic, Ti_2NbAl, exists which is based on the α_2-Ti_3Al structure, with Nb substituting for one of the Ti atoms. This orthorhombic intermetallic combines the advantages of Nb for ductility and

oxidation resistance, with the single phase intermetallic structure. Oxidation experiments on this orthorhombic structure have not been reported until now.

1.3 Microscopy of Corrosion Scales

In the titanium aluminide system, high temperature properties such as oxidation, creep and ductility, as well as fracture toughness and ductility at room temperature, have been studied, but microscopical examinations of the complex system have been few. It was the aim in this work to use a better microscopical understanding of the resulting corrosion scales to illuminate the conditions and parameters where titanium aluminide could be successfully applied.

One limitation of microscope studies in oxidation studies is the ambiguity in whether features in the scale occurred at elevated temperature or during the heating and cooling portions of the experiment. The use of the environmental scanning electron microscope (ESEM) allowed in-situ observation of phenomena, such as preferential oxide nucleation, scale cracking and spallation, and the scale composition in cases of multiple oxides of different morphologies. The coupling of microscopical and oxidation studies yielded a better understanding of the complex corrosion mechanisms in the titanium aluminide system.

Table 1.1 Properties of several high temperature materials:
Comparison of superalloys to the lower weight titanium-containing alloys.

Properties	**Ti-based Alloys**	**Ti_3Al-based**	**TiAl-based**	**Superalloys**
Density (g/cm^3)	4.5	4.1-4.7	3.7-3.9	8.3
Young's Modulus RT (GPa)	96-115	120-145	160-176	206
Yield Strength (MPa)	380-1150	700-990	400-630	-
Tensile Strength (MPa)	480-1200	800-1140	450-700	-
Creep Limit (°C)	600	750	1000	1090
Oxidation Limit (°C)	600	650	900-1000	1090
Ductility RT (%)	10-20	2-7	1-3	3-5
Ductility HT (%)	High	10-20	10-90	10-20
Structure	hcp/bcc	ordered hexagonal (DO_{19})	face-centered tetragonal ($L1_0$)	fcc ($L1_2$)
T_m (°C)	1670	1600	1460	~1300
Fracture Toughness (MPa $\sqrt{m}$)	High	13-30	10-20	25

Chapter 2

Literature Review

Within the past two decades, there has been a renewed interest in intermetallics for use as high temperature materials particularly in turbine engine components. Since intermetallic crystal structures involve long-range ordered superlattices, they generally exhibit yield strengths and high-temperature creep strengths greater than those of conventional disordered metallic alloys. Initially, titanium aluminides were first investigated in the early 1950's, but dismissed for most practical applications due to their extreme brittleness. Efforts at optimizing and tailoring their properties began again in earnest when engine operating temperatures began pushing the upper limit for use of conventional materials. The next likely avenue for improved efficiencies appeared to be the weight savings possible from the lighter weight titanium aluminide alloys, with densities of approximately half of those for currently used superalloys. Additionally, beneficial approaches exploited in other intermetallics, such as reactive element alloying in nickel aluminides, are now considered for possible application in the titanium aluminide system. A large literature has accumulated over the last 15 years addressing these and other features of titanium aluminides. Access to some information has been unfortunately restricted, owing to the sensitive nature of materials development with defense applications.

A further approach has been envisioned in more limited use of titanium aluminides at lower or intermediate temperatures for weight savings, rather than replacing the majority of engine components including those in the hottest regions operating at temperatures above what titanium aluminides can be expected to perform satisfactorily at. The weight savings effected would still be significant and justifies the alternative to universal replacement, until improvements have been made in the mechanical properties of brittle intermetallics for applications in components which rotate under load at higher operating temperatures.

2.1 Titanium Aluminide Compounds

There are three titanium aluminides generally accepted as binary intermetallics in the Ti-Al system. These are γ-TiAl, α_2-Ti_3Al and $TiAl_3$ (the latter is referred to as both δ and η in various phase diagrams). The existence of a fourth with the composition $TiAl_2$ is speculated, some attributing the observation to the ternary compound of $TiAlN_2$. In recent papers, $TiAl_2$ was purportedly produced, but little microstructural or crystallographic evidence was offered to support a single-phase compound, rather than a two-phase mixture of $TiAl_3$ and γ-TiAl (Ma 1995). Principal material properties for γ-TiAl and α_2-Ti_3Al are given in Table 1.1. The third intermetallic, $TiAl_3$, has been less studied (Christodoulou 1990). With the highest proportion of aluminum and the lowest density, this phase would initially seem the most attractive of the titanium aluminides to investigate. It is, however, a line compound that is difficult to produce and isolate. It also has the lowest melting point of the titanium aluminides and -- even more problematic -- exhibits such brittleness and thermal mismatch to the other titanium aluminides and to the oxides of titanium and aluminum that it is hurriedly dismissed from serious consideration. No tensile ductility has ever been reported, and compressive strain at moderate temperatures of 330-620°C is limited to less than 1% (Christodoulou 1990).

Attempts to use this compound as a protective coating (Smialek 1993) resulted in a loss of integrity and spallation. The few attempts at developing it into an intermetallic alloy have concentrated on transforming the tetragonal DO_{22} structure into a cubic $L1_2$ structure by ternary additions. The resulting $L1_2$ structures were more resistant to crack propagation, but failed to exhibit measurable room temperature ductility, which would occasion serious difficulties in part fabrication and in structural integrity under impact.

2.2 Oxidation of γ-TiAl-based Alloys

There has been a large interest in γ-TiAl-based alloys in recent years, and the literature on its high temperature oxidation properties reflects this. Many different factors have been found to have an impact on the oxidation behavior of these alloys. These include the oxygen pressure, the presence or absence of nitrogen (discussed in §2.5), alloying elements (Nb is specifically discussed in §2.6) and impurities. Common features have been observed in oxidation studies, which include layered scale formation, non-protective behavior of unmodified alloys, and nodule formation accompanied by non-uniform scale thickness.

Becker (1992) studied the oxidation of γ-TiAl-alloys containing 50 at.% Al with alloying additions of C, V and Nb. Isothermal oxidation tests were carried out primarily at 900°C. Only one set of experiments was performed at 700°C and no conclusions were drawn from the results. At the higher temperatures, C and V additions were found to detrimentally affect the oxidation kinetics, while Nb additions (at levels significantly lower than those in the present study) improved protection and resulted in the only alloy to form a long-lasting alumina layer.

The effect of gas composition on oxidation kinetics was studied and oxygen content (1 to 100% in argon) was found to have little effect, while nitrogen had a varied yet significant effect. Nitrogen lead to faster oxidation at 1000°C and to slower oxidation

at 900°C for unalloyed γ-TiAl, and to overall slower oxidation of Nb-alloyed γ-TiAl where it promoted formation of a protective alumina layer.

Scales consisted of an outer rutile layer and mixed rutile/alumina layer. An alumina barrier layer sometimes occurred between the two oxide layers. When breakaway oxidation occurred, this alumina barrier layer was found to dissolve and reprecipitate in the outer layer. Analysis of the substrates adjacent to the scales found a sub-surface α_2-Ti_3Al zone resulting from aluminum depletion and a sub-surface zone enriched with up to 20 wt.% Nb (in the Nb-containing alloys). The presence of this α_2-Ti_3Al in the Becker alloys may allow conclusions regarding equilibrium scales to be extended both to α_2-Ti_3Al and to Ti_2NbAl alloys of similar structure and having significant Nb.

A technique similar to reducing the oxygen pressure to favor the formation of alumina is that of preoxidizing a sample in a gaseous environment different from the environment experienced in normal usage. Taniguchi (1994) performed this with powder packs of both Cr_2O_3 and TiO_2, which promoted a more alumina-rich scale; a protective scale was obtained when the packs consisted entirely of oxide powders, as compared to powder mixtures of an oxide and the corresponding metallic element. Layered oxide structures were seen, with rutile predominantly in an outer scale and mixtures of the oxides in inner scales.

A few TEM studies have been performed on oxidized γ-TiAl and γ-TiAl-based alloys. These focus on oxidation at 900°C which is probably the upper limit temperature for the stability of this structure. Lang (1996) concentrated on initial oxidation stages between 4 minutes and 4 hours. Dettenwanger (1996) made TEM samples after 500 hours but focused on the sub-surface depletion zone and the inner scale only. Chemistry

of the entire scale was established using x-ray mapping in an SEM. For these longer oxidation times, scale thicknesses approached 10 μm.

2.3 Oxidation of α_2-Ti_3Al-based Alloys

Oxidation studies of unmodified α_2-Ti_3Al-alloys have been rare, chiefly because a non-protective rutile scale forms and the maximum use temperature is about 650°C. More studies have been made of the oxidation of the related "super" α2-alloys, which are α_2-Ti_3Al-based alloys containing 10-15 at.% Nb. Blank-Bewersdorff (1994) studied microstructural evolution after annealing between 600° and 900°C in 100% oxygen, 100% hydrogen, argon and air. The effect of hydrogen on titanium aluminides is a concern because of the fuels used and the high solubilities of oxygen, nitrogen and hydrogen in α_2-Ti_3Al-alloys. Hydride formation has also been proposed during high temperature corrosion of titanium aluminides, and the α_2-Ti_3Al-based alloys exhibit increased hardness after exposure to hydrogen environments. Kumar et al (1996) studied the oxidation behavior of a Ti-22.8-Al-11.5Nb (at.%) alloy (an alloy with much lower Nb content than that used in the present study) in the range of 700 and 900°C. Elemental mapping was carried out using an SEM, but no TEM studies were conducted.

2.4 Prior Investigations of Ti_2NbAl-based Alloys

Efforts at General Electric Research Laboratories (Rowe 1992) have produced Ti_2NbAl-based alloys using rapid solidification processing as well as conventional casting technologies. These alloys are stronger and tougher than the α_2-Ti_3Al-based alloys. Small amounts of Nb in titanium aluminides improved room temperature mechanical properties, with some sacrifice of some high-temperature strength and creep resistance. The higher Nb-content Ti_2NbAl-based materials proved to have a higher strength-to-density ratio and better room temperature ductility and fracture toughness, with no loss in high temperature mechanical properties. Fracture toughness of

Ti-22Al-27Nb (at.%) samples was measured at 28 MPa-$m^{1/2}$, compared to Nb-containing α_2-Ti_3Al alloys with values of 14 and 19 MPa-$m^{1/2}$. Variants of these compositions containing either 30 at.% Al or Nb, proved to be unlikely candidates for structural applications because of poor room-temperature ductility (for alloys with higher Al content) or poor ductility at elevated temperatures (for alloys with higher Nb content).

2.5 Nitrogen Effect on the Oxidation of Titanium Aluminides

There is still controversy about the effect of nitrogen incorporated in an oxidizing gas. Half the researchers engaged in such studies indicate a detrimental effect and prevention of protective alumina formation when nitrogen is present (Dettenwanger 1996, Lang 1996, Meier 1993).

2.6 Niobium Effect on the Oxidation of Titanium Aluminides

Inclusion of niobium in the alloy compositions also has a strong effect in improving oxidation performance. Several mechanisms to explain the Nb effect have been proposed by Stroosnijder (Ox Met 1996) and others, among which are:

- Formation of a thin (more) stable Ti-rich nitride layer at the scale-alloy interface which acts as a diffusion barrier for anion/cation transport.
- Increase in Al activity relative to Ti activity in the alloy, favoring alumina-rich scale formation.
- Enrichment of Nb in the alloy immediately beneath the scale, changing the diffusion mechanisms such that overall metal and oxygen transport is decreased.
- Doping of the titania lattice by Nb^{5+} ions, decreasing the concentration of oxygen vacancies and/or titanium interstitials and reducing formation of rutile.
- Formation of Nb_2O_5, which forms a mixed oxide with TiO_2 and Al_2O_3, and acts as a glue between otherwise nearly immiscible oxides, enabling the formation of a more coherent scale with elimination of fast-diffusion paths.

- Decrease of oxygen solubility in the alloy.

A beneficial effect from Nb ion-implanted into γ-TiAl-alloys at 927°C was demonstrated by Taniguchi (1996). His use of alumina in a slurry for polishing surfaces prior to oxidation is questionable, since the possibility exists of embedding the alumina particles into the substrate and thus altering the oxidation behavior. An attempt to overcome this potential complication was made by comparing unimplanted materials with implanted materials that were treated in the same fashion, including annealing prior to oxidation to remove implantation damage.

Sunderkotter et al. (1996) studied the effect of Nb in γ-TiAl-alloys oxidized at 800°C in air. Nb was added both as an alloying element as well as by ion implantation.

2.7 Oxidation of Titanium Aluminides at Lower Temperatures

A significant cost savings can potentially be realized by using titanium aluminide alloys (which are of relatively low density) in those portions of jet engines that operate at lower temperatures. It has been reported (Superalloys '88, TMS, 1989) that the cost savings resulting from removing a pound of weight from a jet engine amounts to $800 over the life of the engine. Froes (1992) reports an estimate that approximately 30% of the engine could be ceramics, intermetallics, or ceramic composites. If only half of this 30% involved titanium aluminides (ρ 4.2 g/cc) replacing conventional nickel-base superalloys (ρ 8.3 g/cc), this would provide a weight savings of 2,100 lb for a 28,000 lb engine. This weight savings would provide a total lifetime savings of $168K.

2.7.1 Thermodynamics of the Al-Ti-O System

The formation of alumina is always slightly favored thermodynamically over formation of rutile. But it is not usually mentioned that, as temperature decreases, the stability of alumina increases with respect to rutile (JANAF data, 1985)(See §3.7).

2.7.2 Alloying Additions

Kekare (1997) indicated that for the γ-TiAl-based alloys, ternary additions had little impact on oxidation behavior at the lower temperature of 704°C (in contrast to results from this study, Chapter 5). None of their ternary additions was Nb (despite indications in other literature that Nb improves oxidation resistance). Weight gains for an otherwise unalloyed γ-TiAl-alloy, with 400 and 600 ppm oxygen impurity content oxidized in compressed air at 704°C, were of order 0.13 - 0.17 mg/cm^2.

2.7.3 Temperature Dependence of the Nitrogen Effect

The beneficial effect of nitrogen is seen predominantly at lower temperatures, not higher. Becker et al (1992) for example, observed a switch-over point to no nitrogen benefit at 900°C and linear, catastrophic oxidation at 1000°C.

2.8 Notable Omissions in Prior Oxidation Studies

A search of the published literature on the oxidation of titanium aluminide alloys reveals a lack of previous work in the following areas:

- Oxidation of orthorhombic-Ti_2NbAl alloys has not been well studied at any temperature.
- Oxidation of all titanium aluminides has not been studied at 700°C or other lower temperatures. Although published results at 900°C and higher indicate the formation of non-protective scales, lower temperatures both favor and may result in the formation of protective scale.
- Short-time *in-situ* oxidation studies have not been reported, even though published results (Verma et al 1981) have noted the importance of transient behavior.
- No studies have reported on the mechanical behavior of the composite system consisting of the scales, depletion layers, and their underlying substrates. As part of alloy development efforts, studies have focused on the mechanical properties of the substrates only. Such studies can accurately describe the material's properties only

when a material is first placed into service. For the titanium aluminide alloys with application potential (γ-TiAl alloyed with Nb and Ti_2NbAl), there should be additional studies to see how the scale-substrate composite systems behave in real applications.

- Few TEM studies have been done to elucidate the mechanisms of scale growth at long times. Some TEM studies have been done for short-time exposures at higher temperatures resulting in thin, transient scales which were not typical of those found in application. TEM studies should be carried out on scales formed under conditions were the formation of protective scales might allow the use of titanium aluminides.
- Some microprobe studies have been performed to characterize the composition of scales formed during long-time exposures; however, these have suffered from a lack of resolution. Limited sample thicknesses and finite beam dimensions lead to the overlap of excitation volumes and prevents the resolution of fine features. Witness the niobia rich precipitates in Becker (1992).

Chapter 3

Experimental Procedure

3.1 Specimen Preparation

Titanium aluminides are often given complex heat treatments, to develop microstructures which are lamellar, duplex, or a combination of these two. It was beyond the scope of this work to study the effect of alloy heat treatment on the oxidation; therefore, materials were tested as received, without heat treatment. Comments concerning the potential effects of microstructure on the oxidation results are provided in §4.2.

Due to the characteristically slow growth rate of alumina scales, particularly at the reduced oxidation temperature used in this research, it was imperative that the sample preparation be consistent and reproducible from one experiment to the next and comparable to that reported in open literature. Surface treatment has long been known to strongly influence some oxidation rates and morphologies (see, for example, the microscopical studies of Sawhill et al (1985) and was a concern here since scale thickness was typically less than 1 μm.

A complete listing of all experiments run and resulting characterizations is given in Appendix A.

3.1.1 Slicing

From prior experience, intermetallics can be difficult to cut with conventional diamond or abrasive saws. A low speed saw, like that typically used for sectioning, can take many days to cut one slice from an ingot having 1 cm^2 cross-sectional area. For the Cr_2Nb intermetallic studied earlier (Duncan, 1994), one slice required two weeks. In addition, any vibration of the saw blade magnified cracks and other surface damage in these already brittle materials.

Electrodischarge machining (EDM) was therefore used to make slices 1 mm or thicker using an EDM Technology Model 200B unit operated at the microcurrent setting. A capacitance value (related to the gap between the wire and material being cut) of 9 and a resistance value (related to the sensitivity to contact between the wire and the material) of 2 were typically used. With these settings, slices took 6-8 hours or more to cut depending on the cross-section area. A brass alloy wire (Super Brass 900, InTech EDM Electrotools Inc.) was used, and a 100 μm diameter wire was preferred for proportionately less material loss and a smoother surface finish, and hence a thinner damaged layer. For removal of EDM damage, a minimum of 300 μm was subsequently ground from each face. (See also §7.2.2 for a further analysis of damage done by EDM slicing.)

The low speed saw was used in the preparation of the cross-sections, where the thickness of the IM was less than 1 mm, which allowed for timely cutting with minimal damage to the metal adjacent to the cut surface.

3.1.2 Surface Preparation

Standard metallographic polishing was subsequently employed, using a progression of silicon carbide polishing papers: 120, 180, 240, 320, and 600 grit. Sample thickness and dimensions were measured after the 600-grit step, to prevent scratching the final finish. For the final polishing steps, Microcut™ 800- and 1200-grit silicon carbide

papers were used. Their use avoided contacted with alumina polishing slurries, which could possibly embed alumina particles in the substrate, contaminating the surface and obscuring the effect of any native-grown oxide scale. 1200-grit paper corresponds roughly to a particle size of 2.5 μm; this is coarser than the 0.3 μm slurries typically used in many oxidation studies, but finer than many oxidation studies of titanium aluminides, where polishing was often stopped at 600-grit. The final polish used in this work was deemed to be adequate. The final polish with 800- and 1200-grit was performed no longer than 30 minutes prior to oxidation, and each sample was rinsed with acetone and then methanol immediately prior to insertion into the furnace. These steps comprise a reproducible method for reducing any native oxide remaining on the sample before exposure.

For *in-situ* studies, the presence of 600-grit (15 μm) scratches was useful as an orienting aid, and these scratches were many times left on the surface during final polish, or polishing was simply stopped at the 600-grit step. In common with conventional isothermal tests, each sample was polished no more than 30 minutes prior to the start of an *in-situ* test.

3.1.3 Metallography

The microstructures of all three model intermetallics were characterized. Representative portions of each of the intermetallics were mounted in EpoQuick™ epoxy and allowed to cure overnight in a fumehood. After polishing to 1200-grit silicon carbide, the samples were etched with Krolls reagent for a minimum of 10 seconds and examined in an light optical microscope (LOM). Only in the case of the specimen G, was 10 seconds sufficient; the other two intermetallics required longer etching times to develop contrast in the structure. Light microscopy proved sufficient to resolve the grain structures of G and A2, but the etched SA2 sample was also examined in the environmental scanning electron microscope (ESEM). In the case of SA2, the

microstructure required ESEM and transmission electron microscopy (TEM) to resolve the fine structure. Polaroid photographs were taken of the microstructures in the LOM and the ESEM, and digital images were stored from the scanning transmission electron microscope (STEM).

3.2 Isothermal Corrosion Studies

Isothermal oxidation exposures were performed on the intermetallics to measure kinetic corrosion rates and to compare studies alloy oxidation behavior. The majority of experiments involved exposures of 20 hours and 100 hours; however, several experiments involved only 2 hour exposures. The longer exposures were chosen to parallel service applications, while the shorter 2 hour exposures were chosen to characterize transient oxidation. The short term oxidation experiments also enabled a comparison of scales developed in a microbalance/furnace system to those scales developed in *in-situ* ESEM experiments.

As described below, both a Cahn microbalance/furnace and a DuPont microbalance/furnace system were used in the isothermal corrosion experiments.

3.2.1 Cahn Microbalance Operation

Figure 3.1 provides a schematic of the furnace, Cahn microbalance and gas inlet system. The vertical tube furnace was heated with resistive heating elements. The central tube was of high purity alumina to avoid evaporation of the refractory and reaction of impurities with the oxidants or samples. The inner diameter of this tube was 3.42 cm for a cross sectional area of 9.18 cm^2. This area was used to calculate the linear flow-rate of gases past the sample during an experiment. Platinum gauze was placed at the gas inlet and on a platform directly beneath the hot zone, to aid in the equilibration of the gas mixtures.

The furnace temperature was monitored continuously by a Type-S thermocouple which was run up from the bottom of the furnace parallel to the hangdown chain. To

check the accuracy of this thermocouple and the furnace controller, a standardized special limits Type-S thermocouple (Hart Scientific, serial number S38940) was used. The temperature profile was periodically monitored to verify the temperature stability. The Hart thermocouple was calibrated to the requirements of MIL-STD-45662, with uncertainties of no more than 1.0 degree in the range of 0 to 1100°C using NIST test procedure 249506C.

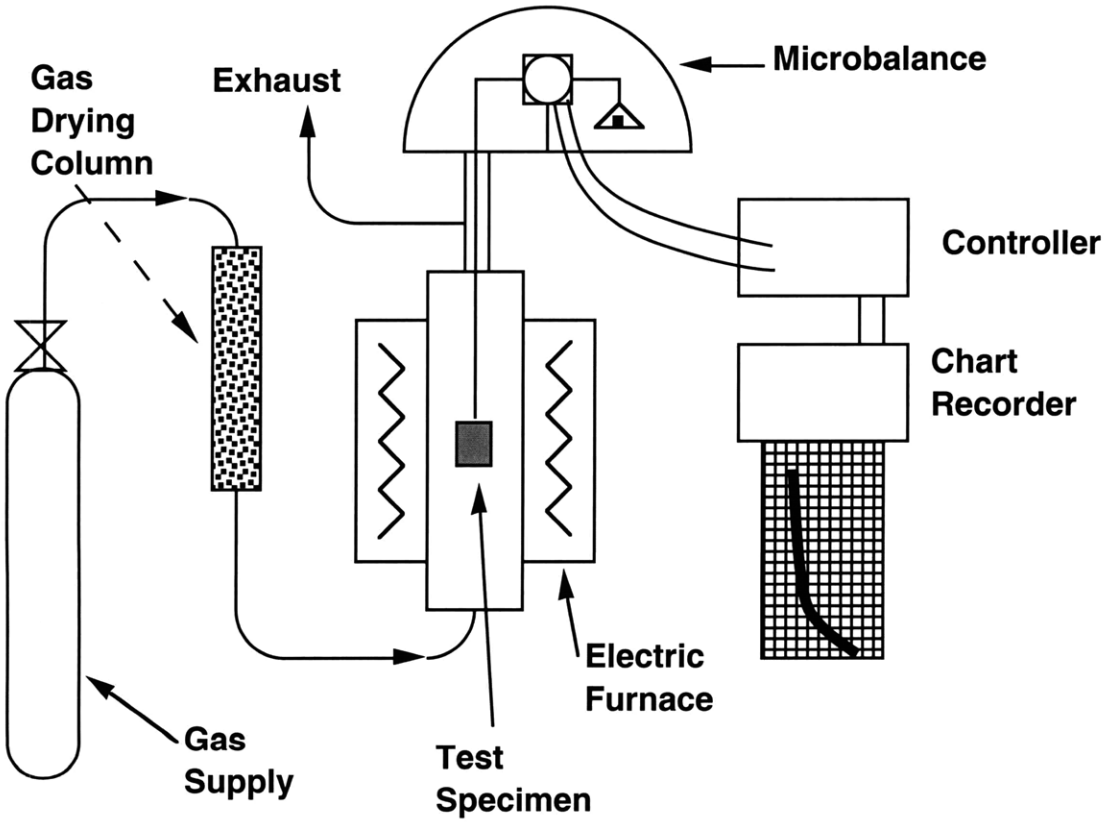

Figure 3.1 Schematic representation of furnace, Cahn microbalance and gas mixing system.

3.2.2 DuPont Microbalance Operation

A tabletop microbalance (DuPont 951 Thermogravimetric Analyzer with the DuPont 9900 Computer/Thermal Analyzer controller interface) was used to perform

additional experiments. A schematic representation of the system is shown in Figure 3.2. The DuPont 951 TGA consists of a fixed, horizontally-mounted tube furnace and a movable quartz sample chamber which encloses the electronic balance. Oxidation samples were hung on the balance by means of a horizontal quartz beam with a notch for accurately positioning the sample. Attached opposite the beam was a hook on which counterweights could be hung to mechanically tare out the majority of a sample's weight.

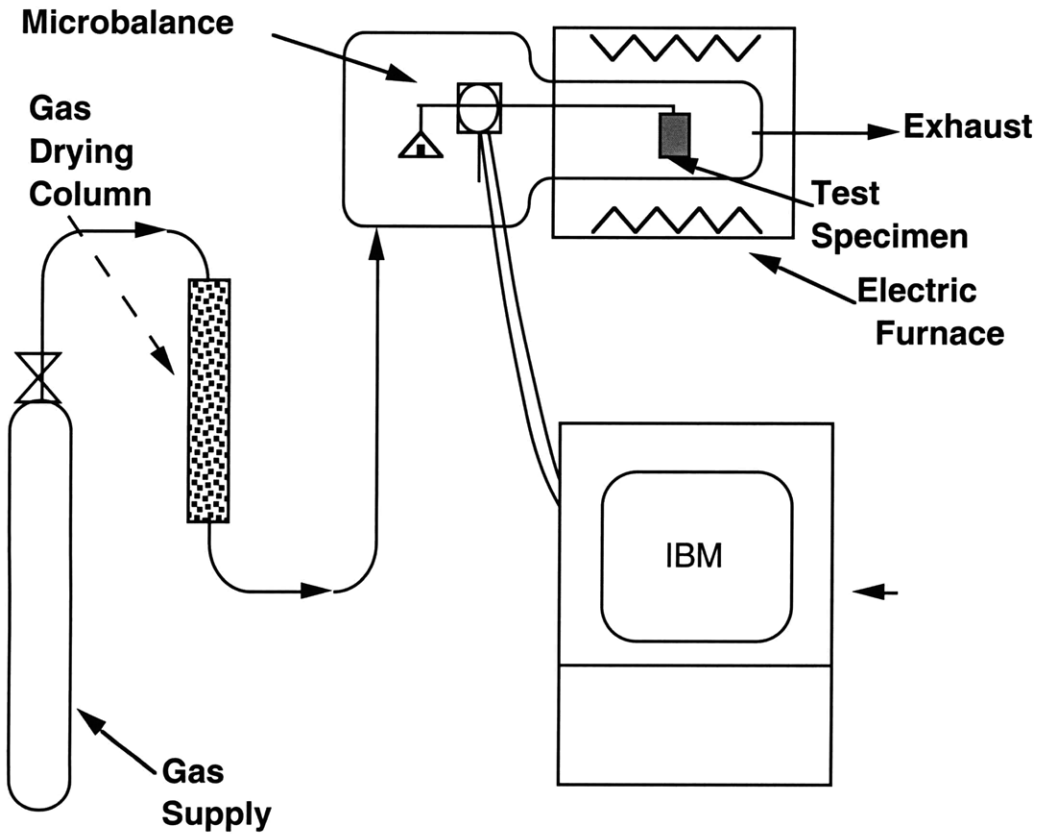

Figure 3.2 Schematic representation of furnace, DuPont microbalance and gas mixing system.

After the sample and counter weights are hung, the quartz sample chamber is closed and the balance and the quartz sample chamber are transported horizontally on a set of rails. The length of the quartz sample beam and the dimensions of the quartz chamber are such

that the oxidation sample was positioned at the center of the hot-zone in the furnace. The DuPont 951 can accommodate a sample size no heavier than 500 milligrams (including the hanging hook if used) and with dimensions no larger than 12 mm long and 7 mm wide.

The DuPont 9900 Computer/Thermal Analyzer is a software-driven controller and data acquisition system. The main menu has two menus -- one for instrument control and one for data analysis. The instrument menu controls are described below. The data analysis menus are described later in the §3.2.4.

Under the instrument control menu are three submenus that control the method (temperature profile), the experimental parameters (such as sampling rate), and the signal control (where the sample weight could be zeroed either before or during a test). With the method menu, one can specify the final temperature and the heating rate (either a controlled ramp rate, or the maximum rate which the furnace would achieve at full power). The temperature profile was programmed into the computer -- typically consisting of several of the following segments:

JUMP	ballistic heat/cool to final temperature and immediately starts the next segment
EQUILIBRATE	controlled heat/cool to final temperature and starts next segment when the temperature is stable
INITIAL TEMP	controlled heat/cool to final temperature and stabilize. Will only continue segment sequence when START is pressed
ISOTHERMAL	hold isothermally at current temperature
SAMPLE INTERVAL	controls the time interval between collected data points
DATA STORAGE	enables/disables data storage
RAMP	controls heating/cooling rate to a set temperature

No cooling segment was used, since the samples were pulled out of the furnace and allowed to air cool. The typical programmed method consisted of JUMP to the desired isothermal temperature, EQUILIBRATE to ensure that the furnace temperature is stable, and ISOTHERMAL for a period of time longer than the intended experiment.

The experimental parameters menu contained the sample description, the method description, and the option to switch gases mid-experiment, which was not utilized in these experiments. The signal control menu contained the weight calibration data and offered automatic or manual zero functions with which the initial weight could be zeroed and which are described in more detail in §3.2.4. Lastly, the signal control menu also displayed the current set point and the segment times and temperatures.

A standardized special limits thermocouple was used to calibrate the temperature and a correction factor of 5°C was used for all the experiments conducted in the DuPont analyzer. Prior to carrying out experiments with the DuPont system, a calibration of the lever arm of the microbalance was performed using a precision-calibrated 50 mg weight and the correction factor of 1.104 to the balance reading was determined and utilized for the duration of the tests.

3.2.3 General Microbalance Operation

The gas flow rates were calibrated and verified using a soap bubble and burette prior to using the microbalances. The flow was established and allowed to equilibrate for several minutes. The time for the bubble to sweep a particular volume was measured with a stop watch. This time was measured a minimum of three times to ensure a constant flow rate and the measurement repeated if the flow rate varied. The rates were checked at many points along the flow range and especially at the extreme ends. A plot of the bubble rates versus flow rates was plotted and points were repeated if a straight line fit to the data had a root mean square (RMS) deviation of less than 0.95. Often, the RMS

deviation was 1.00 or very close. These data were plotted for each gas composition run through the furnaces, and the points were rechecked over time to verify their constancy.

After final polishing and rinsing, the sample was suspended from the microbalance or hung on the quartz beam. Counterweights were added to the opposite side of the balance. For the DuPont balance, the heating program was started to equilibrate the temperature. It took less than 3 minutes to reach 700°C, and the furnace was allowed a minimum of 10 minutes to settle into the temperature. The desired gas mixture was introduced into the system to flush out the ambient air, and the gas currents inside the balance and furnace were allowed to equilibrate. When a gas mixture other than air was used, extra care was taken to flush out the residual ambient air thoroughly to avoid contaminating the gas composition. Erroneous gas environments could have a significant impact on the sample results, for example when the effect of nitrogen was investigated. Flooding was done with a flow rate several times higher than the operating flow rate. The operating flow-rates for the Cahn balance was 0.15 l / min or greater. For the DuPont balance, flow rates in the range of 0.3 - 0.5 l / min were used as suggested in the manual.

At least 5 minutes before the start of the experiment, the flooding flow rate was reduced to the oxidation flow rate. Final precise balance zeroing was accomplished with a potentiometer; the offset was recorded. Static electricity was found to cause erratic readings; therefore, the balance housing and furnace tube were rid of static before each run by spraying with an ammonia solution (Windex™) which was allowed to dry by evaporation. Wiping the glassware was avoided, as this could introduce additional accumulated charge.

In both balances, the sample was rapidly inserted into the furnace and brought to reaction temperature. In the DuPont balance, the furnace tube and microbalance were slid into the furnace until the sample was centered in the hot zone; the segment time was

then noted. Insertion into the hot zone of the furnace took on average less than 0.3 seconds. To compensate for the apparent increase in weight due to the thermal expansion of the quartz beam (which changes the lever arm moment), the sample was allowed to heat for 2 minutes and then the weight was re-zeroed. This procedure eliminates an abnormally large weight gain for the first time interval (6 minutes) and brings the initial weight closer to zero for the relative weight differences which are needed for analysis. During an experiment, a plot of weight gain versus time was displayed in real time, and the oxidation conditions were monitored (the temperature is recorded in a file and rarely varied more than 1 degree over a 20 hour experiment, except in unusual instances). The gas flow rate was checked periodically and recorded, to note any variance from the initial setting (also a very rare occurrence, which resulted in the experiment data being discarded).

Sample insertion for the Cahn system involved suspending the sample by a hang down chain attached to a magnet so that it was located in the cold zone above the furnace as the experiment was being set-up. The sample was lowered into the hot zone in fewer than five seconds, and kinetic data were collected after adjusting the electronic weights, a procedure requiring less than one minute in most cases.

At the end of each experiment, the sample was rapidly cooled to room temperature by sliding the furnace tube away from the furnace in the DuPont system or by raising the chain and sample in the Cahn system. Data collection continued (and the weight losses compared to the weight gains registered at the beginning of the run) and the samples took on average 10 minutes to reach ambient temperature, as determined by a thermocouple located within 1 cm of the sample coupon.

Sampling frequency could be varied and was typically 9 seconds per point. Longer, 100-hour runs in the DuPont system required a slower sampling frequency of 50 seconds per point to avoid having the file fill up a 5" floppy disk. The DuPont balance

was left on permanently to avoid any instabilities that occurred when first turned on, during which time the balance over-corrects and requires some time for the transient to damp out. In addition, the floppy disks containing the controller software were those originally supplied with the instrument some 20 years ago and were not copiable; so, to avoid having the system crash with no ability to reboot, the system was left on at all times.

3.2.3 Comparison of Microbalances

One obvious advantage with the availability of both the Cahn and DuPont microbalances was the potential to carry out two oxidation experiments simultaneously. Although the test results were generally the same, there were distinct differences between the two systems.

The main advantage of the Cahn microbalance was the large furnace tube and long hot zone, which allowed larger samples to be reacted. When pre-oxidizing substrates for *in-situ* straining studies, this large furnace capability enabled multiple samples to be processed simultaneously. The maximum weight allowed on the Cahn microbalance is 10 g total. After subtracting the weight of the hangdown chain, approximately 3.2 g, the maximum sample weight was approximately 7 g. Sample widths were restricted only by the furnace tube diameter, which at 3.42 cm far exceeded any dimension of the typical oxidation specimen. The length of specimens was restricted to 2 cm by the thermocouple sheath coming from the bottom of the furnace. However, the hot zone length over which the temperature varied less than 1°C extended only over 3 cm, which proved the ultimate limit on sample length.

The main disadvantages of the Cahn were its poorer resolution and sensitivity, the reliance on a strip chart recorder, and the long length of glass tubing that enclosed the hangdown wire above the furnace. The strip chart recorder occasionally failed to maintain a constant chart speed or had other problems that resulted in a loss of data for

some period of time. The long length of glass tubing above the furnace resulted in static electricity problems, which would cause the hangdown wire to drift to the glass resulting in erroneous weight readings. The static problems could be partially remedied by operating the microbalance at a reduced sensitivity and by regular application of the ammonia cleaning solution (Windex™) followed by a settling period of 1 hour or more, during which the balance equilibrated and the static charge dissipated. Unfortunately, the static electricity problems often occurred at the beginning of experimental runs, where the weight gains were the greatest and therefore sampled more frequently. This made it impossible to procure reliable data for short-term or transient behavior, since the results were not reproducible on the 1 or 2 hr scales. The Cahn was, therefore, much more attractive for longer oxidation runs where transient effects were of less interest.

The main advantages of the DuPont microbalance system were its greater sensitivity and precision, which are higher by a factor of about five compared to the Cahn balance, and its significantly smaller and less massive furnace, which was easier to change in temperature than that used with the Cahn microbalance. Indeed, the temperature of the DuPont system was raised to the oxidation temperature for each experiment. The temperature of the Cahn furnace was set, repeatedly monitored and adjusted, and then allowed to stabilize at least 24 hours before temperature stability was achieved to within $\pm$ 1°C. Following this equilibration, the furnace in the Cahn system was maintained at the same temperature (700° or 800°C) for weeks or months while experiments were carried out. The reference thermocouple was monitored continuously to verify the furnace temperature, and the furnace was occasionally checked with the standard thermocouple.

3.2.4 Thermogravimetric Data Analysis

The Cahn and DuPont microbalance systems record weight or weight change as a function of time. Because oxidation is predominantly a surface phenomenon, it is

standard practice to normalize thermogravimetric data by the specimen surface area. Specimen surface areas were calculated in several ways. When the sample had a regularly shaped cross-section such as a circle or rectangle, the area was calculated using sample dimensions. When the sample had an irregular cross-section, the specimen profile was traced onto 1 mm x 1 mm graph paper, and the area determined by counting squares. The contributions of the specimen sides (edges) and of the hanging hole were also included in the total surface area determinations; the cylindrical surface area created by the hanging hole adds to the overall surface area, while the two circular areas removed from the faces subtract from the overall surface area. A Mitutoyo 293-701 digital micrometer with an accuracy of $\pm$ 0.001 mm, was used to measure all specimen thickness and lateral dimensions. In some instances, such as shorter runs or experiments with G samples which typically displayed very low weight gains, the above methods did not provide an adequately accurate value of specimen surface area. To achieve more accurate areas, the samples were digitally optically scanned with a known length scale and area, and the area calculated using Image Pro® software. For scanned areas, the areas of the hanging hole on both sides were also carefully measured. Image Pro® software had a measuring menu that enabled one to calculate both lengths and areas. These were both used with the calibrating features (the length scale and known area) to compensate for any systematic errors in the sample measurements. Both auto-trace and manual tracing were performed, and all measurements were made a minimum of 3 times for reproducibility.

The Cahn and DuPont microbalances record their data in different formats. With the Cahn balance, the weight data is continuously outputted in analog form on a strip chart recorder, whereas, with the DuPont balance, the digital data are written periodically on a floppy disk. To the greatest extent possible, the data analysis protocols were kept

the same for each microbalance, so that results could be meaningfully compared for the two instruments.

The strip chart recordings from the Cahn had a slowly changing signal due to weight change of the sample combined with a low amplitude, rapidly changing, noise signal due to unknown causes (possibly adjacent pedestrian traffic and general building vibrations). This noise was eliminated from the data by manually drawing a curve centrally through the data trace. A value of zero on the weight (y) axis was assigned to the (y) value of this curve at zero time. Data (weight gain) were then read from the chart as follows: points were taken every 6 minutes (0.1 hr) for the first hour, every 12 minutes for the second hour, a point was taken at 2.5 hours and then at every hour up to 40 hours, and then every two hours. This protocol allowed for the collection of many data points at the beginning where the weight gain was most rapid and where transient behavior is of prime interest.

The measured weight gains were normalized by the surface area of the sample and plotted against the square root of time. These data were fit with a straight line using least-squares linear regression. The slope of this line was used in calculating a parabolic rate constant for the weight gain.

Data analysis using the DuPont Thermal Analyzer software accompanying the microbalance measurement software draws on two main programs. The first was the real-time plotter, RT-PLOT-1.1, which displays on the monitor the specimen weight in real time during an experiment. Parameters along either axis (weight gain on the y axis and time on the x axis) could be displayed as well as temperature. Temperature was monitored closely in the initial experiments, until such time that it was determined that the temperature had varied no more than a total of 1°C over a 20-hour experiment duration. Later, the stored temperature was consulted only when an anomalous weight change was recorded (such as would happen with power surges or building vibrations).

The second program, TGA-2.0, was a more complete plotting program with routines for rescaling, customizing (paint, annotate, determine specific point values), analyzing (with step transitions, tangents, inflections, half heights) and printing the data.

Data from the DuPont microbalance and analyzer are typically outputted to a dedicated plotter via the RT-PLOT and TGA programs. Since the DuPont microbalance system used in this study lacked a plotter, the numerical data were simply displayed on the monitor and then transcribed to a data sheet. The data values were read at the same time intervals as those used when reading the strip charts from the Cahn. As with the Cahn, weight gain data were normalized by the surface area of the sample and plotted against the square root of time. The data were again fit with a straight line using least-squares linear regression. The slope of this line was used in determining the parabolic rate constant of the weight gain.

Although each experiment in the DuPont microbalance had been re-zeroed after 2 minutes of exposure, the parabolic plots frequently had non-zero intercepts on the weight (y) axis. Similar observations were made for plots from experiments run in the Cahn where a zero was assigned by extrapolation of the hand-drawn curve. Whenever the plot of normalized weight gain vs. square root of time had a non-zero intercept, the value of the intercept was used to adjust all subsequent weight gain data so that zero weight gain would correspond to the start of the experiment. This re-zeroing allowed a more meaningful comparison of the linear TGA plots and had no impact on the value of the computed parabolic rates, since the latter depend on the slope of the parabolic plot lines.

After correcting the Cahn or DuPont data for zero, the resulting total weight gain per unit area was compared to the value obtained by weighing each sample on a Mettler balance before and after oxidation. If the numbers did not agree, the data were discarded,

and the experiment was run again. A typical variation in the weight gain per area measured was 9 %.

It should be noted that the parabolic rate constants calculated determined in this study are the thermogravimetric constants (mass change) and not corrected to the true parabolic constants (thickness change). The principal reason for leaving the data in this uncorrected form is the morphological complexity of the scales resulting from oxidation experiments. For a simple single component scale, the thermogravimetric parabolic rate constant could be converted into a rate constant for the overall scale thickness growth by using the conversion factor of molecular weight and stoichiometry and assuming the growth of a fully dense scale. For the complex scales formed in this study, an accurate conversion to true parabolic rates would require an determination of the scale composition and of the relative amounts of each scale component. In this study, the oxide or oxynitride scales produced were often thin and not well delineated and therefore difficult to accurately characterize. Since the comparison of one sample to another was the main goal of this study, such conversion was not deemed necessary. Whether explicitly stated or not, many literature values are also reported in this fashion.

3.3 SEM Analysis

3.3.1 Scale morphologies

Sample surfaces and cross-sections were examined primarily in the environmental SEM, which allowed samples to be imaged without application of conductive coatings (gold or carbon) which may have altered the structure. The absence of any coating also allowed other surface analysis techniques to be employed subsequently without concern for sample contamination from the evaporated coating. (e.g. glancing angle x-ray diffraction (GAXRD)). Since coatings weren't necessary, the samples could also be re-exposed, for cyclic oxidation studies.

3.3.2 Fracture Cross-sections

The ESEM was used to produce binary x-ray energy-dispersive spectroscopic (XEDS) maps of specimen cross-sections, particularly those obtained by fracture. Fracture cross sections allowed observation of grain structure and reduced sample contamination accompanying polishing. In addition, the slightly irregular surface improved image contrast; the smooth polished surface proved difficult to focus on.

Fracture cross sections were prepared as follows: First, a small slice was cut from the oxidation specimen. The location of the slice was chosen so that the saw blade passed through the hole drilled for the hook; this effectively resulted in a pre-notched specimen, which fractured in the hole region more often than not. Fracturing was accomplished by cooling the slice of material in liquid nitrogen temperatures (77K) for a minimum of 1 minute while holding the sample with pre-cooled pliers and then striking or driving the slice at an angle against a flat surface. A towel or appropriate pad was used to collect the broken pieces. The two fractured sample pieces were mounted onto a specimen stub or in a vise, with the substrate and the cross-section surface face-up, and then viewed in the ESEM. Specimens were fractured shortly before examination, to reduce further oxidation or incidental contamination on the sample.

The x-ray mapping was conducted in the ESEM using Link x-ray hardware and Genie® software controlled the digital imaging. The detector was located 2° below the sample holder and required tilting the sample (by approximately 10-20°) to allow emitted X-rays to reach the detector. Highly irregular surfaces created artifacts because of the high sensitivity to specimen-to-detector distance and due to the configuration of the detector relative to the sample. Studies were made using windows of 128 or 256 gray scales and 8 bit precision. Dwell times ranged between 5 ms and 50 ms, with 50 milliseconds being typical for the samples in this study and a counter-dwell of 51 microseconds. An electron image was collected along with the x-ray maps, but

principally for orientation purposes. Images with scale bars were made on the untilted sample so that dimensions could be determined without errors due to foreshortening.

3.3.3 *In-Situ* Hot Stage

Although adaptations have been made to conventional SEMs to accommodate in-situ corrosion studies, the extremely low oxygen partial pressures on the sample surface prevent realistic simulation of actual corrosion conditions. The ESEM has overcome this problem by using a differential pumping system and is capable of imaging gaseous corrosion products forming at gas pressures ranging from high vacuum down to 20 torr. Secondary electrons emitted from the sample are accelerated towards the detector and collide with gas ions enroute. These collisions liberate more ions and cause a cascade discharge which increases the detected signal. In addition, positive ions generated have the benefit of neutralizing any charge build-up on the specimen surface, thus making it possible to work with uncoated specimens.

The ESEM is equipped with a hot stage attachment that can nominally reach temperatures of 1000°C, but based on preliminary calibrations, the surface temperature reaches only about 900°C. More complete and careful calibrations were not conducted after it was determined that the ESEM resolution was inadequate for studying the oxidation of titanium aluminides. Resolution and image contrast can be changed by altering various parameters. The filament type, gas type, presence or absence of water vapor in the ESEM chamber as well as the voltage, current and aperture all play a role and can be optimized for imaging.

Samples for *in-situ* experiments were typically polished to 100 to 200 μm thickness, after determination that thicker samples took significantly longer for the surface to reach oxidation temperature. As mentioned earlier, samples were polished to 1200-grit silicon carbide, and then scratched with 600 grit silicon carbide grit to introduce orientation markers. Alternatively, samples were polished only to 600 grit silicon

carbide, then degreased with acetone and ultrasonically cleaned with methanol. Samples were fixed into a 5 mm alumina crucible, and the crucible fixed temporarily to the furnace with a high temperature ceramic cement to prevent movement of either sample or crucible during heating from the convective forces within the furnace. The crucible sits directly over the heating elements and thermocouple and is typically covered with a heat shield which protects the chamber and specifically the microscope's electron detector from the heat. The heat shield restricts the field of view to about 0.25 mm^2 and also limits the minimum working distance. Energy dispersive x-ray spectrometry (EDS) is not feasible, because the detector is located 2° below the horizontal and it is not possible nor advisable to tilt the hot stage. In addition, the detector window is not heat resistant.

The standard stage is replaced by the high temperature stage. The temperature is controlled manually, as this minimizes the chance of damage to the furnace. The final oxidation temperature is achieved in several steps, so that the heating rate is not so high that an acceptable image of the specimen could be retained at all times. During heat-up there were often drastic contrast changes that occurred at specific temperatures which varied from sample to sample. An initial run was used to monitor and record these changes and the temperatures at which they occurred, in order to maintain focus at high magnifications during subsequent runs. The stage has flowing water cooling, which was not found necessary until temperatures of 500 - 600°C. The start of water cooling also has an impact on the image quality and requires adjustments to brightness and contrast.

The atmosphere in the ESEM can be selected and controlled. Room air can be used, which passes over a wet wick to provide moisture that improves image quality by the production of additional electron interactions. Alternatively, auxiliary gas can be used, which could be dried or left with residual moisture from the gas cylinder. The ionizability of each gas or gas mixture variously governs image quality. Nearly any gas

can be used, with precautions taken for corrosive gases which might damage the inside of the ESEM stage. Pure oxygen was not used, owing to the danger of igniting the pump oil while being evacuated. The ESEM can be operated up to pressures of 20 torr (3 kPa), but more typically in a range from 1-10 torr. It was found that lower pressures in the 2 torr range worked best for the high temperature work.

The *in-situ* studies reported here were all performed while heating the sample in the desired gaseous environment. This was a process that took up to 1/2 to heat till the desired temperature and contrasts with the rapid "hot insertion" technique of the ex-situ studies, where the sample is "instantly" immersed into the desired temperature and the sample attains the target temperature in only a few minutes. Efforts were undertaken to attempt the heating portion of the exposure in either a non-corrosive or non-oxidizing environment. As is so often the case, corrosion was minimized, but not eliminated, even when using reducing gas mixtures such as forming gas, a mixture of argon- 6% H_2. Efforts to use a getter located next to the sample failed in the sense that the getter performed its function too well, and continually preferentially consumed the oxygen, even when the oxygen was intended to corrode the sample. Attempts to calibrate the size of getter, to be "depleted" or fully oxidized when the sample was at temperature were not successful.

The approach taken for observing and recording most studies was to stay fixed on a specific site, locatable by landmarks, which were often scratches. This entailed a full-time endeavor, with the sample often charging and the image drifting off the screen. Additionally, the contrasts and brightness were often changing and required continuously adjustment. Additionally, the stigmation was also checked and altered as needed. Often for ease of comparison, the magnification was left fairly constant. At times, this could lead to a limited view of what was occurring, by either focusing on either too large or too small of an area. Switching between magnifications could cause confusion in comparison

of the size scales of observed phenomena. This limitation is also a drawback for TEM or even microscopy in general. A larger magnification allows a closer perspective of the process, yet the blown-up view also yields the possibility of missing the "larger picture" and studying a non-typical, or non-representative event.

Stigmating was done at a higher magnification, however. A split screen with dual magnifications was useful to observe fine scale and more macroscopic events (cracking, an overall change in brightness or contrast due to scale growth or overgrowth). The image output is also attached to a videocassette recorder to monitor the experiment continuously and be replayed later.

Observations were made during heating of the sample, at the set temperature for a selected time duration, and during cooling. Scale cracking and spallation were expected to occur mostly during cooling.

Micrographs were taken of the specimen before and after exposure in the hot-stage at conventional ESEM operating parameters. This provided better images since the field of view and the working distance were not restricted by the furnace and heating shield. These micrographs were also used for direct comparison to ex-situ samples, taken with the conventional ESEM stage and conditions.

3.4 X-Ray Diffraction Analysis

3.4.1 Glancing Angle X-Ray Diffraction

Glancing angle x-ray diffraction (GAXRD) was conducted using a Rigaku 70 mm radius scanning diffractometer mounted on a 12 kW rotating Cu anode source. Typically θ was fixed at 0.5° and the diffraction angle 2θ was scanned from 20° to 75°. No significant peaks occurred at values higher than 75°, and there is larger error in the smaller angle peaks. In addition, the limited scale volume on the typical sample resulted in a comparatively large background signal in the 2θ = 5-20° region, which obscured any x-ray peaks located there. The source was operated at close to its maximum allowable

parameters (60 kV and 180 mA) to maximize the diffraction signal. Scans were made with step intervals of both 0.05° and 0.02° and compared for noise, with the interval of 0.05° being used most often for glancing angle spectra. A scattering slit 0.2 mm wide was used; no height limiting slits were used. Spectra were collected with the same parameters so that scans from different samples could be compared. GAXRD proved useful because of its shallow penetration and its emphasis on the signal from the thin film or scale over that of the substrate, (eliminating confusion from many substrate peaks). Many peaks of alumina and rutile overlap as do the various niobium oxides with each other, so quantitative comparisons were often difficult. Tables of the peak positions and intensities for typical phases detected in the current study are given in Appendix C.

3.4.2 Rutile /Alumina Ratios

An effort was made to analyze at least semi-quantitatively the relative amounts of rutile to alumina in the corrosion scale. Selected peaks were step-scanned to provide accurate relative intensities; the peaks selected were the strongest peaks of each oxide that were removed from the peaks of any other compound in the Ti-Al-Nb-O-N system. These peaks were compared to peaks of the substrate before oxidation to ensure that the oxide peak did not overlap with any substrate peak (see Table 3.1 for peak positions and indices). The step scans were conducted with steps of 0.05 and 0.02° and compared for noise levels; most typically, these scans were conducted with a step interval of 0.02° and a fixed signal collection time of 6 seconds.

Table 3.1 Oxide peak positions and indices

Compound	hkl	2θ Value
Rutile - TiO_2 (PDF #21-1276) tetragonal P42/mnm	(110) (strongest peak)	27.45°
	(211)	54.32
	(101)	36.09
	(111)	41.23
Corundum Al_2O_3 (PDF #42-1468 replacing#10-173) Rhombohedral	(113) (strongest peak)	43.36
	(104)	35.15
	(116)	57.50
	(012)	25.58

Identifiable peaks more than 1° apart from any other neighboring oxide or substrate peak were chosen. Peaks that did not overlap with other strong identifiable peaks were designated as usable peaks for that compound or phase.

3.5 TEM Analysis

3.5.1 Specimen Preparation

Cross-section (transverse) TEM sample preparation was based on the technique developed Drs. Wayne King, Catherine Cotell and Bruce Pint with suitable modifications for the intermetallics used in this study. The technique calls for making a "sandwich" of two strips of the oxide and substrate of interest. The transverse sections yielded much more information than sections parallel to the substrate surface because larger portions of the scale could be examined and the location of the various interfaces could be easily determined; establishing the precise depth of parallel-section scales was difficult.

The typical oxidized specimen had a surface area of approximately 1 cm^2 with a hole drilled at the top for hanging in the furnace. A strip off the top was cut at the top through the hole to make the fracture cross-section for the SEM as described above. Two further strips were scored for parallel TEM sections, these would normally be ultrasonically drilled using a 3 mm trepanning tool in a Gatan 601 ultrasonic drill. Parallel sections were not pursued in this study because satisfactory transverse sections were achieved and because the jet electropolisher that was instrumental in their production had met an earlier demise.

After scoring, the opposite face of the specimen was polished until the score marks polished through. The two resulting strips were sandwiched between two Ta half cylinders and then forced with glue into a 3 mm o.d. stainless steel tube. The two oxide faces of interest faced each other and were centered as close as possible to the center of the sandwich. Hardman® green epoxy cement was used for the gluing, because it is clear, resistant to water and high temperatures, and exhibits sufficient hardness. The stainless steel tube was glued with 5-minute epoxy inside a brass rod which precludes burr or saw damage to the subsequent slices. Figure 3.3 shows a schematic view from Cotell (1988) of the transverse section "sandwich".

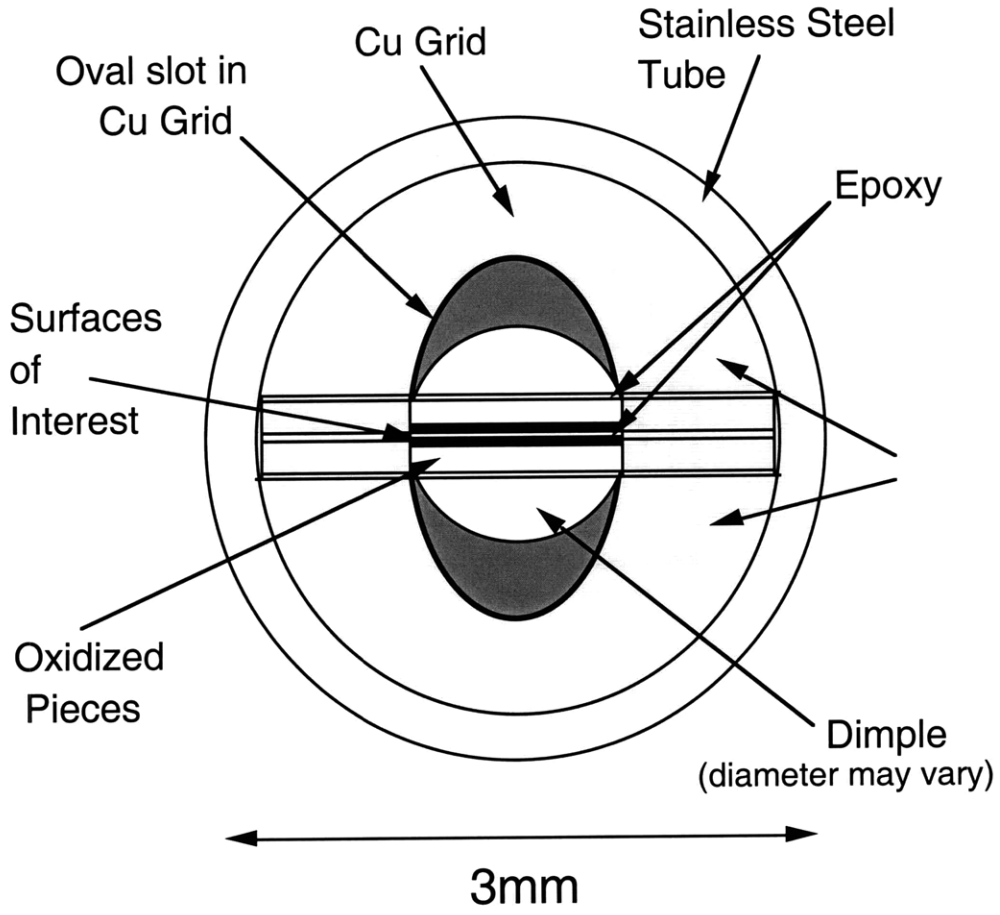

Figure 3.3 Schematic view of one slice of the transverse section "sandwich"

Slices of this "sandwich" are cut to a thickness between 300 and 400 μm. A Buehler Minimet® automatic polishing device was used to polish one side of this slice to approximately 100-120 μm with a 1 μm finish. The other side was dimpled in two stages, initially with 3 μm diamond paste and the final 20 μm or so polished with 1 μm diamond paste. The final thickness after dimpling was estimated to be 10 μm, which provided some leeway for error in the original slice thickness. A copper grid (with either a hole or slot, depending on the sample) was glued onto the dimpled sample for additional support. The sample was then ion-milled with a Gatan dual ion mill. Milling to a hole was carried out initially with a 15° incidence angle; a Gatan 600-32 laser

terminator was used to detect the incipient hole. After a hole is appeared, the sample was milled for 15-minute increments with the angle reduced to 12°. The sample was sometimes milled without rotation to selectively mill away a particular region of the sample, or milled from one side only, with the other side shrouded to prevent deposition of milled materials onto the other surface. A Wild-Heerbrugg light optical microscope operating a 400X magnification was used to determine if thin areas appeared promising. The sample was examined briefly in the TEM and milled more if necessary. Samples examined in the STEM were coated with a thin layer of carbon.

An attempt was made to eliminate the Ta halves by using thicker specimen/oxide strips, gluing together and coring out the intermetallic by use of EDM. However, this procedure proved unsuccessful: the strips did not always remain adhered to each other; the EDM did not always sense the two glued strips as conductive; the electrode did not always cut uniformly enough to allow convenient insertion into a stainless steel tube; and the alignment of the core, so that the oxide of interest remained in the center, could not be done accurately enough in the EDM.

Focused ion beam milling (FIB) and the tripod polishing were also considered. Inconvenient access to a FIB machine proved the major drawback to FIB milling. Tripod mechanical polishing was deemed to offer no time savings, and the brittle intermetallic substrate did not hold up well when polished to thicknesses much below 60 μm.

3.5.2 TEM Operation and Conditions

Conventional TEM work was conducted using one of two JEOL Co. (Tokyo Japan) model 200-CX TEMs, one with a tungsten filament used to check for electron transparency, the second with a LaB_6 filament used for imaging and diffraction studies.

3.5.3 STEM Conditions

The principal electron optical instrument used in this study was a 300 kV UHV field-emission scanning transmission electron microscope (FEG-STEM) equipped with x ray energy dispersive spectroscopy (XEDS) and parallel electron energy-loss spectroscopy (PEELS). The instrument, a Vacuum Generators Microscopes Ltd. (East Grinstead, UK) model 603B, was capable of producing a 0.5 nm electron probe; the XEDS system was an Oxford Instruments/ Link system featuring a windowless detector.

3.6 Image Processing

Increasingly electron microscopy images are no longer recorded on photographic film and printed from negatives but recorded, stored and manipulated digitally.

3.6.1 EM Images

Polaroids (Polaroid Type 55 film with both positive and negative) as well as video prints were still used for the ESEM. Positive images were subsequently digitally scanned using Photoshop software at resolutions of at least 300 dpi (depending on the file size). Images were recorded digitally on the JEOL 6320 field emission and the STEM and read into similar image files.

3.6.2 X-ray maps

The Link X-ray analytical systems used for both the ESEM and STEM put images of the cross-section and the digital x-ray maps of selected elements into one study file. Each had its own individual Link format, which was not compatible with each other without conversion. Files were removed from the Link computers onto floppy disks. Using software written by Dr. A.J. Garratt-Reed, the individual maps and image were extracted from each x-ray map study. The images were then processed similar to scanned images.

3.6.2.1 Black and White X-ray Maps

Black and white x-ray map images were simply extracted from their respective files and processed as normal scanned images. Since the images in the study were not recorded with scale markers and because the sample was tilted at least 15° to create the x-ray maps, the approximate scale bar was generated by using an ESEM image of the same area recorded while normal to the electron beam and used on the corresponding x-ray map.

3.6.2.2 Synthesized Color X-ray Maps

After extraction of the individual files, each map was assigned a color in Photoshop and then assigned a level of transparency (typically about 50%, depending on the individual map color and the total number of maps in the composite image. STEM images had no magnification scale indicator, so an approximate scale bar was generated from a STEM-SEM image of the same area as the corresponding x-ray map.

3.7 Thermodynamic Calculations Processing

Thermodynamic stability diagrams, depicting for each alloy element its respective stability with respect to oxygen and nitrogen and the thermodynamically possible oxide and nitride phases, were calculated using the aid of Outokumpu HSC Chemistry for Windows software, version 2.0, ©1994. Equations describing the stability of each compound with respect to the elemental metal and gaseous oxygen or nitrogen were written and saved and used to compile individual and composite diagrams (seen in Sections 4.4.1 and 4.4.2) at 700, 800 and 900°C. The thermodynamically feasible oxides and nitrides selected for the diagrams are listed in Table 3.2.

Table 3.2 Thermodynamically stable oxides and nitrides in the Ti-Al-Nb systems.

Alloy Element	Oxide(s)	Nitride(s)
Al	Al_2O_3	AlN
Ti	TiO, TiO_2, Ti_2O_3, Ti_3O_5, Ti_4O_7	TiN
Nb	NbO, NbO_2, Nb_2O_5	NbN, Nb_2N, Nb_3N

The standard free energies for each reaction were computed and compared when possible to other values in either the JANAF tables or literature values and differences noted.

3.7.1 Composite Stability Diagrams

The major assumption in constructing composite stability diagrams was the chemical independence of the scale phases or the non-interaction of one oxide on the other oxide stability. It is known, however, that the oxide titania can dissolve the "stable" alumina; therefore, this assumption has only utilitarian value.

Chapter 4

Materials

There are three intermetallic compounds identified in the Ti-Al binary system diagram: α_2-Ti_3Al, γ-TiAl, and η-$TiAl_3$. The existence of the $TiAl_2$ is still in dispute. Figure 4.1 shows these intermetallic compounds in the Ti-Al phase diagram.

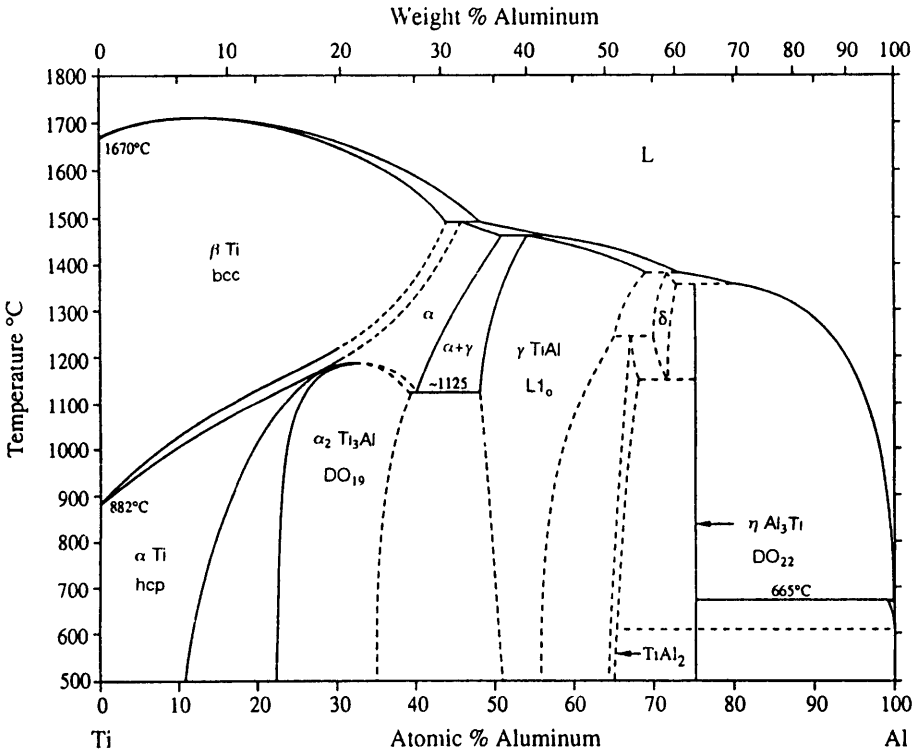

Figure 4.1 Phase diagram of the Ti-Al system (after McCollough et al 1989).

Of the three intermetallics, $TiAl_3$ is the most obvious candidate for a composition that would produce a protective alumina corrosion scale because of the high aluminum content. It is also the lightest of the intermetallics. However, $TiAl_3$ lacks sufficient ductility to manufacture even simple components. Attempts to use the $TiAl_3$ as a coating on other titanium aluminides have failed because the large thermal mismatch between $TiAl_3$ and the scale products, as well as other titanium aluminides.

Of the two remaining titanium aluminides, γ-TiAl has the next highest aluminum content. Typically, due the extreme stability of alumina relative to most other oxides, only a few atomic percent of aluminum is required in an alloy to form a continuous, protective scale. The similarity in stability of titanium oxides allows the kinetically faster forming rutile to nucleate at the same time as the thermodynamically more stable alumina in transient oxidation stages; the rutile nuclei inhibit formation of the continuous alumina scale required to slow corrosion in later stages. Because of the reduced activity of Al in the γ-TiAl, a 50 at.% Al composition is borderline in providing a protective scale. One major drawback to γ-TiAl based alloys is its low ductility and fracture toughness, and much of the research effort for γ-TiAl alloys has been focused on improving these room temperature properties.

The poor mechanical properties of γ-TiAl have given rise to consideration of the α_2-Ti_3Al compound instead for elevated temperature applications. It exhibits more ductility and fracture toughness at room temperature. A weakness in α_2-Ti_3Al is its high titanium content. Inherently, alumina formation is not stable for the α_2-Ti_3Al alloy and this lowers the upper oxidation limit to the rather low value of 650°C. Alloy additions to α_2-Ti_3Al are being explored to increase oxidation and creep resistance. An extreme example of Nb addition in the α_2-Ti_3Al system is the formation of orthorhombic o-Ti_2NbAl, which has one Ti replaced by Nb in the α_2-Ti_3Al structure.

Preliminary mechanical testing of the o-Ti_2NbAl alloy has shown great promise. Oxidation studies have not been conducted or reported. The slight increase in the density, owing to the Nb addition, would be acceptable if the result were a material that was both ductile enough for part manufacture and produced a thin, protective scale, presumably alumina based.

The thermomechanical processing for alloys of this type is typically complex, and, not a significant focus for this study. The influence of differences in grain size and microstructure was investigated in the *in-situ* observations, but the study was primarily comparative between alloys based on o-Ti_2NbAl and the unalloyed γ-TiAl and α_2-Ti_3Al titanium aluminide compounds.

4.1 Intermetallic Alloys

Table 4.1 lists the compositions and labels for the alloys used in this study. In this work, SA2 and o-Ti_2NbAl are used interchangeably, despite the fact that the composition of SA2 has only 23.5 at.% Nb rather than the stoichiometric 25 at.% amount. Analysis of the SA2 alloy showed the major phase to be the orthorhombic phase. Alloys G and A2 are each labeled as a single phase, although some small portion (3-5%) is composed of the opposing intermetallic compound. The A2 alloy is composed of primarily α_2-Ti_3Al with a small fraction of the alloy grains consisting of alternating α_2-Ti_3Al and γ-TiAl laths. Similarly, the G alloy is composed of primarily γ-TiAl with a small fraction of the alloy grains composed of alternating γ-TiAl and α_2-Ti_3Al laths.

Table 4.1 Compositions, labels and processing for alloys used in this study

Alloy Label	Composition (atomic percent)	Based on Intermetallic	Processing or Heat Treatment
G	Ti-47.9Al	γ-TiAl	HIPed at 1177°C for 2hr at 104 MPa
A2	Ti-25Al	α_2-Ti_3Al	Cast as finger ingot
SA2	Ti-25Al-23.5Nb	orthorhombic-Ti_2NbAl which is based on α_2-Ti_3Al	Forged

4.2 Metallography

Microstructures of alloys G and A2 were very similar except in scale. Figures 4.2 and 4.3 show the light optical micrographs of the two substrate microstructures at 165X magnification. Both had grains with embedded two-phase colonies of lamellar α_2-Ti_3Al and G, the thinner lathes being those of the opposite intermetallic to that of the nominal alloy composition. A2 had more angular, irregular, serrated and slightly elongated grains; the grains in G were more uniform and smooth.

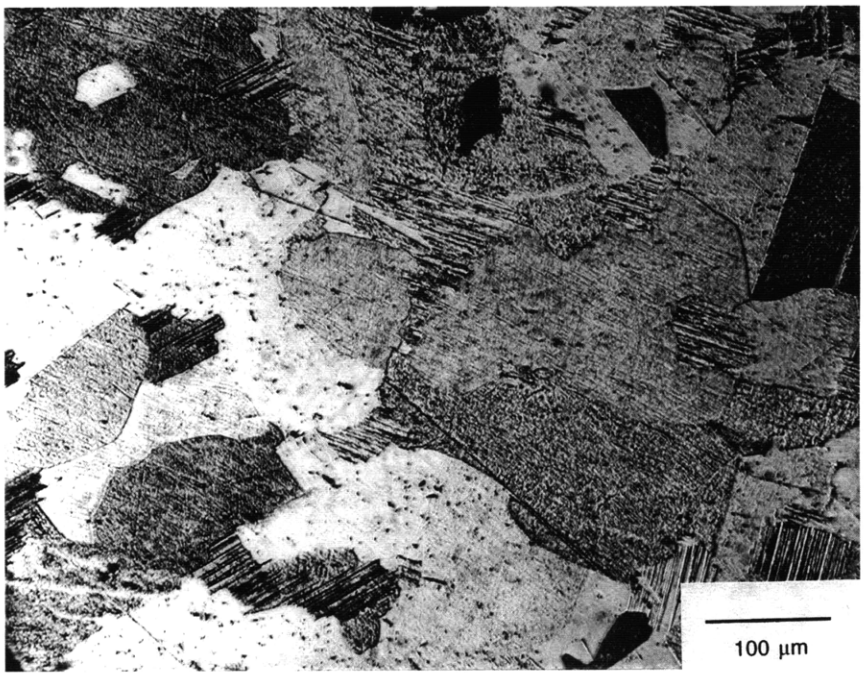

Figure 4.2 Light optical micrograph detailing the microstructure of G at 165X after etching in Kroll's reagent

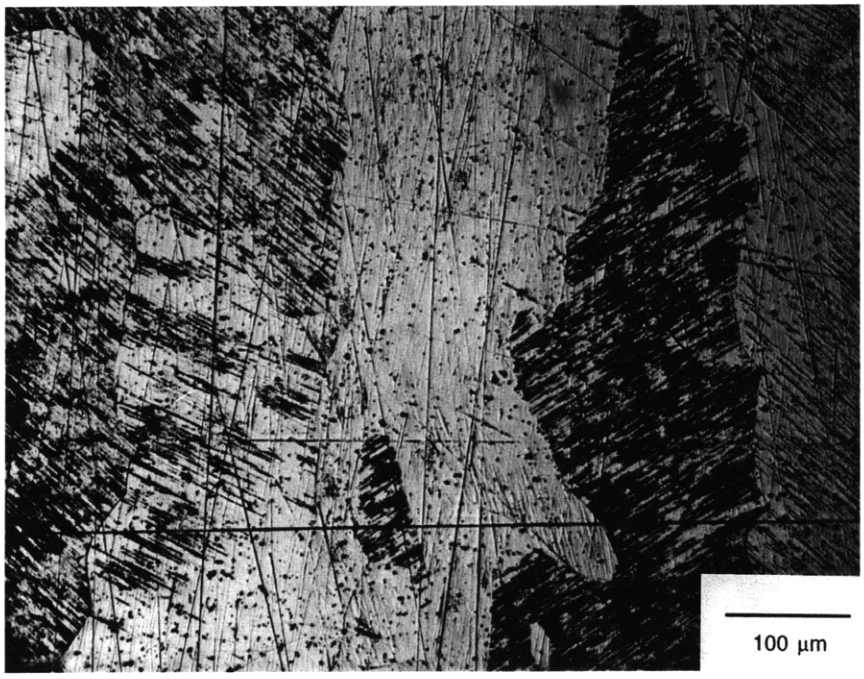

Figure 4.3 Light optical micrograph detailing the microstructure of A2 at 165X after etching in Kroll's reagent

The microstructure of SA2 at the same magnification appeared different from that of either A2 or G. The microstructure was much finer, and no regular grains were evident at light microscope resolution . Rather, a homogenous substrate was apparent with very directional ovoid features with darker outlines which sometimes coalesced and formed strings along the material processing direction. Figures 4.4 and 4.5 show the SA2 microstructure at two magnifications.

Observations of the etched SA2 in the ESEM were not particularly revealing due to the lack of contrast from the polished specimen. Digital x-ray maps conducted on the initial material showed no significant enhanced or depleted regions of Ti, Al, Nb or O.

TEM foils were made from the SA2 substrate using the same technique as that used for the oxidized samples. TEM of these foils allowed the microstructure of SA2 to be studied at still higher magnifications (Figure 4.6), as well as x-ray maps to be obtained at higher resolution than possible with ESEM (whose x-ray mapping resolution was limited to ~1 μm).

4.3 X-ray Analysis

XEDS was used to determine the phases and distribution of elements in the substrates before and after exposure. GAXRD was used to characterize the phases present and detectable in the initial substrates. Digital x-ray mapping performed on electron microscopes was used to determine substrate homogeneity. For G and A2, the grain size was large enough to be distinguished by LOM. The smaller grain size of the SA2 substrate necessitated the use of TEM.

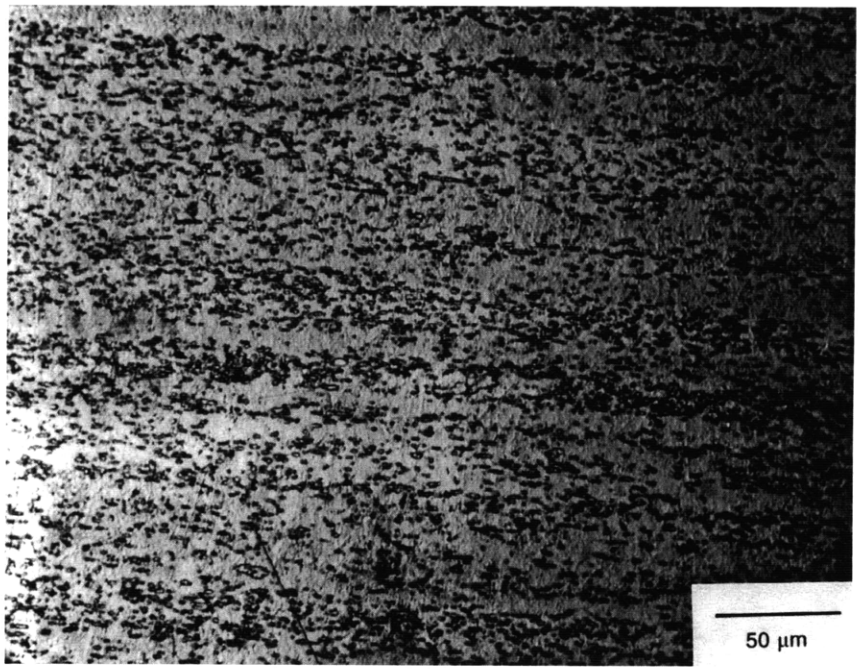

Figure 4.4 Light optical micrograph detailing the microstructure of SA2 at 330X after etching in Kroll's reagent

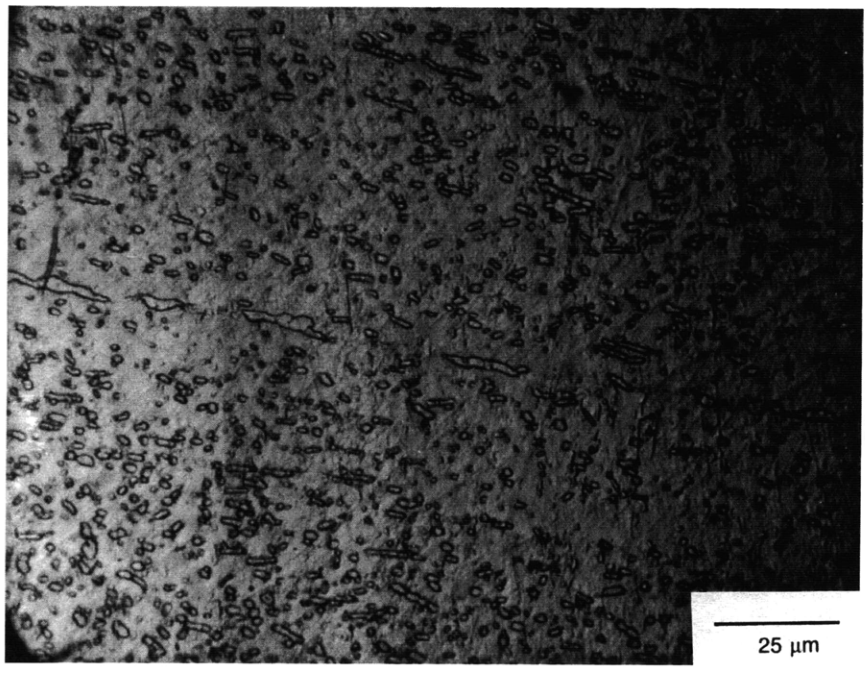

Figure 4.5 Light optical micrograph detailing the microstructure of SA2 at 660X after etching in Kroll's reagent

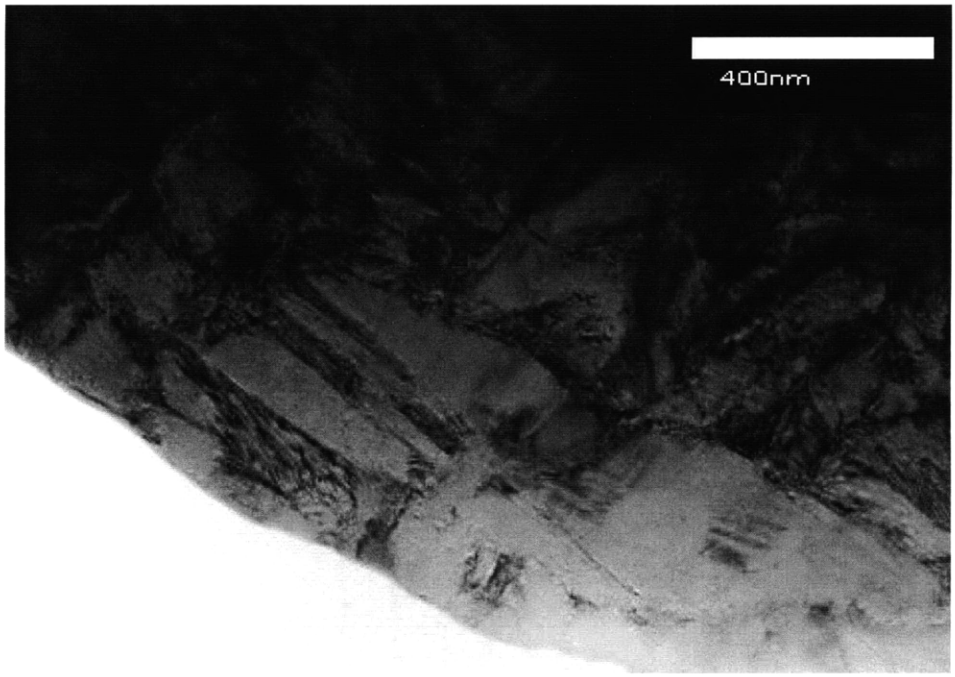

Figure 4.6 STEM micrograph detailing the microstructure of SA2 substrate alloy

4.3.1 GAXRD

Conventional x-ray diffraction would normally suffice for characterizing bulk metallic substrates such as those used in this study. However, since GAXRD was necessary for analyzing the thin scales, GAXRD was also used to characterize the substrates. In this way, substrate peaks could be readily identified in GAXRD spectra of the scales under similar collection conditions.

Powder diffraction cards that matched the substrate phases occurring in this work are given in Tables 4.2 and Table 4.3 with peak positions rounded to the nearest tenth of a degree and their intensities noted. Figures 4.7 and 4.8 depict the GAXRD scans for both G and A2, with the peaks identified in the corresponding JCPDF card superimposed.

Table 4.2 γ-TiAl peaks from PDF card # 42-1137

Fixed Intensity (%)	h k l	2θ Value (°)	Notes
100	111	38.9	
50	200	45.0	
50	020	45.8	
50	202	65.5	
50	220	66.1	
50	113	79.0	out of the range scanned in this study
50	131	80.1	out of the range scanned in this study
10	001	22.0	out of the range scanned in this study
10	110	31.7	

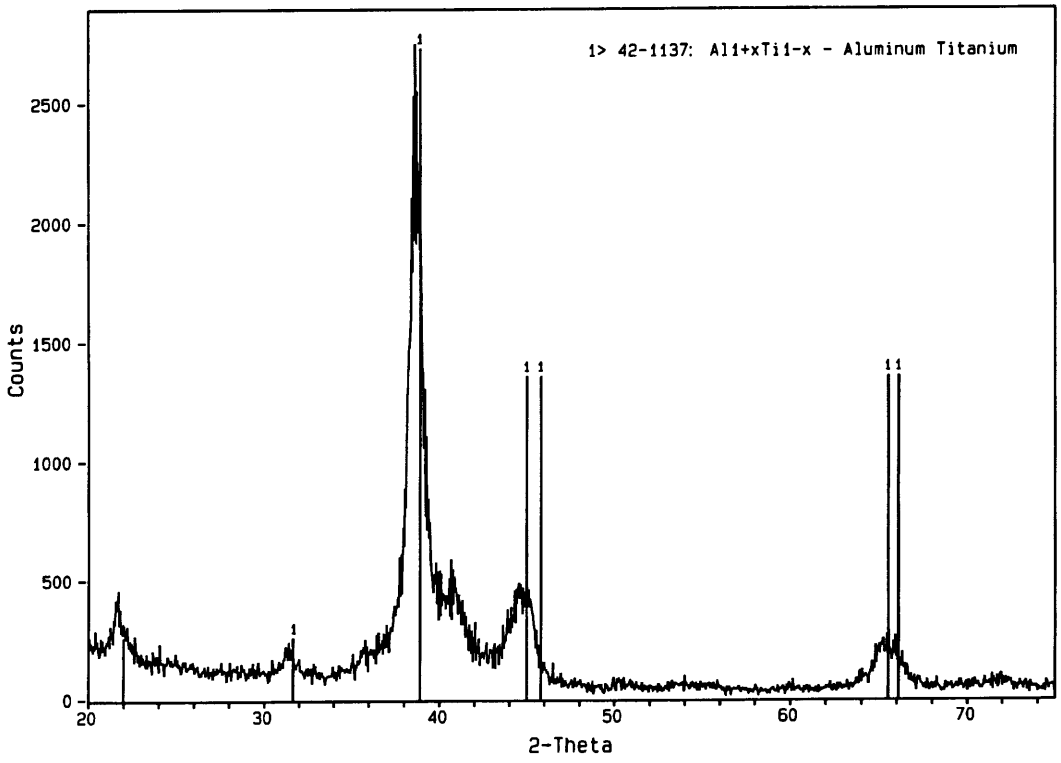

Figure 4.7 GAXRD spectra of the G substrate with peaks from JCPDF card #42-1137 for $Al_{1+x}Ti_{1-x}$ (x=0.28) (g-TiAl) superimposed on the diffraction scan.

Table 4.3 α_2-Ti_3Al peaks from PDF card # 9-98

Fixed Intensity (%)	h k l	2θ Value (°)	Notes
100	201	40.9	
70	002	38.8	
60	202	53.9	
60	203	71.7	
50	200	35.9	
50	220	64.5	
50	423	145.8	out of the range scanned in this study
40	222	77.8	
40	421	112.4	
40	224	116.7	
40	205	124.6	
40	602	158.5	
30	401	79.2	
30	403	104.7	
20	101	26.2	

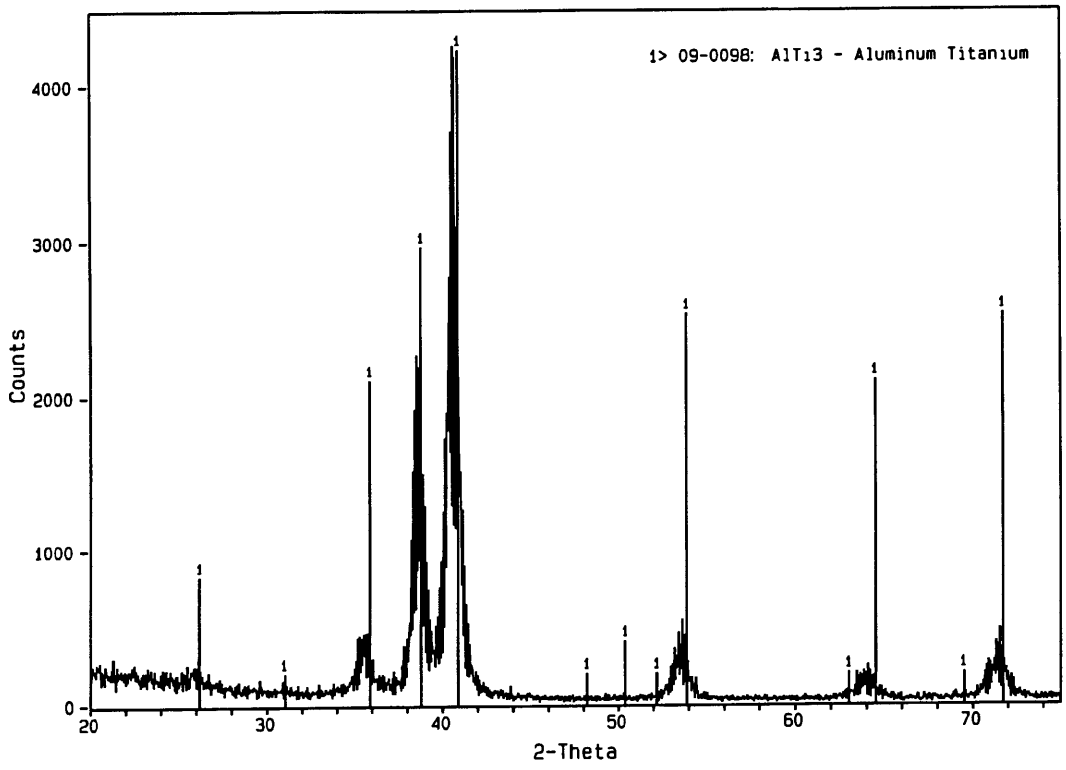

Figure 4.8 GAXRD spectra of the A2 substrate with peaks from JCPDF card #9-98 for $AlTi_3$ (α_2-TiAl) superimposed on the diffraction scan.

4.3.1.1 G Substrate

GAXRD spectra of the G substrate taken at 0.5° incidence is shown in Figure 4.7. Peaks from the PDF card #42-1137 for γ-TiAl are overlaid. When a search was conducted to match the G substrate spectrum, only two γ-TiAl files were found. A purely stoichiometric TiAl had the lowest figure of merit (FOM) at a value of 5.5 (the lower the FOM, the closer the match of the file to the peaks found in the spectra). However, the PDF card was of dubious accuracy derived from a 1951 study that was not conducted using a diffractometer or on film. The second γ-TiAl file (JCPDF card #42-1137) was generated in 1990, after the renewed interest in titanium aluminides, and had a FOM of 8.3. All the peaks from the card are evidenced in the spectra, with substrate values shifted to smaller 2θ values. The composition scanned for the JCPDF card was Ti-64 at.% Al, compared to the Ti-47.9 at.% Al used in this study, and the higher Ti content results in the unit cell having larger dimensions, resulting in peak shifts to smaller 2θ values (larger d spacings). In addition, there were discrepancies from the intensities in the PDF card file. Therefore, preferential grain orientation could not be deduced from the GAXRD data.

Also evident in the G spectra is the presence of some α_2-Ti_3Al peaks, matching PDF card #9-98. The strongest peak of α_2-Ti_3Al (201) is located at 40.9°, which is clearly evident in the G substrate spectra. The next highest intensity peak of α_2-Ti_3Al lies only 0.1° from the most intense γ-TiAl peak, so if this α_2-Ti_3Al peak were present, it would be obscured by the shoulder of the (111) peak of G. Unfortunately the next strongest α_2-Ti_3Al peaks are at intensities of 60%, so if these peaks are present in the G, their intensities are not significantly greater than the noise present at those 2θ values .

To determine if internal or external oxidation of the alloy occurred during processing, the presence of oxides in the substrate scan was investigated. A listing of the

XRD peak locations and intensities for all phases investigated in this study is found in Appendix C. The strongest peak of rutile (100) showed no signal above background and was considered an accessible peak, as it was located several degrees away from any γ-TiAl or α_2-Ti_3Al peaks. Hence, rutile in the substrate was ruled out in levels detectable by XRD. Establishing the presence or absence of aluminum oxide was more difficult because of peak overlaps. The accessible peaks were either near substrate peaks or obscured by the broadening of peaks due to small grain size of the substrate. The (116) peak is far removed from any neighbors, but at the higher angles, one would not expect as much intensity, and indeed no peak is visible. Thus, within the limits of XRD, no notable alumina was present before oxidation.

4.3.1.2 A2 Substrate

GAXRD scans for the A2 substrate were also generated at 0.5° incidence and a representative scan is given in Figure 4.8. Peaks from the PDF card # 9-98 for $AlTi_3$ are overlaid and the peaks correlate well. A computerized search was conducted to match the substrate spectrum, which turned up two α_2-Ti_3Al titanium aluminide files. Both were stoichiometric Ti_3Al, with card 9-98 having a FOM of 12.8 compared to a FOM = 15.4 for card 14-451. Again, there is some shift of 2θ values in the substrate spectrum to positions slighter lower than indicated on either α_2-Ti_3Al card, though with this substrate, there is no significant Ti excess. The values of the shift are approximately 0.2° compared to the larger shift values of 0.5° for G. The substrate peaks are also somewhat broadened, indicating small grain size, as evidenced in the metallographic results. It was much more difficult to determine amounts of γ-TiAl in the A2 substrate, since the strongest γ-TiAl peak (111) is nearly coincident with an α_2-Ti_3Al peak. Other γ-TiAl peaks are significantly less intense and were not detected in the scan; therefore, within the resolution of XRD, there is no evidence for a second phase. However, it is clear from the metallography that A2 displayed a lamellar structure.

In searching for evidence of alumina in this substrate, it was noted that a peak at 35.5° is either the (200) peak of α_2-Ti_3Al greatly shifted or the alumina (104) peak; there is, however, only a small peak where the nearly-as-intense (113) alumina peak should be. Any other alumina peaks, if present, are below the background noise. No rutile peaks were observable above the background noise.

4.3.1.3 SA2 Substrate

Figure 4.9 shows the GAXRD spectra of both SA2 and A2 at the same scale and scanned at the same conditions. There are many similarities in the two spectra. There is also notable shifting in the SA2 spectra of the two strongest α_2-Ti_3Al peaks of (201) at 40.9° and (002) at 38.8°. The largest shift occurs for the α_2-Ti_3Al (202) peak, which is shifted to a 2θ value nearly 2° higher and a similar shift value is seen for the (220) peak at 64.5°. A shift is not seen for the peak at 71.7°, this (203) peak being nearly identical in position for both A2 and SA2. In addition, a negligible shift is seen for the (101) peak at 26.2°, with the corresponding SA2 peak appearing much more intense. As this peak does not correspond to any Al or Ti oxide or the G substrate, it was taken as an indication of texture in the A2 or SA2 substrates.

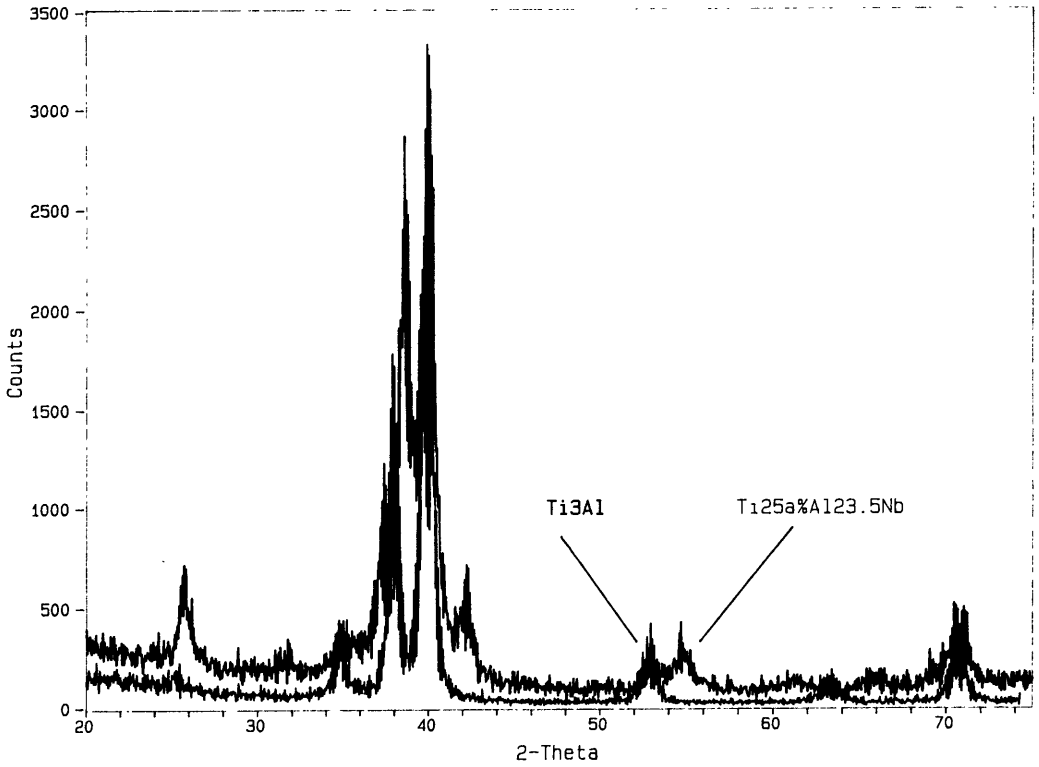

Figure 4.9 GAXRD spectra of the SA2 and A2 substrates.

Additionally, for the G spectrum, there is shoulder on the strongest peak at approximately 41°. The shoulder is also seen in the SA2 scan but, not in the A2 scan. When looking for the presence of γ-TiAl in the SA2 substrate, a small intensity increase above background was evident in the SA2 scan at 2θ 66°, where the (202) and (220) peaks of γ-TiAl should appear. There is, however, no indication of the (200) and (020) peaks of γ-TiAl at 2θ 45°. The (110) γ -TiAl peak may be in the SA2 spectrum at 31.7°, but the (001) peak of similar intensity at 22.0° is lost in the background if it is present at all. Sample scans were all collected under similar conditions, so it is concluded that experimental complications are not responsible for the freak anomalies seen in some but not other sample types.

4.3.2 X-ray Maps of the Substrates

A further investigation on the compositional and phase homogeneity of the substrates was conducted using XEDS digital maps in ESEM and STEM. Even with grains sizes on the order of 100 μm or more, the elemental distribution as mapped in the ESEM appeared uniform throughout the sampled areas. The probe size did not allow for resolving the fine detail of the laths in the lamellar grains. In SA2, where many microstructural features were much smaller than 1 μm, the approximate resolution of x-ray mapping in the ESEM, mapping of TEM samples of the substrate in the STEM was performed. Figure 4.10 gives the STEM binary XEDS maps and corresponding electron image of the SA2 substrate. The Ti distribution appears uniform throughout, but laths are enriched in Nb and correspondingly, somewhat diminished in Al x-ray intensity. This depletion in Al signal can not be accounted for by the phases (Ti, Nb) Al_3 nor Ti_4NbAl_3, since both of these have an increase in Al content relative to the Ti_2NbAl. This may be accounted for by the presence of a small portion of (βTi, Nb) which may be ordered or disordered. The ordered high temperature form is termed the β*. The STEM image also indicates a faulted structure which Mozer (1990) also reported.

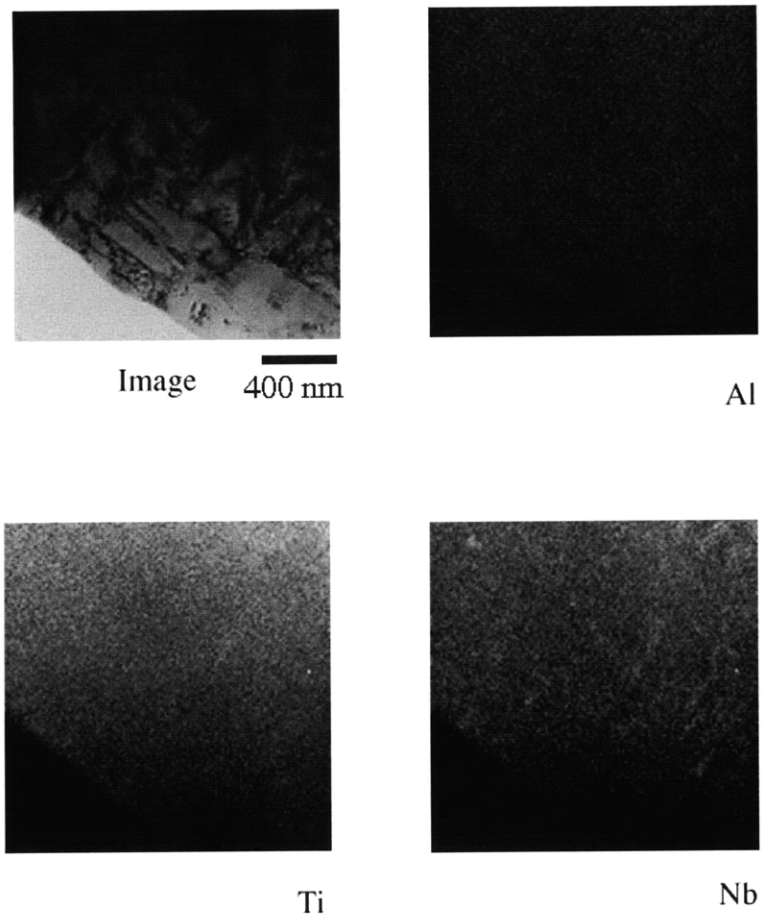

Figure 4.10 STEM binary XEDS maps and corresponding electron image of SA2 substrate before oxidation.

4.4 Thermodynamic Stabilities

The similarity in thermodynamics between alumina and titania is considerably different from those seen in the majority of alloys. A larger gap in standard free energies of elements in many alloys is exploited by preferentially oxidizing one component over all other components. As seen in Figure 4.11, the free energy of alumina formation is only slightly lower than that for titania formation. The small thermodynamic advantage of alumina is further attenuated by the rapid titania formation kinetics. This causes the Ti-Al dilemma, with a competition between the similarly stable Al and Ti oxides that can be shifted towards the less stable titania because of its more rapid growth rate.

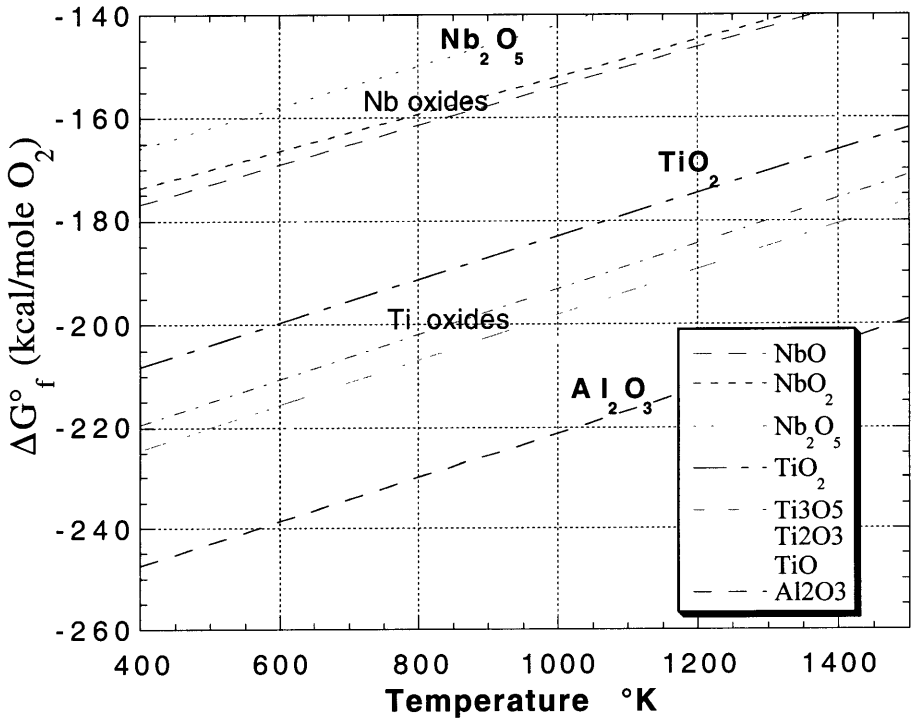

Figure 4.11 Standard free energies plotted versus temperature in the Al-Nb-Ti-O system (constructed from Reed 1971).

One starting point for predicting which corrosion product will form during exposure is a phase stability diagram. In corrosion, there are also kinetic considerations that may be controlling, rather than thermodynamics, but the thermodynamically favored phases give one an idea at least where the system would head if not constrained by time or available kinetic routes.

A typical diagram for mixed gas corrosion has partial pressures of two gases as its axes and lines separating two phase regions. The lines are defined by the thermodynamic free energies relating the two phases. For example, for the vertical boundary between TiN and TiO, there exists the equilibrium relationship:

$$2TiN(s)+O_2(g) \Leftrightarrow 2TiO+N_2(g) \qquad (4.1)$$

The equilibrium constant, K, for this equation is given by:

$$K = \frac{[a_{TiO}][P_{N_2}]}{[a_{TiN}][P_{O_2}]} \qquad (4.2)$$

where a_x represents the activity of condensed species x and P_y the partial pressure of gaseous component y. The relationship between the free energy change and the equilibrium constant is:

$$\Delta G = -RT \ln [K] \qquad (4.3)$$

Initial assumptions are that the activities, a_x, of the solid metals and oxides are unity and that the activities of the gases are equal to their partial pressures, P_y. The activities of the metals can be subsequently varied in relation to their composition in the intermetallic alloy, and experimentally determined values can be substituted to establish the effect of a metal alloy activity on the system equilibrium. Individual diagrams were

constructed for each metal of the intermetallic system. For titanium aluminides, the diagrams for the Ti and Al were super-imposed, which assumed that there are no interactions between oxidation products of one metal with the oxidation products of the other. All three metal diagrams were superimposed for interpretation of the SA2 structure. This assumption is not always justified, since there are cases where one oxide will reduce or dissolve another; for example, in the Ti-Al-Nb-O-N system, the alumina may be dissolved by rutile at later stages. This non-interaction assumption is, however, a simple starting point for the analysis.

4.4.1 Phase Stability Diagrams in the Cr-Nb System in Mixed Gaseous Environments

Diagrams for the Cr-Nb system were calculated at 800 and 900°C in the mixed gas environment of sulfur and oxygen. Details of accompanying experiments and analysis can be found in Duncan's (1994) study of Cr-Nb alloy oxidation (the Cr-Nb system also exhibits intermetallic compounds). The anomalous behavior of Nb in the presence of oxygen in this system provides one reason for investigating the behavior of Nb in the Ti-Al system. The Cr-Nb-O-S system contained one less metal component than the Ti-Al-Nb-O-N, and conclusions drawn from the former system were expanded to the more complex system of the titanium aluminides.

4.4.1.1 Phase Stability Diagrams in the Cr-Nb-O-S System at 800°C

This composite stability diagram given in Figure 4.12 was computed for analysis of the majority of the experiments conducted in mixed oxygen/sulfur gaseous environments were reacted at this temperature. This temperature represents a typical operating temperature under these conditions.

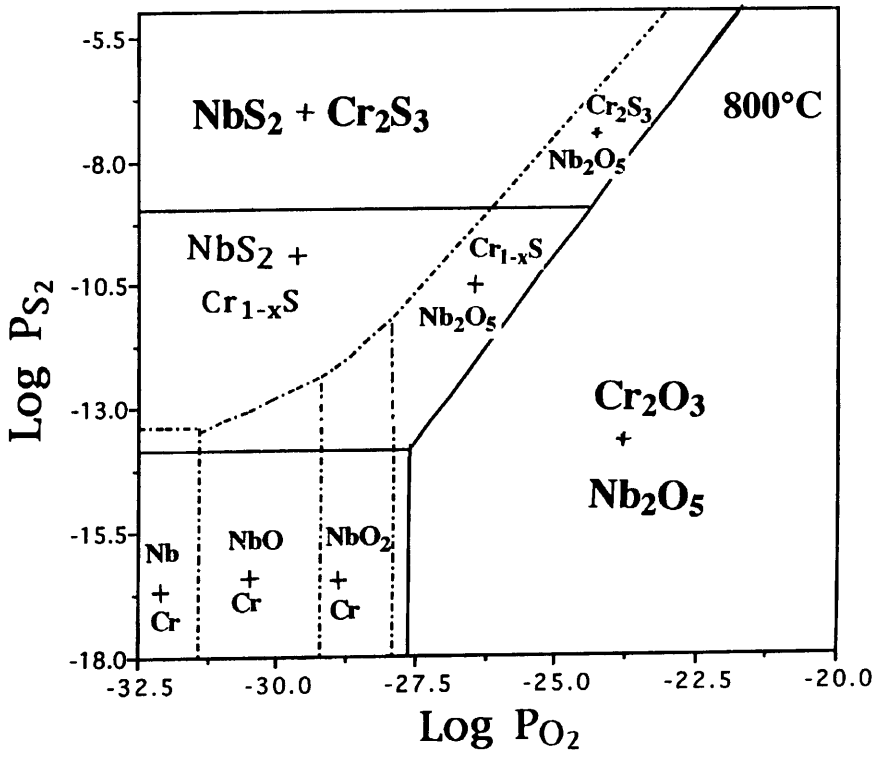

Figure 4.12 Stability diagram for the Cr-Nb system at 800°C constructed by superimposing the diagrams for Cr and Nb at this temperature.

4.4.1.2 Phase Stability Diagrams in the Cr-Nb-O-S System at 900°C

While the temperature of 900°C is a bit higher than typically experienced in these applications, the composite diagram was calculated for a) comparison to the lower temperature diagram at 800°C for evaluation of the effect of temperature on the equilibria and b) comparison to extensive work done on the kinetic boundary of pure Cr compared to the Cr stability diagram (LaBranche 1985). The calculated stability diagram for this system at 900°C is given in Figure 4.13.

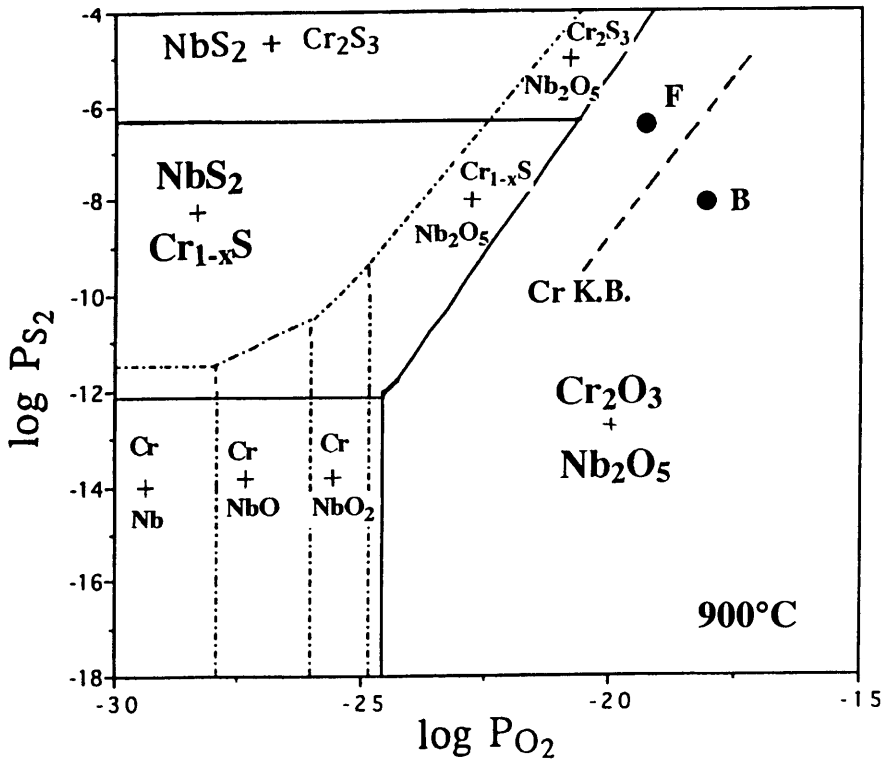

Figure 4.13 Stability diagram for the Cr-Nb system at 900°C constructed by superimposing the diagrams for Cr and Nb at this temperature. The dashed line indicates the kinetic boundary for pure Cr as determined by LaBranche 1985.

4.4.1.3 Conclusions about Nb Behavior from the Cr-Nb-O-S System

Protective corrosion behavior of Nb in the Cr_2Nb intermetallic compound was observed. Experiments were conducted at gas concentrations that fell within the predicted Nb_2O_5 phase field with no significant portion of the notoriously porous and non-protective Nb_2O_5 phase being detected in the corrosion scales. Analysis suggested that a lower Nb oxide was formed, with a probable composition of NbO_2. This shift in the thermodynamic behavior resulting from the alloy oxidation kinetics is indicated as a kinetic boundary on stability diagrams. The behavior of Cr_2Nb followed the calculated kinetic boundary for pure Cr as determined by LaBranche 1985. The possibility of a similar beneficial Nb oxidation behavior in the Ti-Al intermetallic system in mixed gaseous environments was investigated.

4.4.2 Phase Stability Diagrams in the Ti-Al-Nb Systems in Mixed Gaseous Environments

Diagrams were constructed for each of the three constituent elements at 700, 800 and 900°C representing their relative stability in both nitrogen and oxygen environments.

4.4.2.1 Phase Stability Diagrams at 700°C

Figure 4.14 displays the stability regions for Al, Ti and Nb respectively at 700°C. For the simplest diagram, the Al diagram, it is evident that pressures greater than 10^{-49} atm of oxygen will produce an alumina oxide scale and a partial pressure of approximately 10^{-23} atm of nitrogen to form the nitride. These gas pressures are exceedingly small, and contamination can easily account for amounts much greater than this, especially for oxygen, which often is an impurity at levels greater than 1 ppm, or 10^{-6}, atm in ultrahigh purity gas cylinders. The free energy of formation for α-Al_2O_3 is -327.3 kcal/mole compared to -51.4 kcal/mole for nitride formation at this temperature.

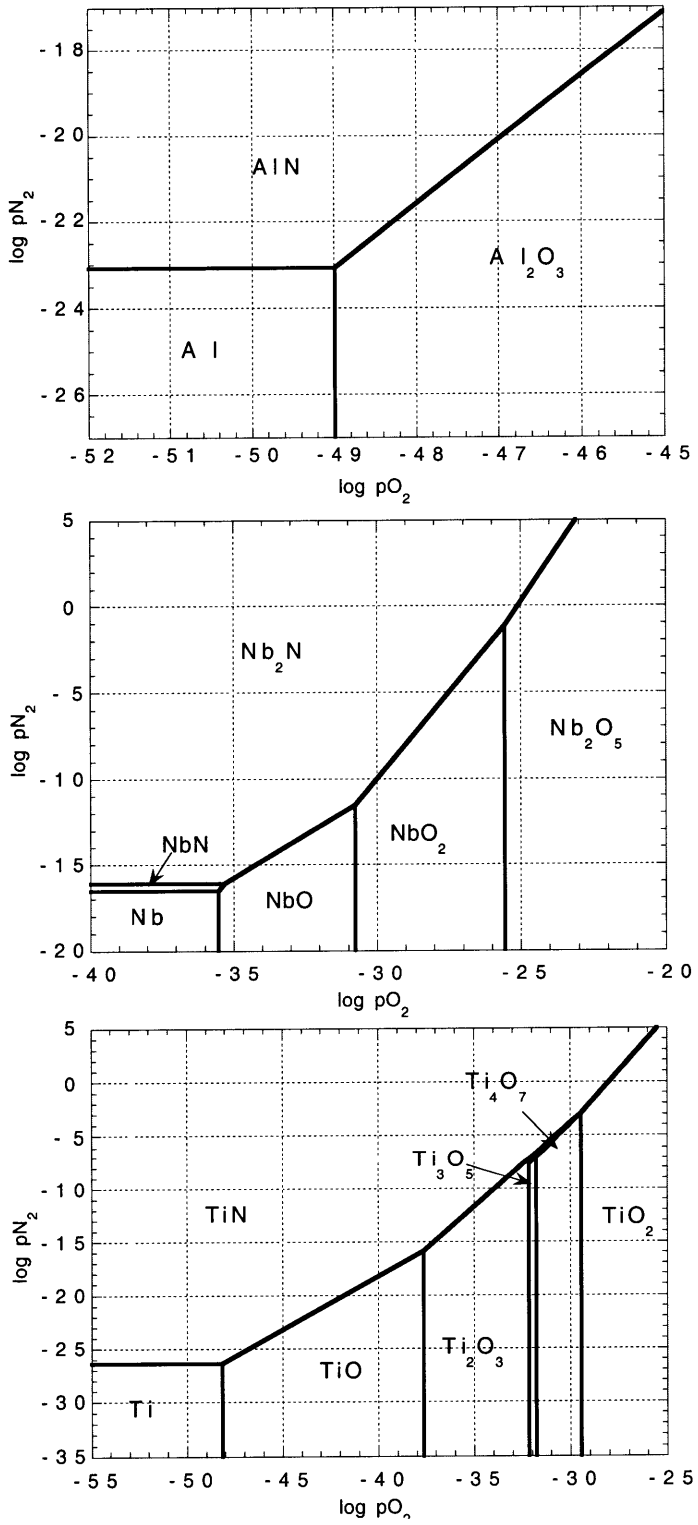

Figure 4.14 Stability diagrams for the Al, Nb, Ti systems at 700°C in nitrogen and oxygen.

The Ti stability diagram indicates that the oxide of titanium is, again, more stable than the nitride. The energy difference in this case is much smaller; the free energy of formation for TiO_2 is -107.2 kcal/mole, compared to -58.7 kcal/mole for TiN. In this system, the minimal oxygen partial pressure for oxide formation is approximately 10^{-29} atm, and the minimum nitrogen partial pressure for nitride formation ~10^{-26} atm. These pressures are very close to each other, and similar for aluminum nitride formation, but much greater than for aluminum oxide formation. Also, in this system, the metallic element can exhibit multiple oxidation states in the oxides. The most stable oxide (TiO_2) forms on the outer gas/scale interface, but another phase may be more stable in the interior of the scale. This is because the partial pressure of oxygen can be much lower within the scale because diffusion is kinetically limited by the concentration gradient of diffusing species established in the scale.

The Nb diagram is similar to the Ti diagram, with multiple oxides. It also includes two possible nitrides, NbN and Nb_2N. Again, the equilibrium oxygen partial pressure for formation of Nb_2O_5 is 10^{-26} atm, with a free energy of formation of -352.1 kcal/mole. Figure 4.15 shows the superposition of the Al, Nb and Ti stability diagrams at 700°C.

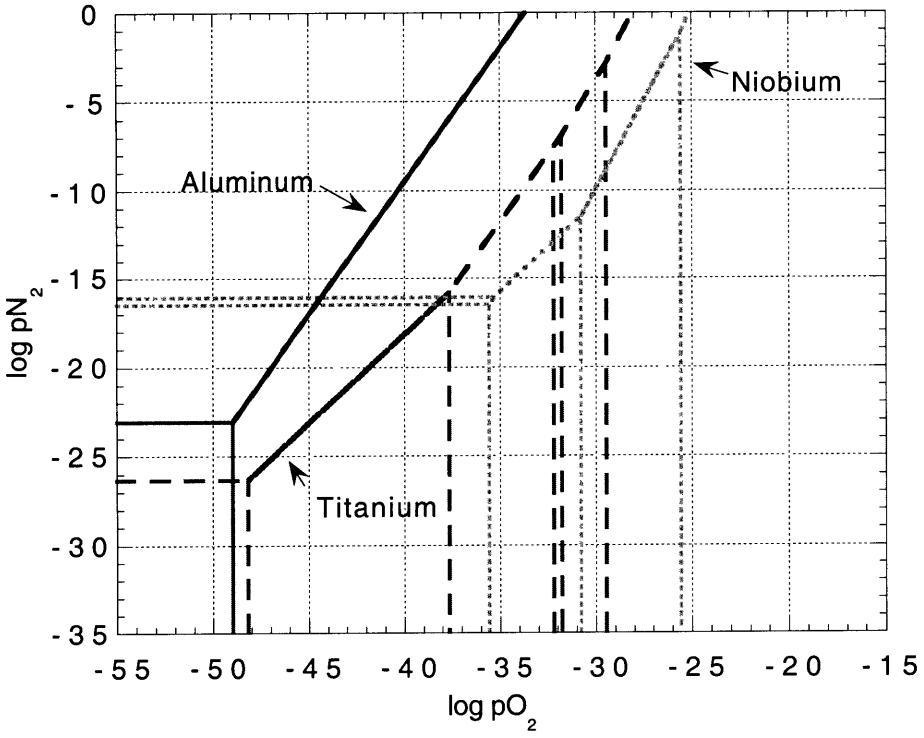

Figure 4.15 Composite stability diagram for the Al-Nb-Ti system at 700°C in nitrogen and oxygen constructed by superimposing the diagrams for Al, Nb and Ti at this temperature.

4.4.2.2 Phase Stability Diagrams at Higher Temperatures

Diagrams for 800°C and 900°C were calculated to provide a closer comparison to experiments reported in the literature, since most oxidation studies have been conducted at higher temperatures. Additionally, the comparison of the diagrams at two different temperatures highlights trends in the stability, permits some predictions to be made of what phases are expected, and can be used to explain when dramatic differences are observed between thermodynamically predictions and kinetic realities. Figures 4.16 and 4.17 shows the superposition of the Al, Nb and Ti stability diagrams at 800°C and 900°C.

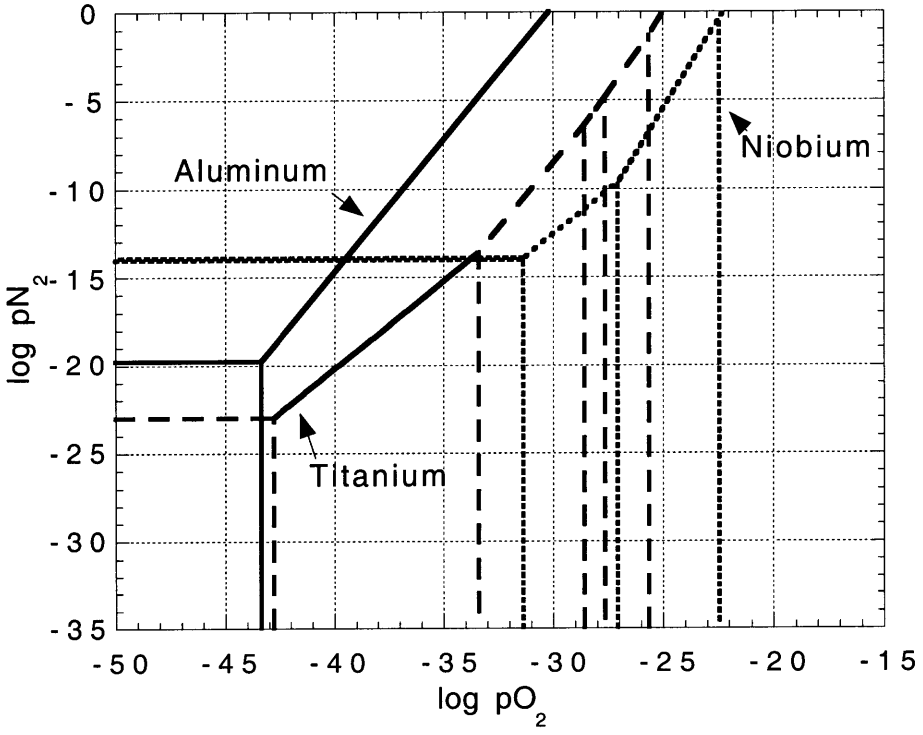

Figure 4.16 Composite stability diagram for the Al-Nb-Ti system at 800°C in nitrogen and oxygen constructed by superimposing the diagrams for Al, Nb and Ti at this temperature.

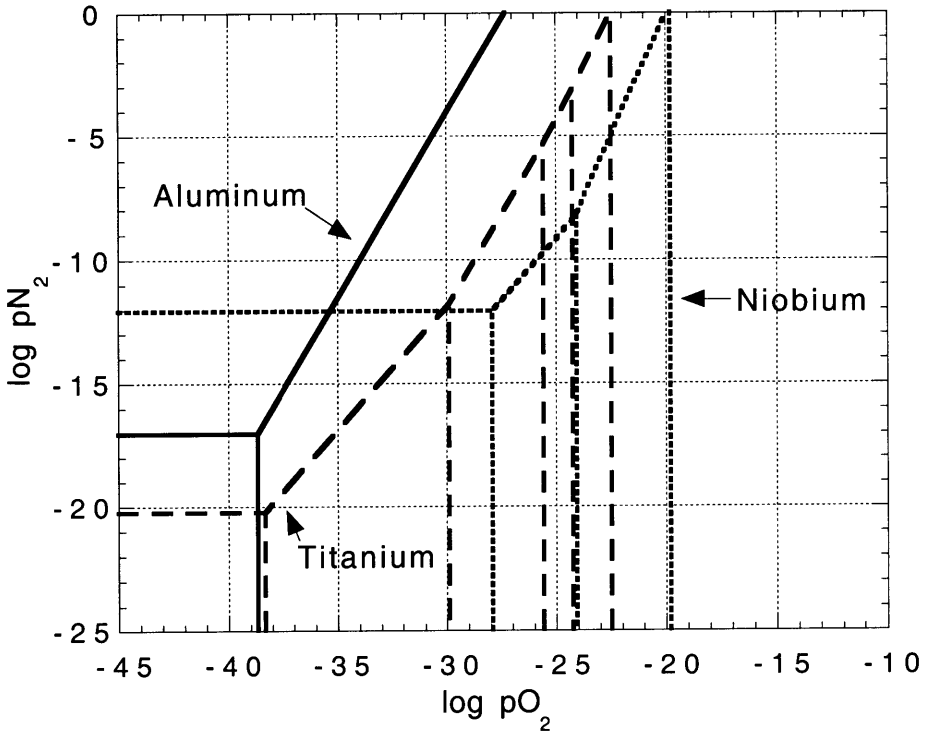

Figure 4.17 Composite stability diagram for the Al-Nb-Ti system at 900°C in nitrogen and oxygen constructed by superimposing the diagrams for Al, Nb and Ti at this temperature.

Chapter 5

Oxidation Studies

Any potential material for aerospace or automotive applications must have a balance of material properties, including high temperature strength, ductility, fracture toughness, impact resistance and high temperature corrosion resistance. A model set of three titanium aluminide intermetallics - unalloyed γ-TiAl, unalloyed α_2-Ti_3Al and unalloyed Ti_2NbAl (an orthorhombic intermetallic structure) was chosen and investigated under a variety of experimental conditions. The results are presented and discussed in this chapter. Oxidation at temperatures of 700 and 800°C was studied (as compared to temperatures of 900°C and higher used by other investigators), since the scales grown at these lower temperatures appeared more protective than those grown at higher temperatures and the composition of the scale was known to change dramatically with temperature. Unfortunately, the change of scale composition with temperature does not allow the conventional practice of accelerating corrosion by raising the experimental temperature.

The effect of nitrogen on the high temperature oxidation of titanium aluminides is a controversial area. The "nitrogen" effect was studied on the model set of titanium aluminides (G, A2 and SA2) by reacting the intermetallics in gas mixtures with and without nitrogen (nitrogen-oxygen mixtures and argon-oxygen mixtures). The effect of

the oxygen concentration on the corrosion rate was also studied by varying the amount of oxygen in the gas mixtures. Corrosion studies were also conducted in pure oxygen and pure nitrogen for comparison. In all experiments, there was a comparative study of the oxidation behavior of the three intermetallic alloys.

Characterization and analysis of the scale structures and compositions was carried out in all cases. Table 5.1 gives the compositions and labels for the gases used in this study. The results in this chapter are structured as follows:

- The three intermetallics were studied at 800°C in order to make comparisons to literature results (800°C is the lowest temperature studied by other researchers) and to the present set of oxidations performed at 700°C, for the purposes of calculating activation energies. Comparison of the corrosion rates for the three alloys at 800°C to those at 700°C allowed activation energies for scale formation to be calculated, as well as composition to be followed as a function of temperature.
- The effect of nitrogen was studied by conducting corrosion experiments in nitrogen-5% oxygen, argon-5% oxygen, nitrogen-20% oxygen (dried compressed air), and argon-20% oxygen. Results in 5% oxygen mixtures were compared to those for in-situ oxidation studies, where the reduced pressure in the ESEM reduced the oxygen activity. Differences in scale morphologies of scales grown *in-situ* versus *ex-situ* were investigated.
- The effect of oxygen activity was studied by comparing experiments conducted in 5% oxygen, 20% oxygen and pure oxygen. Both argon-oxygen and nitrogen-oxygen mixtures were used in these comparisons.
- Oxidation of the three intermetallics was studied in pure oxygen to investigate corrosion mechanisms in the absence of a nitrogen effect.
- The nitridation rates of the three alloys were investigated by experiments in laboratory grade nitrogen. Pure Nb specimens were also exposed to pure N_2 to obtain

the Nb nitridation rate at 700°C for comparison to those of the three titanium aluminides and for deconvoluting the different nitride contributions in the total scale growth. The effect of oxygen impurities in the gas mixtures was also noted.

Table 5.1 Summary of gas mixtures and their labels

Gas Mixture Label	Volume % oxygen	Balance of gas mixture
05A	5% oxygen	argon
05N	5% oxygen	nitrogen
20A	20% oxygen	argon
20N	20% oxygen	nitrogen
OO-	100% oxygen	
NN-		100% nitrogen

Thermogravimetric kinetic rates for experiments conducted at 700°C are given in Table 5.2. Raw data and comments can be found in Appendix A. The thermogravimetric rates are presented rather than the true parabolic rates. The reasons for this are two fold: a) assuming a simple mixture of rutile and alumina still requires a more precise measurement of the relative amounts of each which was not possible with the GAXRD measurements and b) the assumption of only two oxides of alumina and rutile was exceeded in many cases, with the existence of mixed oxides involving two or more metal components, oxide solubilities and the existence of nitrides, oxynitrides and niobium containing scales.

Table 5.2 Thermogravimetric parabolic rates determined in this study at 700°C.

ALLOY	GAS COMPOSITION	Experiment Length - Microbalance		
		Parabolic rates in units of g^2/cm^4-sec		
GAMMA		20 hr - DuPont		100 hr - Cahn
	N_2-5%O_2	Not Run		2.0×10^{-14}
	N_2-20%O_2	9.1×10^{-15} 2.8×10^{-15} 8.0×10^{-14} 4.2×10^{-14}		6.2×10^{-15} 7.4×10^{-15}
	Ar-5%O_2	Not Run		2.3×10^{-14}
	Ar-20%O_2	2.5×10^{-14}		1.2×10^{-14}
	100% oxygen	5.0×10^{-14} 8.3×10^{-15}		5.5×10^{-15} 2.2×10^{-15}
ALPHA TWO	GAS	20 hr - DuPont		100 hr - Cahn
	N_2-5%O_2	Not Run		3.8×10^{-13}
	N_2-20%O_2	6.0×10^{-13} 1.2×10^{-13} 5.4×10^{-14}		3.9×10^{-13}
	Ar-5%O_2	Not Run		5.2×10^{-13}
	Ar-20%O_2	5.0×10^{-13} 2.4×10^{-13} 2.2×10^{-13}		6.0×10^{-13}
	100% oxygen	8.9×10^{-13} 7.9×10^{-13} 8.7×10^{-13}		1.4×10^{-12} 1.3×10^{-12}
SUPER ALPHA TWO	GAS	20 hr - DuPont		100 hr - Cahn
	N_2-5%O_2	Not Run		4.7×10^{-14}
	N_2-20%O_2	4.9×10^{-14} 4.0×10^{-14} 2.9×10^{-14}		7.3×10^{-14}
	Ar-5%O_2	Not Run		1.7×10^{-13} 1.9×10^{-13} 2.3×10^{-13}
	Ar-20%O_2	6.0×10^{-13} 4.2×10^{-13} 7.4×10^{-13}		3.3×10^{-13}
	100% oxygen	2.4×10^{-12} 1.5×10^{-12} 1.9×10^{-12} 1.4×10^{-12}		1.9×10^{-12}
	pure nitrogen (with oxygen impurity)			3.1×10^{-14} 4.2×10^{-14}

Note: Each entry corresponds to a separate experiment.

5.1 Oxidation Experiments at 800°C in Argon-20% Oxygen

A majority of the oxidation studies was conducted at 700°C. Experiments were run at 800°C to allow comparison with kinetic values published in literature and with the results from the 700°C experiments. Comparisons of the results at both 700 and 800°C allowed calculation of activation energies. The ex-situ studies at 800°C were also compared to in-situ experiments conducted in the ESEM at 800°C. There was a concern that a different equilibrium would occur in the titanium aluminides as the test temperature varied, and that the scale composition and behavior would be entirely different in nature. This is a particular concern for multicomponent alloys growing complex scales, compared to simple alloys which grow single component scales such as alumina which has a stable growth temperature range over several hundred degrees.

All three intermetallic alloys were oxidized in the DuPont microbalance at 800°C in an argon-20% oxygen mixture for 20 hr. Figure 5.1 shows TGA data for oxidation of the three intermetallic alloys. This figure is an excellent example of the typical kinetic data obtained and of the general trends exhibited. In particular, the corrosion rate of the SA2 alloy fell intermediate between that of the A2 alloy (which displays the fastest oxidation rate) and G alloy, which often had a kinetic rate so low it approached the sensitivity limits of the microbalances. All three rates were parabolic and exhibited fits of 0.988 or better when weight gain per area was plotted against the square root of oxidation time. In fact, rates in this study generally exhibited a parabolic fit of greater than 0.99. The fit of 0.988 belonged to the A2 sample which displayed two regions of parabolic behavior during the 20 hr experiment; the rate quoted in the table refers to an overall average fit over the entire curve. Figure 5.2 illustrates the method of determining the oxidation rate by plotting the normalized weight gain against the square root of time. From the slope, the thermogravimetric rate is extracted. From the weight gains, the estimated scale thicknesses were 1 and 6 μm for G and A2 respectively. Appendix B

contains the calculations for estimating scale thickness of scales of complex composition. However, even though the scales were rather thin, they were all mostly opaque to light, with a gray hue, usually indicative of a significant fraction of rutile in the scale. Only alloy A2 gave some macroscopic indications of scale spallation, with darker gray patches under spalled regions and the majority of the scale a whitish gray. The scale on alloy G was more patchy, indicating a difference in scale thickness relative to individual grain orientations. The scale on alloy SA2 was a uniform matte gray.

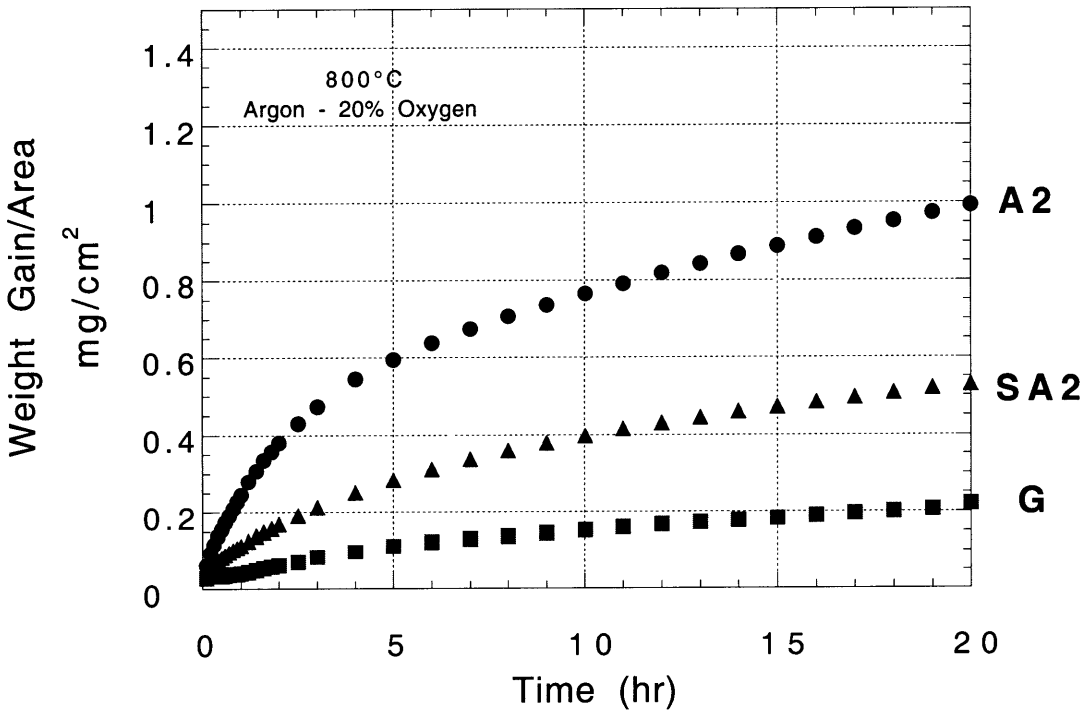

Figure 5.1 Linear plot of weight gain kinetics for alloys G, SA2 and A2 exposed to argon-20% oxygen at 800°C for 20 hours in the DuPont microbalance.

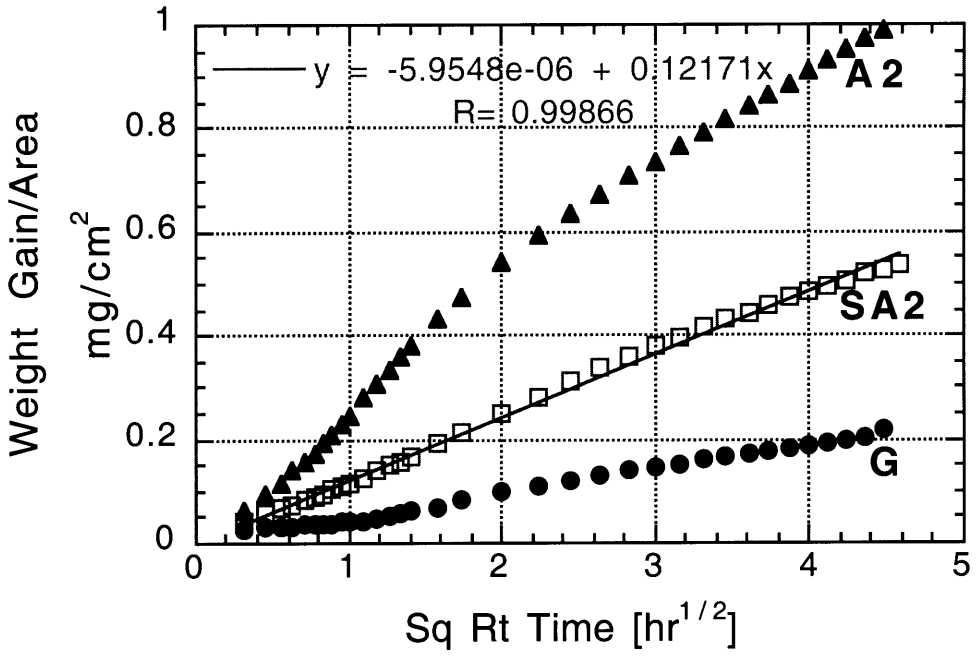

Figure 5.2 Parabolic plot of weight gain kinetics for alloys G, SA2 and A2 exposed to argon-20% oxygen at 800°C for 20 hours in the DuPont microbalance.

Oxidation rates at 800°C were at least one order of magnitude higher than those measured at 700°C. These higher rates resulted in increased experimental reproducibility. Table 5.3 lists the parabolic rates determined at 800°C for this gas mixture.

Table 5.3 Thermogravimetric parabolic rates determined in this study at 800°C for 20 hr in argon-20% oxygen.

ALLOY	Parabolic rates in units of g^2/cm^4-sec
G	6.3×10^{-13}
A2	1.4×10^{-11}
SA2	4.1×10^{-12}

5.1.1 SEM Results

ESEM micrographs of alloy G sample reacted at 800°C reveal a thin scale with contrast variations that correspond to the original shape of substrate grains viewed in metallography. Irregular dark areas which appear depressed are interspersed between larger areas exhibiting a grayish salt and pepper contrast. Occasional spikes or needles are randomly distributed. Even though the scale is thin, it is patchy with "oatmeal"-like flakes or granules on the surface whose edges charge up in the ESEM, see Figure 5.3. Higher magnifications of individual flakes reveal still smaller flakes and occasional needles within each larger flake. There is little difference at higher magnification between the darker and grayish regions corresponding to the different substrate grains.

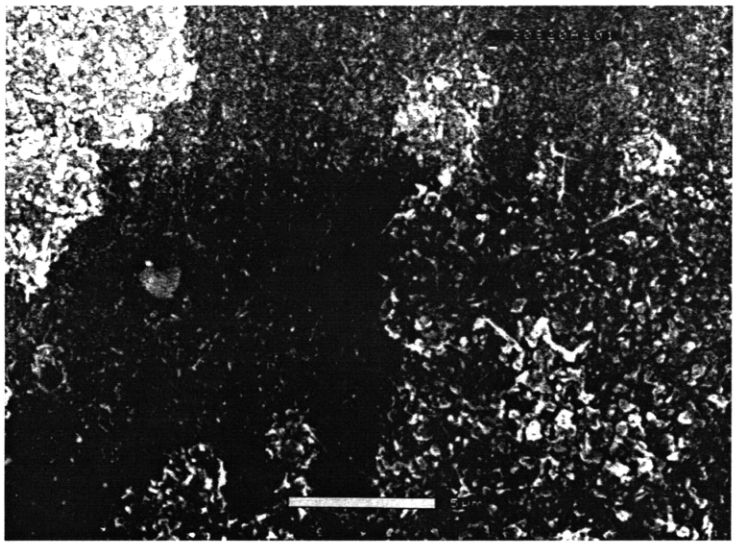

Figure 5.3 ESEM micrograph of alloy G exposed to argon-20% oxygen at 800°C for 20 hours.

The thin scale on alloy SA2 (see Figure 5.4) shows similarities to that grown on alloy G, with small patchy areas. Darker and lighter contrast variations are on a smaller size scale, in the same way as metallography showed that grains on the initial SA2 substrate are smaller than those of the G substrate. The scale near the edges of the sample

exhibited large voids of diameter tens of μm. Higher magnification images of the scale showed patchiness, which was more angular than that on alloy G and had a nodular morphology. Images obtained at 10K magnification show what appear to be dark holes or voids in the scale surface with individual dimensions smaller than 1 μm.

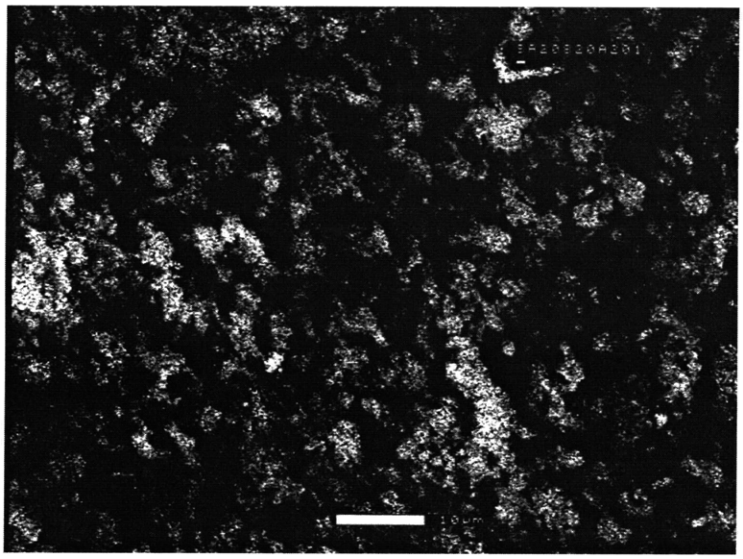

Figure 5.4 ESEM micrograph of alloy SA2 exposed to argon-20% oxygen at 800°C for 20 hours.

Alloy A2 exposed to argon-20% oxygen at 800°C exhibited macroscopic spallation of the scale, especially evident at the edges of the specimen. Higher magnification images, Figure 5.5, of the spalled areas revealed a scale of approximately 5 μm in thickness, which agreed with calculated scale-thickness estimates. The scale is covered with needles, and the surface under the spall is bumpy and irregular, with small nodules. Cracks are evident in the specimen, not only at the edges (the most common location for cracks) but also in the center of specimen faces. Higher magnification images of these cracks show needles and spikes spanning the crack openings. Still higher magnifications also show rounder patches under the needle "forests".

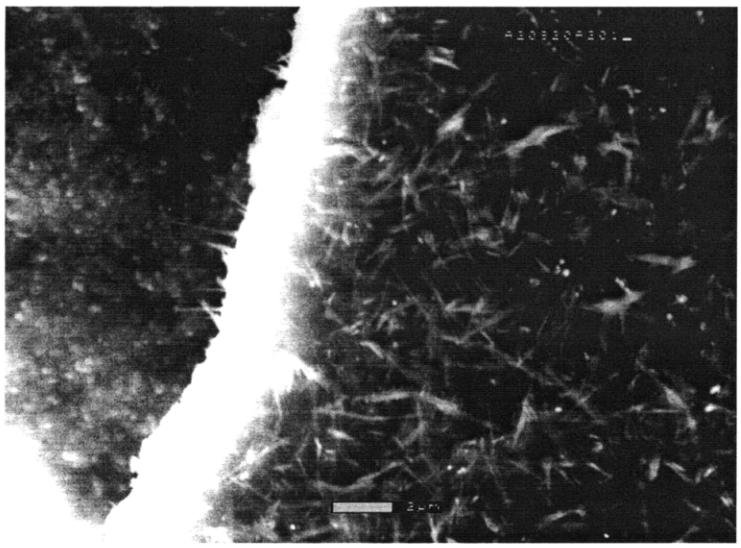

Figure 5.5 ESEM micrograph of alloy A2 exposed to argon-20% oxygen at 800°C for 20 hours.

5.1.2 GAXRD Results

The ratio of rutile to alumina volumes was calculated from integrated GAXRD peak intensities. The results are listed in Table 5.3. Glancing angle x-ray results for the alloy G sample reacted at 800°C revealed distinct alumina peaks, which matched well with the PDF card and had no significant peak shifts. Rutile was also found in the scale. No prominent peaks were found beyond those for rutile and alumina; specifically, no peaks for nitrides, oxynitrides, $AlNbO_4$ or $TiAl_2O_5$ were found that would indicate significant amounts of these compounds other than as very minor phases. Only a small peak was found at the location of the strongest peak of G substrate. The strongest peak of γ-TiAl coincides with the second strongest peak of α_2-Ti_3Al, and it may be that α_2-Ti_3Al formed in an Al-depletion area underneath the oxide scale may have contributed to that peak. The strongest peak for α_2-Ti_3Al may be incorporated as a shoulder on one of the rutile peaks. Substrate peaks of less intensity were not detected.

Table 5.4 Ratios of rutile to alumina volumes grown on three titanium aluminide substrates at 800°C after 20 hours in argon - 20% oxygen

Specimen Substrate	Rutile/Alumina volume ratio
G	11.2
SA2	13.0
A2	36.9

The thick scale grown on the A2 sample completely obscured the two strongest substrate peaks. In addition, the distinct peak of A2 at 2θ 72° is absent. No significant gamma peaks were seen (nor were they expected). The free peak of alumina was barely noted and perhaps shifted to slightly lower values. Rutile peaks were very prominent, making the rutile/alumina ratio very large. This sample exhibited very low background, and no other peaks were found.

The SA2 sample after exposure to argon-20% oxygen had some detectable alumina, though a much smaller amount compared to the strong rutile peaks. It is possible that some α_2-Ti_3Al intermetallic peaks are present in the spectrum, as a minor phase. No significant γ-TiAl peaks were evident. The presence of both Nb_2O_5 and $AlNbO_4$ could not be excluded, but their presence was unclear since their major peaks occurred at small 2θ. The SA2 samples had the largest background (at times up to half of the maximum peak in the XRD scan, especially in the small 2θ regime. Peaks form the niobium-containing oxide were also rather removed from any other compound peaks. A summary of all phases found in the titanium aluminide scales at 800°C after exposure to argon-20% oxygen is given in Table 5.5.

Table 5.5 Summary of phases found on the titanium aluminides reacted at 800°C in argon-20% oxygen for 20 hours using GAXRD

Substrate	Alumina Al_2O_3	Rutile TiO_2	Mixed Oxide $TiAl_2O_5$	Mixed Oxide $AlNbO_4$	Niobia Nb_2O_5	Substrate Peaks
G	**Y**	**Y**	**W**	**ND**	**ND**	**G, A2 weak**
A2	**?**	**Y**	**?**	**ND**	**ND**	**A2**
SA2	**Y**	**Y**	**Y**	**?**	**Y**	**A2, G?**

Y - detected, Weak - detected weakly, ND - not detected, ? - possible

5.2 Oxidation Experiments at 700°C: Effect of Nitrogen in the Gas Environment

Most of the oxidation experiments were conducted at 700°C with the goal of producing more protective scales at the lower temperature. This more protective scale would be achieved through the reduction of the rutile component and the enhancement or enrichment of the alumina component, as predicted by the stability diagrams of the Al-Ti-Nb-O-N system. Table 5.6 summarizes the thermogravimetric experiments conducted at 700°C.

Table 5.6 Summary of oxidation experiments carried out at 700°C in microbalances

700°C	**Alloy (microbalance)**					
Gas Label	**Super Alpha Two**		**Alpha Two**		**Gamma**	
	Cahn	**DuPont**	**Cahn**	**DuPont**	**Cahn**	**DuPont**
Ar-5% O_2	X		X		X	
N_2-5% O_2	X		X		X	
Ar-20% O_2	X	X	X	X		X
N_2-20% O_2	X	X	X	X	X	X
O_2	X	X	X	X	X	X
N_2	X	X				

X - Experiments run at these conditions

5.2.1 Kinetic Results in Argon-5% Oxygen

Samples were oxidized in the reduced oxygen content of argon-5% oxygen to simulate the reduced total pressure experienced in the ESEM and to study the effect of oxygen content and the nitrogen effect by comparison to nitrogen-5% oxygen. In view of the small corrosion rates, the samples were exposed for periods of 100 hr. A few samples were reacted for only two hours to simulate the exposure time in the ESEM. The resulting surfaces appeared barely tarnished, and the weight gains were so small (0.03 to 0.08 μg), that most of the thermogravimetric data was not reproducible or experimentally significant.

The weight gains for all three alloy substrates exposed in argon-5% oxygen at 700°C are shown in Figure 5.6. The curves followed the general trend previously observed at 800°C for these intermetallic alloys (§5.1), with SA2 behavior intermediate between that of G (least weight gain) and A2 (greatest weight gain). The scale on alloy A2 was the most opaque, of a gray-white color and roughly 3 μm in thickness. The scales on G and SA2 substrates were much more translucent, with some patchy areas of grayer scale corresponding to certain grain orientations. The film on alloy G had a gold-pink color, and that on alloy SA2 a pink/green color.

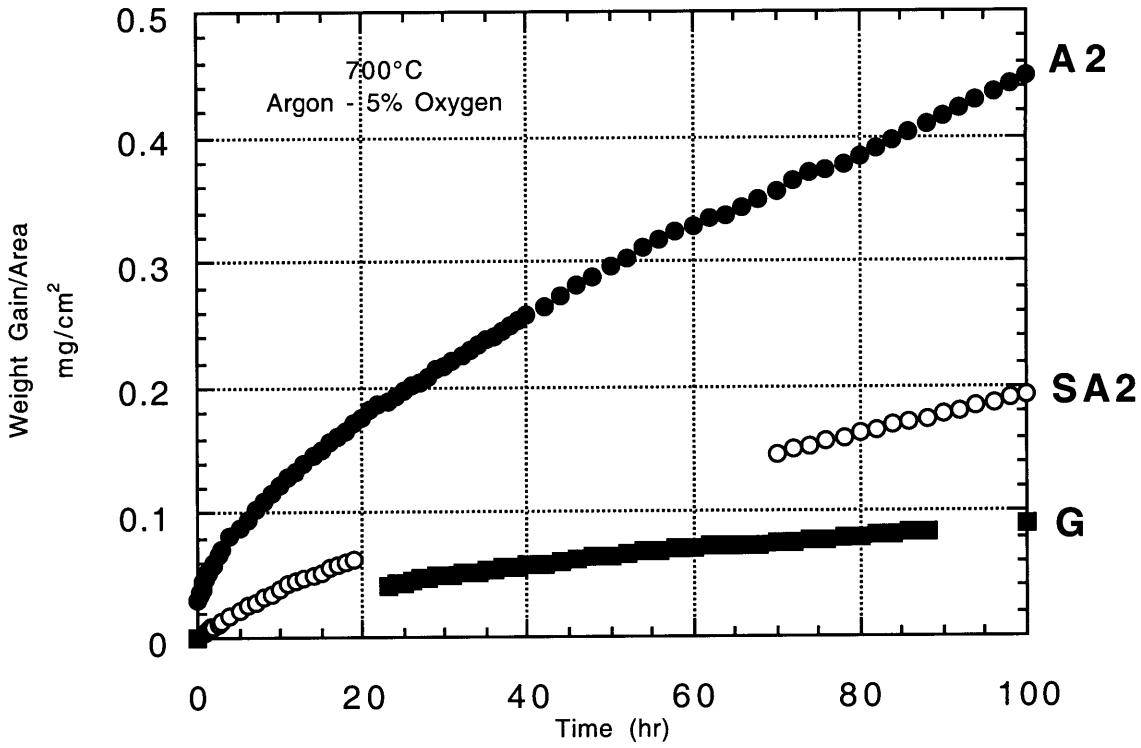

Figure 5.6 Weight gain kinetics for alloys G, SA2 and A2 exposed to argon-5% oxygen at 700°C for 100 hours in the Cahn microbalance.

5.2.2 Kinetic Results in Nitrogen-5% Oxygen

Samples were exposed to nitrogen-5% oxygen to compare to the argon-5% oxygen samples and to study the impact of nitrogen in the gaseous environment. Overall weight gains for this gas mixture were lower than for argon-5% oxygen. Reproducibility was good since even the slowest weight gain seen in G was repeated and agreed to within 20%.

The weight gains for all three intermetallic alloys run in nitrogen-5% oxygen at 700°C are shown in Figure 5.6. The typical trend for these three intermetallic alloys was

seen, with the weight gain of alloy SA2 intermediate between those of G and A2. The scale on alloy G was very thin and a transparent gold-pink with speckles of slight color variation coinciding with different grain orientations. The scale on alloy SA2 was translucent green and purple, and the scale on alloy A2 was grayish white and more opaque than the other two.

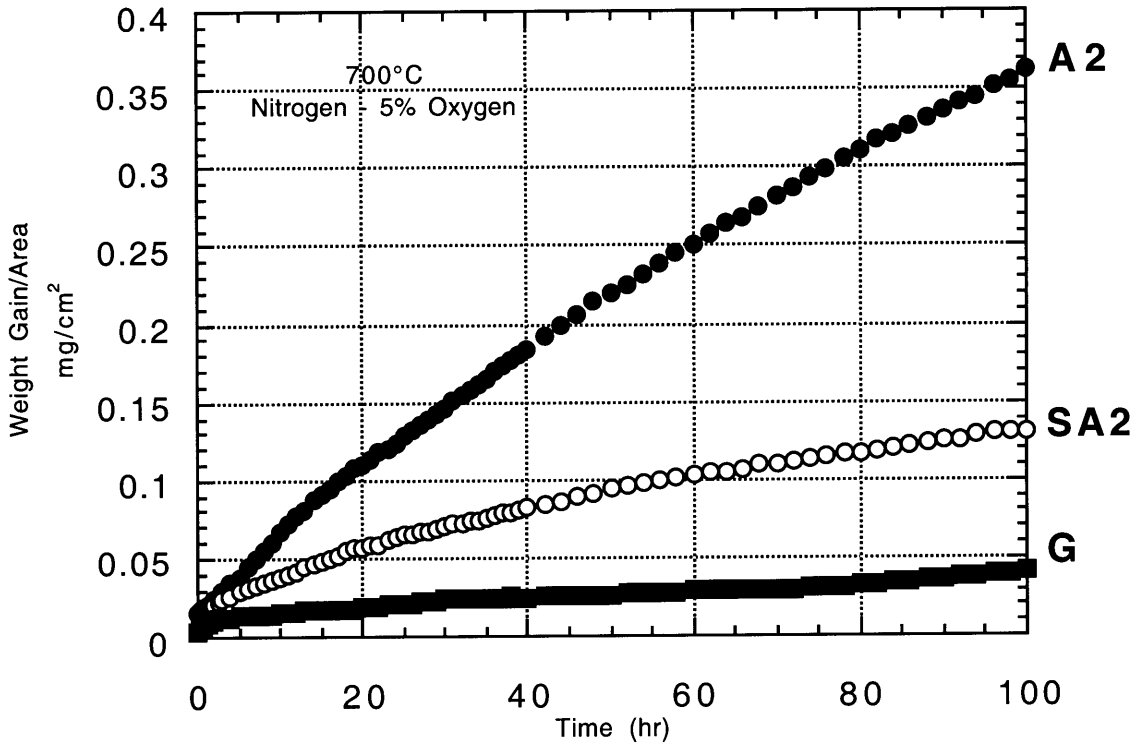

Figure 5.7 Weight gain kinetics for alloys G, SA2 and A2 exposed to nitrogen-5% oxygen at 700°C for 100 hours in the Cahn microbalance.

Comparing the weight gains in oxidation of all three intermetallic alloys in both argon-5% oxygen and nitrogen-5% oxygen, Figure 5.7, it is clear that, the effect of nitrogen in the mixed gas is to lower the overall corrosion rate. The presence of nitrogen affected the oxidation rate of alloy SA2 the most.

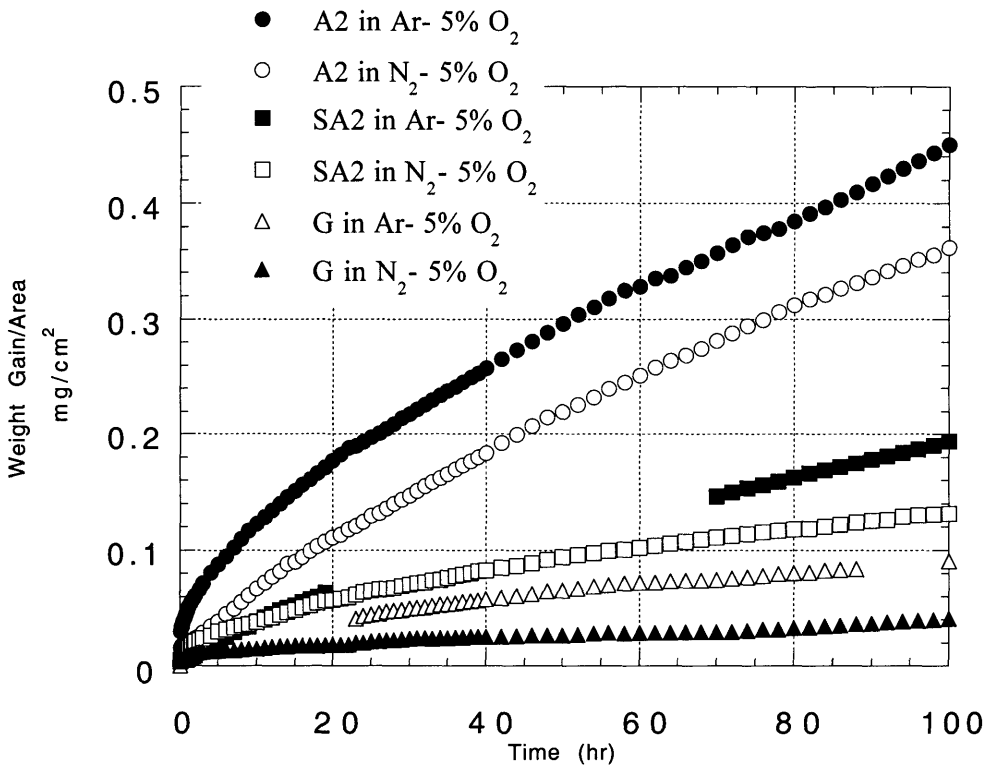

Figure 5.8 Weight gain kinetics for alloys G, SA2 and A2 exposed to argon-5% oxygen and nitrogen-5% oxygen at 700°C for 100 hours in the Cahn microbalance.

5.2.3 Kinetic Results in Argon-20% Oxygen

Experiments were run for 20 hr in the DuPont microbalance and for 100 hr in the Cahn microbalance in the mixture of argon-20% oxygen. Results were then compared to those seen in air to similarly isolate the effect of nitrogen .

5.2.3.1 Oxidation for 20 Hours in the DuPont Microbalance

The three intermetallic alloys oxidized at 700°C for 20 hours in argon-20% oxygen exhibited comparative behavior similar that observed under the previous conditions, with alloy A2 gaining the most weight, alloy G gaining the least weight and

alloy SA2 gaining a weight intermediate between the two. After 20 hours, the mass per unit area gained for alloy A2 was approximately 1 mg/cm^2, for alloy G 0.2 mg/cm^2, and for alloy SA2 0.5 mg/cm^2. These weight gain data are plotted in Figure 5.8.

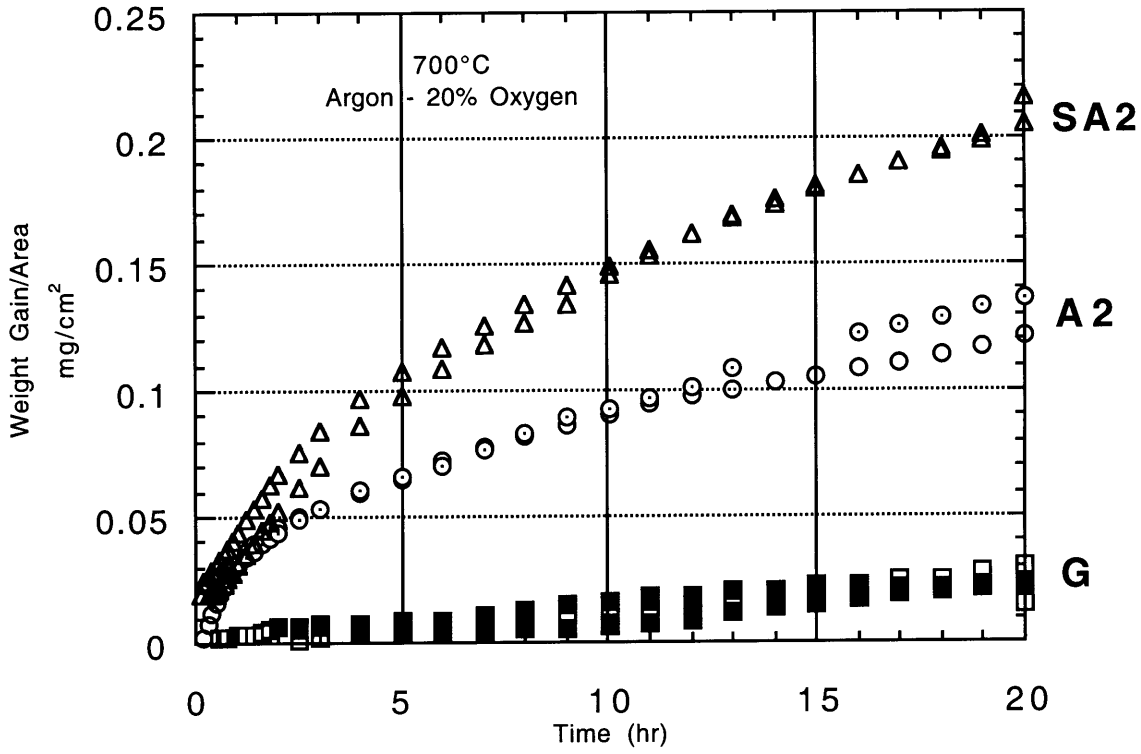

Figure 5.9 Weight gain kinetics for alloys G, SA2 and A2 oxidized at 700°C for 20 hours in argon-20% oxygen in the DuPont microbalance.

The extremely low weight gain of alloy G samples posed some problems for obtaining accurate kinetic data. Five samples were oxidized with only one giving reliable data over the entire experiment time. Small weight gain anomalies that would average over time with little influence on overall oxidation rate for the other intermetallic alloys had a proportionately larger influence on the kinetic rate observed for alloy G because of

the very small weight gains. The final sample gave a parabolic rate of 2.5×10^{-14} g^2/cm^4-sec. This rate was deemed sufficiently definitive because the five samples all ended up similar in appearance, both macroscopically and microscopically, and had microbalance weight gains that agreed with weight gains measured on the Mettler balance after each oxidation run.

Measurements taken on three alloy A2 samples yielded kinetic rates ranging from 2.2 to 5.0×10^{-13} g^2/cm^4-sec. Two samples yielded approximately equal rates, 2.2 and 2.4×10^{-13} g^2/cm^4-sec, but the weight gains as measured by the microbalance and the Mettler balance had larger discrepancies. The weight gain for the sample with the larger parabolic rate was only 2% error different in the two instruments and corresponded to a parabolic rate which closely matched that determined from 100 hr experiments.

Weight gain measurements taken for three alloy SA2 samples yielded parabolic rates ranging from 4.2 to 7.4×10^{-13} g^2/cm^4-sec. No noise or other data anomalies were observed and the data fitted parabolic behavior well (with fits of 0.995 or better). Despite these good fits, the sample with the low value exhibited up to 20% in weight gains measured by the microbalance and the final Mettler balance reading.

5.2.3.2 Oxidation for 100 Hours in the Cahn Microbalance

The lower sensitivity of the Cahn microbalance relative to the DuPont was compensated for by its being able to run larger sample sizes for longer times. Parabolic rates at 100 hr agreed well with those measured after 20 hr with the DuPont balance. No consistent trend was discerned in the use of the two microbalances: some oxidation rates were lower and some higher in the two determinations. Figure 5.9 illustrates the weight gains at 700°C after 100 hour exposure to argon-20% oxygen.

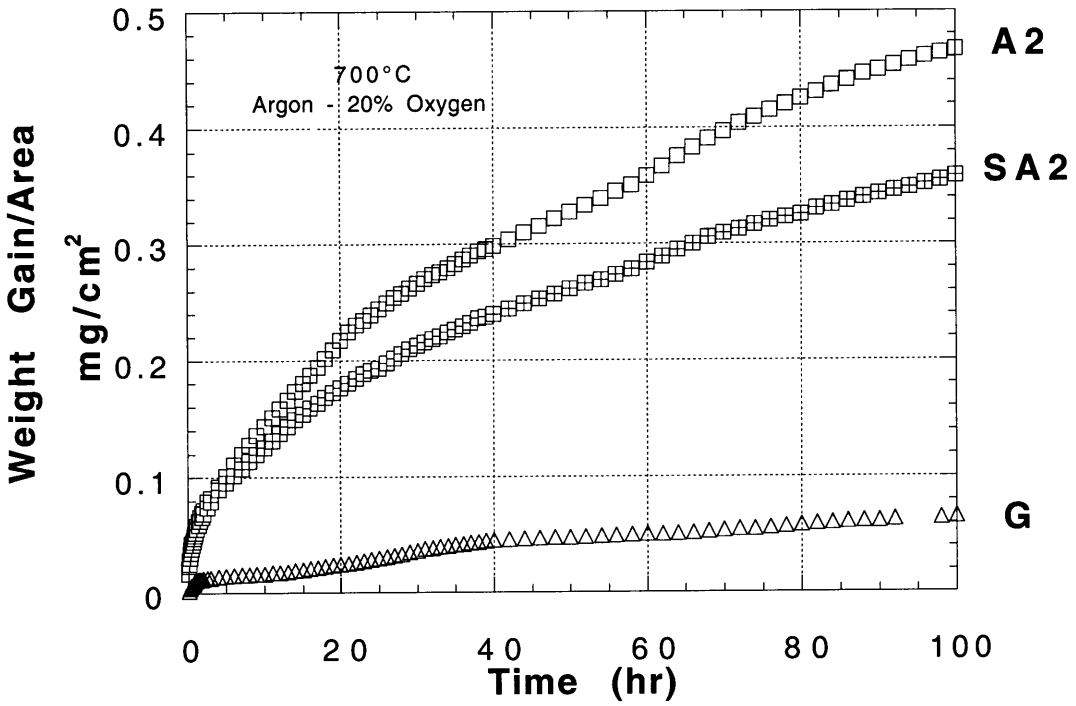

Figure 5.10 Weight gain kinetics for G, SA2 and A2 alloys exposed at 700°C for 100 hours in argon-20% oxygen in the Cahn microbalance.

5.2.4 Kinetic Results in Nitrogen-20% Oxygen

Samples were exposed for 20 hr in the DuPont microbalance and for 100 hr in the Cahn microbalance to a nitrogen-20% oxygen gas mixture. The mixture simulated air, which would be a typical gaseous environment to which these intermetallic alloys would be exposed in real applications. The cylinder of the nitrogen-20% oxygen mixture was used, rather than laboratory air, to allow the gas to be dried and to flow through the furnace in an identical fashion to the other gas mixtures. Despite weight gains which are smaller than those measured for the argon-20% oxygen exposures, agreement between samples and microbalances was very good. Figure 5.10 shows that the behavior of the

three intermetallic alloys remains similar to that observed with the other gas mixtures. As seen for the 5% oxygen mixtures, the nitrogen in the mixture lowers the overall corrosion rate. One difference noted is that the rate spread for alloy SA2 in the two different gases is larger for the 20% oxygen admixtures than was seen for the 5% oxygen admixtures.

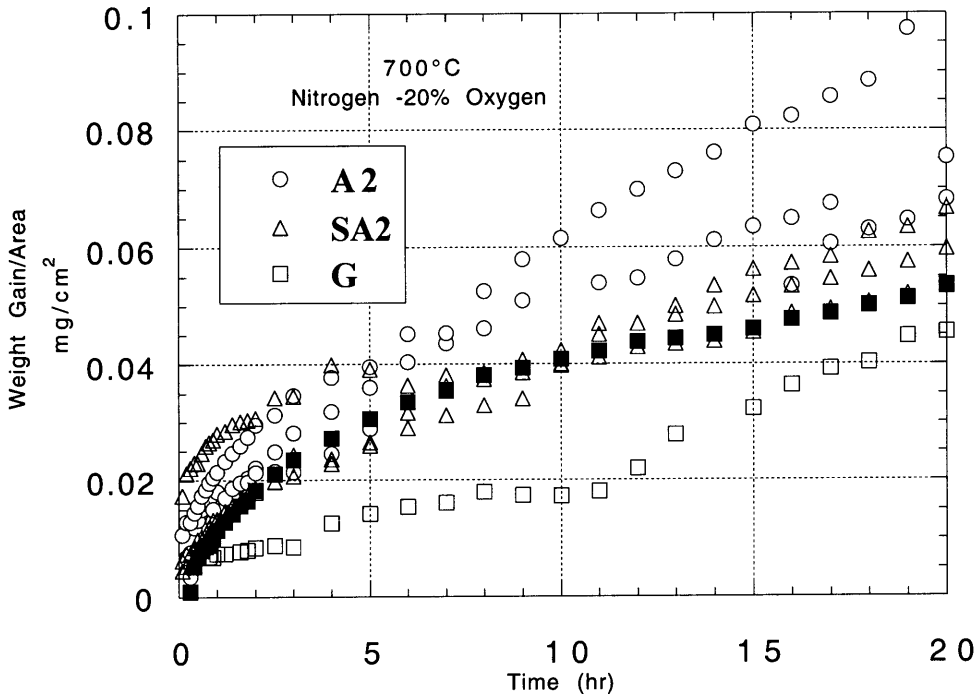

Figure 5.11 Weight gain kinetics for G, SA2 and A2 alloys exposed at 700°C for 20 and 100 hours to nitrogen-20% oxygen in both microbalances.

5.2.5 SEM Results in Argon-Oxygen Mixtures

Corrosion scales grown in the argon-oxygen mixtures showed more instances of non-uniform scales and whiskers.

The scale on alloy G oxidized in argon-5% oxygen showed features similar in nature to those formed in nitrogen-5% oxygen but on a much larger scale. For example, fuzzy ridges of rutile were seen in both mixtures, but require magnifications of 5000X to

be visible following oxidation in nitrogen-5% oxygen and only half that following oxidation in argon-5% oxygen. Figure 5.12 shows a section of a lamellar showing variation of scale morphologies over each lath composition.

Additionally, spallation was observed in the argon mixtures after only 20 hours; spallation on samples reacted in nitrogen mixtures were only observed after 100 hours.

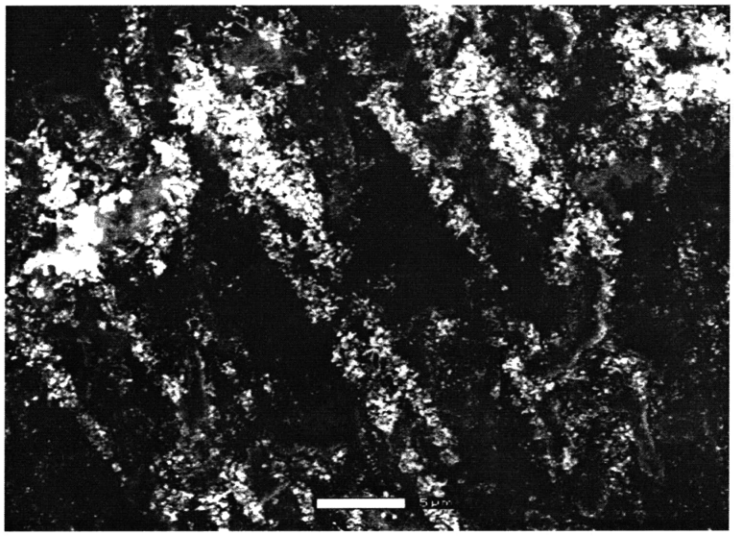

Figure 5.12 ESEM micrograph of alloy G exposed to argon-5% oxygen at 700°C for 100 hours.

The surface of alloy SA2 after exposure looked very similar to that of the initial substrate. Artifacts from the surface finish are apparent and scale features were often related to these polishing remnants. Comparison of alloy SA2 oxidized in argon-5% oxygen and in nitrogen-5% oxygen shows very little difference in oxidation behavior between the two, and little change from the initial substrate condition. The elongated grains of darker contrast of the second alloy phase are visible still. The scale is typically only visible in local substrate surface anomalies arising in polishing: scratches, high points and linear arrays of pits resulting from polishing had notably oxidized as

evidenced by the presence of charging in the ESEM and concomitant blurring of the image at these features.

Faceted nodules were noted on samples. An example of such nodules is given in Figure 5.13.

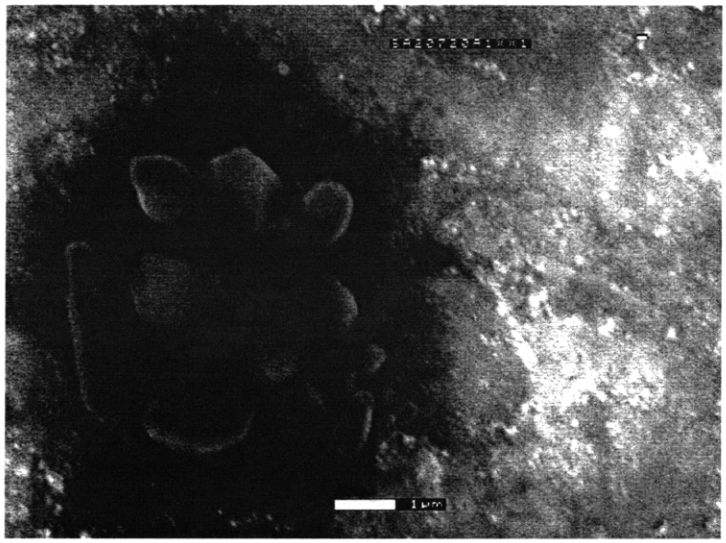

Figure 5.13 ESEM micrograph of alloy SA2 exposed to argon-20% oxygen at 700°C for 100 hours.

5.2.6 SEM Results in Nitrogen-Oxygen Mixtures

The scales on samples oxidized in nitrogen-20% oxygen exhibited more homogeneity in the scale and grain texture than those observed on samples oxidized in argon-20% oxygen. Alloy G oxidized in the nitrogen-20% oxygen mixture looked barely tarnished, and the extremely low weight gains support this observation.

The alloy G specimen also showed little change from its initial substrate condition. That some scale had formed was evidenced by the charging at magnifications of about 5000X. Spallation was evident, as seen in Figure 5.14. Not all cracks resulted in spallation, as some cracks were observed to end in the scale, and the scale remained

largely attached.

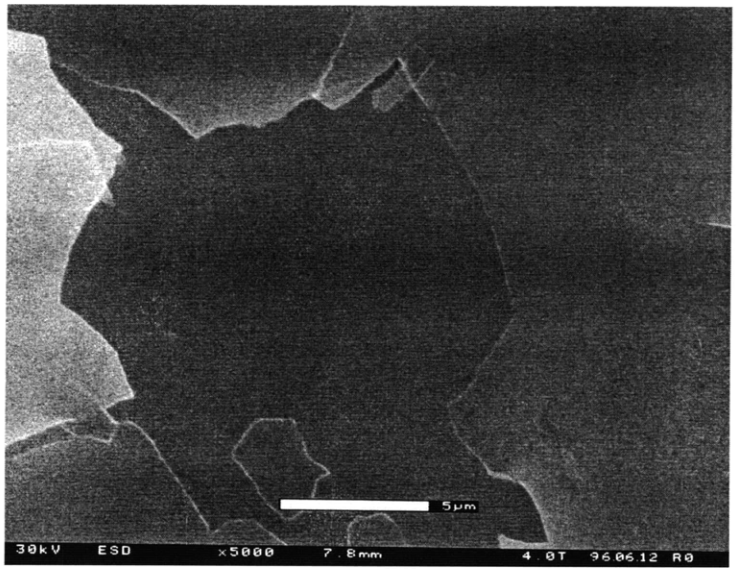

Figure 5.14 ESEM micrograph of alloy G exposed to nitrogen-5% oxygen at 700°C for 100 hours.

The scale on alloy A2 was visibly thicker than on the other two intermetallic alloys and showed macroscopic spallation at the edges. Fine whiskers were seen only at high magnifications (> 10,000X in the ESEM) or in cracked portions of the scale where whiskers and scale may have regrown. What appears to be holes at lower magnifications are at higher magnifications seen to be local thickness variations in the scale.

A higher magnification of these regions (Figure 5.15) show whiskers overgrowing portions of thinner scales.

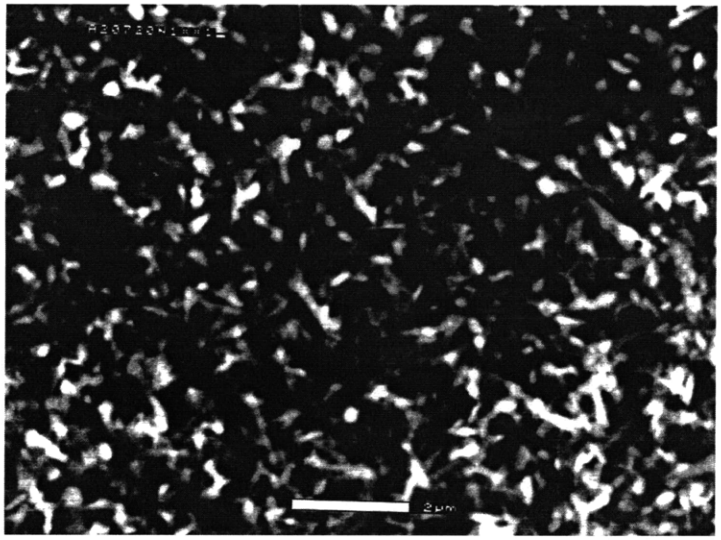

Figure 5.15 ESEM micrograph of alloy A2 exposed to nitrogen-20% oxygen at 700°C for 100 hours.

The scale grown on alloy SA2 appeared the most adherent but not always the most homogenous. The scale was thin enough to show clearly the surface finish beneath (Figure 5.16). Higher magnification micrographs indicates some amount of nodules as well as small spheres which may indicate the presence of Nb_2O_5 over local pores or cracks. This is similar to spheres seen in 100% oxygen environments, § 5.3.

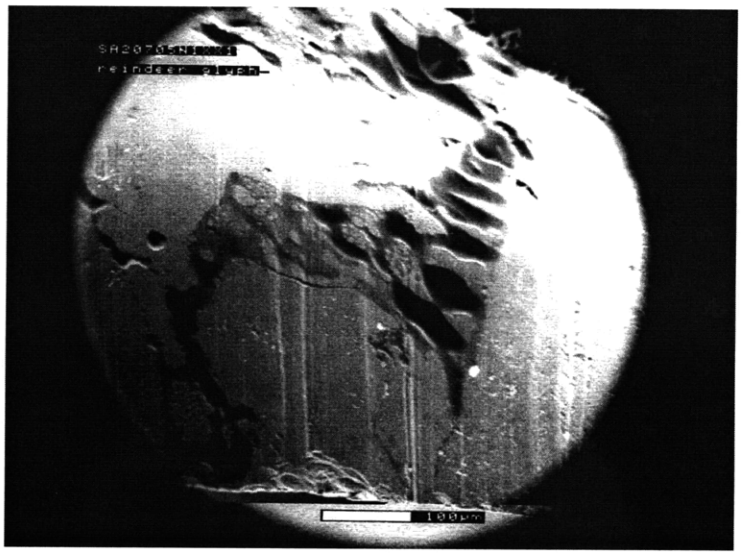

Figure 5.16 ESEM micrograph of alloy SA2 exposed to nitrogen-5% oxygen at 700°C for 100 hours.

Again, the scales on these aluminide alloys tended to be very thin, even after 100 hours at 700°C. Alloy G appeared to exhibit preferential oxidation of certain grain orientations as some areas looked darker and different from others; however, these visual differences could also be due to differences in oxide orientation. The overall scale appearance was pink - yellow and varied due to the thickness rather than due to the proportion of rutile. After 100 hours, macroscopic evidence of spallation on the A2 alloy was noted in concert with a mottled gray scale. The SA2 alloy had a very thin translucent tarnish, with yellow and pink streaks corresponding to the underlying grains of the SA2 substrate.

5.2.7 GAXRD Results

Only 100-hr studies were conducted for the 5% oxygen admixtures. Rutile/alumina ratios were again determined and are given in Table 5.7, along with the ratios calculated for 100 hour exposures in the argon-20% oxygen and nitrogen-20% oxygen gases. Ratios larger than 50 were taken to be greater than the equipment sensitivity and are noted as the scale containing only rutile. Although substrate peak shifts were observed from the peak positions listed in the JCPDS file for each of the titanium aluminides, the peak positions for the oxide scales grown on the intermetallic alloys never varied by more than $2\theta = 0.4$ from the PDF card values for the relevant oxide compounds. The smaller shift in peak positions can be attributed to the tighter stoichiometry of the oxides compared to those of the intermetallics and to the higher stiffness of the oxides which results in less strain for any given residual stress.

Table 5.7 Ratios of rutile to alumina grown on G, SA2 and A2 alloys after 100 hour exposures at 700°C in 5% and 20% oxygen mixtures with nitrogen and argon.

	GAS COMPOSITION			
Specimen Substrate	**N_2-5%O_2**	**Ar-5%O_2**	**N_2-20%O_2**	**Ar-20%O_2**
G	1.2	5.2	0.8	4.7
SA2	2.0	4.9	3.5	9.3
A2	15.4	67.5	31.1	68.5

5.2.7.1 Oxidation in Nitrogen-5% Oxygen and Argon-5% Oxygen Environments

Tables 5.9 - 5.11 located at the end of this chapter outline the phases identified on each titanium aluminide at 700°C for all gases used in this study. The GAXRD intensities after exposure of substrates to the argon-containing gas mixtures were higher than those for substrates exposed to the nitrogen-containing mixtures, suggesting a thinner scale, a conclusion which correlates well with the thermogravimetric data. The stronger GAXRD signal increased the signal/noise levels and enhanced the ease of identifying phases; however, the argon mixtures in general resulted in less alumina than did the nitrogen gas mixtures.

a) Phases Detected on Alloy G

Alloy G was the only titanium aluminide studied whose scale patterns displayed distinct alumina peaks in all the gas mixtures. For oxidation in nitrogen-5% oxygen, the ratio of rutile to alumina was nearly one to one, while in argon-5% oxygen, the relative amount of rutile increased approximately 4-5 times. Alloy G substrate peaks were still visible after oxidation for 100 hours and were sharper and less broad than those peaks in the substrate patterns before exposure. A2 substrate peaks were also visible both before and after oxidation, with no detectable change in the ratio of γ-TiAl to α_2-Ti_3Al. The substrate peaks exhibited a shift relative to the initial substrate peak positions -- to positions that more closely matched the JCPDS card for γ-TiAl.

The higher signal and reduced background noise in the sample oxidized in argon-5% oxygen permitted identification of the mixed oxide $TiAl_2O_5$. This oxide may also be present after oxidation in nitrogen-5% oxygen, but in smaller amounts not detectable above the greater background noise.

There are peaks that cannot be indexed using JCPDS data for the three intermetallic compounds, or for rutile, alumina or the mixed oxide. These peaks instead match well to the six most intense peaks of the aluminum oxynitride, $Al_{27}O_{39}N$. As

further proof, these peaks are noticeably absent in the argon-oxygen mixtures, where any nitrogen impurity is too small to have formed detectable amounts of the oxynitride. Of all the substrates, the match to the aluminum oxynitride is the closest for alloy G oxidized in nitrogen-5% oxygen.

b) Phases Detected on Alloy A2

For the alloy A2 samples oxidized in argon-5% oxygen and in nitrogen-5% oxygen, alumina was a far less prominent component and was clearly detected only in the nitrogen mixture. The presence of rutile is distinct for samples exposed to both nitrogen-5% oxygen and argon-5% oxygen. Small amounts of α_2-Ti_3Al substrate peaks were detected, with less peak broadening than for the unexposed substrate. No γ-TiAl peaks were observed.

After oxidation in nitrogen-5% oxygen, both the mixed oxide, $TiAl_2O_5$, and the aluminum oxynitride were detected. For the sample oxidized in argon - 5% oxygen, only rutile was distinguishable. The presence of the mixed oxide and substrate peaks was not ruled out but, if present, were very weak compared to the rutile peak intensities. As with the other substrates, samples reacted in argon-5% oxygen exhibited much larger peak intensities overall due to the thicker scale.

c) Phases Detected on Alloy SA2

GAXRD patterns for the scales grown on alloy SA2 in argon-5% oxygen and the nitrogen-5% oxygen gas mixtures were more complicated because of the presence of Nb present in the substrate and in niobium containing oxides in the scales.

As with the other titanium aluminides, the nitrogen-5% oxygen exposures produced a more distinct alumina presence compared to rutile- but both were still present. Peaks were somewhat broadened for both oxides. The A2 substrate peaks were detectable for both gas compositions, though these were less intense after the argon-5% oxygen oxidation. Faint γ-TiAl peaks could be seen only for

nitrogen-5% oxygen oxidation, presumably because of the thinner scale. Both gas mixtures grew a mixed $TiAl_2O_5$ scale. The formation of an aluminum oxynitride in the nitrogen-5% oxygen mixture was not definitively indicated by XRD.

Niobium-containing oxides were found after exposure to both gas mixtures. These phases were identified as niobia, Nb_2O_5, as well as the mixed oxide, $AlNbO_4$. There were no other significant unaccounted-for peaks.

5.2.7.2 Oxidation in Argon-20% Oxygen and Nitrogen-20% Oxygen Environments

The titanium aluminide alloys were oxidized in argon-20% oxygen and nitrogen-20% oxygen for 20 and 100 hours, so that the evolution of the scale composition could be followed with time in addition to studying the effect of nitrogen in a mixture duplicating the oxygen content of air.

a) Phases Detected on Alloy G

Alloy G samples exposed to nitrogen-20% oxygen for only 20 hr showed negligible amounts of alumina compared to amounts seen after exposure for 100 hours. The alumina peaks were shifted slightly to smaller 2θ values. Peaks from the alloy G substrate were still evident, with some being attenuated and most remaining broadened as before. The strongest peak became sharper, and the higher 2θ peaks remained essentially the same width. Peaks from the small α_2-Ti_3Al component of the substrate were seen for the argon-20% oxygen mixtures at both 20 and 100 hours. α_2-Ti_3Al is seen only weakly at 20 hours and not at all after 100 hr in nitrogen-20% oxygen. The relative intensities of the substrate peaks remained about the same.

The mixed oxide $TiAl_2O_5$ appears as a minor phase in both gas mixtures for both oxidation times. The presence of aluminum oxynitride, $Al_{27}O_{39}N$ is consistent with minor peaks for the nitrogen-20% oxygen exposure, but was not detectable for the

argon-20% oxygen environment.

b) Phases Detected on Alloy A2

Alloy A2 reacted in argon-20% oxygen produced rutile in the scale at 20 and 100 hours, but the alumina peaks became weaker at the longer exposure time. The α_2-Ti_3Al substrate peaks were still visible after both exposures.

Six peaks appear at 20 and 100 hours that were not detected before oxidation. The oxynitride was not detected, and there was evidence of the mixed Ti-Al oxide whose peak intensities decreased overall from 20 to 100 hours.

Both alumina and rutile were distinctly present in the scale formed on alloy A2 oxidized in nitrogen-20% oxygen for 20h. The α_2-Ti_3Al substrate peaks were also present, with the same shift as seen in the unreacted specimen. There was some indication that γ-TiAl appeared as well, as a very minor component. The mixed oxide is also present, with several major peaks evident. The presence of the oxynitride of Al is consistent with minor peaks, with small angle shifts as compared to the PDF values.

For the alloy A2 specimens reacted in nitrogen-20% oxygen for 100 hr, rutile was obvious in the scale, but the alumina peaks were much weaker. Owing to the greater scale thickness, it is not known if the diffraction pattern comes mostly from the outer scale, in which alumina is less prominent than in the inner region which would have been observed in the thinner scale after shorter exposures. After longer exposure, the α_2-Ti_3Al substrate peaks are still present, but very weak relative to the oxide peaks. No γ-TiAl peaks were seen when the intensity of the α_2-Ti_3Al was barely discernible. The mixed Ti-Al oxide and the aluminum oxynitride are seen at both exposure times.

c) Phases Detected on Alloy SA2

Oxidizing alloy SA2 in both 20% oxygen admixtures resulted in the presence of both alumina and rutile, with alumina peaks being weaker in the argon-20% oxygen.

Considerable peak broadening as well as a rather high background were evident, but most peaks were still detectable. The α_2-Ti_3Al peaks from the substrate were detectable but no γ-TiAl peaks were observed. Peaks from the mixed oxide were present in all the samples, but weaker after 100 hours in argon-20% oxygen than at 20 hours and after 20 hours in nitrogen-20% oxygen than in argon-20% oxygen. The oxynitride is possibly present in the samples exposed to the nitrogen admixtures, but the peaks were obscured by the substrate peaks which remained visible at the higher 2θ values.

The presence of niobia could be construed from certain peaks but was not definite, since the major and several minor peaks lie under broadened peaks for alumina and rutile. There were shoulders on these peaks that would seem to indicate a niobia presence. Nb_2O_5 is detected after 100 hours in nitrogen-20% oxygen but not after 20 hours and after both exposure times in argon-20% oxygen. The mixed $AlNbO_4$ oxide, which is evidenced by a shoulder on the strongest rutile peak (at $2\theta = 27.5°$), appears in all the samples except that oxidized for 100 hours in argon-20% oxygen, where its detection was inconclusive.

5.3 Oxidation Experiments at 700°C in 100% oxygen

Some published studies on the oxidation of these intermetallic alloys in pure oxygen at higher temperatures show a lowered oxidation rate compared to experiments carried out at smaller oxygen concentrations, presumably due to a change in scale formation mechanism or structure. Experiments in this study showed that 100% oxygen yielded greater oxidation rates at 700°C. One exception was noted. In pure oxygen, the scale on alloy SA2 grew faster than that on alloy A2, which had not been typical of the series. Oxidation tests were run for 20 hr in the DuPont microbalance and for 100 hr in the Cahn microbalance.

5.3.1 Kinetic Results

After 20 hours in pure oxygen, the comparative behavior of the three intermetallic

alloys differed from the pattern established in mixed gases, as seen in Figure 5.17. Only in 100% oxygen did the alloy SA2 yield the least protective scale and fastest oxide growth of the intermetallics. This fast rate persisted through 100 hour exposures (Figure 5.18), where weight gains for both alloys A2 and SA2 became very close to each other. Parabolic rates obtained from both 20 hour and 100 hour exposures agreed well with one another. Table 5.8 gives the average K_p for each intermetallic alloy for both oxidation times.

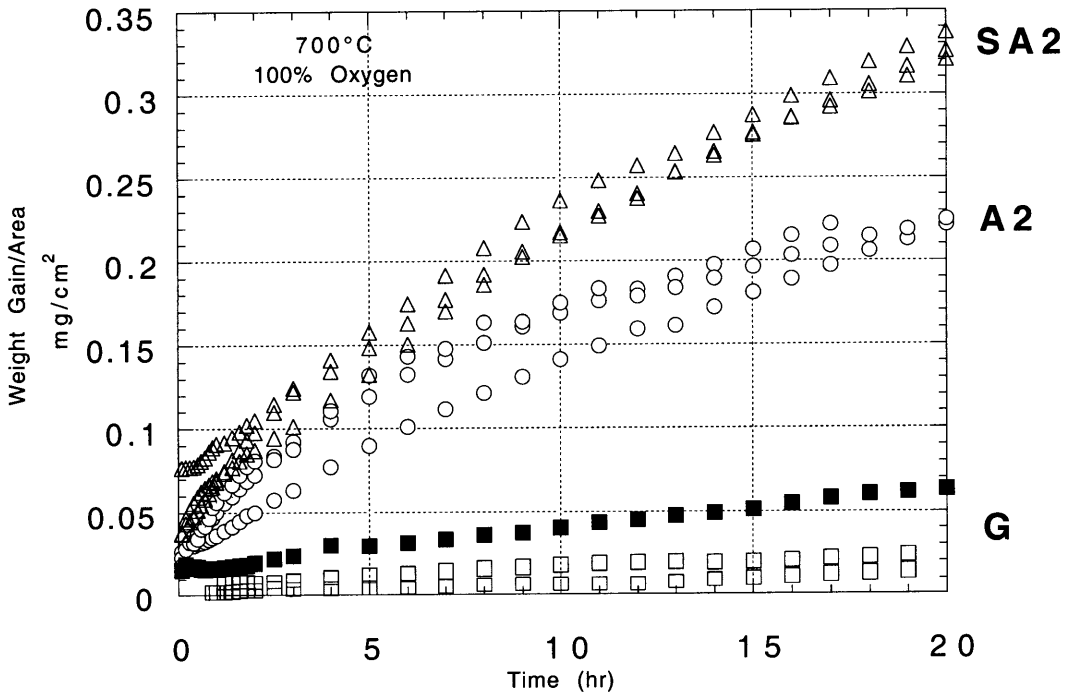

Figure 5.17 Weight gain kinetics for alloys G, SA2 and A2 exposed at 700°C for 20 hours to 100% oxygen in the DuPont microbalance.

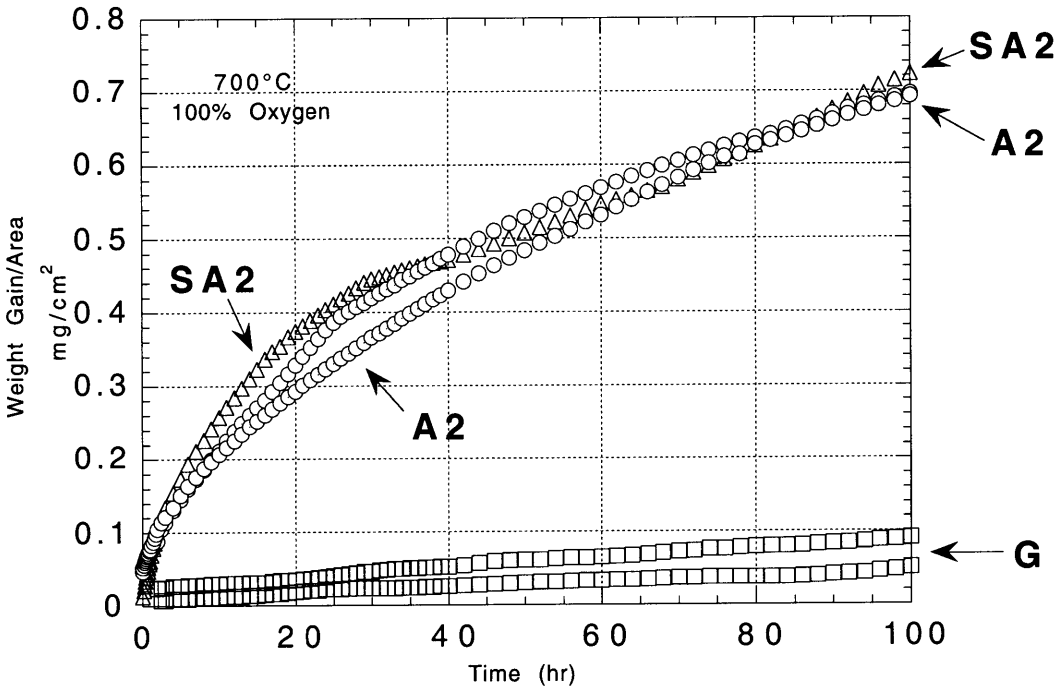

Figure 5.18 Weight gain kinetics for alloys G, SA2 and A2 exposed at 700°C for 100 hours in 100% oxygen in the Cahn microbalance.

Table 5.8 Average thermogravimetric parabolic rates determined in this study at 700°C for 20 hours and 100 hours in 100% oxygen.

ALLOY	Parabolic rates in units of g^2/cm^4-sec
G	5.3×10^{-15}
A2	1.1×10^{-12}
SA2	1.8×10^{-12}

5.3.2 SEM Results

The scales grown on alloy G showed massive spallation after 100 hours. Nodules were apparent under remnants of the scale that appear to have triggered the spallation events.

The scale on alloy A2 exposed in pure oxygen appears to be less whisker-like than for oxidation in environments with lower oxygen content. The scales are less angular and easier to image in the ESEM. The whiskers appear to be smoothed and filled in. Again, local depressions of the scale surface are apparent, even at 20 hours.

Again, the scale on alloy SA2 was adherent, but showed some local variations. Figure 5.19 gives a sample of some typical scale features observed.

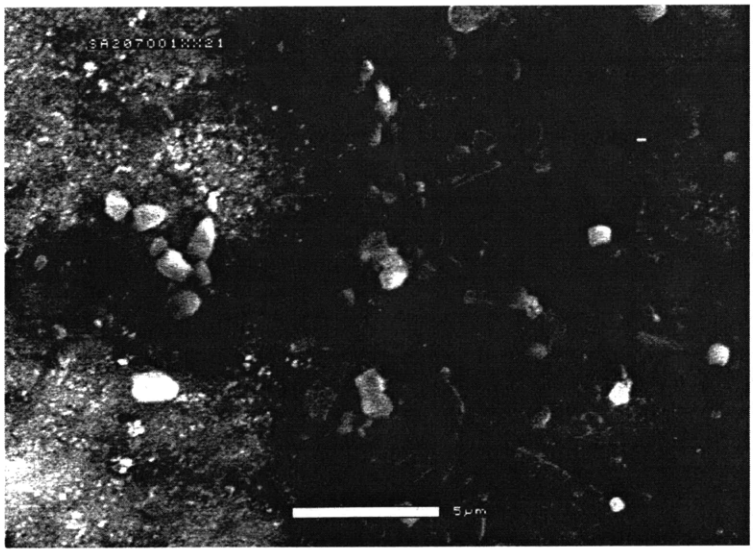

Figure 5.19 ESEM micrograph of alloy SA2 exposed to 100% oxygen at 700°C for 100 hours.

5.3.3 GAXRD Results for Oxidation in Pure Oxygen

X-ray diffraction revealed not only the trend in scale composition grown in oxygen for the three intermetallic alloys, but also changes in the scale composition as a function of time at 20 hour and 100 hour points.

a) Phases Detected on Alloy G

Scales formed on alloy G after exposure to pure oxygen for 20 hr showed the distinct presence of rutile and the strong likelihood of alumina. Substrate peaks were also evident, with the γ-TiAl substrate peaks being most prominent, but α_2-Ti_3Al peaks also present. The estimated scale thickness on alloy G for 20 hr oxidation at 700°C in oxygen is a fraction of a μm, so it is not unexpected that even at glancing angle conditions the x-rays penetrate through the thin scale and retrieve information from the underlying substrate phases.

The mixed oxide $TiAl_2O_5$ was also evident in the patterns, as a minor phase. The presence of the Al oxynitride is not ruled out at 20 hr, but the peaks were far too weak to be definitive.

The diffraction pattern at 100 hr was very similar to that seen at 20 hr. More peaks appear at positions consistent with Al oxynitride, but at such low intensity as to still be inconclusive; the peaks are also shifted slightly relative to the PDF data. However, the presence of an oxynitride is not impossible, since even UHP oxygen may have sufficient nitrogen impurities to produce nitrides.

b) Phases Detected on Alloy A2

The scale formed on alloy A2 specimen oxidized for 20 hr in pure oxygen, exhibited strong rutile peaks and also some alumina peaks. The strongest α_2-Ti_3Al substrate peaks were present, and their positions were less shifted from the PDF positions than those for the initial substrate before exposure. No appreciable amount of γ-TiAl was evident. Peaks consistent with the mixed Ti-Al oxide were present but Al oxynitride was

not detected. The diffraction pattern for the 100 hr exposure was similar, with an increase in the amount of alumina relative to rutile and the relative intensity of the α_2-Ti_3Al substrate peaks diminished due to the increased scale thickness.

c) Phases Detected on Alloy SA2

Both alumina and rutile were seen after oxidation of alloy SA2 in pure oxygen for 20 hr. The peaks for α_2-Ti_3Al were clearly seen and γ-TiAl peaks are possibly present. The mixed oxides, $TiAl_2O_5$ and $AlNbO_4$ were both observed as minor phases. Niobia ,in the form of Nb_2O_5, is evidenced in an intense peak at low 2θ. Al oxynitride was not detected.

After 100 hr, the scale on alloy SA2 was seen to dramatically increase in the intensity of the rutile peaks, while the alumina peaks were significantly diminished. The background also increased so that it was harder to distinguish the minor phases above background. Both the mixed oxide of $TiAl_2O_5$ and niobia appear as weak phases, but the presence of the mixed Al-Nb oxide was not as clear. Neither α_2-Ti_3Al nor γ-TiAl substrate peaks were evident. Al oxynitride was not detected.

5.4 Oxidation Experiments at 700°C in Laboratory-Grade Nitrogen

The SA2 alloy was exposed to laboratory-grade nitrogen at 700°C to determine the role of nitrogen in the scale and the kinetic effects of nitridation and to allow comparison of the kinetic rates to those of the other nitrogen-oxygen mixtures.

5.4.1 Kinetic Results

The weight gains for the samples exposed in 100% nitrogen at 700°C are shown in Figure 5.20.

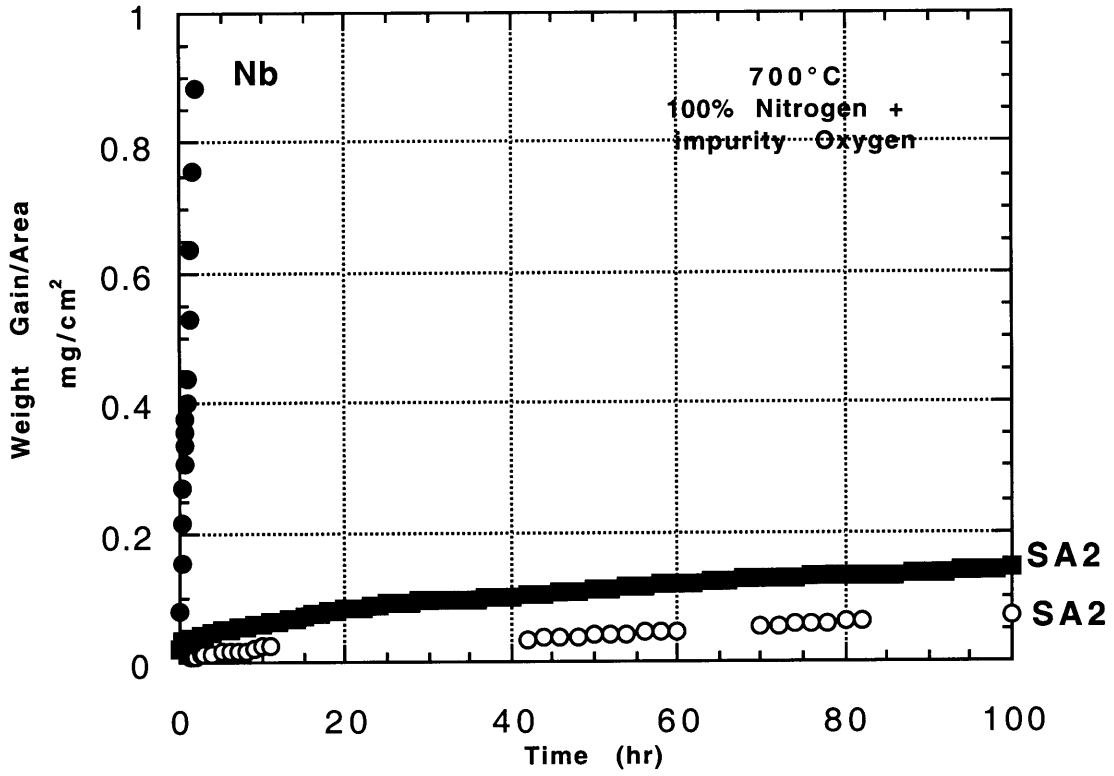

Figure 5.20 Weight gain kinetics for alloy SA2 and 99.98% pure Nb exposed to laboratory-grade nitrogen at 700°C for 20 and 100 hours.

5.4.2 SEM Results

SEM images of alloy SA2 reacted in nitrogen showed a very featureless scale surface, with substrate polishing artifacts, such as scratches and pits, very much in evidence as surface scale features. Samples run in the two different microbalances displayed the same microstructure. Overall contrast was very low and no prominent features were seen in the scales, such as needles, whiskers, flakes or the like. No cracks were seen in the scale, even at the sample edges. Figure 5.21 shows a representative

microstructure.

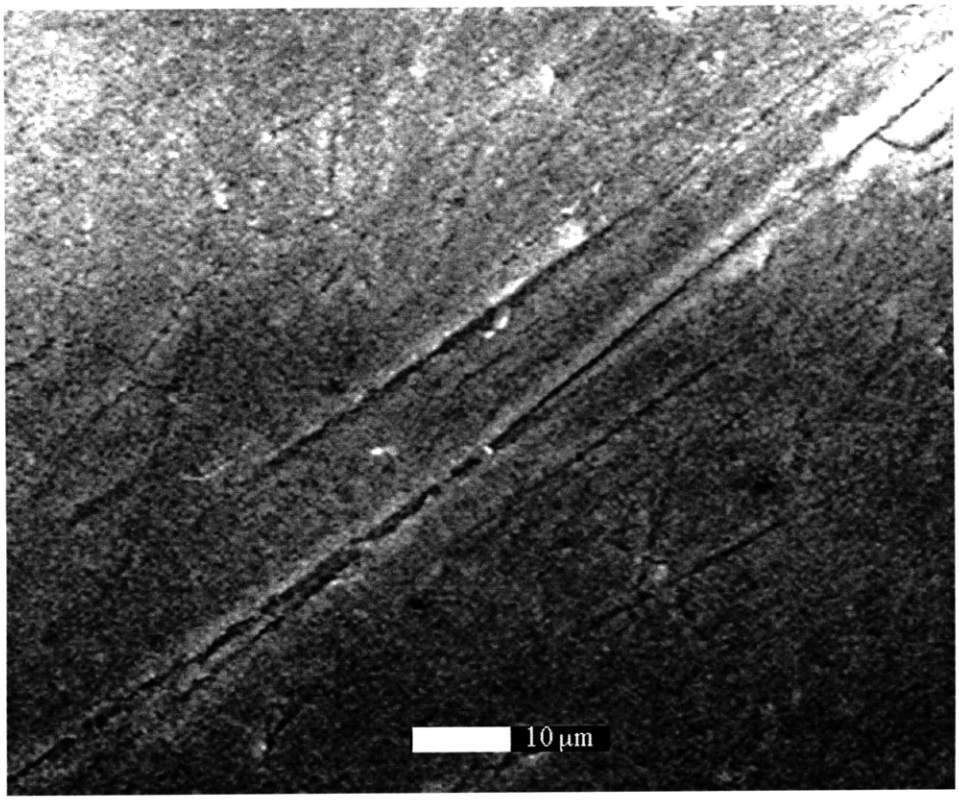

Figure 5.21 ESEM micrograph of alloy SA2 surface after exposure to laboratory-grade nitrogen at 700°C for 100 hours.

5.4.3 GAXRD Results

The x-ray patterns from samples nitrided in the two different microbalances were very similar. Location, broadness and relative intensity of the peaks were virtually identical. There was a higher background at lower 2θ values than generally seen for exposures to environments with much higher oxygen contents.

The scale contained both alumina and rutile, but unlike in many other scales, the rutile was not predominant. Both samples showed clear α_2-Ti_3Al substrate peaks. The peaks more resembled those of the A2 substrate than those of the original SA2 substrate. Peaks for γ-TiAl also appeared, but the original ratio of α_2-Ti_3Al to γ-TiAl peaks was

decreased.

Al oxynitride was the strongest of the extra phases besides rutile and alumina. There was a weak match to the mixed oxide $TiAl_2O_5$, and possibly to Nb_2O_5 and the mixed oxide $AlNbO_4$. The last two oxides were less precise since a multitude of phases resulted in large, convoluted peaks.

5.4.4 Comparison of Nb Exposed to Nitrogen Environment

Samples of 99.98% pure niobium metal were exposed to laboratory-grade nitrogen to determine the nitridation kinetics. The zero-grade nitrogen had a minimum purity of 99.998%, corresponding to a total maximum impurity of 20 ppm of oxygen if it were assumed that all the impurity were oxygen, or $p_{O2} = 2 \times 10^{-5}$ atm. for the gas at 1 atm. The nitrided sample exhibited linear weight gain kinetics with a rate approximately 1.6 x 10-7 g/cm^2 s. The rapid thermogravimetric weight gain indicated that the oxygen impurity in the cylinder formed the oxide preferentially over nitrides in the system. The experiments still proved useful in studying the effect of a drastically reduced oxygen pressure on the corrosion rates. By determining what types of Nb oxides formed on the pure Nb sample, it was possible to reduce the number of niobium oxides that were investigated on the SA2 alloy substrates. This was helpful, since there are 31 different niobium oxides indexed in the JCPDS database. When the GAXRD patterns of the oxide was compared to PDF data for Nb oxides, several Nb_2O_5 patterns matched peak positions as well as a few NbO_2 patterns. Using intensities to refine the matches yielded only one entry that achieved over 80% intensity matches (88%), with the NbO_2 cards yielding a 20% or lower intensity match. The matching oxide was a low temperature orthorhombic Nb_2O_5 produced at 700°C. This same niobia card yielded a good match to an oxide produced when the SA2 alloy was exposed to oxygen, either alone or in a gas mixture.

The nitrided Nb sample became matte gray in the center of the large surface areas

(where oxide spallation was also noted) and exhibited a thin white rim only on the very sharp edges of the sample and the hanging hole.

ESEM micrographs showed a non-protective scale formed on the Nb, with many pores, channels and cracks. Figure 5.22 reproduces a micrograph taken at a center of the specimen face, away from the spalling edges. A higher magnification micrograph (Figure 5.23) shows the porosity seen in the scale, which is far greater than for any scale grown on any of the intermetallic alloys.

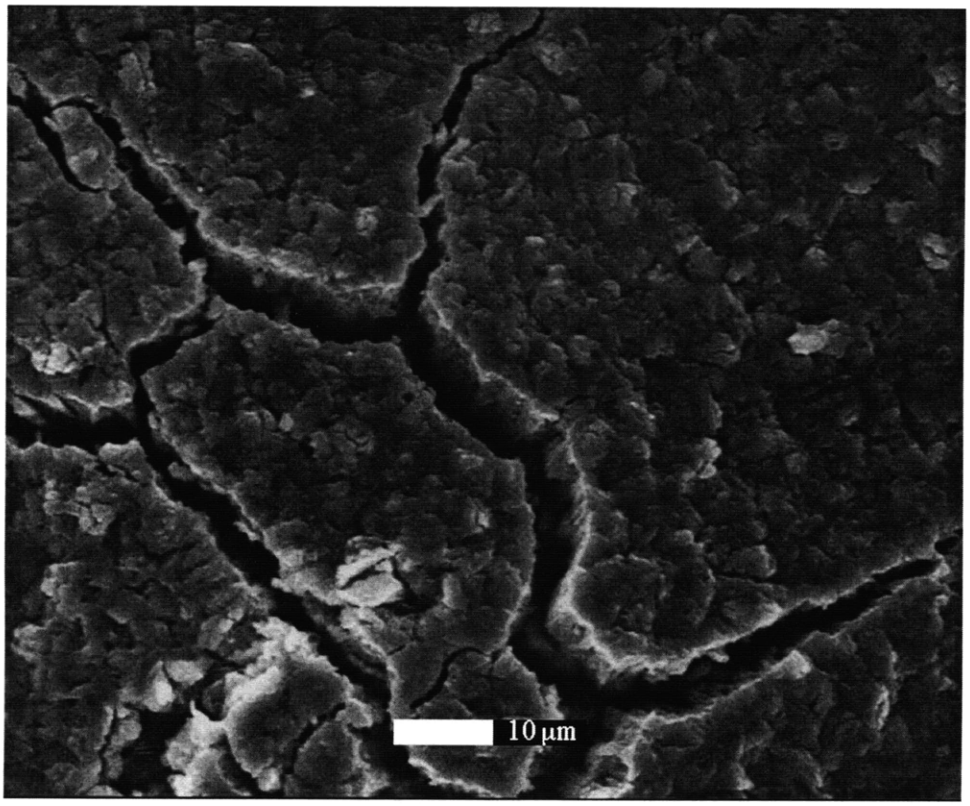

Figure 5.22 ESEM micrograph of 99.98% pure Nb surface after exposure to laboratory-grade nitrogen at 700°C for 20 hours.

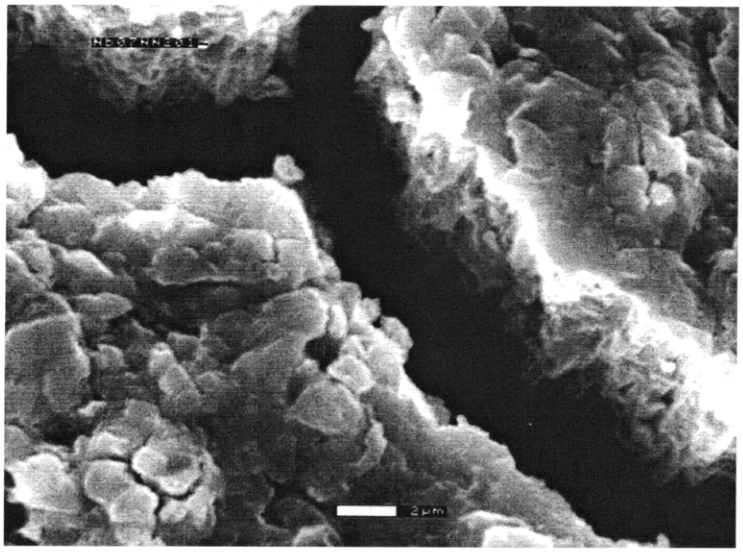

Figure 5.23 Higher magnification ESEM micrograph of 99.98% pure Nb surface after exposure to laboratory-grade nitrogen at 700°C for 100 hours.

5.5 Oxidation Experiments at 700°C: Effect of Oxygen Content

5.5.1 Oxygen-Argon Gas Mixtures

The thermogravimetric data, microscopic details and x-ray diffraction patterns of the titanium aluminides after exposure to the various gas mixtures have been provided earlier. In Figure 5.24, for comparison, are plots of the linear weight gains, comparing only the effect of oxygen content with the argon making up the balance of the gas mixture. The intermetallic SA2 alloy is used for illustration, keeping in mind that the pure oxygen case showed the greatest increase in weight of all the intermetallic alloys in the series.

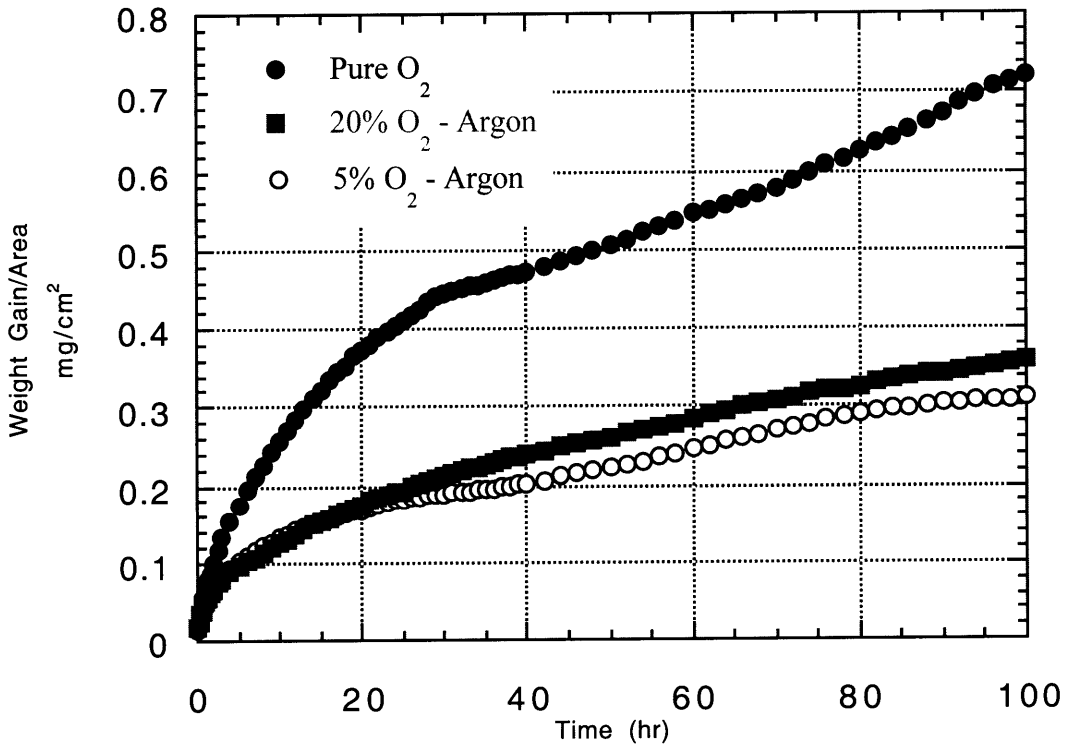

Figure 5.24 Weight gain kinetics for alloy SA2 exposed to three different argon-oxygen mixtures at 700°C for 20 hours.

5.5.2 Oxygen-Nitrogen Gas Mixtures

In this section, the kinetic data obtained are re-plotted in Figure 5.25 to display the effect of oxygen concentration. Each of the samples has been thoroughly described in previous sections. For illustration, the SA2 substrate has been selected. The weight gain data for the pure nitrogen run are included as well, since that represents a very low impurity of oxygen in the nitrogen cylinder and therefore the lowest oxygen concentration of the entire nitrogen-oxygen series. The other intermetallic alloys exhibited a similar behavior.

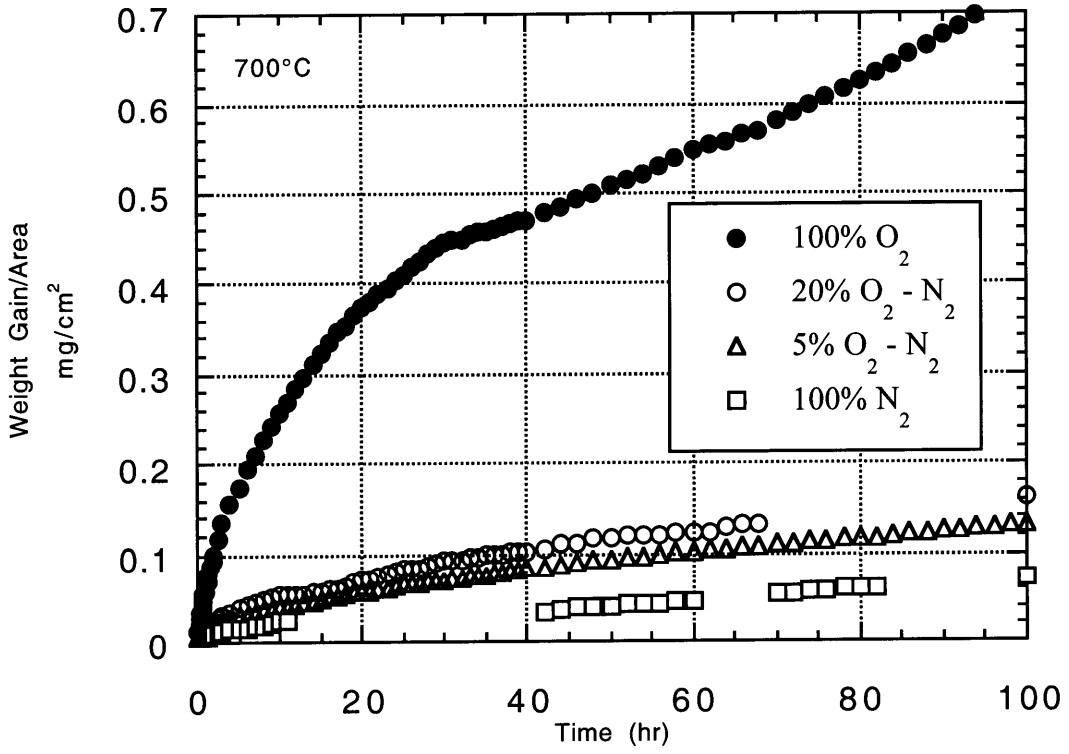

Figure 5.25 Weight gain kinetics for alloy SA2 exposed to four different nitrogen-oxygen mixtures at 700°C for 20 hours.

Table 5.9 Summary of phases detected on alloy G oxidized at 700°C using GAXRD

Gas Mix - Experiment Length	Alumina Al_2O_3	Rutile TiO_2	Mixed Oxide $TiAl_2O_5$	Aluminum Oxynitride $Al_{27}O_{39}N$	Substrate Peaks
05A- 100 hours	**Y**	**Y**	**Y**	**ND**	**G, A2**
05N- 100 hours	**Y**	**Y**	**?**	**Y**	**G, A2**
20A- 20 hours	**Weak**	**Y**	**Weak**	**ND**	**G, A2**
20A- 100 hours	**Y**	**Y**	**Weak**	**ND**	**G, A2 weak**
20N- 20 hours	**Weak**	**Y**	**Weak**	**Weak**	**G, A2 weak**
20N- 100 hours	**Weak**	**Y**	**Weak**	**?**	**G, A2**
Pure O_2- 20 hours	**Weak**	**Y**	**Y**	**ND**	**G, A2**
Pure O_2- 100 hours	**Y**	**Y**	**Y**	**?**	**G, A2**

Y - detected, Weak - detected weakly, ND - not detected, ? - possible

Table 5.10 Summary of phases detected on alloy A2 oxidized at 700°C using GAXRD

Gas Mix - Experiment Length	Alumina Al_2O_3	Rutile TiO_2	Mixed Oxide $TiAl_2O_5$	Aluminum Oxynitride $Al_{27}O_{39}N$	Substrate Peaks
05A- 100 hours	?	Y	?	ND	A2 weak
05N- 100 hours	Y	Y	Y	Y	A2 only
20A- 20 hours	Y	Y	Y	ND	A2, G?
20A- 100 hours	Weak	Y	?	ND	A2, G?
20N- 20 hours	Y	Y	Y	Y	A2, G?
20N- 100 hours	Y	Y	Y	Y	A2, G?
Pure O_2- 20 hours	Weak	Y	?	ND	A2, G?
Pure O_2- 100 hours	Y	Y	?	ND	A2?, G?

Y - detected, Weak - detected weakly, ND - not detected, ? - possible

Table 5.11 Summary of phases detected on alloy SA2 oxidized at 700°C using GAXRD.

Gas Mix - Experiment Length	Alumina Al_2O_3	Rutile TiO_2	Mixed Oxide $TiAl_2O_5$	Al Oxy-nitride $Al_{27}O_{39}N$	Mixed Oxide $AlNbO_4$	Niobia Nb_2O_5	Substrate Peaks
05A- 100 hours	Y	Y	Weak	ND	Y	Y	A2 weak
05N- 100 hours	Y	Y	Y	?	Y	Y	A2, G?
20A- 20 hours	Weak	Y	Y	ND	Weak	Weak	A2
20A- 100 hours	Weak	Y	Weak	ND	?	Weak	A2 weak
20N- 20 hours	Y	Y	Weak	?	Weak	ND	A2
20N- 100 hours	Y	Y	Y	Weak	Weak	Weak	A2
Pure O_2- 20 hours	Y	Y	Weak	ND	Weak	Y	A2, G?
Pure O_2- 100 hours	Weak	Y	Weak	ND	ND	Weak	A2, G?
Pure N_2- 100 hours	Y	Y	Weak	Y	?	?	A2

Y - detected, Weak - detected weakly, ND - not detected, ? - possible

5.6 Discussion of Instrumental Results

5.6.1 TGA Results

Results are given in thermogravimetric rates rather than in the more pure parabolic rates. Parabolic rates would require a more complete knowledge of the scale composition. This would be difficult to quantify with the complex scales seen in this study, since precise amounts of alumina to rutile were difficult enough to determine without the additional components of mixed oxides and oxynitrides.

Mechanistically, from Wagner's theory of high temperature parabolic oxidation, the parabolic rate constant could be related to diffusion coefficients of the ions in the scale. Most literature values were often given in thermogravimetric values, if the type of constant computed was specified. The thermogravimetric rates could be directly compared.

5.6.2 GAXRD Results

A computerized search and match sequence was conducted to compile a list of potential scale products. Chemistry was used to restrict the matches within the inorganic materials database. Ti, Al and O and N were allowed but not required in all the matches. In the case of the SA2 alloy, Nb was also allowed in the product matches. All computer suggested matches were evaluated for fit and feasibility.

5.6.2.1 Mixed Oxides and Oxynitrides

Personal communication with Pettit (1997) indicated the possibility of the mixed oxide -- $AlNbO_4$. Lang et al group discovered $Al_{27}O_{39}N$ in γ-TiAl-based samples, so this compound, Al_3O_3N, $Al_{2.7+0.33x}O_{4-x}N_x$ and other oxynitride variations were investigated A potential new phase forming beneath the corrosion scale, is termed the new cubic phase (NCP) or alternatively, the X or the Z phase. This is a cubic structure, depleted in Al, with a composition lying between α_2-Ti_3Al and γ-TiAl and possibly incorporating oxygen into the structure. Some possible formulas are Ti_3Al_2, Ti_2Al or

$Ti_5Al_3O_2$. None of these are listed in the x-ray database as cubic structures. An unsuccessful attempt was made to obtain a sample of the isolated cubic phase from other researchers (Quaddakers 1996) for comparison to peaks found in this study. Spectra of the corrosion scales were matched against the products listed in Table 5.12.

Table 5.12 Corrosion products, structures and JCDPF card #'s examined in this study.

Compound	Structure	JCPDF card #
Al_2O_3	rhombohedral	42-1468
TiO_2	tetragonal	21-1276
$Al_{2.7+0.33x}O_{4-x}N_x$	cubic	18-52
$Al_{27}O_{39}N$	monoclinic	26-33
Al_3O_3N	___	36-50
$AlNbO_4$	monoclinic	41-347
Nb_2O_5	orthorhombic	27-1003
Al_2TiO_5	orthorhombic	41-258

5.6.2.2 Substrate Peaks After Oxidation

All specimens were examined after oxidation for the presence of γ-TiAl and α_2-Ti_3Al substrate peaks. It occurred that A2 gave no detectable γ-TiAl signal initially, but would develop γ-TiAl later after the depletion of Ti from rutile formation. A depletion zone occurring from the transformation of an initial intermetallic into another titanium aluminide would have occurred beneath the scale. Since scale thicknesses were on the order of a μm or less, some scales were thin enough to allow x-ray penetration of the substrate.

However, penetration and sampling of any depleted zone by GAXRD did not ensure that the amount of transformed substrate was sufficient to be detected or clearly resolved from other scale product spectra.

5.6.2.3 Unidentified GAXRD Peaks

Despite the complexity of the scale, no significant peaks were identified that could not be accounted for by a corrosion product or an intermetallic substrate or a shifted spectrum of either.

5.6.2.4 Overlapping GAXRD Peaks

The mounting putty used for mounting specimens in the GAXRD exhibited strong peaks that overlapped with peaks of interest in this study. All contaminated spectra were repeated with a cleaned sample or another sample exposed under the same conditions. Peaks for the calcite ($CaCO_3$) mounting putty are given in Appendix C.

The SA2 specimen has the most potential for peak overlap because of the extra component of Nb which yielded more corrosion products. Additionally, the GAXRD spectra of the initial SA2 is already shifted relative to the α_2-Ti_3Al spectra, and this shift places it in a region where the majority of intense peaks for alumina and titania lie.

The problem of rutile peak overlaps is small due to the location of its most intense peak at 27°. The next intense peak of rutile is at 54°, which lies between near one of the A2 PDF card peaks. Since in this study, neither the A2 nor the SA2 exhibited peaks that matched at 54°, but occurred approximately 1.5° shifted to either side (higher for the SA2 and lower for the A2). With the elevated temperature exposures, the substrates themselves transformed. This lead to a broad blur of peaks in the 54° region which was difficult to attribute to either the substrate of either SA2 or the A2 and the 211 rutile peak.

Niobium oxides and its mixed oxides were relatively easy to detect since the majority of the strong peaks occur below $2\theta = 40°$ which is a region removed from most peaks for phases of interest in this system. The alumina (012) peak of lies close to a peak of $AlNbO_4$ but the second strongest peak of this mixed oxide is also present in most instances, to aid in its identification. Refer to Appendix C for a complete listing of the peak positions and intensities investigated for this study.

5.6.2.5 Peak Shifting

The substrate peaks for γ-TiAl lie higher than the peaks found in the SA2 spectrum. This shifting of the 2θ values in the SA2 alloy is attributed to the larger amount of Ti in the SA2 (52.1 at.%) compared to the Ti in the γ-TiAl JCDPF card (36 at.%). The larger atomic size (and content) of Ti would shift the d spacings to smaller 2θ values. In the spectra of SA2 after exposure, the substrate peaks were shifted to larger 2θ values, that more closely match the PDF file for $Al_{1+x}Ti_{1-x}$. This could be accounted for by a depletion of Ti in the SA2 by rutile formation.

5.6.2.6 Peak Intensities

Overall, agreement between peak intensities of the JCDPF cards and the intensities in the GAXRD spectra of this investigation was low. Discrepancies can be explained in several ways:

- preferential orientation of the scale or substrate recrystallization
- convolution of several peaks in complex, multi-component scales
- obscured intensities due to low intensity of minor phases, or
- a skewed intensity ratio due to sampling of incomplete thickness of scale.

Any crystal texture or epitaxial tendency of the scale will alter the relative intensities compared to those indexed in the JCDPS.

The thickness of the scale could exceed the depth of x-ray penetration of the GAXRD. This was especially an issue for A2, which had the thickest scales of the tested alloys. The GAXRD spectra is only representative of that sample volume actually penetrated by the glancing angle x-ray incident beam. The scale composition of the outer scale would lend more weight to the spectra. In cases of complex scales, such as the alternating layers, this lack of penetration could misrepresent the composition of the scale if one component, such as alumina or rutile grew in alternating layers and was not scanned in the spectra due to its being buried in the scale below the penetration of the

sampling incident x-ray beam. However, spallation occurred in several samples and the GAXRD would represent an average over the penetrated volume plus those inner layers that were exposed.

Hence, the calculated ratios of rutile to alumina calculated from peak intensities gave only an estimation of the scale protectiveness.

Chapter 6

TEM of Titanium Aluminide Oxidation Scales

The procedure for sample preparation of transverse cross-sections modeled after King, Cottell and Pint was detailed in §3.5.1. This technique has been refined and proved successful for many corrosion scales. However, TEM of scales with multiple phases or layers has been rare. Spallation, a problem for corrosion in general, becomes even more so when trying to thin a flaking, porous scale to electron transparent thicknesses. Additionally, the intermetallic substrate with its accompanying brittleness made for difficulties with handling and TEM preparation, since conventional cutting techniques were often unsuccessful. Residual stresses in the macroscopic oxidation specimens resulted in cracks which were magnified when reducing the specimen size to be studied.

An ESEM view of a successful TEM sample is shown in Figure 6.1 The two strips of oxidized sample are positioned with the interfaces of interest facing each other and centered in the 3 mm disc. The half-circular rods that complete the TEM sandwich were chosen for mechanical compatibility, for comparable thinning rates to the oxide and substrate and for an elemental composition whose XEDS peak energies overlap least with those of the sample elements of interest. The choice was usually Ta, since the ion milling holder was also made of this metal and its use reduced the introduction of additional contaminants. Several attempts were made to use the substrate itself, forming a 3 mm core out of two abutting sample faces.

A laser terminator was used to detect the first hole in the sample, after the appearance of which the sample was removed and assessed for electron transparency. The sensitivity of the laser sensor could be altered to continue milling until the hole was larger, or the subsequent milling was carried out carefully for short intervals. Having two strips aided in centering the area of interest in the center of the specimen for optimum milling as well as doubling the area of potential interface thinned for each TEM sample. Figure 6.2 shows an ESEM view of the interface area, showing accompanying non-uniform milling and milling damage to the underlying substrate.

Obtaining optimal sample thinness of the sample was a subjective act, since it was too time consuming to examine the specimen in the TEM after each milling interval. A light microscope with the ability to image in both reflected and transmitted light aided in a coarse assessment. The samples were extremely fragile and prone to fracture while loading into a TEM sample holder, so minimizing this hazard was a principal aim. A decision often had to be made to select only one instrument in which the specimen could be analyzed, since the sample often survives only through one sample loading.

6.1 Analytical STEM of SA2 Substrate

As described in §4.2 and 4.3.3, the resolution of the LOM and the ESEM proved insufficient for elucidating the finer microstructure of SA2 alloy, so TEM samples were prepared of the alloy before oxidation. A specimen was prepared from material as cut in the EDM and given the same surface finish as the oxidation specimens. Principal aims of were to establish the phase distribution in the substrate and the presence of any additional phases, as well as to establish correlations between grain structure and composition which overgrew particular grain compositions or orientations. This last aim remained largely unrealized because of the difficulty of sample preparation and the usual necessity to choose either oxide or substrate in cross-section sample, but not both. Often the choice

was made to thin the oxide preferentially to the substrate to provide detailed information about the scale unobtainable with other techniques.

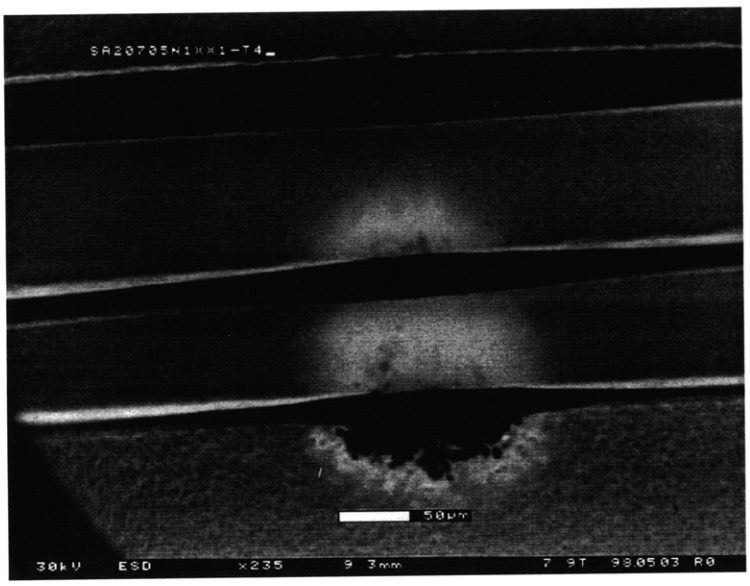

Figure 6.1 ESEM micrograph of cross-section TEM sample of SA2 exposed to nitrogen-5% oxygen at 700°C for 100 hours.

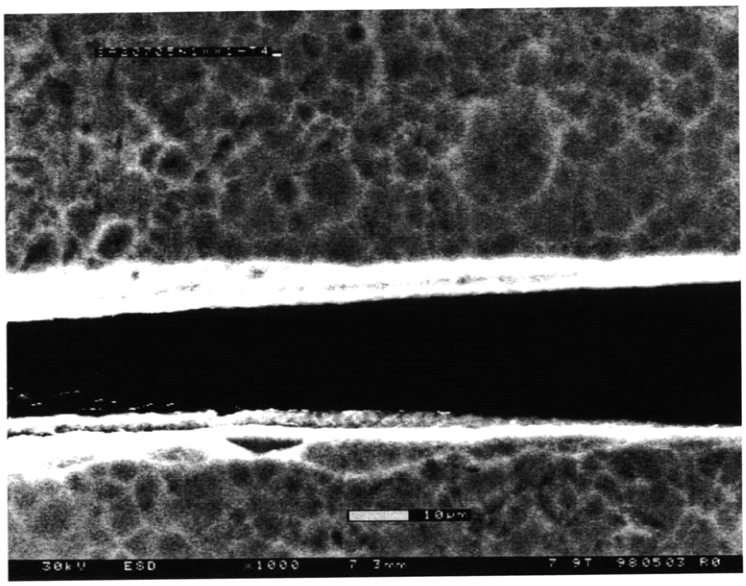

Figure 6.2 ESEM micrograph of cross-section TEM sample of SA2 exposed to nitrogen-5% oxygen at 700°C for 100 hours.

6.1.1 SA2

Surprisingly, the microstructure of the SA2 was found to mimic the microstructures of both the G and the A2 substrates, but on a much smaller scale, the SA2 features being much finer than either. Figure 6.3 shows the substrate material in both bright and dark field STEM images. This alloy exhibits the fine acicular (Widmanstätten) microstructure that others have found in Ti_2NbAl-based alloys. The needles are approximately orthogonal to each other and have lengths much finer than 1 μm.

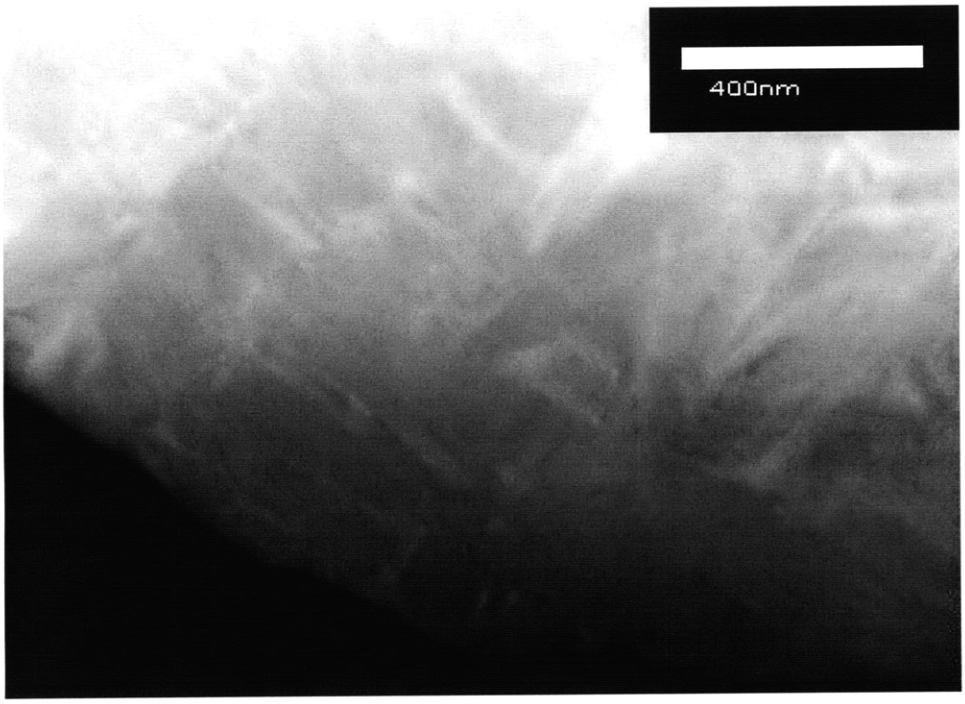

Figure 6.3 Bright field STEM micrograph of cross-section TEM sample of SA2 before oxidation. The region of the sample investigated is approximately 100-200 μm below the polished surface.

A digital XEDS map of the same area (See Figure 4.10) using the STEM revealed mainly homogeneous material, with some small pockets of segregation of Nb which correlated to areas of Al depletion. The Nb-Al phase diagram, Figure 6.4, gives the calculated ternary isothermal at 700°C. A higher Nb content than the Ti_2NbAl compositions, would suggest either (βTi, Nb) or possibly the Nb_3Al intermetallic, which has lower Al content than the Ti_2NbAl of the major component.

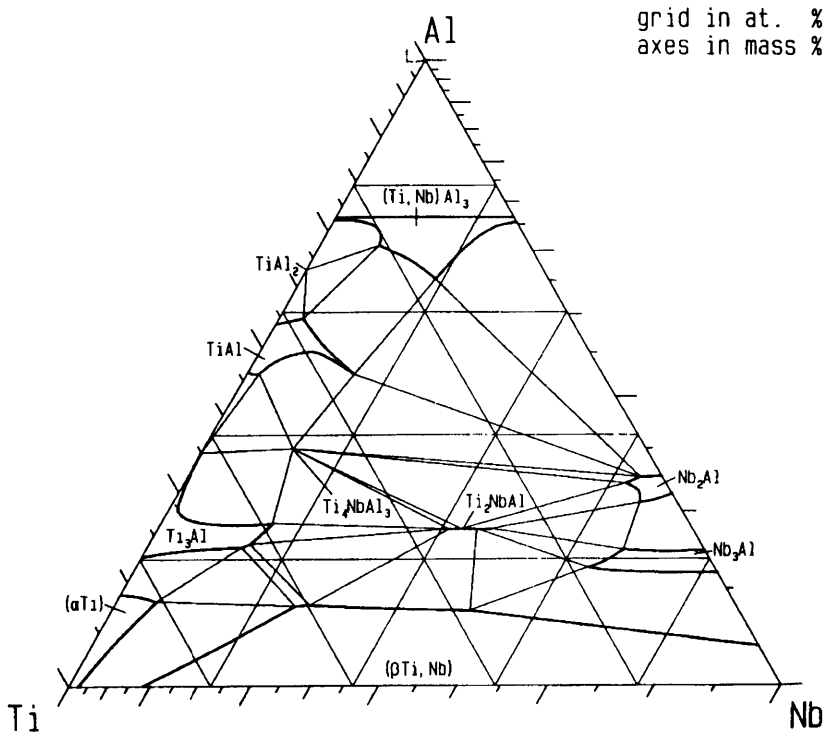

Figure 6.4 Ternary phase diagram of the Al-Nb-Ti system from Kattner (1991).

6.1.2 Analysis of EDM Damage on SA2

A sample thinned from a region within 50 μm of the EDM-machined surface did not reveal any new microstructural features, such as recrystallization or grain growth. The surface was irregular, which was evident macroscopically. The quality of the TEM

sample did not allow the chemistry to be analyzed, such as whether deposition of Cu or Zn from the brass EDM wire occurred.

6.2 TEM Sample Preparation Variations

Many of the samples that did not display obvious spallation under ESEM examinations showed evidence of spallation when examined using TEM. The samples were fragile and did not always survive being loaded multiple times into a EM holder without loss to scale or substrate. Several methods were devised to better secure the scale prior to proceeding with the standard sandwiching technique, in order to increase the yield of meaningful TEM samples.

Alternative TEM sample preparation techniques were contemplated and attempted, including focused ion beam (FIB) milling and ultramicrotomy. The strength of the intermetallics proved to be a grave hazard to the microtome knife and the large dissimilarity in scale and substrate strengths caused many of the sections to fall apart.

6.2.1 Ni Plating

One first attempt was to electroplate over the scale to provide physical constraint. Initial attempts at plating the oxidized samples quickly revealed that the electrical conductivity of the thin scale was poor enough to prevent uniform plating of nickel. Large islands of deposited Ni were apparent. Even the thinnest scales grown on the G substrate were sufficiently insulating to cause problems.

6.2.2 Au Sputter Coating Followed by Ni Plating

A thin sputtered conductive coating of Au, such as applied prior to conventional SEM, was deposited first on the oxidized samples prior to Ni plating. A thickness of nominally 50 μm was plated onto the sputter coated surface and the TEM sandwich prepared as before. This technique also proved to have significant limitations. The milling rate of the Ni proved vastly different from that of the rest of the TEM sample, with the result that the Ni plate milled away at a much faster rate; the milled Ni then re-

deposited on the rest of the sample, contaminating much of the area of interest. The Ni absorbed significant amounts of the XEDS signal, especially the lower x-ray energies, and particularly for oxygen, whose x-ray signal was never particularly strong, even in the best cases. Even a sample that appeared to be little contaminated exhibited significant Ni XEDS signal over the whole cross-section. Figure 6.5 gives the individual elemental maps and corresponding electron image for one specimen prepared in this manner.

Of the several oxidized specimens that were successfully sandwiched using this Ni plating technique, none proved satisfactory as TEM samples.

6.3 Analytical STEM of Oxidized SA2

The greatest number of TEM samples were prepared from oxidized SA2, because no prior oxidation studies could be found in the literature, and because the influence of niobium on the intermetallic structure (as opposed to Nb in solid solution) was of prime interest. The few prior TEM investigations of oxidized titanium aluminide alloys had been conducted on γ-based alloys. The present results permit a direct comparison of the oxidation behavior of the two alloys.

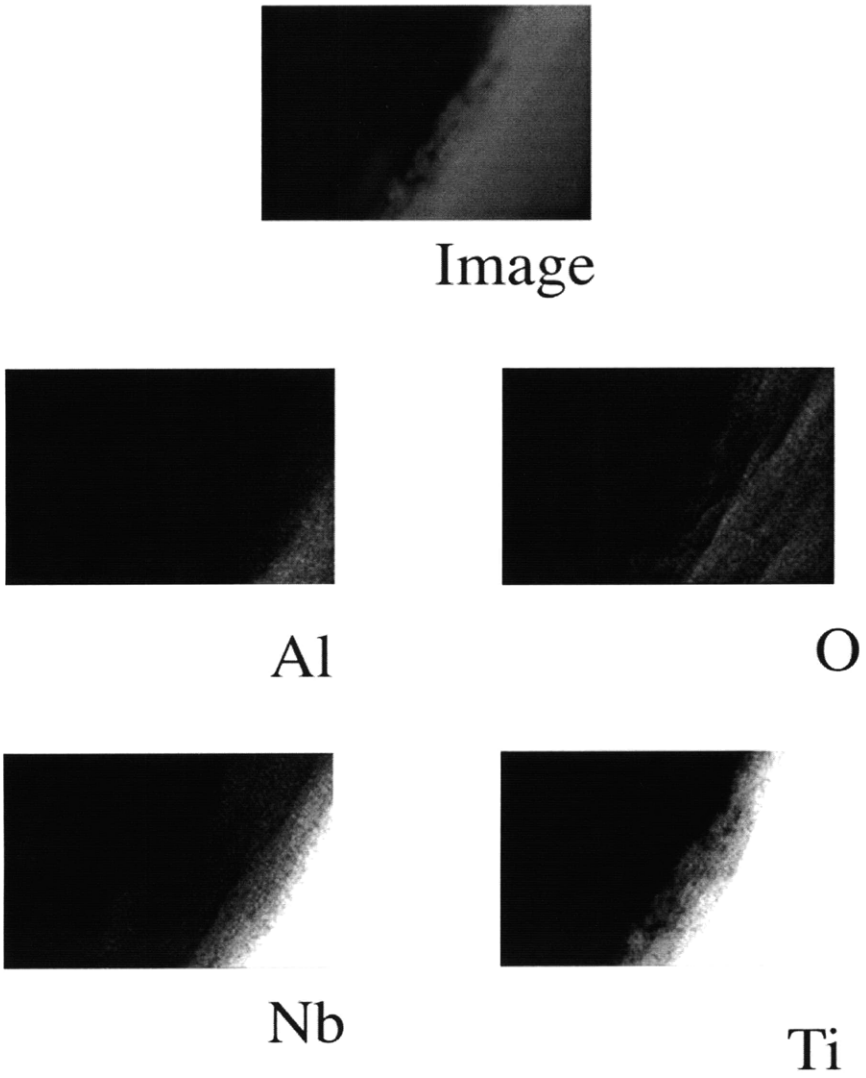

Figure 6.5 STEM binary XEDS maps and corresponding electron image of alloy A2 exposed to argon - 5% oxygen at 700°C for 100 hours.

6.3.1 Oxidation of Alloy SA2 in Nitrogen - 5% Oxygen.

Examination of SA2 oxidized in the nitrogen - 5% oxygen gas mixture yielded information on the effects of Nb in the alloy and N in the gaseous environment.

6.3.1.1 STEM Results for Alloy SA2 in Nitrogen - 5% Oxygen

Four separate TEM specimens were made of this sample, of which one was initially successful in STEM examination but lost the thin area when examined later in the conventional TEM, and a second was examined only in STEM. Subsequent efforts to re-thin the thicker portions of the first sample were unsuccessful.

The STEM results show that the scale produced on SA2 in nitrogen-5% oxygen is a layered structure with compositional variation. The repeating stacking layers were approximately 150 nm in thickness. There is an enrichment of Nb at the metal/oxide interface at locations that show lower signal in both Al and Ti. This enrichment gives a strong indication of a niobia inner layer. Below the presumed niobia is also a enhanced nitrogen signal, as well as the presence of some oxygen. It is unclear which of the metallic elements predominate in this location, so the next layer might possibly be a oxynitride of Ti and Al or an oxynitride of all three elements. The top of each repeated layer is notably concentrated in Al. This aluminum is presumably in the form of α-Al_2O_3 which is detected in the GAXRD. In one case, there was a portion of the scale where two complete layers remained attached to the substrate. Figure 6.6 shows a bright-field image and corresponding XEDS x-ray maps for this portion. Figure 6.7 shows the x-ray maps overlaid with a color assigned to each element, to more clearly distinguish the elemental distributions.

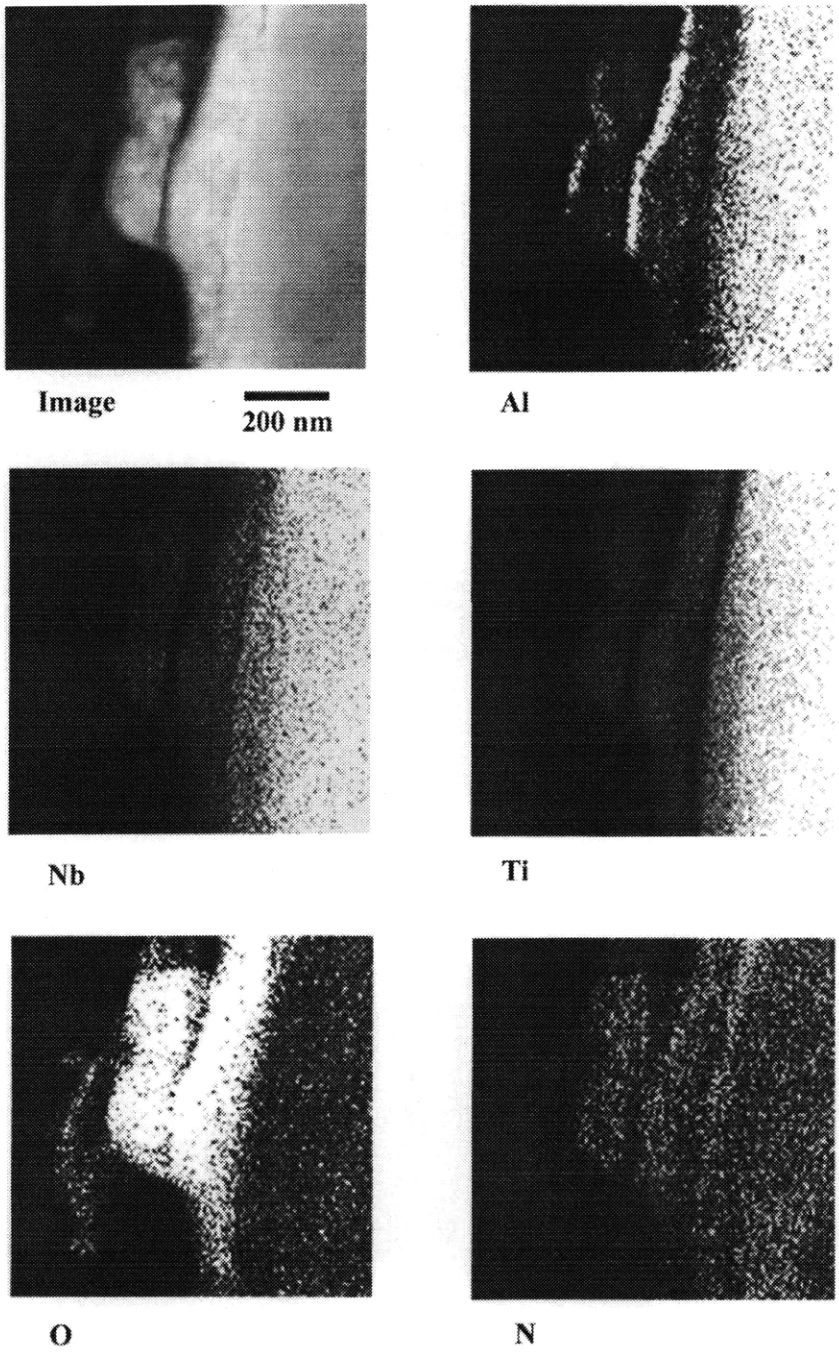

Figure 6.6 STEM binary XEDS maps and corresponding bright field electron image of alloy SA2 exposed to nitrogen - 5% oxygen at 700°C for 100 hours.

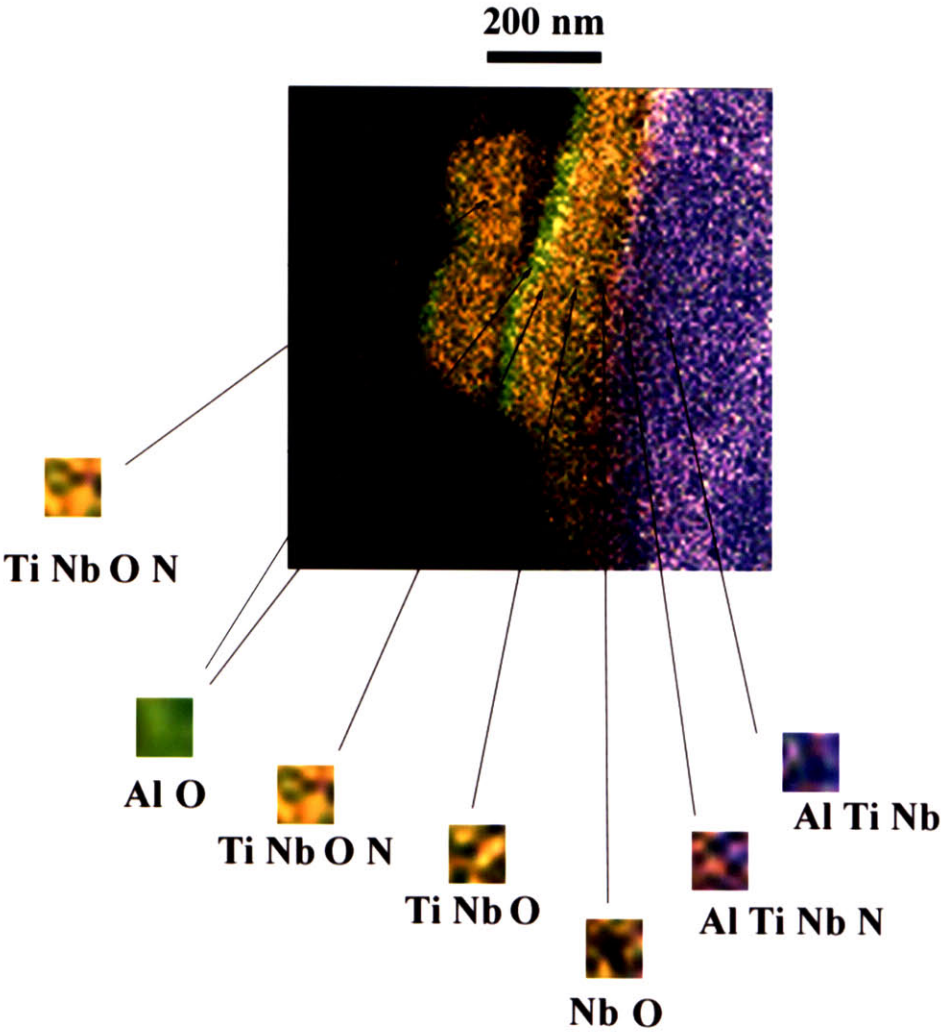

Figure 6.7 Composite STEM XEDS map of alloy SA2 exposed to nitrogen-5% oxygen at 700C for 100 hours; produced by overlaying 5 elemental maps, each with an assigned color

Numerous cracks or separations could be seen between layers and especially at the oxide/metal interface. The interface is often non-planar.

A higher magnification image of the delaminated region shows a gap on the order of tens of nm. X-ray maps taken from this region reveal a concentration of Nb on the upper side of the separation. Both nitrogen and oxygen enhancement can also be seen below the crack, indicating probable oxynitride formation. Figure 6.8 shows the bright-field STEM image and x-ray maps for this region of the specimen.

Identical results were obtained in the fourth TEM sample. Figure 6.9 presents the bright-field STEM image and x-ray maps for the repeated layers.

Even more interesting than reproducing the repeated layer result with a sample from another region was finding a crack in the scale at the metal/oxide interface that appears to be partially filled with niobia. This result would seem to indicate that at least some cracks form at temperature and heal as oxidation proceeds. Figure 6.10 shows the STEM bright field image and x-ray maps for this observation.

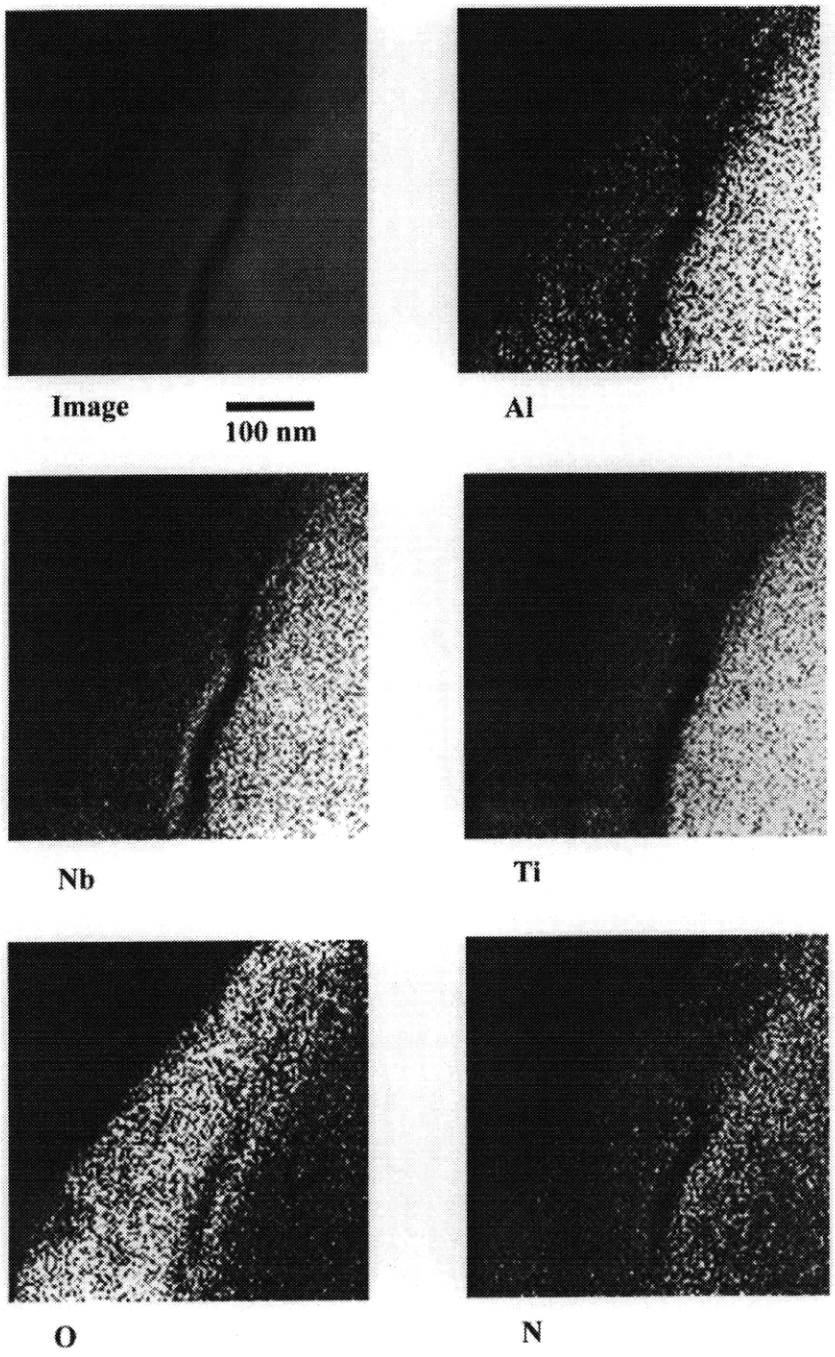

Figure 6.8 STEM binary XEDS maps and corresponding bright field electron image of alloy SA2 exposed to nitrogen - 5% oxygen at 700°C for 100 hours.

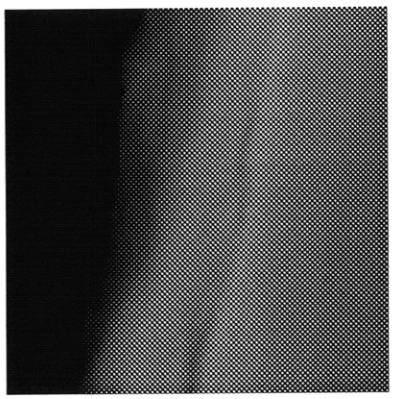

Image

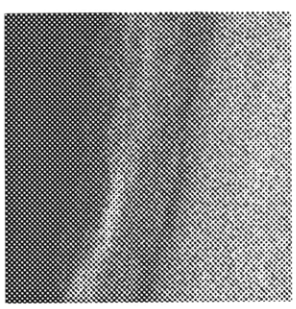

Al

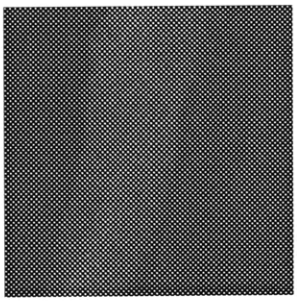

O

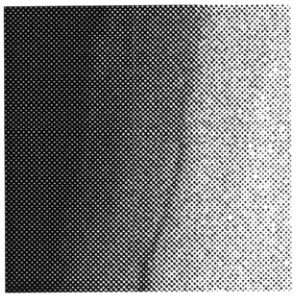

Nb

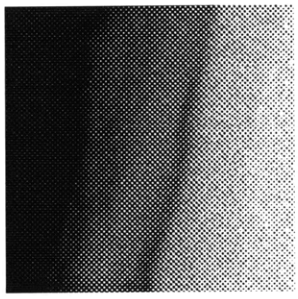

Ti

Figure 6.9 STEM binary XEDS maps and corresponding electron image of alloy SA2 exposed to nitrogen-5% oxygen at 700C FOR 100 hours.

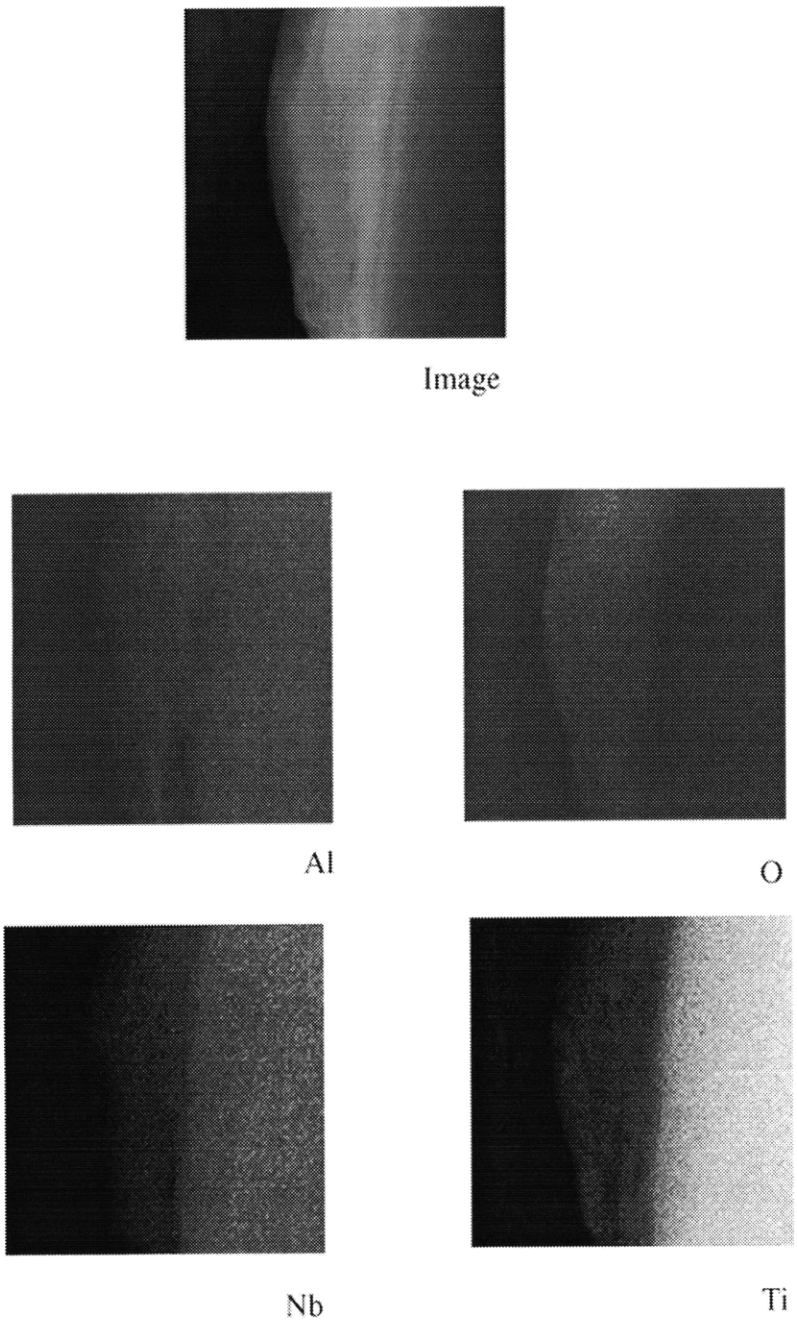

Figure 6.10 STEM binary XEDS maps and corresponding BF electron image of alloy SA2 exposed to nitrogen - 5% oxygen at 700°C for 100 hours.

6.3.1.2 TEM Results of Alloy SA2 in Nitrogen - 5% Oxygen

The conventional TEM exhibits better image quality than the TEM mode of the STEM. For this reason, the samples were also examined in the conventional TEM after analysis in the STEM. Unfortunately, the same scale portions could not be located. Figure 6.11 shows a thicker portion of the scale that remained intact and the associated electron diffraction pattern.

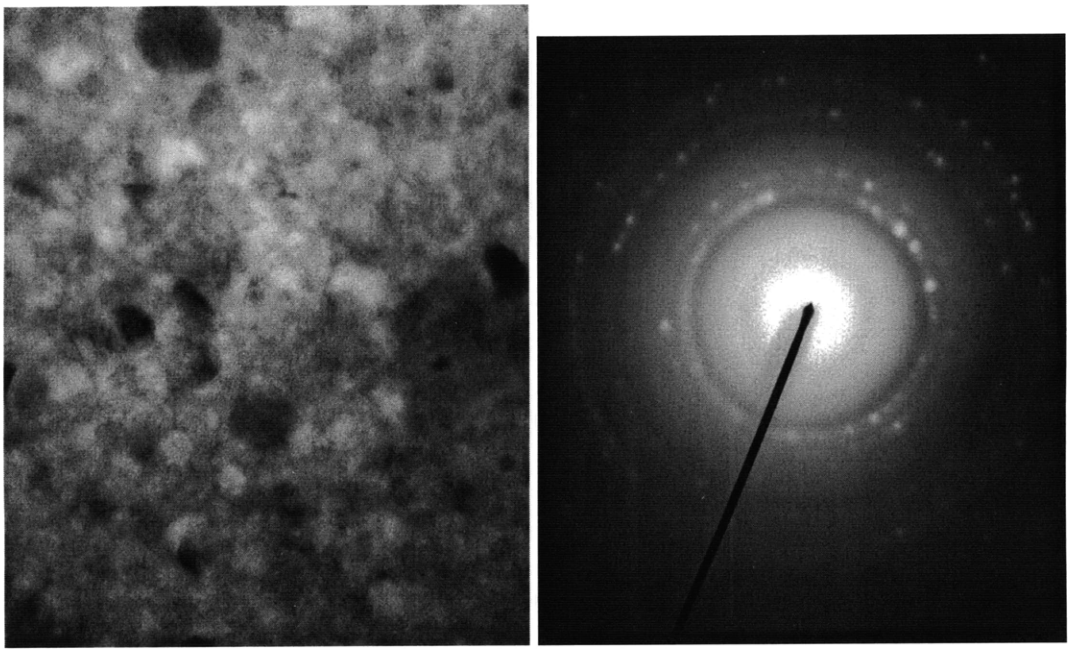

Figure 6.11 TEM micrograph and corresponding diffraction pattern of alloy SA2 exposed to nitrogen - 5% oxygen at 700°C for 100 hours.

6.3.2 STEM Results for Alloy SA2 Oxidized in Oxygen

Alloy SA2 was exposed to pure oxygen for 20 hours and made into a STEM sample. The scale that grew was porous and also layered but more grossly. The layers were approximately 0.5 μm thick, or approximately three times the thickness of those found on alloy SA2 oxidized in nitrogen-5% oxygen. Between layers there appeared to be empty space which could represent cracks or pores. The scale thickness, measured in areas where epoxy appeared to have retained the majority of the scale, was approximately 2.8 μm, compared to a thickness estimated from the weight gain data of 1.8 μm. Porosity can account for some of this discrepancy, since the thermogravimetric estimation assumed a fully dense scale. Figure 6.12 shows the layered structure in this sample and the partial delamination occurring.

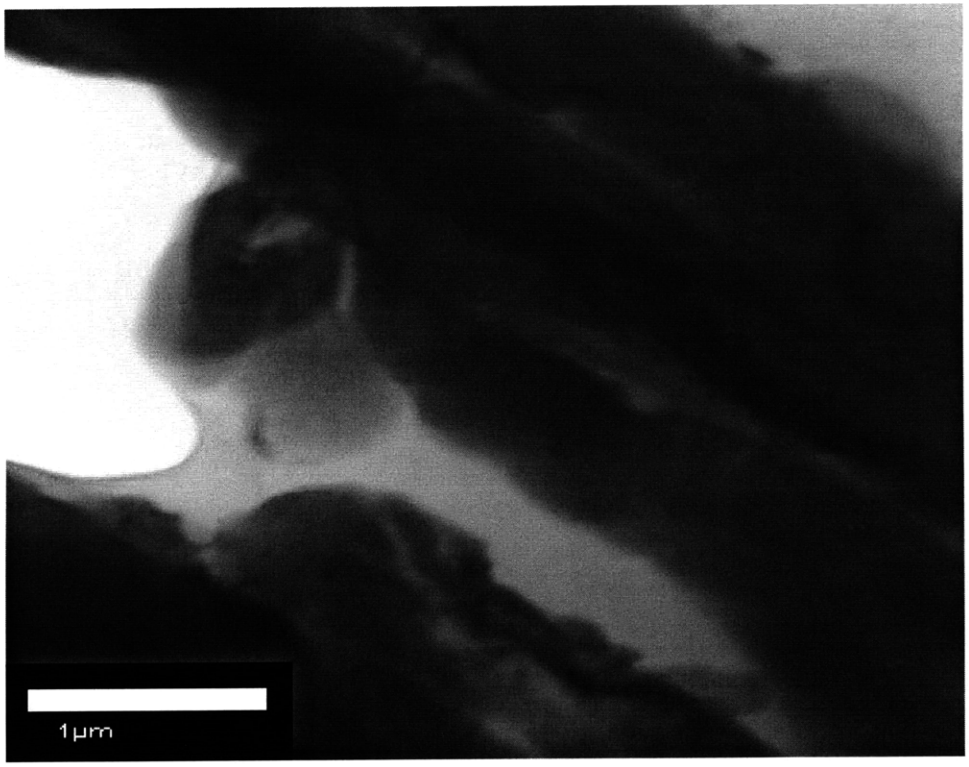

Figure 6.12 STEM micrograph of alloy SA2 exposed to 100% oxygen at 700°C for 20 hours.

The layers are not always parallel to one another. The composition, as determined by XEDS mapping, showed little chemical variation among the layers, unlike the enriched alumina layer in the sample oxidized in nitrogen-5% oxygen. The sample had insufficient thin area to determine compositional variation in the substrate alloy immediately below the scale. Figure 6.13 shows a scale of approximately 2 μm thickness with some of the layers canted with respect to the metal/oxide interface.

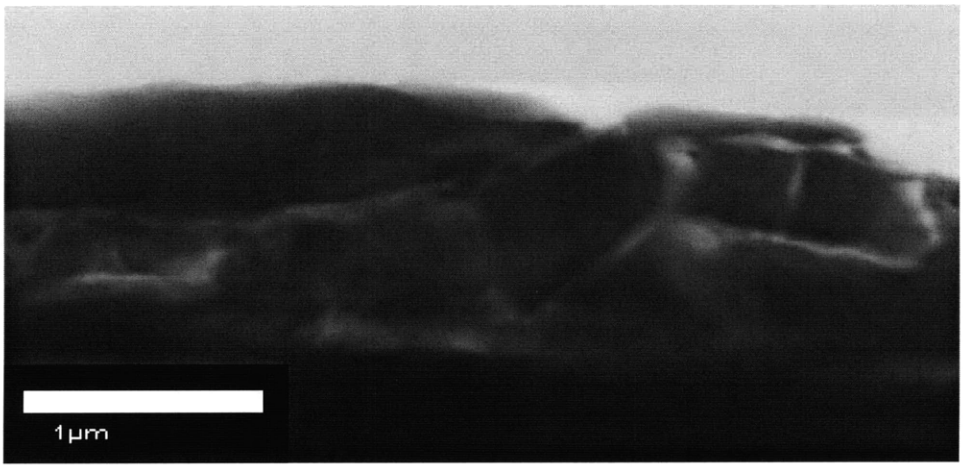

Figure 6.13 STEM micrograph of alloy SA2 exposed to pure oxygen at 700°C for 20 hours.

Chapter 7

In-Situ Studies

7.1 In-Situ Oxidation in the ESEM

Previous electron microscope studies of high temperature corrosion scales have been made after oxidation. Changes that occur during oxidation or cooldown of these scales have gone unobserved. The ESEM and its accompanying hot stage allow *in-situ* observation -- at least from the outer surface -- of the evolution of scales during oxidation, offering better understanding of the mechanisms of scale growth and particularly failure of protective scales and coatings. Observations of other metal systems have shown that scales grown in the SEM in gaseous environments resemble those grown *ex-situ* (Rapp 1984, Touryan 1993).

Mixed scales are a common product of titanium aluminide oxidation, as seen in §5. A range of temperatures and alloy compositions exist, however, where alumina is principally formed. Observation of scale growth in the ESEM offers the prospect of understanding this selectivity and other effects in the early stages of oxidation. Even alloys which grow overall protective scales may have rutile or mixed rutile/alumina components present. SEM examination of oxidized alloys has shown that the rutile is distinguishable from the alumina. *In-situ* observation was therefore proposed to determine if preferential oxidation of one phase over other phases occurs and could explain differences in transient behavior in systems which exhibit similar overall growth kinetics.

Some possible oxidation-related features which would be observable in the ESEM are inter- and trans-granular fracture, crack initiation sites, cracks in scales which continue into the substrate, cracks or defects in the substrate which initiate scale cracks, effects of grain boundaries in scales and substrates, changes in scale morphologies in response to external stress, spallation and re-oxidation, local stress concentration effects, critical strains necessary for cracks, creep and overall mechanical degradation.

Spallation and cracking is typically investigated after the event has taken place. Scale breakdown occurs due to growth or external stresses and due to mechanical stresses generated from differences in thermal expansivities of the scale and substrate. The ESEM allows a dynamic view into these phenomena at temperature and during cooling. Effects of local scale compositions, porosity, and morphologies can be studied. Cracks in brittle scales can propagate into substrates and vice versa, compromising the strength of the material and accelerating environmental degradation. The growth of a protective scale at elevated temperature is alone not sufficient for acceptable corrosion resistant behavior, since thermal cycling occurs in many applications of these alloys. The scale must be adherent at temperature and after cooling.

7.1.1 Alloy A2 Oxidized to 800°C

Before the model set of titanium aluminides used in this study was received from Wright Patterson Air Force Base, a few pieces of uncharacterized Ti_3Al were used to conduct preliminary *in-situ* studies to establish the optimal ESEM operating conditions and general oxidation behavior.

The surface of a polished specimen of this material appeared similar to that of the A2 alloy substrate. The surface finish was also similar, with both surfaces containing polishing trenches and pits. Moist air, from room air passed over a wet wick prior to

entering the ESEM chamber, was used in this oxidation experiment, and all subsequent *in-situ* oxidation studies.

Oxidation and surface changes were evident even below the nominal temperature of 200°C. Figure 7.1 shows the nucleation of small oxide nodules at approximately 200°C. The larger, brighter oxide pieces are residual alumina cement used to fix the sample and crucible and were often used as orientation guides to keep the same region of the sample in view.

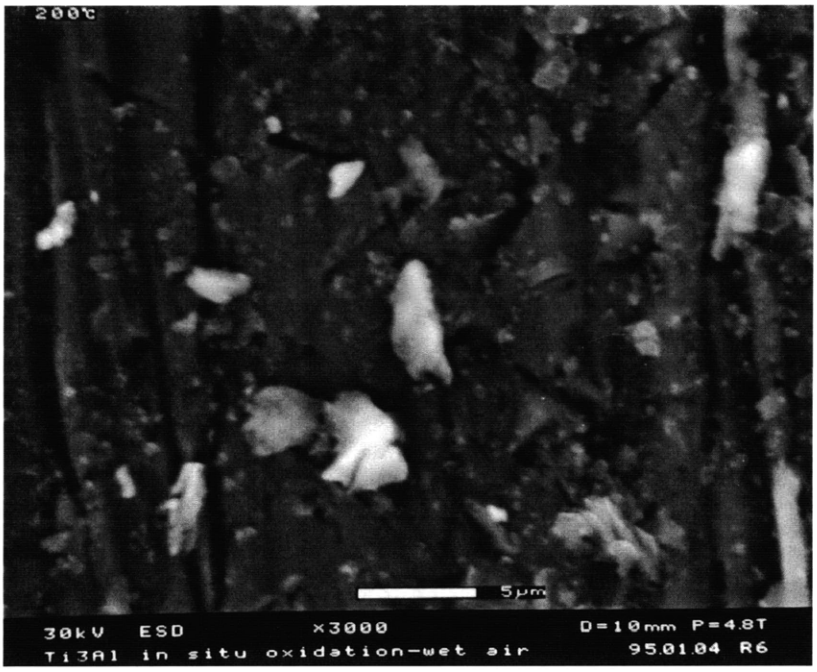

Figure 7.1 ESEM micrograph of Alloy A2 oxidized *in-situ* in moist air showing small oxide nodules nucleated at approximately 200°C.

These nodules nucleated and grew as the temperature was increased. At some temperature between 600 and 700°C, a distinct fuzziness on the sample surface was

discerned, corresponding to the growth of whiskers and blades of rutile. Residual polishing ridges became gradually indistinct around 700°C, and after only a short time at the target temperature of 800°C, only an occasional hole or polishing depression could be seen on the surface. After 0.5 hour at temperature, the scale comprised a uniform distribution of blade-like whiskers. No cracking or other notable events were noticed during cooling.

Observations after cooling showed better resolution of the whiskers. Magnification showed rutile whiskers more or less normal to surface. A survey of the sample indicated no anomalous regions or features at variance from what was observed *in-situ*.

Macroscopically, the scale appeared uniformly opaque to the eye and of a grayish blue color. A fracture cross-section was made of this sample which shows the whisker morphology (Figure 7.2).

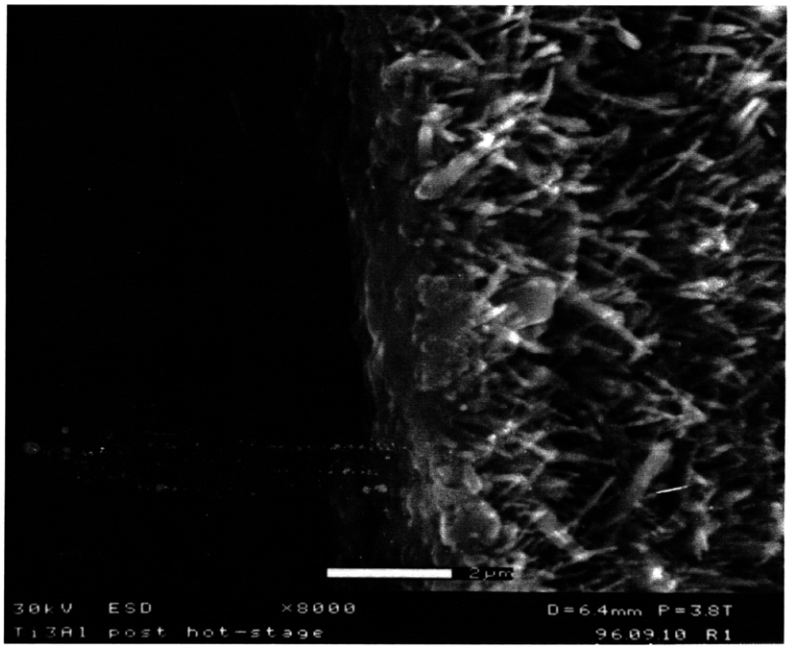

Figure 7.2 ESEM micrograph of Alloy A2 oxidized *in-situ* in moist air showing small oxide nodules nucleated at approximately 200°C.

7.1.2 Alloy A2 Oxidized to 700°C

A sample of alloy A2 was made which had a thickness of approximately 1 mm and mounted in the ESEM hot stage. Initially, this substrate exhibited very little contrast except for the polishing artifacts. Nodules of presumed oxide (observed by the presence of localized charging) were already forming by the time the specimen had reached 300°C. At higher temperatures such of 400-500°C, blades and whiskers of oxide could be seen to be filling, and in some instances bridging, the polishing trenches. At 600°C, nodules of oxides appeared to be growing ridges and extending across lathes and small trenches. Many of these "armed" nodules took on a spider-like appearance. No lamellar structure, as seen in the metallography of the initial substrate, was apparent. The only contrast variation at elevated temperatures came about due to preferential oxidation of the edges of the polishing trenches, which then charged and appeared in lighter contrast than the rest of the substrate.

The substrate after one hour at 700°C had an overall undulating scale surface, which also followed the original substrate contours, and its polishing features. Features resembling scale-like flakes, accompanied by charging around their perimeters, appeared over all the surface and obscured polishing trenches and finer features. Higher magnification of individual flakes showed that within the flakes were also smaller flakes, Figure 7.3. Higher magnifications were required to observe scale features at 700°C, as compared to at 800°C, and a perusal of the entire sample indicated no regions with whiskers or other easily characterized morphology.

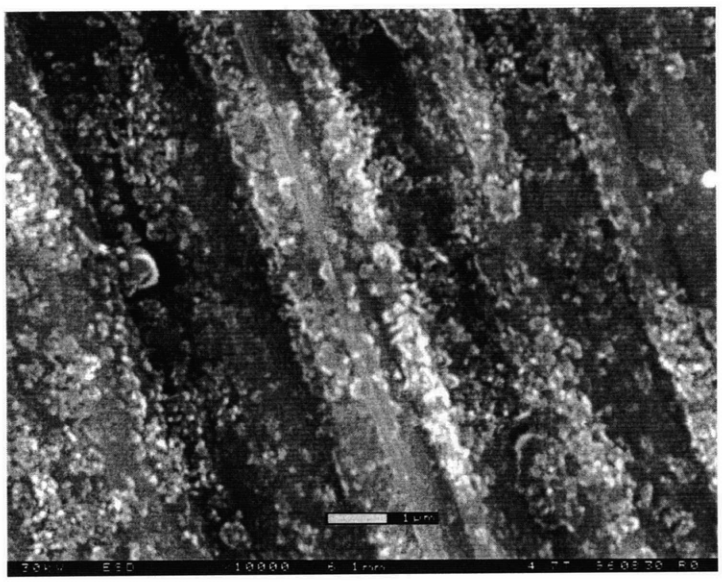

Figure 7.3 ESEM micrograph of fracture cross-section of Alloy A2 oxidized *in-situ* in moist air to 700°C.

Macroscopically, the scale was translucent covered or replaced in patches by a more opaque, rusty gray scale. A fracture cross-section of this sample is shown Figure 7.4.

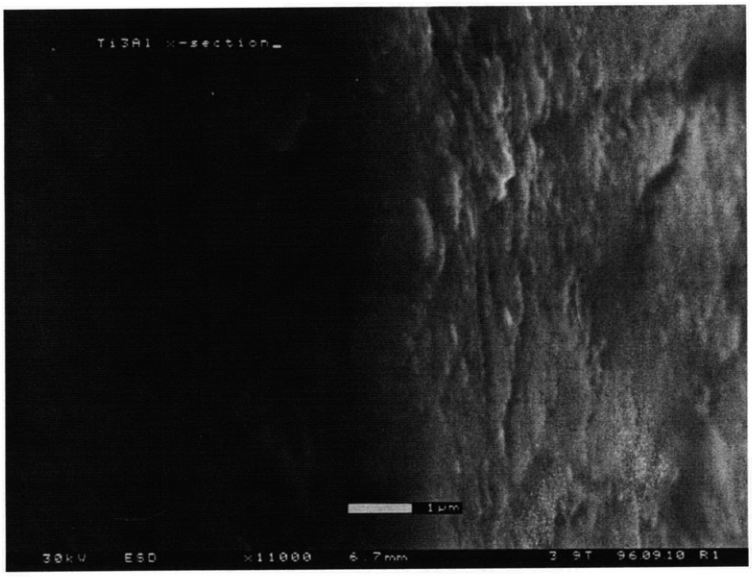

Figure 7.4 ESEM micrograph of fracture cross-section of Alloy A2 oxidized *in-situ* in moist air to 700°C.

7.1.3 Alloy G Oxidized to 700°C

A wedge-shaped slice of alloy G sample was cut which contained macroscopic scratches along the cutting direction. A small piece was fractured from this slice, measuring a few millimeters at its largest dimension, with a cross-section of 1 mm at the thickest portion and tapering to an edge over a distance of 2 mm. The sample was fixed with high temperature alumina cement into the crucible such that the flat cut surface was parallel to the detector. Even with the rough cut surface, the surface showed little contrast before heating in the hot stage. It was unclear whether the parallel linear features seen arose from the slicing saw damage or from the lamellar structure of the substrate. At temperatures slightly above 200°C, the different substrate layers became more apparent, with one phase (presumed to be α_2-Ti_3Al because of its lower proton/electron density) appearing lighter and more porous. The porosity could be due to grain pullout during polishing. The lighter phase also occupies a much smaller area fraction as do α_2-Ti_3Al laths within a primarily γ-TiAl substrate.

The contrast between the laths becomes more obvious as temperature is increased and one phase appears to preferentially oxidize. The charging and increased secondary electron contrast increase allow the different layers (presumed G and A2) to be distinguished.

Overall, the oxidation features on alloy G were much finer than on any other substrate in this series. High magnifications were required to locate preferential oxidation sites, and it was noted that areas that had been examined under higher magnifications suffered electron beam damage in that area for some time afterwards. The scale appears to be thicker over certain of the substrate lamellae, rather than only over all lamellae of the same phase.

At temperatures of 300° and higher, distinct nodules could be viewed growing on the darker G lamellae. They may also have appeared on the lighter lamellae but had insufficient contrast to be resolved. These nodules persisted up to the final temperature of 700°C, increasing in density but little in size. Nodules, roughly spherical, were ~ 0.1 μm when first detected at 330°C and approximately the same size and appearance at the final isothermal temperature of 700°C.

During cooling, nodules were observed to have grown fairly uniformly distributed across the sample surface. After exposure, the sample had a lightly tarnished finish, with a macroscopically blue, translucent scale. A fracture cross-section (Figure 7.5) was made of the sample after *in-situ* examination and subsequent GAXRD investigation.

Figure 7.5 ESEM micrograph of fracture cross-section of Alloy G oxidized *in-situ* in moist air to 700°C.

7.1.4 Alloy SA2 Oxidized to 700°C

The SA2 *in-situ* sample was obtained from a very thin (0.2 mm) slice cut by EDM that was polished with 600 grit paper down to approximately 0.1 mm thickness. A thin

2-mm strip of this slice was cut with the low speed saw and fractured to a smaller size (~0.04 mm^2 surface area) to fit into the crucible.

The initial surface was significantly different from that of the other substrates. Contrast was higher owing either to raised surfaces or sections with notable parallel regions, either lamellar grains or regular scratches from the polishing in some sections or grains, but not all.

Examination of the same area at both ~80°C and 190°C indicated that oxide flakes were already forming in this low temperature regime, but with increasing temperature increased in number and density. At higher temperatures, ~200°C, much finer, more regular nodules of oxide were seen to form. There appeared to be no preferential site for nucleation, on either a raised surface, the uniform surface, or the lamellar grains as seen in Figure 7.6. Up to the target temperature of 700°C, no other features appeared. This was confirmed by micrographs, taken following cool-down, which again show the irregular topography, with an indication of oxide flakes.

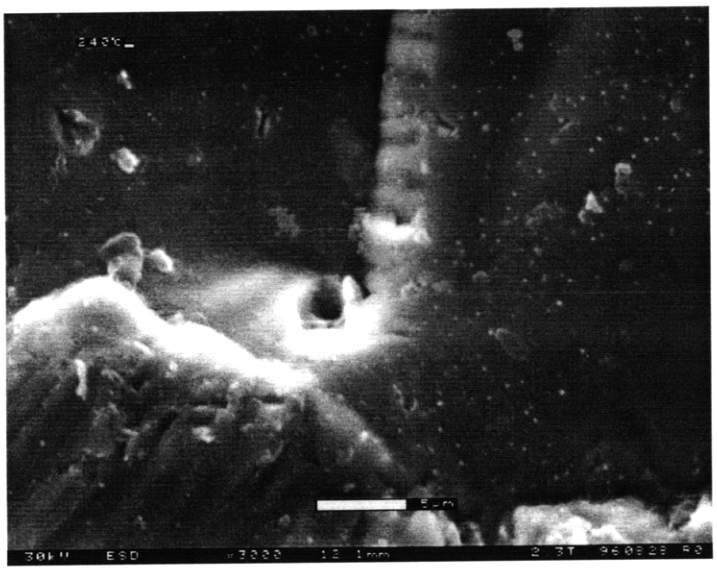

Figure 7.6 ESEM micrograph of Alloy SA2 oxidized *in-situ* in moist air to 700°C.

Macroscopically, the scale appeared very thin and translucent, with a gray and slight blue tinge to it. This scale was very similar in color and appearance to the scale grown *in-situ* on alloy G. A fracture cross-section was made of the *in-situ* specimen for further analysis (see Figure 7.7).

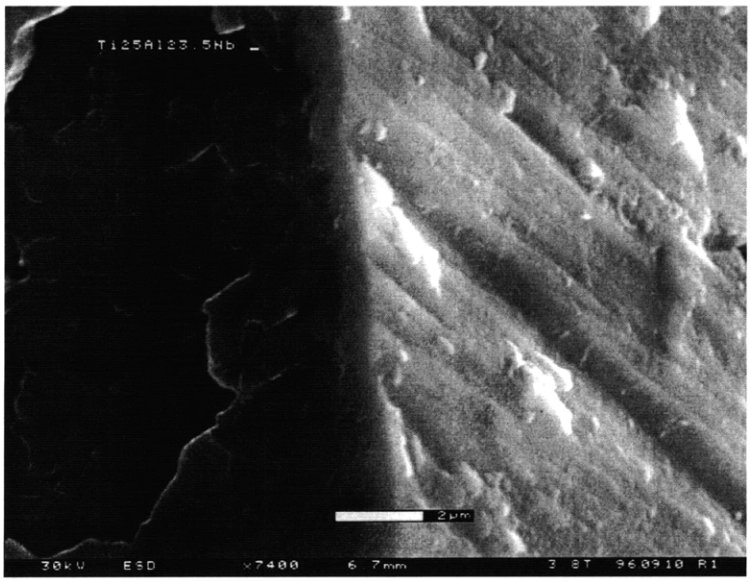

Figure 7.7 ESEM micrograph of fracture cross-section of Alloy SA2 oxidized *in-situ* in moist air to 700°C.

7.1.5 ESEM Maps and Fracture Cross-sections

In an effort to correlate any preferential oxidation observed during *in-situ* experiments with observable microstructural features, both plan view and cross-section x-ray maps were made of the samples after *in-situ* oxidation.

The most segregation observed in the *in-situ* samples occurred in the A2 sample heated to an 800°C final temperature. Images and x-ray maps of the cross-section exhibit a very obviously whiskered and sometimes bladed outer layer. An enhanced Ti signal was seen in the outer layer as well, which is made even more significant because the outer layer

was not fully dense. Within the dense scale, under the whiskers, a homogeneous mixture of Ti, Al and O was mapped.

The A2 sample, heated to only 700°C, achieved a scale thickness of slightly less than 1 μm, about half the scale thickness of the 800°C sample for similar oxidation times.

The combination of little observable segregation in the x-ray maps and a dearth of significant microstructural features observed in *in-situ* ESEM led to the conclusion that any differences in oxidation behavior of the intermetallics, especially between A2 and SA2, must be on a scale smaller than observable in the ESEM.

Chapter 8

Discussion

8.1 Titanium Aluminide Alloy Selection

The titanium aluminides hold great potential for lightweight replacement of high temperature materials, with their densities approximately one half that of the conventional superalloys currently employed. As intermetallics, they have the additional advantage for high temperature corrosion resistance that diffusion processes are slowed in the ordered superlattices of intermetallic compounds.

A satisfactory engine material must possess a balance of materials properties. Ideally, the material would have superior strength, high temperature creep and corrosion resistance, as well as acceptable room temperature mechanical properties. Unfortunately, the strongest materials can often suffer from insufficient ductility and fracture toughness, especially at lower temperatures. There is often an inverse correlation between materials properties which require optimization, and it is particularly true for the materials choice in high temperature applications.

8.1.1 $TiAl_3$

When first examining the titanium aluminide system, one would select the $TiAl_3$ composition as the most promising candidate for high temperature corrosion resistance because of it has the greatest Al content. However, the extreme brittleness of this material quickly leads to its dismissal from consideration. In addition to proving difficult

to manufacture in its line-compound composition, it displays large thermal mismatch with the resulting corrosion scales, as well as with other titanium aluminides. Efforts to remedy this have met with limited success (Ma 1995).

$TiAl_2$ can be removed from consideration, as even its existence is disputed and its narrow range of composition would lead to manufacturing difficulties. Some researchers attribute the Ti:2Al composition ratio to a $TiAl_3$-type compound with large amounts of nitrogen dissolved in a lattice with the formula $TiAl_2N$.

8.1.2 γ-TiAl

The γ-TiAl structure, with 50 at.% Al, turns out to have just sufficient Al to provide continuous Al_2O_3 scales. While the γ-TiAl-based alloys can be modified to promote formation of a protective alumina corrosion product, the effect on the room temperature mechanical properties proves to be significant. Improvement of lower-temperature mechanical properties often occurs at the expense of the high temperature properties and vice versa.

8.1.3 α_2-Ti_3Al

The α_2-Ti_3Al structure possesses the best room temperature mechanical properties of the titanium aluminides, but its large Ti content, and therefore the propensity for forming the less protective titania scales, severely limits its maximum use temperature. However, alloying can induce the formation of a protective scale while retaining the ductility and fracture toughness.

8.1.4 Titanium Aluminides with Nb Doping

Certain alloying elements when added to titanium alloys stabilize the β or high temperature phase of Ti, and this β-phase has additional slip systems which allow for better mechanical properties. β-stabilizers include the Group VA elements - vanadium, niobium and tantalum. Experiments have shown similar alloying effects in the titanium

aluminide systems. However, in exposures at elevated temperatures, the VA alloying additions proved to have disastrously poor oxidation resistance. Contrary to the catastrophic and non-protective corrosion of the Group VA metals in oxygen, the Nb alloyed titanium aluminides performed noticeably better than unalloyed alloys. Additions of Ta were investigated less, probably due to the heavy weight penalty that would overshadow the weight savings sought in the titanium aluminide systems.

When γ-TiAl-based alloys were alloyed with Nb, the oxidation behavior was improved. However, mechanical restrictions of the brittle γ-TiAl were still an issue. Modifying the alloy to form a duplex alloy structure achieves acceptable mechanical properties. Additions reported in the literature in the γ-TiAl systems ranged up to a few atomic percent niobium, a rather small amount that resulted in no phase separation between titanium aluminides and another Nb rich phase.

When Nb is used for alloying α_2-Ti_3Al based alloys, the mechanical properties are less of an issue, since the α_2-Ti_3Al intermetallic already has acceptable properties in this area. The weakness in the α_2-Ti_3Al system is the reduced oxidation resistance temperature because of the increased Ti content in the system.

A commercial alloy has been developed from the Nb-doped α_2-Ti_3Al titanium aluminides. This contains Nb in amounts of 10-15 at.% and is termed "super alpha two" or "super α_2" alloy. In addition, this alloy contain small amounts of Mo and V, the Mo for creep resistance and V as a β-stabilizer. This alloy is composed of two phases: α_2-Ti_3Al and β or B2, (the latter is an ordered derivative of β).

An option to solid solution alloying elements is the use of an intermetallic that incorporates the Nb into the intermetallic structure, rather than as a two phase material. A single phase material is likely to be more corrosion resistant at high temperatures because there are fewer short-circuit paths for the preferred reaction of a more reactive

phase compared to those for the other phases.

In the Ti-Al-Nb ternary system (see Figure 6.4), there are two ternary intermetallics recognized in the literature: these are Ti_2NbAl and $Ti_{(3 \text{ or } 4)}NbAl_{(2 \text{ or } 3)}$. The exact composition of this last compound is disputed, depending on the temperature and the researcher (Gama 1993). Regardless of its composition, Ti_3NbAl_2 or Ti_4NbAl_3, it is evident that the latter compounds have a significant (Ti+Nb) : Al ratio which could adversely affect the high temperature corrosion resistance.

The Ti_2NbAl composition is a promising candidate because it has

1) the Nb content for favorable mechanical properties and good high temperature corrosion resistance, and 2) a crystal structure derived from α_2-Ti_3Al but with less Ti owing to the substitution of Nb. This ternary compound has potential for combining the best features of both the γ-TiAl and α_2-Ti_3Al compositions. Additionally, the existence of the intermetallic composition Ti_2NbAl allows for a similar microstructure, comprising predominantly one intermetallic phase with a small dispersed portion of a second phase--whose distribution can be tailored to optimize materials properties. For example, fine lamellar grains have been shown to improve the ductility of the titanium aluminides, and Ti_2NbAl alloy microstructures also display this feature. Such a microstructure is considered preferable to a more macroscopically segregated two-phase alloy comprising an intermetallic and a solid solution in which one phase, most probably the solid solution, serves as a preferential path for faster diffusion and dominates the corrosion rate.

8.2 The Ti-Al Dilemma

An example of the balance in material properties being an issue can be seen in the titanium aluminide system. Interest in this intermetallic system is high because of the low density of the intermetallic compounds. However, the balance of all properties essential to a high temperature material is also needed. The weight savings needs to be coupled with an acceptable corrosion resistance. The scale that grows on the candidate

material needs to be slow growing and also compact to provide some protection. These requirements are not easily attainable in actual operating conditions.

8.2.1 Similarity of Oxide Stabilities

In a typical alloy system, an oxide (or other corrosion scale) of one alloy component is significantly more thermodynamically stable (noble) with respect to the oxides of the other components. Formation of this most stable oxide is favored over the other oxides. A transient oxidation effect may produce some nucleation of less stable oxides in cases where the kinetics for formation of the base oxides are faster than those for the noble component. Typically small nuclei of the less stable oxide are dissolved or overgrown by the dominant stable scale product. In some cases, for examples Al-containing superalloys also containing oxygen-reactive elements like Y or Zr, a content of only a few atomic percent Al is required for the formation of a continuous protective alumina scale (Pint 1993).

The thermodynamics are considerably different in the titanium aluminide family because the standard free energies of formation of alumina and titania are very similar. Figure 8.1 shows the Ellingham/Richardson diagram for common oxides in alloy systems, expanded in the TiO_2 and Al_2O_3 regime from that given previously in Figure 4.11. As seen in Table 8.1, the free energy of alumina formation is slightly lower than that for titania formation. As temperature is lowered from 900 to 700°C, the gap between the alumina and titania energies increases. However, the differences are still much smaller than those seen in the majority of other alloy systems. The small thermodynamic advantage of alumina is further attenuated by the rapid titania formation kinetics. TiO_{2-x} has a defect structure (Ti interstitials and oxygen vacancies) that allows for fast diffusion of both oxygen and cations through the oxide.

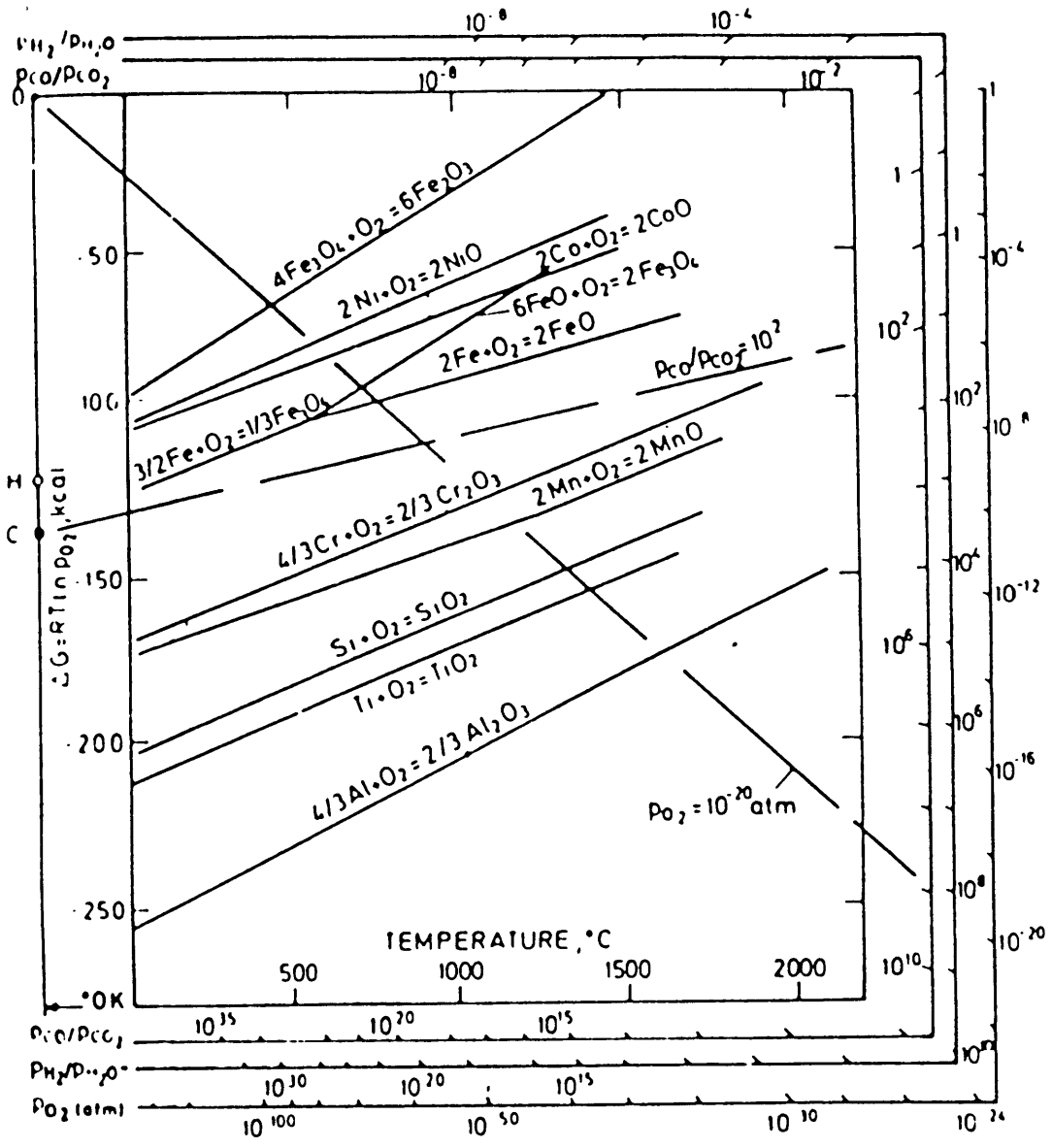

Figure 8.1 Ellingham/Richardson diagram for some oxides of importance in the high temperature oxidation of metals and alloys. The diagram is a plot of the standard free energy of formation of the oxides per mole of oxygen versus temperature.

Table 8.1 Gibbs standard free energies of formation for oxides and nitrides in the Al-Nb-Ti system at 700°C. Values calculated per one mole of reactant gas.

Reaction	ΔG [kcal]	Equilibrium gas pressure $\log_{10}$ p [atm]
Oxides		
4/3 Al + O_2 —> 2/3 Al_2O_3	-218.2	-49.0
2 Nb + O_2 —> 2NbO	-158.2	-35.5
Nb + O_2 —> NbO_2	-147.6	-33.1
4/5 Nb + O_2 —> 2/5 Nb_2O_5	-140.8	-31.6
Ti + O_2 —> TiO_2	-183.4	-41.2
Nitrides		
2Al + N_2 —> 2 AlN	-102.7	-26.4
4 Nb + N_2 —> 2 Nb_2N	-73.6	-23.1
2Ti + N_2 —> 2 TiN	-117.4	-16.5

8.2.2 Layered Oxide Resulting from Preferential Substrate Oxidation and Depletion

The conditions that determine the formation of a protective scales on titanium aluminides are easily altered to favor one phase or another. Theoretically, an alumina scale should form on a γ-TiAl alloy over most of the concentration range in the alloy phase field, and (with alloy additions) the equilibrium in α_2-Ti_3Al alloys can be shifted towards protective alumina formation rather than less protective titania. A cycle can be established while oxidizing a γ-TiAl based alloy in which formation of a protective alumina scale depletes the Al in the alloy, causing a local shift of the substrate composition to that of α_2-Ti_3Al. The depletion of Al continues to a point where an alumina scale is no longer thermodynamically stable over the depleted composition, and the consequential formation of rutile will cause a local Ti depletion. The cycle continues until the sub-surface alloy zone beneath the scale again resembles the γ-TiAl composition, and the cycle is repeated. A layered structure comprising alternating titania-

and alumina- rich scales is observed, especially at elevated temperatures (Becker 1993).

The oxidation sequence is further complicated by the two-phase microstructure which is often induced for improved mechanical properties. Microstructural refinement, in the form of a lamellar structure or two-phase colonies with some lamellar portion, is produced intentionally to achieve an overall optimization of materials properties other than corrosion resistance. An alloy close to γ-TiAl stoichiometry will often be composed of primarily γ-TiAl grains, with a fraction of other grains being α_2-Ti_3Al lamellae or laths. The α_2-Ti_3Al alloy microstructures are the reverse, with α_2-Ti_3Al interspersed with small, fine γ-TiAl laths. An oxide growing at the oxide alloy interface (into the alloy) thus sequentially encounters local alloy compositions with different Ti/Al ratios.

In the present study, the cyclic alternation is found to be exacerbated in cases where nitrogen is present in the oxidation atmosphere because of the stability of titanium nitrides. The Al depleted zones are then subject to nitride formation which adds to the Ti depletion. TiN is the most stable nitride and is readily formed. The effect of nitrogen is discussed further in §8.5.

8.3 Scale Growth Mechanisms

A determination of the ion diffusion mechanisms controlling formation of even a simple corrosion scale can be a study onto itself. Marker and isotope studies are used to identify the predominant mobile species. These determinations get very much more complicated with a multi-component scale, as in the case of a combination of alumina and rutile. The composite stability diagrams presume the non-interaction of oxides with each other and simple compound formation, such as oxide or nitrides. In the titanium aluminide system, it is known that these simple assumptions fail and mixed oxides of two or more of the cations form, in addition to the various oxynitrides. These factors lead to a considerable challenge in deducing growth mechanisms in the complex titanium aluminide system in a multicomponent gaseous environment. The incorporation of Nb

into the intermetallic systems further increases the complexity.

8.3.1 Growth Mechanisms in Scales Composed of a Single Oxide

For analysis of the multiple component system, the mechanisms in the simple single component systems were examined first.

8.3.1.1 Growth Mechanisms of Al_2O_3

There is no agreement concerning the defect structure and type of migrating species even in the heavily studied alumina scales. It is conjectured that the alumina scale growth arises from a combination of oxygen migration into the scale and cation diffusion outward. Pint (1992) demonstrated that the growth mechanism can be altered by the use of reactive elements, which are oxygen active and can either enhance oxygen ion transport or inhibit cationic mobility.

8.3.1.2 Growth Mechanisms of TiO_2

Of the modifications of titanium oxide, the one observed below 1000°C is the rutile version. The lower oxides are only seen at reduced oxygen pressures as well as when oxidized in gaseous mixtures containing air (nitrogen) or water vapor (Kofstad 1988). The anatase is the low temperature modification of TiO_2, and rutile exists at higher temperatures. However, the CRC Handbook of Chemistry and Physics (Lide 1992) ascribes to anatase a brown or black color which is not seen in any samples, especially in the A2 samples with the largest amount of rutile. Additionally, in the Search/Match program used in conjunction with the GAXRD and XRD results, the Figure of Merit (FOM) was always most favorable for rutile compared to either anatase or brookite.

Nonstoichiometry of rutile is expressed as $Ti_{1+y}O_{2-x}$, indicating an excess of metal or deficiency in oxygen. It is thought that interstitial ions of titanium predominate at low oxygen activities and high temperatures. High temperatures is thought to be demarcated by 900°C or above. the low oxygen activities could result from a low oxygen

partial pressure in the gas mixture, or as a result of the reduction of oxygen pressure as one progresses into the oxide corrosion scale. On this basis, the inner part of the scale would be expected to grow by outward titanium migration (though the oxygen pressures are low there) while at the outer portion of the scale, in contact with the gas which has the highest oxygen activities, the inward oxygen diffusion is expected predominate over the outward cation movement.

A layered, lamellar structure is evidenced in the linear oxidation region of titanium oxidation. The evolution of this scale is seen in Figure 8.2. Despite the existence of several stable oxides in the Ti-O system, including: Ti_2O, TiO, Ti_2O_3, Ti_3O_5, Ti_nO_{2n-1} as well as TiO_2, the oxide shows no change in composition with scale thickness. The scale composition is typically TiO_2 with very little evident variation in stoichiometry. A change could be expected thermodynamically if the oxygen potential across the scale varies and reaches, sequentially, the equilibrium pressure for the next lower oxide. One explanation is that the scale is porous or heavily cracked so that the oxygen potential is more uniform across the scale. The observed scale layering results from the proposed growth mechanism, with outward cation movement resulting in a rumpled scale, which localizes stresses, causes cracking and induces an accelerated local oxidation in the cracked regions. An explanation is that the defect structure of TiO_{2-x} provides significantly faster transport than other Ti oxides.

It is proposed that a similar layering mechanism is in effect in the multicomponent, titanium aluminide system. Voids and pores are evident, and the nodes observed in plan view represent the locally stressed regions of short circuit oxidation.

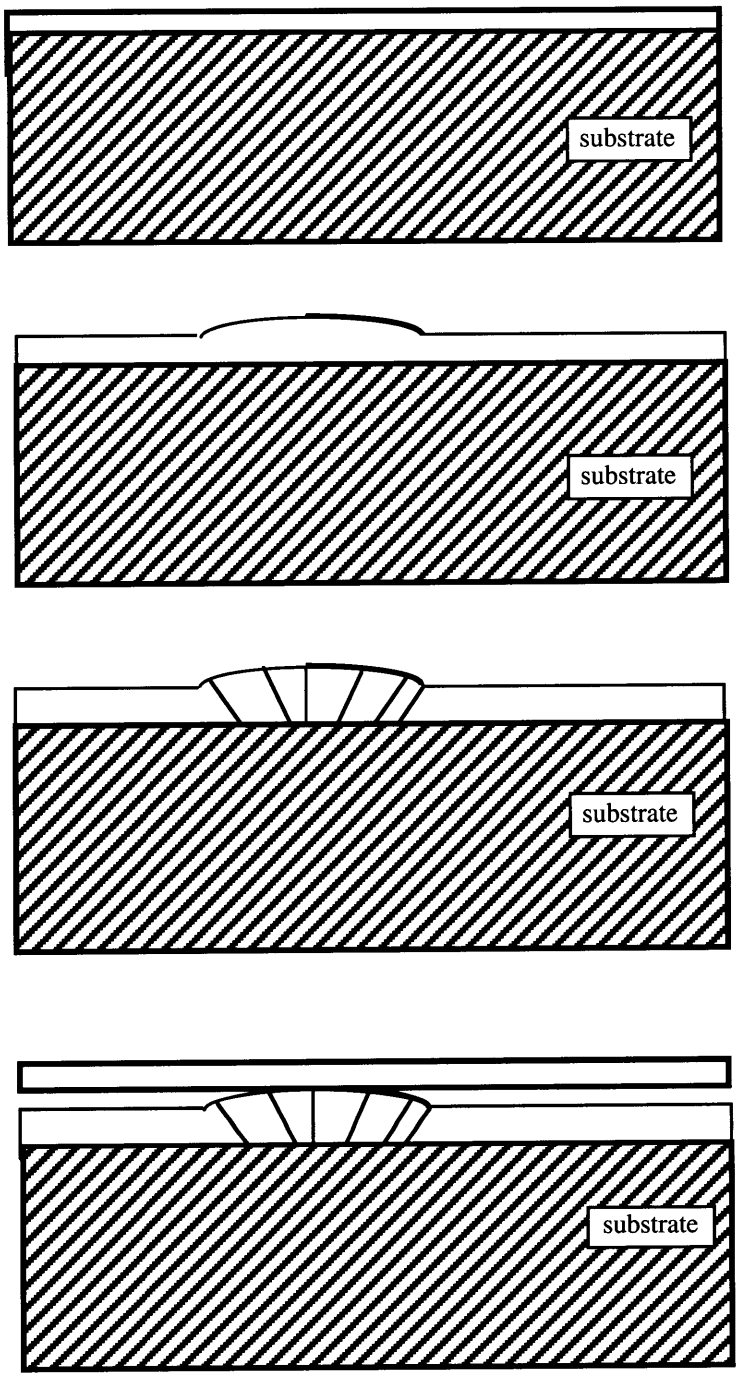

Figure 8.2 Formation of a corrosion scale with layers of identical composition.

8.3.1.3 Growth Mechanisms of Niobia

No niobia mechanism has been documented, primarily because even at temperatures lower than those used in these experiments, the oxidation of niobium is linear and non-protective, resulting in an absence of scales for any species to diffuse through.

8.3.2 Growth Mechanisms in Scales Composed of Multiple Oxides

Rarely do alloy substrates grow a single simple corrosion scale, even in simpler alloys where the stability of one oxide is significantly more stable than the oxides of the other metal components. For this reason, the analysis of multiple oxide scales is required. This complex scale could be a mixture of several oxides or a mixed oxide -- an oxide with more than one metal in the chemical compound.

8.3.2.1 Parallel and Serial Growth Pathways

In the simplified case of a corrosion scale composed of two, mutually nonsoluble compounds, usually oxides or occasionally nitrides, two possible paths exist through the complex scale. Both of these mechanisms are displayed in Figure 8.3.

The parallel path occurs in a scale composed of randomly mixed oxides of both types In this scale geometry, the kinetics are rate limited by the fastest step, or by diffusion in the fastest growing scale. A serial path is seen in systems where continuous, dense scales are formed of different compositions. The overall kinetics of the duplex scale will be determined by the slowest step in the layers, or by the slowest diffusion rate.

8.3.2.1 Comparison to Literature Results

No thermogravimetric rates were given explicitly by Kekare 1997, but weight gains for unalloyed γ-TiAl-alloys (0.13 - 0.18 mg/cm^2) were approximately twice as high than values obtained for G alloys in this study (0.05 - 0.06 mg/cm^2). Similarly, their observed weight gains, while overall exhibiting parabolic behavior, displayed irregular fluctuations, which occurred most often in this study with the slowest growing corrosion

scales. One explanation for the discrepancy lies in the gas. Both studies used compressed air, but their study neglects to mention whether the gas was dried before introduced into the thermogravimetric set-up. Any presence of water in the gas would greatly influence the oxidation rate as the oxygen dissociation in water is and faster than the dissolution of molecular oxygen.

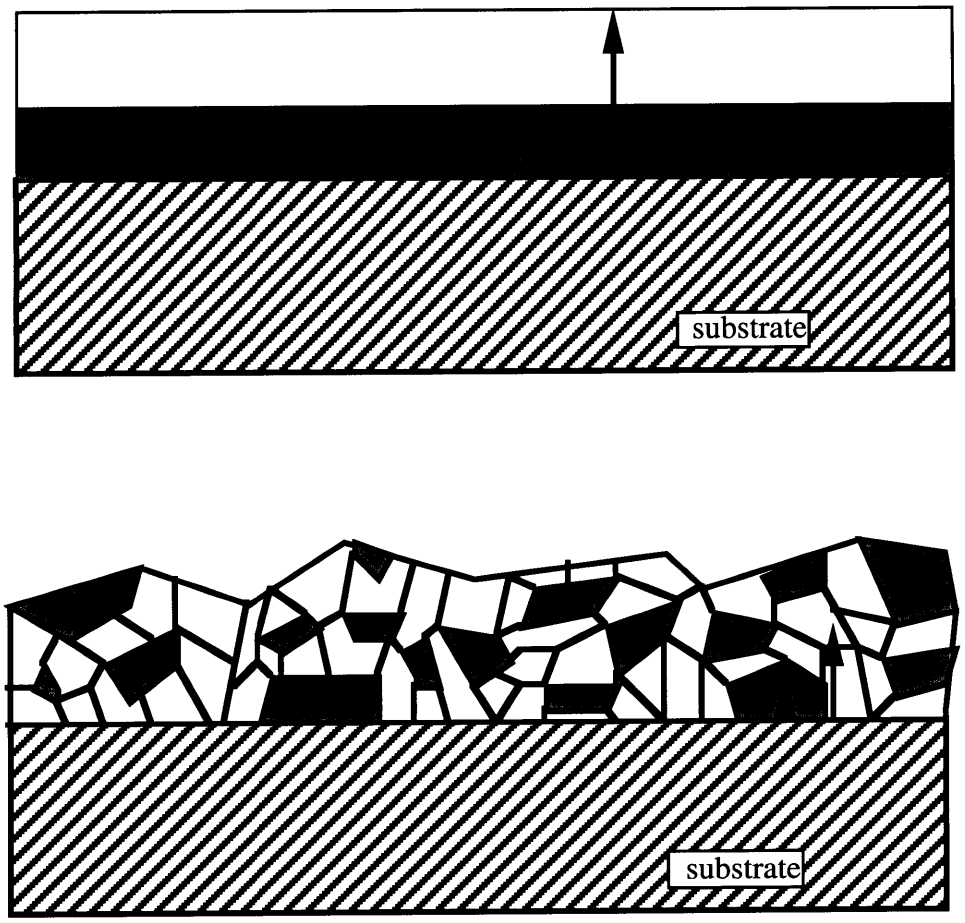

Figure 8.3 Schematic showing possible diffusion paths through a multiple component scale.

8.3.3 Sub-surface Zones

When scale growth is entirely governed by outward diffusion, corrosion scales are all formed at or above the original substrate surface. In cases where at least some portion of the corrosion occurs by inward growth, then the potential exists for sub-surface regions composed of compositions varying from the outer scale and the bulk substrate.

8.3.3.1 Depletion Zones

Another feature of the Ti-Al system is the existence of multiple phases in the alloy phase diagram which permits the substrate to transform in order to accommodate the depleted composition. This is thought to occur when alumina is formed over a γ-TiAl structure. The potential for depleted zones that result in a change in the equilibrium scale composition is especially an issue in the titanium aluminide system and a schematic illustrating this is given in Figure 8.4. A γ-TiAl based alloy which is depleted directly underneath the corrosion scale may yield localized regions of α_2-Ti_3Al, resulting from the Al depletion from preferentially growing an alumina rich sale. After sufficient time, the depleted zones may themselves become depleted in Ti, because of the titania-rich scale that is expected for form over the α_2-Ti_3Al regions.

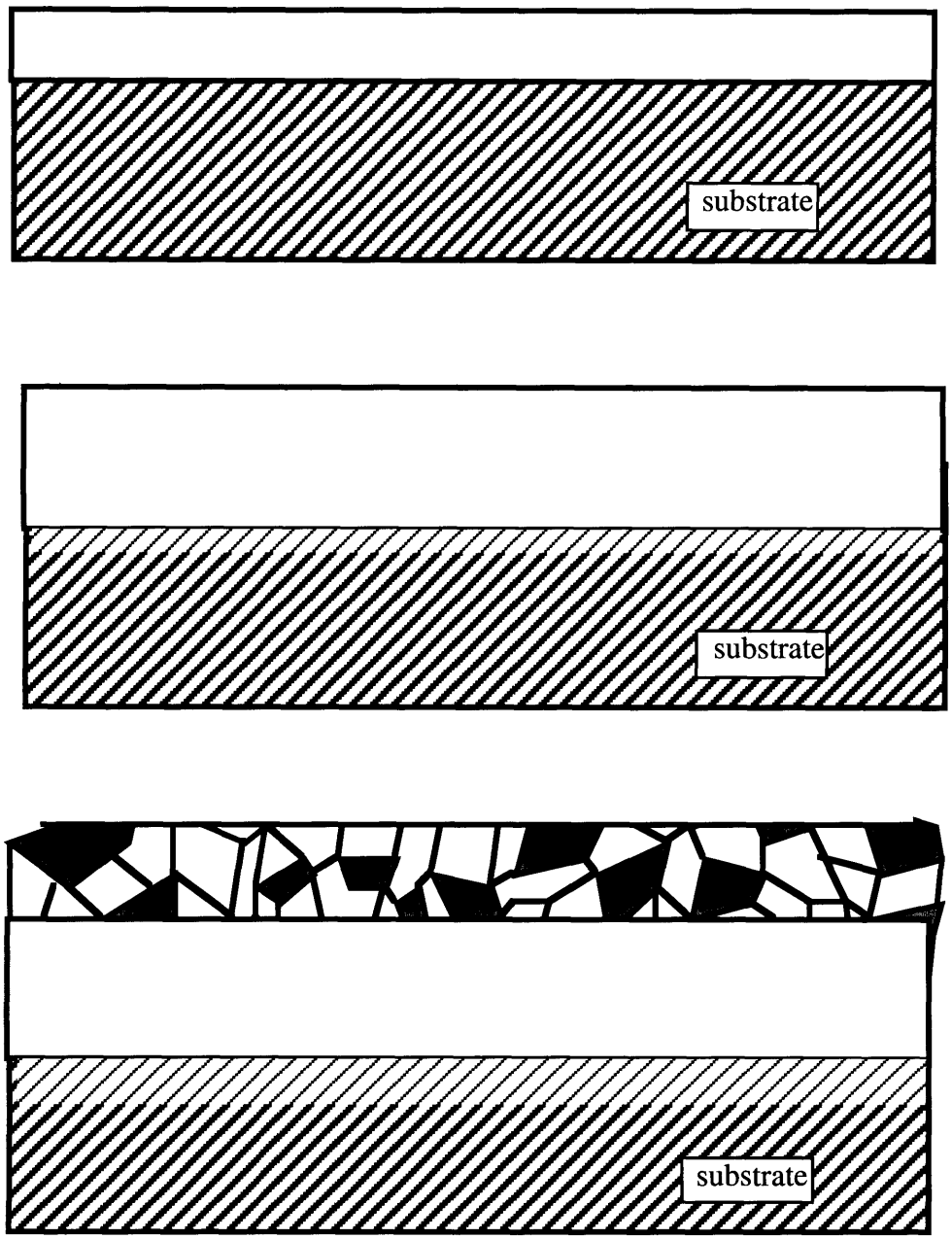

Figure 8.4 Schematic showing the development of depletion layers and the resulting scale composition changes in a system where the original substrate is capable of composition changes.

8.3.3.2 Internal Oxidation

Internal oxidation is a phenomenon unique to the high temperature oxidation of alloys as opposed to a single metal system. The oxidation mechanism in unalloyed systems is either inward or outward ion movement or some combination of both, through the scale and the scale grain boundaries. Regardless of the ion movement direction, the scale is formed external to the unreacted metal interface. In the case of internal oxidation of an binary alloy, the oxidant moves into the alloy and encounters the less reactive metal element (the more reactive metal element having already formed an external scale) and reacts on the interior of the sample. Two factors can be used to determine the necessary conditions for internal oxidation in a particular system. The first is the critical partial pressure of gas compared to the Gibbs free energy of formation of the oxide and the activities of the metal and the oxide (usually considered unity in the case of precipitating a pure internal oxide). This is given in general terms for a generic internal oxide of stoichiometry BO_x by

$$p_{O_2} > \left(\frac{a_{BO_x}}{a_B} \right)^x \exp\left\{ -\frac{2\Delta G^\circ(BO_x)}{xRT} \right\} \tag{8.1}$$

In internal oxide formation it is simple enough to determine the free energy, which remains constant regardless of the alloy system, but the impact of alloying elements and the variation in metal activities may cause deviation from ideality.
A similar criterion for internal oxidation is the solubility product

$$K_{sp} = [a_B] \cdot [a_O] \tag{8.2}$$

With an appropriate combination of free energies for both internal and external scales, activities and diffusion coefficients for the species involved, and with the solubility of oxidants in the alloy system, it can be seen that predictions might be made in simple

binary alloy systems regarding what products would be expected and their respective locations, whether internal or external. In multicomponent systems, with multiple oxidants and with imprecisely known influences of one species on the behavior of all the others, one can appreciate that the complexity of factors render such predictions difficult if not impossible.

Internal oxidation can be an indicator for several mechanisms. First, an alloy oxidizing internally indicates a mobility difference of the different metallic ions and a substantial thermodynamic stability difference in the potential oxides. Secondly, in order for the oxidant to reach the less stable component, there must be an inward component of oxygen or oxidant motion as well as a solubility of the oxidant ion in the alloy system. If the oxide scale were to grow by purely outward cation motion, there would be no oxidant in the interior of the alloy to form an internal oxide. Similarly, but less commonly, if the solubility of the oxidant in the alloy system was sufficiently small, the oxidant would precipitate out along its diffusion paths, and possibly inhibit its further penetration. It has been demonstrated that the defect nature of oxides and grain boundaries is sufficiently high to accommodate an excess of soluble ions compared to the bulk alloy.

8.3.3.3 Dissolution of Oxygen or Nitrogen into the Alloys

The oxygen solubility in the α_2-Ti_3Al structure is approximately 20 at.%. A similar amount might be expected to dissolve in the Ti_2NbAl structure, owing to the similarity in structures. For comparison, the solubility of oxygen in titanium is 30 at.%, while the solubility in niobium is only 5 at.% (and this is at 1500°C, where solid solubility is higher in the Group VA metals (Kofstad 1988)). The solubility of oxygen in Al is usually considered to be negligible. Given the equilibrium partial pressure between Al and alumina ($p_{O_2} = \sim 10^{-50}$ atm at 700°C), the oxygen ions would be expected to react with Al in the alloy and form alumina.

No information on nitrogen solubilities was found, but (as noted previously) it has been proposed that the $TiAl_2$ intermetallic in the Ti-Al phase diagram is, in fact, the nitrogen-saturated compound $TiAl_2N$. The disputed $TiAl_2$/$TiAl_2N$ compound may be another case where an anion is first substantially dissolved in the alloy.

8.4 The Niobium Effect

The origin of the effect of Nb as an alloying element on corrosion behavior of the titanium aluminides is still unknown. The proposed Nb theories from Stroosnijder and Lang given in Chapter 2, are repeated here:

- Formation of a thin (more) stable Ti-rich nitride layer at the scale-alloy interface which acts as a diffusion barrier for anion/cation transport.
- Increase in Al activity relative to Ti activity in the alloy, favoring alumina-rich scale formation.
- Enrichment of Nb in the alloy immediately beneath the scale, changing the diffusion mechanisms such that overall metal and oxygen transport is decreased.
- Doping of the titania lattice by Nb^{5+} ions, decreasing the concentration of oxygen vacancies and/or titanium interstitials and reducing formation of rutile.
- Formation of Nb_2O_5, which forms a mixed oxide with TiO_2 and Al_2O_3, and acts as a glue between otherwise nearly immiscible oxides, enabling the formation of a more coherent scale with elimination of fast-diffusion paths.
- Decrease of oxygen solubility in the alloy.

Several of these theories are related. Ti nitride formation, Nb enrichment and a mixed continuous niobia scale could all contribute as barriers to fast diffusion. Doping shifts the Al and Ti activities, and the shift in activities will result in a change in oxide solubilities. Doping effects of various niobium oxides dissolved into either alumina or titania scales will hence be discussed here. The notations from Kröger and Vink (1956) will be followed.

8.4.1 Nb Doping of Titania Scales

We first dissolve the various niobium oxides in the titania lattice to observe the impact on the diffusion of the defect structures in the oxide scale. The accepted defect structure in titania is either oxygen vacancies or titanium interstitials (Kofstad 1988). For Nb_2O_5, we get the following reaction, which incorporates niobia into titania

$$Nb_2O_5 + V_O^{\bullet\bullet} \xrightarrow{TiO_2} 2Nb_{Ti}^{\bullet} + 5O_O \tag{8.1a}$$

$$2Nb_2O_5 + Ti_i^{\bullet\bullet\bullet\bullet} \xrightarrow{TiO_2} 4Nb_{Ti}^{\bullet} + Ti_{Ti}^{x} + 10O_O \tag{8.1b}$$

These equations predict reduction of oxygen vacancies or the consumption of titanium interstitials in the scale. The net effect of either of these equations on the diffusion and kinetics of titania formation is a reduction of the diffusion rate and therefore the overall corrosion rate. This same procedure is followed for the other niobium oxides by examining the impact of oxygen vacancies only, since the results are the same as those for cation interstitials. NbO_2 dissolved into titanium oxide yields

$$NbO_2 \xrightarrow{TiO_2} Nb_{Ti}^{x} + 2O_O \tag{8.2}$$

In this instance, +4 oxidation states for both the Nb and the Ti result in no change in the defect concentration and the diffusion of the titania is expected to be the same.

Finally, NbO dissolution into a titania matrix is described by

$$NbO \xrightarrow{TiO_2} Nb_{Ti}'' + V_O^{\bullet\bullet} + O_O \tag{8.3}$$

This reaction increases the number of oxygen vacancies and would be expected to **accelerate** the diffusion and the rate of rutile formation, an effect which is not seen when adding Nb. Note also that for the non-stoichiometric oxide, NbO_x, $1<x<2.5$, there exist two possible regimes as the titania scale is doped (with niobia of that oxidation state):

The regime for $1<x<2$, where we expect the titania growth to be accelerated; and that for $2<x<2.5$, where the kinetic rate of titania formation would be slowed. In addition, the nonstoichiometric niobia would have its own inherent defects, which could greatly impact the kinetic rates.

8.4.2 Nb Doping of Alumina Scales

One of the assumptions for the above analysis is that the predominant diffusion mechanism will occur in the titania, because of the faster diffusion rate in the titania relative to that in the alumina. This assumption would be expected to hold in the random, mixed scales found on the non-protective alloys, but not on alloys that have either alternating scales or an inner layer of oxide. The former would comprise a parallel-path system where the kinetics are determined by the diffusion of the fastest species. In a scale composed of layers of alternating compositions, the diffusion is no longer controlled by the fastest step through parallel paths, but rather the slowest step through a series of paths. In this instance, formation of a continuous layer of alumina would be the principal controlling step, as the diffusion through this layer would be the slowest.

We consider only point defects as the imperfections in aluminum oxide (which is primarily Al_2O_3, since no other aluminum oxide compositions are stable) rather than line, planar or electronic defects to make the case simpler. The defect structure of alumina is still unknown and is thought to vary greatly, especially in the presence of oxygen active metals (reactive elements) as proposed by (Smialek et al 1995 and Pint 1993). Using the model of chromia scales, there are three regions of defects. For the area near the metal/oxide interface, cation interstitials and oxygen vacancies dominate. Near the gas/scale interface, there are oxygen interstitials and cationic vacancies. Intermediate levels (of oxygen pressure) lead to the stoichiometric defects of either Frenkel or Schottky type. Frenkel defects are defects of only one lattice, either the cation or anion lattice and are combinations of interstitials and vacancies. Schottky defects have

vacancies on both anion and cation lattices.

From Hobbs 1996, the oxides of both Al and Cr tend to be p-type conductors (with the electronic conductivity of alumina being far smaller than that of chromia). This result yields either oxygen interstitials or cation vacancies, as defined by growth mechanisms where reactions at the gas/oxide interface predominate.

Using the same analytical procedure as above for the titania, gives the following equations for the doping of alumina scales by niobia.

$$Nb_2O_5 + 2V_O^{\bullet\bullet} \xrightarrow{Al_2O_3} 2Nb_{Al}^{\bullet\bullet} + 5O_O \tag{8.4}$$

$$NbO_2 + \tfrac{1}{2}V_O^{\bullet\bullet} \xrightarrow{Al_2O_3} Nb_{Al}^{\bullet} + 2O_O \tag{8.5}$$

$$NbO \xrightarrow{Al_2O_3} Nb_{Al}' + \tfrac{1}{2}V_O^{\bullet\bullet} + O_O \tag{8.6}$$

From these equations, it is seen that only the growth and dissolution of the NbO oxide will enhance alumina scale growth, if the oxygen vacancies are the defect structure that dominates in the alumina growth. Of course, which doping scheme occurs depends on the local p_{O2} in the particular portion of the scale involved.

The following three sets of equations follow the analysis for both n- and p-type alumina behavior. Note that the first equation in each set repeats the analysis when presuming oxygen vacancy dominance.

$$Nb_2O_5 + 2V_O^{\bullet\bullet} \xrightarrow{Al_2O_3} 2Nb_{Al}^{\bullet\bullet} + 5O_O$$
$$Nb_2O_5 + \tfrac{4}{3}Al_i^{\bullet\bullet\bullet} \xrightarrow{Al_2O_3} 2Nb_{Al}^{\bullet\bullet} + 5O_O \quad \textbf{(n type)}$$

(8.7 a-d)

$$Nb_2O_5 \xrightarrow{Al_2O_3} 2Nb_{Al}^{\bullet\bullet} + \tfrac{4}{3}V_{Al}^{'''} + 5O_O$$
$$Nb_2O_5 \xrightarrow{Al_2O_3} 2Nb_{Al}^{\bullet\bullet} + 2O_i'' + 5O_O \quad \textbf{(p type)}$$

$$NbO_2 + \tfrac{1}{2}V_O^{\bullet\bullet} \xrightarrow{Al_2O_3} Nb_{Al}^{\bullet} + 2O_O$$
$$NbO_2 + \tfrac{1}{3}Al_i^{\bullet\bullet\bullet} \xrightarrow{Al_2O_3} Nb_{Al}^{\bullet} + 2O_O \quad \textbf{(n type)}$$

(8.8 a-d)

$$NbO_2 \xrightarrow{Al_2O_3} Nb_{Al}^{\bullet} + \tfrac{1}{3}V_{Al}^{'''} + 2O_O$$
$$NbO_2 \xrightarrow{Al_2O_3} Nb_{Al}^{\bullet} + \tfrac{1}{2}O_i'' + 2O_O \quad \textbf{(p type)}$$

$$NbO \xrightarrow{Al_2O_3} Nb_{Al}' + \tfrac{1}{2}V_O^{\bullet\bullet} + O_O$$
$$NbO \xrightarrow{Al_2O_3} Nb_{Al}' + \tfrac{1}{3}Al_i^{\bullet\bullet\bullet} + O_O \quad \textbf{(n type)}$$

(8.9 a-d)

$$NbO + \tfrac{1}{3}V_{Al}^{'''} \xrightarrow{Al_2O_3} Nb_{Al}' + O_O$$
$$NbO + \tfrac{1}{2}O_i'' \xrightarrow{Al_2O_3} Nb_{Al}' + O_O \quad \textbf{(p type)}$$

8.4.3 Thermodynamics and Stability Diagrams

The following analysis refers to the stability diagrams from Chapter 4, Figures 4.14 - 4.17.

Of the three primary oxides in the Al-Ti-Nb system, Nb_2O_5 is the least stable. However, the kinetics for the formation of this oxide are the fastest of the three. In this situation, there is a competition between thermodynamics and kinetics.

Prior work has shown the reduction of oxidation rate with the addition of Nb to γ-TiAl alloys. No clear explanation exists for this Nb effect, and many mechanisms have been proposed. These have been detailed in §2.6. In addition to the mechanisms already cited, it is proposed here that another mechanism is possible: namely, the reduction of the oxygen partial pressure (activity) across the semi-protective scale that forms on either A2 or SA2, in the form of a mixture of alumina and titania. The equilibrium partial pressures for Al/Al_2O_3 and for Ti/TiO_2 are vastly lower than the equilibrium oxygen partial pressure for equilibrium between Nb_2O_5 and the next lower Nb oxide (NbO_2). Therefore, the partial pressure of oxygen in the interior of the scale and at the scale/metal interface is expected to be significantly lower than that at which Nb_2O_5 is expected to form. This reduction now alters the stability field for Nb and oxygen to a lower niobium oxide- either NbO_2, NbO, or simply NbO_x. Niu (1996) demonstrated that the oxygen partial pressure in the gas mixture need only be comparable to that value required for equilibrium of NbO_2 in order for the formation of Nb_2O_5 to be avoided or minimized.

8.4.4 The Niobium Effect in the Cr-Nb Intermetallic System

Similar behavior of Nb has been observed in other intermetallic systems, as described below.

8.4.4.1 Thermodynamics Compared to Kinetic Boundary

The work of this author (Duncan 1994) indicated similar results in mixed gases at higher temperatures in the Cr-Nb system, where formation of a protective niobia was also

seen with slower and non-linear growth rates and adherent scale formation, confirming by Inouye (1960). In the Cr-Nb system at 800° and 900°C, Nb_2O_5 is anticipated at oxygen partial pressures of greater than ~10^{-27} and ~10^{-25} atm, respectively. However, the lowest oxygen partial pressure that any experiment was subjected to was ~10^{-21} atm, definitely within the Nb_2O_5 stability field. While there were indications of a small amount of Nb_2O_5 formation in the form of porous, nodular features located near small cracks or pores in and otherwise uniform scale, no Nb_2O_5 was detected in the remainder of the scale. In this earlier study, as in the present work with the Ti-Al-Nb system, an additional gas component (in this case sulfur) was seen to play a role in determining the final balance between the thermodynamics and kinetics of scale formation. Unlike in the present work, the assumption of simple compounds (NbO_2, Cr_2O_3, NbS_2) formed by reaction with either of the gases (O_2, S_2), with little interaction amongst the products, was more valid. In the Ti-Al-Nb-O-N case, the presence of mixed oxides (as well as the oxynitrides that were also detected) effects significant deviations from the ideally-computed composite stability diagrams. Nevertheless, the composite diagrams are a starting point for determining potential or expected phases and can be used to indicate trends or to identify the likely contributions that both thermodynamics and kinetics play in the titanium aluminide oxidation.

8.4.4.2 Protective NbO_x Behavior

For specimens with a Nb oxide or Nb oxynitride in the inner scale (as indicated by XRD), it is unclear and often difficult to determine the oxidation state of Nb. It is also possible that, with the series of Nb oxides thermodynamically available, a sequence of all possible niobium oxides forms, but there is no indication yet of such a series. The analogy is similar to that of Ti, which also forms a series of stable TiO_{2-x} oxides with $0 < x < 1$. However, when Ti metal is exposed to atmospheric pressures of oxygen below 1000°C, only the rutile modification is ever detected (Kofstad 1988).

It is presumed here that Nb_2O_5 formation occurs. The kinetics, even at the lower temperatures studied in the present experiments, are markedly linear. For comparison, a 100% Nb sample was reacted in 100% nitrogen with only trace oxygen impurities. The resulting scale was primarily an oxide, with little protective value due to large cracks and scale defects.

8.5 The Nitrogen Effect

Much controversy surrounds the influence of nitrogen in the oxidizing environment of titanium aluminides. Both beneficial and detrimental effects to scale growth kinetics and scale morphology have been claimed. There are reports of rates in air being significantly higher than those observed in 100% oxygen, despite the five times greater oxygen concentration in 100% oxygen. For experiments without nitrogen, Becker (1992) reported independence of the oxidation rate on the oxygen concentration, for gases with ranges of 1% oxygen-balance argon to 100% oxygen.

For the few studies that have involved experiments at lower temperatures and investigated the effect of nitrogen in gas mixtures at these temperatures, it has been reported that a certain temperature exists below which the nitrogen has an effect of lowering the overall scale growth rate. Becker reported that, above 900°C, titanium aluminides of γ-TiAl-based compositions displayed linear oxidation rates when exposed to air, while the same alloys exposed to 100% oxygen formed mostly protective scales with parabolic rates. This result, when coupled to the results of this study at lower temperatures, suggests that the nitrogen effect is a strong function of temperature and, at the temperatures proposed in this work as a practical working range, the nitrogen component in the gas is beneficial and desirable.

In this study, nitrogen in the gas mixture reduced the thermogravimetric oxidation rate seen in all the alloys. Other results in the literature have shown the effect of

nitrogen both increasing and decreasing the rates. In the present study, the presence of argon in the environment promoted the formation of the mixed oxide ($TiAl_2O_5$) and presence of nitrogen aided the formation of the oxynitride $Al_{27}O_{39}N$. In the absence of nitrogen, the oxidation kinetics of SA2 approach those seen for A2. The agreement occurs in the region between 5 to 20% oxygen.

8.5.1 Nitrogen Effect with Niobium Absent

TiN is the most favored nitride in the titanium aluminide system. Given the depletion of Al in γ-TiAl-alloys during formation of the favored alumina oxidation product, it is proposed that formation of TiN contributes to a corresponding depletion of Ti and hence restoration of a more favorable Ti ratio in the alloy. TiN is an exceptionally brittle material and not expected to contribute in a positive manner towards scale adherence, because its higher thermal expansion coefficient mismatches that of the alloy and the other possible oxides. Indeed, even the thin, slow growing scales grown on the G alloy, which had the largest alumina content in its scale composition, showed spallation from thermal stresses in cooling. Hence, the favorable nitrogen effect is likely to be only a chemical and not a mechanical one.

8.5.2 Nitrogen Effect in the Presence of Niobium

By analogy to niobia, which is not the most stable oxide in the Al-Nb-Ti system, the niobium nitrides are also the least stable of the possible nitrides. Again, it may be expected that formation of the thermodynamically most stable product (Nb_2O_5) may be kinetically disadvantaged by a less protective scale product (NbN_x), which nonetheless wins the race, at least in the short-term.

8.6 Activation Energies for Alloy SA2 Oxidation

The kinetic data for oxidation of the three alloys in argon - 20% oxygen at both 700 and 800°C were plotted on an Arrhenius plot, Figure 8.5 and the slopes used to calculate activation energies, Table 8.2.

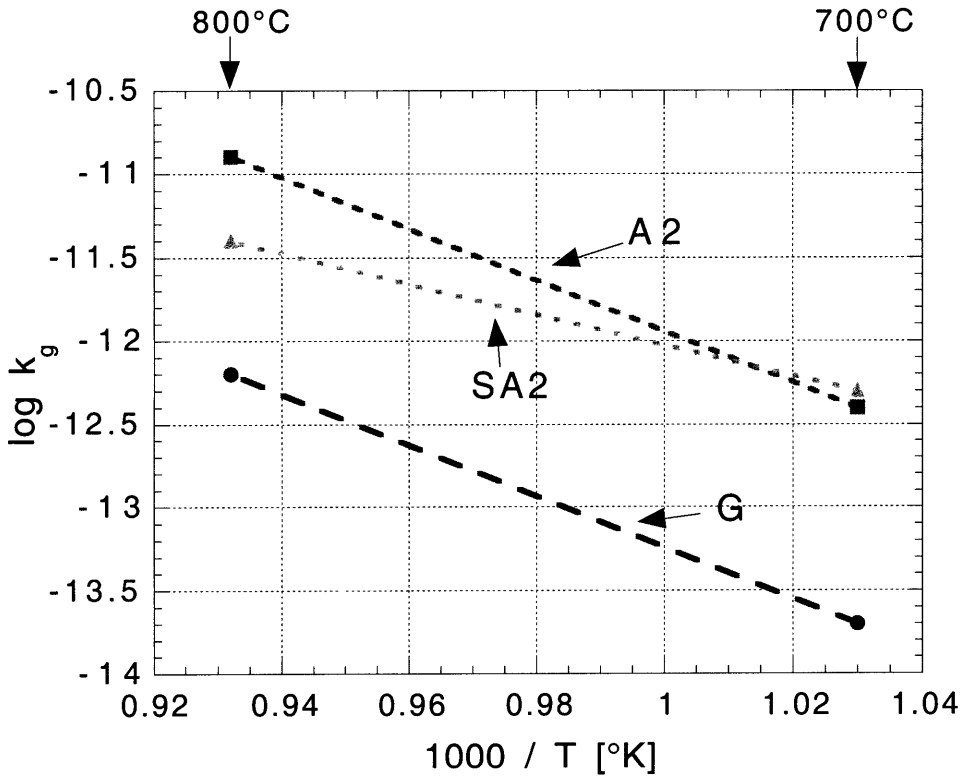

Figure 8.5 Arrhenius plot of parabolic rate constants for oxidation of the three alloys exposed to argon-20% oxygen at 700°C and 800°C.

Table 8.2 Activation energies for oxidation of the three alloys exposed to argon-20% oxygen calculated between 700 and 800°C.

Alloy	Activation Energy [kcal/mole]	Activation Energy [kJ/mole]
G	70	293
A2	70	293
SA2	21	175

The comparable activation energies of G and A2 are not an indication of the identical mechanism operating in the two systems, since the two alloys have greatly differing kinetic rates (Kofstad 1988). One of the key assumptions is that the oxidation mechanism remains constant over the temperature range used for calculating the activation energy. As indicated earlier, and noted by other researchers, the composition of the scale grown over titanium aluminides is extremely sensitive to temperature, and the assumption of a constant mechanism for oxidation may not hold over the 700 and 800°C temperature range used. However, since this assumption is used in other studies to calculate the energy, then it may be useful as a comparison value. Various activation energies for oxidation and diffusion gathered from literature are listed in Table 8.3 .

Table 8.3 Activation energies from literature for oxidation and diffusion in the temperature range ~900°C.

Alloy and/or Process	Activation Energy [kJ/mole]
Pure Ti (Chaze 1982)	239
Ti-48at.%Al (with less than 1at.% dopants) (Kekare 1997)	324-343
Ti-49at.%Al (Welsch 1989)	419
Ti-26at.%Al (Welsch 1989)	255
Ti-14Al-20Nb-3V-2Mo (wt.%) in 100% O_2 (Super Alpha-2) (Blank-Bewersdorff 1994)	185
Ti-14Al-20Nb-3V-2Mo (wt.%) in air (Super Alpha-2) (Blank-Bewersdorff 1994)	222
O diffusion in TiO_2 (Unnam 1986)	234
Ti diffusion in TiO_2 (Venkatu 1969)	257
O diffusion in Al_2O_3 (Oishi 1960)	460
Al diffusion in Al_2O_3 (Oishi 1960)	477

8.7 Dependence of K_p on the Gas Partial Pressure

Using thermodynamics to aid in the discernment of the expected, most stable oxide. Thermodynamics can be used to predict what oxide should be the most stable in a given system. From the free energy versus temperature diagram, given in Figure 4.11, the closeness in stability of both Al and Ti oxides has been remarked on. This causes the Ti-Al dilemma. The Ellingham/Richardson diagram, in Figure 8.1, shows more clearly the relationship that exists between the Al and Ti oxide dynamics. Here it is evident that the alumina is always more stable than titania.

Oxidation kinetics are often dependent on the gas pressure, as explained by defect chemical analysis. Depending on the different defects, a ceramic compound can display several regimes of gas partial pressure dependence. Brouwer-like diagrams used to illustrate these dependencies were constructed for the SA2 alloy in nitrogen- (Figure 8.6) and argon-containing (Figure 8.7) mixtures.

The first reveals a linear relationship of log K_p to log p_{O_2} in argon-oxygen mixtures with a slope of 0.73. The linear relationship suggests a single dominant mechanism in oxidation, but the slope of approximately 3/4 is not close to the slope expected for alumina formation (3/16). It could also represent some fixed combination of other mechanisms. The K_p dependence for Nb oxide formation is not known, since experimentally the kinetics are always linear with porous scale formation.

The relationship between oxygen partial pressure and the oxidation of SA2 in nitrogen mixtures (Figure 8.7) changes more dramatically from concentrations ranging from 100% oxygen down to levels of oxygen impurity. In these mixtures, it is clear that both the presence of nitrogen and the concentration of oxygen have a great impact on the kinetic rate dependence, indicating probable mechanistic changes with oxygen pressure changes.

The slope of the rate compared to oxygen pressure is approximately 1/8 at small (<5% oxygen) concentrations. The dependence jumps to the much larger values (~2) when greater amounts of oxygen are present. Neither of these slopes corresponds to a known defect mechanism in the oxides found in the Ti-Al-Nb system.

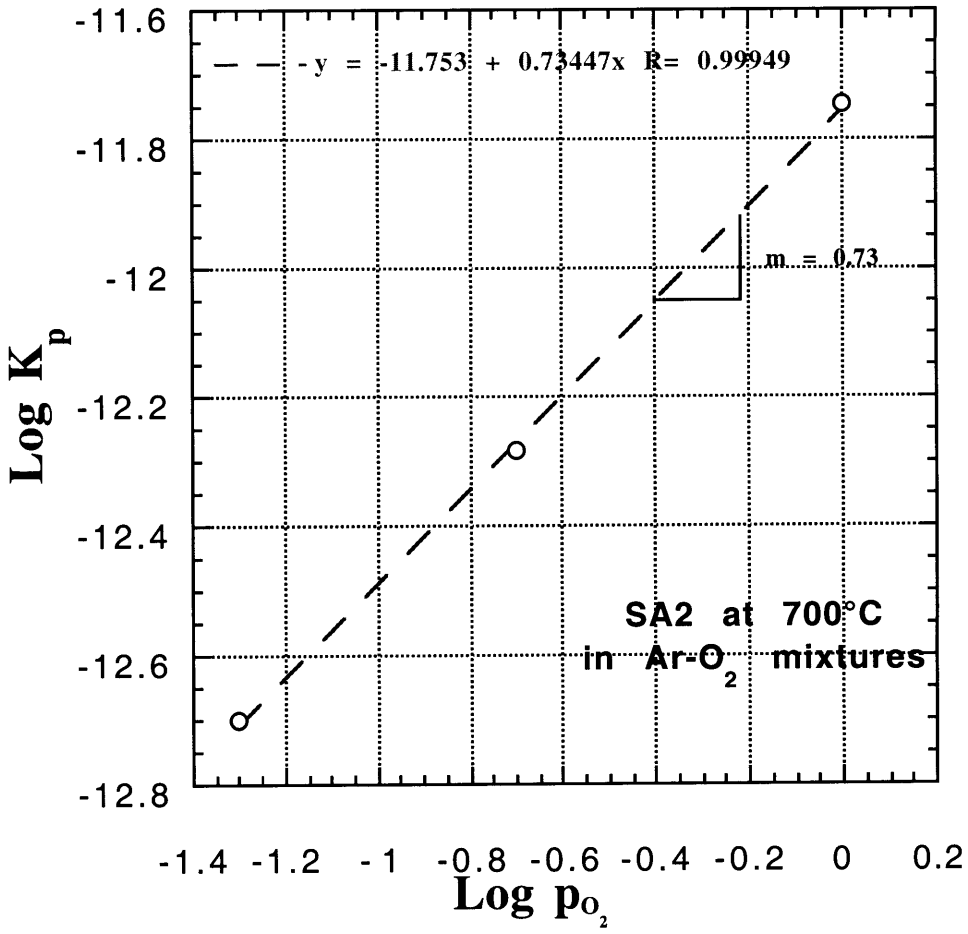

Figure 8.6 Log K_p versus log partial pressure oxygen for alloy SA2 in argon-oxygen mixtures.

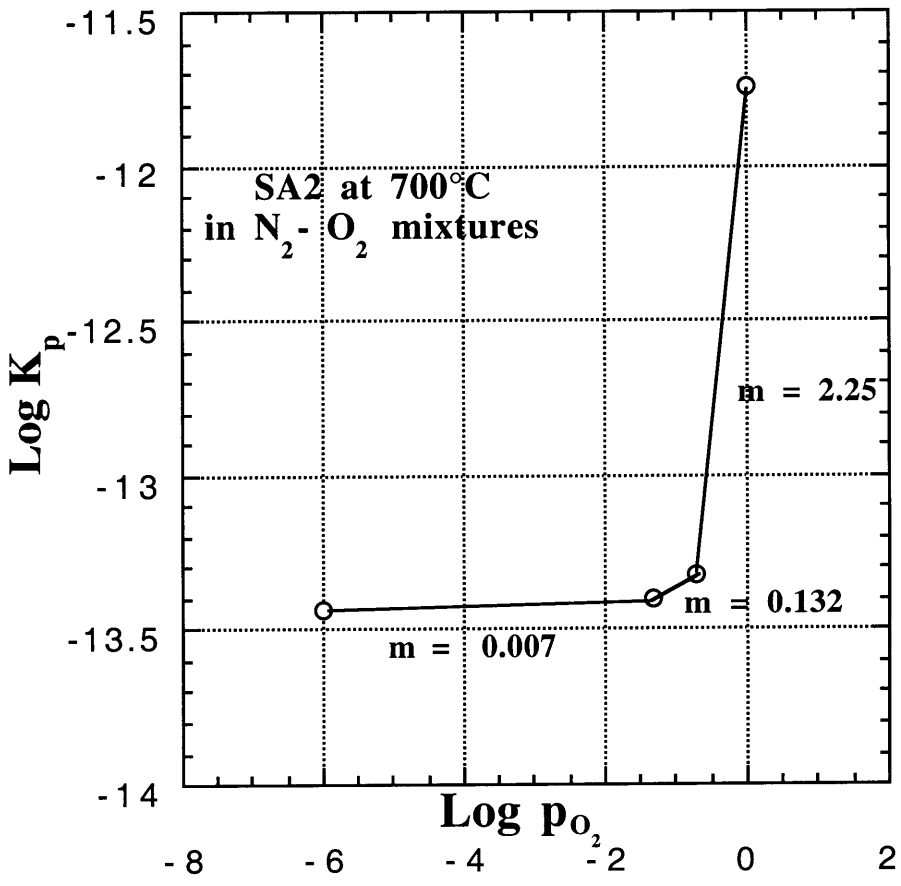

Figure 8.7 Log K_p versus log partial pressure oxygen for alloy SA2 in nitrogen-oxygen mixtures.

8.8 Alloy SA2 as a Prospective High Temperature Material

Results from this study indicate great promise for Ti_2NbAl based alloys. Alloys based on an intermetallic tend to have more consistent oxidation properties than those exhibited in solid solution alloys.

The Ti_2NbAl alloys have better mechanical properties than those for typical alloys but better oxidation resistance than α_2-Ti_3Al alloys. The latter property is especially notable in nitrogen containing gases of low oxygen concentrations, which is precisely the conditions expected for aircraft applications.

Figure 8.8 detailing the proposed evolution of the multiplex scale in the SA2 alloy. A mixed scale of both alumina and titania is formed which reduces the oxygen partial pressure at the oxide/metal interface. The reduction of pressure allows for the formation of a protective niobium compound (either an oxide, nitride, oxynitride or some mixture of these). Diffusion through this continuous niobium-rich layer favors the formation of alumina. Repeated layers occur when cracks or voids occur that disturb the serial scale structure.

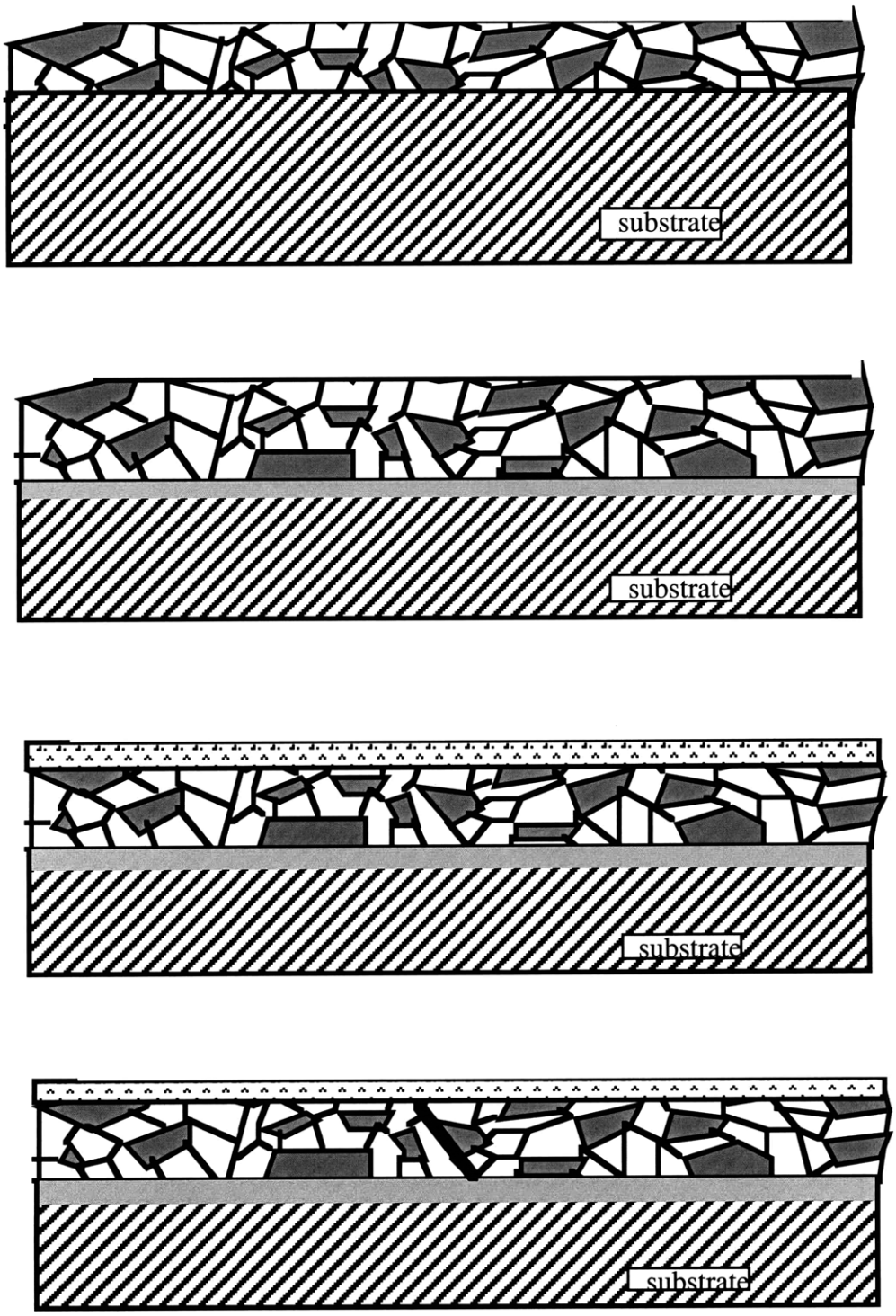

Figure 8.8 Layered scale formation during oxidation of SA2 alloy in nitrogen-5% oxygen.

It should be pointed out again, that this study focused on a model set of otherwise undoped titanium aluminides including one with Nb substitution. Earlier results on the properties of niobium-containing titanium aluminides, which studied the impact of varying the Nb and Al content, concluded that potential alloys fall into a narrow range (Rowe 1992). When the concentration of either Nb or Al reached 30 at.%, mechanical properties began to suffer. The Nb content of the SA2 alloy falls below this limit and therefore is among viable compositions.

Many of the factors that are used to improve materials for both high and low temperature properties could also be used in the SA2 alloy. These include oxide dispersion strengthening and reactive element alloying. These additives have favored the formation of protective scales, especially alumina, in super alloy systems, and could be exploited in titanium aluminides.

Pre-oxidation of the alloy to pre-form a protective scale is another technique to improve the oxidation resistance of a material. Taniguchi et al (1995) have demonstrated this for γ-TiAl-alloys. Ti_2NbAl and Ti_2NbAl-based alloys are excellent candidates for this technique since it was seen that lowering the oxygen pressure promotes continuous alumina layer formation. In fact, the higher oxygen contents of the pre-oxidation environment, which is higher than would be expected in service, promoted an increased amount of niobia in the scale.

Additional coatings to improve oxidation resistance are also viable for Ti_2NbAl-based alloys. This are detailed by (Taniguchi 1994) and include aluminizing, chromizing, coatings of a yttrium-alloyed superalloy, and ceramic coatings.

The efficacy of titanium aluminides use has already been established in limited applications for low temperature parts in test engines; the further expansion of these materials to intermediate temperature parts could provide significant savings over the engine life.

Chapter 9

Conclusions

1) The titanium aluminide system offers great promise for providing lighter weight, high temperature materials. Ductility (in the case of γ-TiAl alloys) and oxidation resistance (in the case of α_2–Ti_3Al alloys) have led to efforts to modify both alloys, especially with the addition of Nb. Results have shown improved oxidation performance, but significant reservations about suitability in some applications persist.

2) One complication in the Ti-Al system is the existence of multiple intermetallic phases. The thermodynamically stable scale over each alloy phase is different, and is alterable by various alloy additions. A protective alumina scale is predicted over γ-TiAl based compositions and can be shifted to be stable over the appropriately alloyed α_2–Ti_3Al. After exposure to oxidizing environments, the resulting scale formation can lead to a local depletion of the alloy beneath the scale which effects phase transformations in the other intermetallic compositions. The resulting new intermetallic phase is associated with a different equilibrium corrosion scale composition, and this shift in the equilibrium results in an alternating layer structure. The layered scale structure is less than optimal for corrosion resistance.

3) Niobium, which is typically added to stabilize the β-phase, also improves the high temperature oxidation resistance, by contrast with the typical catastrophic oxidation of Nb alone. The exact reasons for this improvement have not been discovered. The doping effect of Nb on the alumina and titania scales would suggest, from a conventional point defect analysis, that incorporation of Nb_2O_5 in the oxide scale could improve the corrosion resistance, by slowing the scale growth kinetics. Kinetic results do not suggest the formation of Nb_2O_5, however.

The formation of a protective Nb oxide is, however, suggested at reduced oxygen pressures that occur within oxide scales because of the oxygen potential gradient. This is seen in the Cr-Nb system, where protective Nb behavior was observed, despite thermodynamic predictions to the contrary. Similarly, a nitride or the oxynitride of Nb could also serve as a protective layer.

4) The presence of nitrogen in the oxidizing gaseous environment resulted in a reduction of the overall oxidation rates for all intermetallic alloys in this study.

In the alloys with no Nb additions, the nitrogen in the environment results in a titanium nitride, probably TiN or Ti_2N, evidenced by a yellow scale. This nitride production has the effect of lessening the Al depletion resulting from preferential alumina scale production. However, especially in the case of G alloy, the nitride formed may be continuous and brittle and results in a deleterious impact as evidenced by scale spallation.

The interaction of nitrogen in the alloy with the Nb content is more complex. The equilibrium is shifted, and the presence of a niobium oxide or oxynitride moderates the detrimental brittle behavior of the titanium nitride.

It is unclear why reports of the nitrogen effect, observed in the oxidation of titanium aluminides in mixed gaseous environments, vary from one research group to the next. No significant difference in experimental procedure is noted. There may be an uncertain contribution from moisture in room air.

5) The overall scale growth mechanism appears to be one of mixed mode. Some oxidant inward movement is presumed, as evidenced by the depletion zone and the formation of what may be the "new cubic phase". Pores and other small voids indicate outward cation movement and vacancy formation due to the volume mismatch between the resulting oxide and substrate.

6) Activation energies for oxidation, calculated for the alloys between 700°C and 800°C in argon-20% oxygen mixtures, yielded values of $\Delta G°_f$ = 175 kJ/mole for the SA2 alloy and $\Delta G°_f$ = 300 kJ/mole for both A2 and G alloys. The SA2 value agrees with a value obtained for a commercial Super Alpha-2 alloy and the 300 kJ/mole matches closely a value obtained for a γ-TiAl-alloy with no dopants. The activation energies for the A2 and G alloys in this environment (argon-oxygen) are similar, or the similarity may be only coincidental and represent different mechanisms, especially since the oxidation rates for the A2 and G are very different.

7) Brouwer-like diagrams constructed for the SA2 alloy indicate a linear relationship of Kp to oxygen partial pressure in argon-oxygen mixtures. The slope of approximately 3/4 is similar to that of diffusion through titania, but too large for the slope expected for alumina formation. The relationship in nitrogen-oxygen mixtures displays many regions of different slopes, which do not correspond to any known defect mechanism in the oxides found in the Ti-Al-Nb system.

8) Results from this study indicate great promise for Ti_2NbAl based alloys. Alloys based on an intermetallic tend to have more consistent oxidation properties than those exhibited by solid solution alloys.

The Ti_2NbAl alloys have better mechanical properties than those for typical γ-TiAl alloys but better oxidation resistance than α_2–Ti_3Al alloys. The latter property is especially notable in nitrogen-containing gases of low oxygen concentrations, which is precisely the conditions expected for their aircraft applications.

The present studies were carried out on model systems, with little or no mechanical improvements typical with these materials and with no additional alloy additions. The results therefore represent conservative estimates for material behavior and do not preclude the possibility of future improvements by mechanical processing for optimum grain refinement, alloying additions for both mechanical and oxidation property enhancement and surface treatments.

A major issue in the use of surface treatments such as thermal barrier coatings, compared to the use of composites is the concern for catastrophic breakdown of the substrate material in the event of coating failure. In the Ti-Al system, the base material -- especially Ti_2NbAl based alloys -- have proven to have an inherent resistance of their own that would reduce the likelihood of disaster. The efficacy of titanium aluminide use has already been established in limited applications for low temperature parts in test engines; the further expansion of these materials to intermediate temperature parts could provide significant savings over the engine life.

Chapter 10

Future Work

In the interest of surveying an overall representation of titanium aluminide alloys and gas environments to gather the most information on trends that occur in the system, a selected matrix of studies was designed and then only selected samples were pursued in depth because of time constraints. Even within the set of experiments performed, several areas rich in scientific interest remain.

Since the three alloys selected here are a model set of titanium aluminides, the additional impact of the solid solution alloying addition was not investigated. Specifically, two more alloys were obtained, subjected to the identical thermomechanical processing as the G alloy, but with Nb additions as well as one alloy with both Nb and Cr and Nb and Mn. The comparison of the beneficial Cr effect in superalloys (as a getter for oxygen to reduce internal oxidation) to the effect of Cr in titanium aluminides, is the object of intense study (Brady 1995) although it is thought that the existence of Cr has an embrittling effect.

Additional activation energy calculations could provide additional insights. The number of experiments conducted at temperatures above 700°C was limited in this study because of the less protective scales formed. One assumption for the calculation of the Arrhenius activation energy was the existence of a single mechanism over the temperature range used for calculating these values. This may be valid for the argon-oxygen mixtures, when the scale is a more simple, yet less desirable

titania-dominated mixture. The same is evidently untrue for the nitrogen-oxygen mixtures, as evidenced by the large dependence of the parabolic rates on the oxygen pressure. A large dependence of the diffusion rates on the oxygen potentials would lead to the conclusion of a similar dependence of the thermodynamics.

Because of the interest in the more novel and promising SA2 alloy, less effort was exerted in arriving at a detailed understanding of the oxidation mechanisms of both A2 and G. Alloys of similar structure have been more thoroughly studied in literature, but typically at temperatures of 900°C or more. It is clear from the results at 700°C and 800°C that the system is very sensitive to temperature. These results bring both the promise that a lower temperature range may prove more suitable for optimal material application, which was not as evident at the higher range, as well as a difficulty in accelerating the corrosion tests because of the invalidity of the same mechanisms applying at both temperatures.

Reactions at lower oxygen pressures would determine more precisely the K_p dependence on oxygen concentration for both SA2 and the other alloys. The low oxygen pressures would also comprise a more accurate representation of actual operating pressures.

In-depth TEM studies would elucidate the oxide fine structure and more precisely determine details of the composition via electron diffraction. TEM might be instrumental in the investigation into the mechanism that produces the stable α-Al_2O_3 in this system rather than the metastable θ- or δ-Al_2O_3 that forms on superalloys at temperatures less than 1000°C.

10.1 Effect of Group VA Metals as Alloying Elements in Titanium Aluminides

The effect of V doping on the oxidation rate of γ-TiAl-alloys has been studied at 700-1000°C (Becker 1992). Overall, V had a detrimental effect on the parabolic oxidation rate. It would be interesting to study the effect of Ta on the oxidation rate, since V, Nb and Ta along belong to the same group VA in the periodic table. Tantalum

would have a similar doping and valency effect as Nb, with the most stable oxide being Ta_2O_5, very similar to the Nb_2O_5. It also has lower valent oxides, but unlike the stable NbO and NbO_2 compounds, the TaO_x, TaO_y and TaO_z are all metastable. In contrast to the purported protectiveness of the NbO_2, there is no known thin protective tantalum oxide, and Ta oxidation rates are linear, similar to those for formation of Nb_2O_5. A major disadvantage to Ta is its higher density, but for research purposes it is an ideal candidate to study the doping effect with an element that oxidizes in a manner most similar to Nb. Of even more interest, is the synthetic element hahnium, (Z = 105), also a Group VA element. Naturally, little is known about the element and its oxidation behavior; however, with ion implantation, only small amounts would be necessary which could offset the otherwise prohibitive cost.

10.2 Grain Boundary Chemistry Using the STEM

Studies of the segregation of foreign ions along oxide grain boundaries have illuminated the reactive element effect (Pint 1992). Similar studies in the titanium aluminides could advance the understanding of the Nb effect. The STEM at MIT with the nm probe size has the capacity to detect portions of monolayers of ions which have segregated on the boundaries, and the use of the transverse sections could yield information about the degree of segregation relative to depth within the scale. A combination of these studies with the various dopants would clarify whether size or valence was the driving force for segregation.

10.3 Tracer Experiments

Since the dismantling of the SIMS equipment at the Center for Materials Science, the capability to conduct valuable tracer experiments has diminished. Sequential exposures of oxidant isotopes such as ^{18}O and ^{15}N lend an important insight into the growth mechanisms, by allowing the determination of the ultimate position of the tagged elements. Inward and outward growth mechanisms could be determined for both oxygen and nitrogen as well as the impact of one diffusion rate in the presence of the other

oxidant.

10.4 Thermal Cycling

Engine materials will experience thousands of cycles between ambient and operating temperature. Cyclic oxidation and studies of the scale adherence under these conditions are the next logical step for studying the future potential of orthorhombic-based materials.

10.5 *In-Situ* Heating-Straining in the ESEM

Aircraft turbine materials are exposed to severe thermal/mechanical stresses, in addition to corrosive gases at high temperature. Very few studies have investigated materials exposed to the combination, and no dynamic *in-situ* studies with both environments imposed have been reported. The high-temperature straining stage in the ESEM provides a source of quantifiable externally applied stress which can controllably introduce fracture in scales, coatings and substrates, in order to investigate failure mechanisms.

Microscopic phenomena such as segregation were studied with analytical microscopy, as discussed in the last section. *In-situ* observation of macroscopic phenomena coupled with analytical microscopy of finer features could provide the more complete picture of the interaction between oxidation and stresses that occur in service and should be pursued in future studies.

KINETIC RUNS			As of: 5/4/98			Julia C. Duncan, Rm 13-4017, X3-6898
Samp #	Date	Time (hr)	Temp (°C)	Gases Used	Spall	TiAl@700.data, -800.data and TiAl@700.rawdata Description and comments
G (Ti-47.9at%Al; gamma); [hipped @1177°C for 2h & 15Ksi]						
G0705021	7/14/95	2.0	700	5%O2-N2	no	lt blue, non-uniform
*G07051XX1	7/31/95	100.0	700	5%O2-N2	no	goldish speckled film
G0705022	11/30/95	2.0	700	5%O2-N2	no	blue thin film, speckled
G07051XX2	11/30/95	100.0	700	5%O2-N2	no	goldish speckled film; dips, chart sticks ALOT!, faster rate @74hr
G0705A1XX1	2/22/96	100.0	700	5%O2-Ar	no	gold/pink film, dk grey speckles
G07001XX1	3/11/96	100.0	700	pure O2	no	gold/pink film, dk grey grains-similar to 5O%; WL 0-2h; 2 breakaways ?
G0700C01	4/1/96	2h X __	700	pure O2	no	3 cycles so far.....
*G0705A021	4/3/96	2.0	700	5%O2-Ar	no	data looks funny, drops then gains, even though purged!!!
**G0705A022	4/4/96	2.0	700	5%O2-Ar	no	data looks great - but WG far larger than Mettlr or expected!! ; 97 M/A looks odd
*G0705A023	4/9/96	2.0	700	5%O2-Ar	no	repolish.....
G0720N1XX1	10/28/96	100.0	700	20%O2-N2	no	yellow/pink trans scale - CUT for X-TEM
G07001XX2	3/26/97	103.0	700	pure O2	no	uniform ox, mostly dull grey with sm patches/grains pinkish-translucent
G0720A1XX1	4/18/97	100.0	700	Ar-20%O2	no	splotchy darker areas, mostly transluc, yello-pink; chart stops 92-98h
G0720N1XX2	4/23/97	100.0	700	N2-20%O2	no	pink/rusty, translucent and thin scale, uniform
G0720N201	1/21/97	20.0	700	20%O2-N2	no	data good but has several dips towards end...
*G0720N202	1/22/97	20.0	700	20%O2-N2	no	* wasn't destaticized and later had jump of its own??!!
G0720N203-2	2/17/97	20.0	700	20%O2-N2	no	flow stops...
G0720N204	2/19/97	20.0	700	20%O2-N2	no	thin,blue-green scale, iffy data since not hung perpendicular to quartz beam
G0720N205	2/25/97	20.0	700	20%O2-N2	no	1st perpen w/ air
G0720N206	2/28/97	20.0	700	20%O2-N2	no	thin, translucent, not spots; Beautiful curve!!
G0720N207	3/2/97	20.0	700	20%O2-N2	no	thin, non-blotchy green/blue scale
?G07XX201	1/29/97	20.0	700	pure O2	no	2 parts, para and then breakaway??; Not flooded to clear room air!!
G07XX202	2/22/97	20.0	700	pure O2	?	spall? -small dark spots on one side
G07XX203	2/23/97	20.0	700	pure O2	no	thin w/ some darker, "rusty" spots
?G0720A201	3/5/97	20.0	700	Ar-20%O2	no	WL during 1st 4 hr; jump near end
?G0720A202	3/8/97	20.0	700	Ar-20%O2	no	WL first 5 hr...
?G0720A203	3/9/97	20.0	700	Ar-20%O2	no	gas flow slows down during the run; forgot to weigh before removed hook!
G0720A204	4/1/97	20.0	700	Ar-20%O2	no	yellow/rusty spotty, thin scale; flow is stopped at end??
G0720A205	4/8/97	20.0	700	Ar-20%O2	no	thin, rusty splotches
G0820A201	3/10/97	20.0	800	Ar-20%O2	?	patchy cloudy & grey scale (rutile?); purple/pink underneath

Julia C. Duncan, Rm 13-4017, X3-6898

Samp #	Date	Time (hr)	Temp (°C)	Gases Used	Spall	Description and comments
A2 (Ti-25at%Al; alpha 2) cast as finger ingot						
A20705021	7/15/95	2.0	700	5%O2-N2	no	brn/blue tarnish AREA incorrectly!!!
A207051XX1	8/9/95	100.0	700	5%O2-N2	no	visibly thicker than G or SA2; grey-white opaque scale
A20705A1XX1	3/1/96	100.0	700	5%O2-Ar	no	grey-white opaque scale
A20720N1XX1	11/2/96	100.0	700	20%O2-N2	no	mottled grey with perhaps spallation at edges
A207OO1XX1	3/10/97	100.0	700	pure O2	yes	white greyish opaque scale with sm area of spall?
A207OO1XX2	4/27/97	100.0	700	pure O2	sm?	wh-grey scale w/sm small on edges and one side; not UHP to compare kps
A20720A1XX1	5/2/97	100.0	700	Ar-20%O2		?%O2 where SA2-A2 switch....
A20720N021		2.0	700	20%O2-N2	no	sample reused for A20720N203
A20720N022		2.0	700	20%O2-N2	no	sample is where??
A20720N023		2.0	700	20%O2-N2	no	repolished A20720N021, corner broke during drilling;
*A20720N201	1/10/97	20.0	700	20%O2-N2	no	sample TOO SMALL!!, jumps and dips in curve complicate things!!
A20720N202	1/23/97	20.0	700	20%O2-N2	no	NON-UNIFORM - half AWAY from the balance is thicker in scale.... rest is yellow
A20720N203	2/16/97	20.0	700	20%O2-N2	no	Flow stops; data looks jumpy....
A20720N204	2/18/97	20.0	700	20%O2-N2	no	rusty, non-uniform with gradient of transl to opacity; question sample/data
A20720N205	2/26/97	20.0	700	20%O2-N2	no	translucent, grey/iridescent; perpen; area scan is goofy
*A207XX201	1/31/97	20.0	700	pure O2	no	mostly uniform, one side closest to furnace was darker
A207XX202	2/10/97	20.0	700	pure O2	no	uniform, perhaps thin dark area near balance side
A207XX203	2/12/97	20.0	700	pure O2	no	repolish #1 of same params; looks blotchy, LOW WG!!
A207XX204	2/15/97	20.0	700	pure O2	no	mostly uniform except for sliver nearest balance; grey murky scale
A207XX205	2/20/97	20.0	700	pure O2	no	hung perpendicular: looks uniform
A207XX206	2/21/97	20.0	700	pure O2	no	hung perpendic: looks uniform-opaque grey/whitish scale
A20720A201	3/4/97	20.0	700	Ar-20%O2	no	uniform grey/blk; beautiful curve...
A20720A202	3/7/97	20.0	700	Ar-20%O2	no	hook not in notch on quartz beam
A20720A203	3/19/97	20.0	700	Ar-20%O2	no	mostly thin translucent, irid scale, with dker "rusty" spots
A20820A201	3/12/97	20.0	800	Ar-20%O2	yes	white spall with dk grey substrate? underneath

Samp #	Date	Time (hr)	Temp (°C)	Gases Used	Spall	Julia C. Duncan, Rm 13-4017, X3-6898 Description and comments
SA2 (Ti-25at%Al-23.5Nb; "super" alpha 2)				**As forged**		
SA20705021	7/15/95	2.0	700	5%O2-N2	no	bl film, some streaks
SA207051XX1	9/11/95	100.0	700	5%O2-N2	no	speckled green/purple
*SA20705A1XX1	12/7/95	100.0	700	5%O2-Ar	no	grey metallic, striped; M/As don't match!! Kp is similar to samp#2
SA20705A1XX2	2/16/96	100.0	700	5%O2-Ar	no	striped along the grain texture, thin scale
SA20705A021	4/2/96	2.0	700	5%O2-Ar	no	
SA20720N1XX1	10/22/96	100.0	700	20%O2-N2	no	v thin tarnish; yellow w/ pink streaks along grains
SA207001XX1	3/6/97	100.0	700	pure O2	no	thin iridescent sacle; Cahn-long hiatus - glass repair-1st day good...; UHP O2!
SA207NN1XX2	3/31/97	100.0	700	pure N2	no	now in CAHN, with larger sample; seeSA207NN1XX1 below
SA20705A1XX3	4/4/97	100.0	700	Ar-5%O2	no	thin,translucent, iridescent (rainbow) w/pink/green grains
SA20720A1XX1	4/9/97	100.0	700	Ar-20%O2	no	thin, grey scale with grains still visible
SA207001XX2	4/13/97	100.0	700	pure O2	no	med grey, uniform w/ vis grains, not iridescent. UHP@begin, std O2 till end
SA20720N201	1/15/97	1.5	700	20%O2-N2	no	blue tarnish; thin edge eroding away; data LOST!!
SA20720N202	1/17/97	20.0	700	20%O2-N2	no	yellow blue tarnish, perhaps variations on leading edge
SA20720N203	1/20/97	20.0	700	20%O2-N2	no	yell/green to bluish gradient, translucent scale; NOT perpendicular
SA20720N204	2/27/97	20.0	700	20%O2-N2	no	thin, bluish scale; noisy data, sample touches glass tube...
?SA207XX201	1/25/97	20.0	700	pure O2	no	looks uniform, grey ; wide sample may have been non-uniform (not to eye)
SA207XX202	2/7/97	20.0	700	pure O2	no	very thin grey uniform scale!!
SA207XX203	2/13/97	20.0	700	pure O2	no	very thin grey uniform scale!!
SA207XX204	2/24/97	20.0	700	pure O2	no	very thin grey uniform scale!!, not quite matte finish
SA20720A201	3/3/97	20.0	700	20%O2-Ar	no	thin grey sheen
?SA20720A202	3/6/97	20.0	700	20%O2-Ar	no	NP:loses wt first, then low WG??; recovers.....
SA20720A203	3/20/97	20.0	700	20%O2-Ar	no	dull, thin grey sheen
SA20820A201	3/13/97	20.0	800	Ar-20%O2	no	dull, no iridescence, grey matte finish
SA207NN1XX1	3/24/97	100.0	700	pure N2	no	thin, bl/green scale; grade N2??; WG so small in 20 hr that ran till 100hr....

Misc materials

Samp #	Date	Time (hr)	Temp (°C)	Gases Used	Spall	Description and comments
Nb07NN201	4/9/97	20.0	700	pure N2	YES	thin white rim, still grey in center (already spalled?); disk full, lost end data

Notes:
* - iffy data
Bold&BIG is for current sample
? - confusing data
bold is for unanalyzed data
samples below dotted line run on the DuPont
italic is for unanalyzed questionable data
BA: breakaway

Julia C. Duncan, Rm 13-4017, X3-6898					Computer K(p)	P for parabolic rates	Mettler	Mettler	Total	Mettler	Cahn
	Area	Computer			(linear g/cm2 s)	(para g2/cm4 s)	Wt In	Wt Out	Wt Gain	M/A	M/A
Samp#	(cm2)	Slope	R^2		Rate Const	**Comments**	(mg)	(mg)	(mg)	**mg/cm2**	
G0705021	4.848	2.19E-02	.991	P	1.33E-13		843.45	843.63	0.18	0.037	0.040
*G07051XX1	4.897	8.39E-03	.983		1.95E-14	noisy, big discrep in M/As	872.82	872.95	0.13	0.027	0.078
G0705022	4.821	6.57E-03	.993	P	1.20E-14	dips after 12 mins	834.08	834.13	0.05	0.010	0.010
G07051XX2	4.826	3.21E-03	.982	P	2.86E-15	kp for 74-100h=1.6E-14, r=.998	861.90	862.07	0.17	0.035	0.034
G0705A1XX1	4.554	9.05E-03	.994	P	2.28E-14	dipped; lost 23 hr	542.91	543.29	0.38	0.083	0.091
G07001XX1	5.376	0.00445	989-9612	P?	5.50E-15	last 10 hr-kp=7E-13, loss at beg	1214.96	1215.21	0.25	0.047	0.049
G0700C01	5.231	0.02818	.998	P	2.21E-13	thick slice;Great initial data!!	1252.97	--	cyclic	- -	0.039
*G0705A021	4.439	***data not great***				thin,down, then up.....	468.6	468.68	0.08	0.018	
**G0705A022	4.365	***data not great***				thin,Great WRONG data	504.00	504.03	0.03	0.007	
*G0705A023	4.268	***data not great***				repeat above	482.81	482.88	0.07	0.016	
G0720N1XX1	4.227	0.00033	.649	P	~6E-15	data-iffy; kp from Mettler M/A	554.22	554.42	0.20	0.047	0.059
G07001XX2	5.410	0.00284	.998	2P	2.24E-15	2-16h; kp=2.6E-14 for 16-100 hr	1351.37	1351.85	0.48	0.089	0.094
G0720A1XX1	4.784	0.00649	.978	P	1.17E-14	all pts; some wavy-ness	660.57	660.87	0.30	0.063	0.065
G0720N1XX2	4.860	0.00516	.888	P	7.38E-15	all pts, though fit is bad	857.07	857.25	0.18	0.037	0.046
G0720N201	3.655	0.00573	.974	P	9.12E-15	I=.035575;12 drooping pts	275.56	275.65	0.09	0.025	0.026
*G0720N202	4.637	0.00316	.960	P*	2.77E-15	I=.052658;dropped MANY pts	488.52	488.63	0.11	0.024	0.014
*G0720N203-2	3.077						347.46	347.51	0.05	0.016	.06+
G0720N204											
G0720N205	1.849	2986/.02	954/988		4.7E-16(1st 10hr)	1.6E-13 (11-20h)	214.78	214.83	0.05	0.027	0.045
G0720N206	2.149	0.01233	.986	P	4.22E-14		473.07	473.13	0.06	0.028	0.053
G0720N207										#####	
?G07XX201	4.248	0.00201	.948	P,BA	1.12E-15	breakaway? from 13 hr onward	341.66	341.80	0.14	0.033	0.016
G07XX202	2.237	0.01347	.985	P	5.04E-14	1st hr+4hr blip	498.59	498.64	0.05	0.022	0.060
G07XX203	1.833	0.00548	.991	P	8.34E-15	-2hr + drop @end	387.36	387.40	0.04	0.022	0.024
?G0720A201	1.753	from M/A	.940	P	1.90E-14	5-19 hr;kp=1E-16; LOW for M/A	261.48	261.54	0.06	0.034	0.034
?G0720A202	2.114	0.00171	.995	P	8.10E-16	4-9hr; kp=5E-14 for 10-21h	457.53	457.57	0.04	0.019	0.023
?G0720A203	2.104	0.00337	.988	P	3.16E-15	0.7-15h noise@end & flow stopped?	403.65	403.66	0.01	*0.005*	0.015
G0720A204	1.848	0.00276	.991	P	2.11E-15	avg slope&R(2-5h & 14-20hr); flow?	346.98	347.05	0.07	0.038	0.012
G0720A205	1.990	0.00953	.993	P	2.52E-14	2.5-20hr; omit 7&8hr pts	328.11	328.13	0.02	0.010	.027?
G0820A201	1.906	0.04777	.993	P	6.34E-13	all pts	412.13	412.48	0.35	0.184	0.220

Julia C. Duncan, Rm 13-4017, X3-6898					Computer K(p) P for parabolic rates					
	Area	Computer			(linear g/cm2 s) (para g2/cm4 s)	Mettler	Mettler	Total	Mettler	Cahn
						Wt In	Wt Out	Wt Gain	M/A	M/A
Samp#	(cm2)	Slope	R^2		Rate Const **Comments**	(mg)	(mg)	(mg)	mg/cm2	ng/cm2
A20705021	7.640	0.01440	.994	P	5.76E-14 data ok - probably	1093.31	1093.62	0.31	0.041	0.039
A207051XX1	7.940	0.03698	.974	P	3.80E-13 because there are	1240.92	1244.08	3.16	0.398	0.362
A20705A1XX1	7.390	0.04307	.993	P	5.15E-13 larger wt gains	899.63	903.18	3.55	0.480	0.450
A20720N1XX1	4.215	0.03758	.994	P	3.92E-13	828.37	830.01	1.64	0.389	0.392
A207OO1XX1	7.422	0.07194	.995	P	1.44E-12	937.73	943.25	5.52	0.744	0.697
A207OO1XX2	8.500	0.06861	.997	P	1.31E-12 :-)	1735.15	1741.48	6.33	0.745	0.708
A20720A1XX1	7.270	0.04666	.999	P	6.05E-13	1643.70	1647.49	3.79	0.521	0.47
A20720N021								0.21		
A20720N022										
A20720N023										
*A20720N201	0.687	0.04630	.988	P	5.96E-13 1st 1 hr (jumpy): SMALL sample	60.44	60.50	0.06	0.087	0.108
A20720N202	3.220	0.02053	.982	P	1.17E-13	393.50	393.87	0.37	0.115	0.103
A20720N203	1.069	0.01400	.984	P	5.44E-14 0.60685;6-15h droop	156.36	156.47	0.11	0.103	0.068
A20720N204										
A20720N205	1.764	0.01741	.998	P	8.42E-14 couple blips discarded	395.75	395.85	0.10	0.057	0.075
*A207XX201	1.570	0.02443	.995	P	1.66E-13 0.08501;1st 3 pts dropped	318.46	318.56	0.10	0.064	0.109
A207XX202	1.590	0.05658	.997	P	8.89E-13 (1.9E-13:2hr) 2-20 hr (1st 2 ??)	204.19	204.55	0.36	0.226	0.221
A207XX203										
A207XX204										
A207XX205	1.095	0.05320	.999	P	7.86E-13	128.24	128.50	0.26	0.237	0.238
A207XX206	1.474	0.05586	.997	P	8.67E-13	378.00	378.41	0.41	0.278	0.225
A20720A201	1.810	0.04234	1.000	P	4.98E-13 ALL PTS-great data!; M/A high.!!??	340.58	340.93	0.35	0.193	0.190
A20720A202	1.959	0.02920	.997	P	2.37E-13 1st 3 pts & 14-15hr dip	304.13	304.36	0.23	0.117	0.131
A20720A203	2.289	0.02794	.979	P	2.17E-13 all pts (1st hr fast)	415.82	415.98	0.16	0.070	0.121
A20820A201	1.958	0.22639	.988	P	1.42E-11 avg of 2? par regions (0-2h)	336.13	338.06	1.93	0.986	0.992

Samp#	Area (cm2)	Computer Slope	R^2		(linear g/cm2 s)(para g2/cm4 s) Rate Const	**Comments**	Wt In (mg)	Wt Out (mg)	Wt Gain (mg)	M/A mg/cm2	M/A ng/cm2
SA20705021	8.990	0.01310	.994	P	4.77E-14		2196.08	2196.44	0.36	0.040	0.036
SA207051XX1	4.370	0.01304	.998	P	4.72E-14	dips right away; chain?	826.65	827.38	0.73	0.167	0.131
*SA20705A1XX1	4.100	0.02493	984 3-5	P	1.73E-13	2.27-13/5.7-14, init?; stops 2X	972.18	972.92	0.74	0.180	0.249
SA20705A1XX2	5.080	0.02608	.997	P	1.89E-13	dips after 12 mins; stops 1X	992.97	993.90	0.93	0.183	0.194
SA20705A021	3.915	0.03740	.978	P	3.89E-13		703.57	703.98	0.41	0.105	0.085
SA20720N1XX1	5.185	0.01625	.993	P	7.33E-14	0.047443;2-68h; good; sm WL	601.81	602.71	0.90	0.174	0.162
SA207001XX1	9.197	0.01931	.998	P	1.04E-13	all pts!!	1976.27	1978.17	1.90	0.207	0.189
SA207NN1XX2	8.845	0.0124	.995	P	4.27E-14	all pts!!	1593.73	1594.92	1.19	0.135	0.143
SA20705A1XX3	6.413	0.02859	.989	P	2.27E-13	all pts, some jumps	1403.14	1404.79	1.65	0.257	0.297
SA20720A1XX1	5.686	0.03466	.999	P	3.34E-13	all pts,even with chart time miscals	2068.58	2070.65	2.07	0.364	0.358
SA207001XX2	4.234	0.0835	.99?	P	1.94E-12	avg 0-28 + 60-100, gas ran out mid	1468.41	1471.95	3.54	0.836	0.835
SA20720N201	3.55	data lost - but probl not uniform because not perpen hung					263.85	263.98	0.13	0.037	
SA20720N202	3.239	0.01328	.996	P	4.90E-14		222.60	222.79	0.19	0.059	0.060
SA20720N203	3.308	0.01199	.997	P	3.99E-14		305.60	305.78	0.18	0.054	0.057
SA20720N204	2.825	0.01022	.984	P	2.90E-14		459.76	459.96	0.20	0.071	0.067
?SA207XX201	3.978	0.09309	.998	P	2.41E-12		387.24	388.82	1.58	0.397	0.413
SA207XX202	1.4	0.07453	.997	P	1.54E-12	(5.1E-13:2h) 1st hr not used (equip?)	112.84	113.24	0.40	0.285	0.332
SA207XX203	2.31	0.08155	.997	P	1.85E-12	3.5E-13:2h 1st 2 hr sep parab	470.24	470.85	0.61	0.264	0.321
SA207XX204	1.72	0.07044	.996	P	1.38E-12		331.93	332.49	0.56	0.326	0.326
SA20720A201	2.4	0.04658	.999	P	6.03E-13	ALL PTS-great data!	561.67	562.15	0.48	0.200	0.206
?SA20720A202	2.21	0.03902	.995	P	4.23E-13	good fit; despite WL; M/A low!!	474.65	475.10	0.45	0.204	0.171
SA20720A203	2.49	0.05156	.999	P	7.38E-13	drop 1st 3 pts	592.57	593.10	0.53	0.213	0.221
SA20820A201	2.21	0.1217	.997	P	4.11E-12	all pts	400.22	401.35	1.13	0.512	0.528
SA207NN1XX1	2.01	0.01059	.993	2P?	3.12E-14	42-82h;	414.22	414.35	0.13	0.065	0.073

Julia C. Duncan, Rm 13-4017, X3-6898

Samp#	Area (cm2)	Computer Slope	R^2		Computer K(p) (linear g/cm2 s)(para g2/cm4 s) Rate Const	**Comments**	Mettler Wt In (mg)	Mettler Wt Out (mg)	Total Wt Gain (mg)	Mettler M/A mg/cm2	Cahn M/A ng/cm2
Nb07NN201	2.84	0.557	.998	L	1.55E-07	Linear 0-11.6 hr;	576.96	599.39	*22.43*	7.895	11.14

GN (Ti-48at%Al-2Cr-2Nb; gamma + Nb); [hipped @1177°C for 2h & 15Ksi]

Samp#	Time (hr)	Est Scale (μm) Mettler	ESEM/SEM Morphology	SEM Cross Section	Julia C. Duncan, Rm 13-4017, X3-6898 GAXRD (or WAXS)	TEM	CHARACTERIZATION (Date, Results) STEM
G0705021	2	0.21			4/29/96; Z00605		
*G07051XX1	100	0.15	X - 6/6&8/96	X-6/96	4/26/96; Z00598		Vick: x-section Sum 96
G0705022	2	0.06					
G07051XX2	100	0.20					
G0705A1XX1	100	0.47	E 6/6/96		4/26/96; Z00575		
G07001XX1	100	0.26	5/7/98		4/29/1996; Z00604		
G0700C01	2h X __						
*G0705A021	2	0.10			4/29/1996; Z00607		
**G0705A022	2	0.04					
*G0705A023	2	0.09					
G0720N1XX1	100	0.26	5/20/98			x-section 2/97,Ni islands	T1- 4/22/98 -dpld thru-Ni absorbs signal
G07001XX2	103	0.50	5/20/98				
G0720A1XX1	100	0.35	5/6/98		7/15/97; RZ02569		
G0720N1XX2	100	0.21			7/15/97; RZ02570	TEM sandwich - details??	
G0720N201	20	0.14					
*G0720N202	20	0.13					
*G0720N203-2	20	0.09					
G0720N204	20		5/6/98				
G0720N205	20	0.15					
G0720N206	20	0.16			4/17/97;RZ02171		
G0720N207	20	####	5/6/98				
?G07XX201	20	0.18					
G07XX202	20	0.13					
G07XX203	20	0.12	5/3/98		4/17/97;RZ02172		
?G0720A201	20	0.19					
?G0720A202	20	0.11					
?G0720A203	20	0.03					
G0720A204	20	0.21					
G0720A205	20	0.06	5/20/98		4/17/97; RZ02173		
G0820A201	20	1.03	9/3/97		7/15/97; RZ02561		

Samp#	Time (hr)	Scale (μm)	ESEM/SEM Morphology	SEM Cross Section	Julia C. Duncan, Rm 13-4017, X3-6898 GAXRD (or WAXS)	TEM	STEM	CHARACTERIZATION (Date, Results)
A20705021	2	0.23			4/29/1996; Z00606			
A207051XX1	100	2.23	E-6&9/96; 6/97	X-6/96	4/26/96; Z00597 * marked SA2 on X-ray file			
A20705A1XX1	100	2.69			4/26/96; Z00574	both sides Au/Ni -XTEM	T1 4/14/98, bloody mess - TOSS	
A20720N1XX1	100	2.18	5/3/98		7/15/97; RZ02564			
A207OO1XX1	100	4.16	E-9/29/97		7/15/97; RZ02568			
A207OO1XX2	100	4.17						
A20720A1XX1	100	2.92	5/3/98		7/15/97; RZ02566			
A20720N021	2							
A20720N022	2							
A20720N023	2							
*A20720N201	20	0.49						
A20720N202	20	0.64						
A20720N203	20	0.58			4/17/97;RZ02175			
A20720N204	20							
A20720N205	20	0.32	E-10/29/97	map?	4/17/97;RZ02170			
*A207XX201	20	0.36						
A207XX202	20	1.27						
A207XX203	20							
A207XX204	20							
A207XX205	20	1.33						
A207XX206	20	1.56	E-6/25/1997	E-6/29/1997	4/17/97; RZ02174			
A20720A201	20	1.08						
A20720A202	20	0.66						
A20720A203	20	0.39	5/3/98					
A20820A201	20	5.52	E:9/3/97,10/29/97		5/11&7/15/97.RZ02558			

Samp#	Time (hr)	Scale (μm)	ESEM/SEM Morphology	SEM Cross Section	GAXRD (or WAXS)	Julia C. Duncan, Rm 13-4017, X3-6898 TEM	STEM
SA20705021	2	0.22	2/9/98		4/29/96; Z00609; RZ02599		
SA207051XX1	100	0.94	E-9/96;10/97;2/98X	6/29/96-FEG	5/14/97; Z02382	NP:THE map - T? 12/96 T2-4/22 - substrate; T3-contamin	
*SA20705A1XX1	100	1.01	6/25/97;9/96-E		4/26/96; Z00596		
SA20705A1XX2	100	1.03			7/15/97; RZ02563	cut/Au+Ni plate-peel 3/ T1 4/14/98; to thick, remill, nonplanar	
SA20705A021	2	0.59			4/29/96; Z00608; again RZ02598		
SA20720N1XX1	100	0.97	5/3/1998 LOTS	??- cut for it	7/15/97; RZ02565		
SA207001XX1	100	1.16					
SA207NN1XX2	100	0.75	E:2/9/98		7/17/97;RZ02600		
SA20705A1XX3	100	1.44			4/17/97;RZ02168		
SA20720A1XX1	100	2.04	5/6/98		4/17/97;RZ02169		
SA207001XX2	100	4.68	E-9/29/97 & 2/9/98		7/17/97;RZ02597		
SA20720N201	1.5	0.21					
SA20720N202	20	0.33					
SA20720N203	20	0.30					
SA20720N204	20	0.40	5/6/98		4/17/97;RZ02167		
?SA207XX201	20	2.22					
SA207XX202	20	1.60					
SA207XX203	20	1.48	5/6/98		4/17/97;RZ02158-61		
SA207XX204	20	1.83				6/97 - normal prep, no coating T3 - 4/14/98 so-so images	
SA20720A201	20	1.12					
?SA20720A202	20	1.14					
SA20720A203	20	1.19	5/7/98		4/17/97;RZ02166		
SA20820A201	20	2.87	E:9/3/97		5.11&7.15.97;RZ02559		
SA207NN1XX1	100	0.36	E: 2/8&9?/98		4/17/97;RZ02162-65		

Samp#	Time (hr)	Est scale Scale (μm)	ESEM/SEM Morphology	SEM Cross Section	GAXRD (or WAXS)	CHARACTERIZATION (Date, Results) TEM	STEM
Nb07NN201	20	____	E:2/9/98		7/17/97;RZ02___		
Gamma substrate						OM	
A2 substrate						OM	
SA2 substrate						OM	

Appendix B - Thickness Calculations for Mixed Composition Corrosion Scales in Ti-Al-Nb-O-N System

Alumina (Al_2O_3):

WG in mg/ square cm	MW	moles		density of alumina		
mg	1 g	1 mole oxygen	1 mole Al_2O_3	101.96 g	cm3	10000 microns
cm^2	1000 mg	16 g oxygen	3 moles oxygen	1 mole Al_2O_3	3.97 g	1cm

1mg WG/area= 5.35055 microns

Rutile (TiO_2):

WG in mg/ square cm	MW	moles		density of rutile		
mg	1 g	1 mole oxygen	1 mole TiO_2	79.88 g	cm3	10000 microns
cm^2	1000 mg	16 g oxygen	2 moles oxygen	1 mole TiO_2	4.26	1cm

1mg WG/area= 5.85974 microns

Appendix C - X-Ray Diffraction Peaks and Intensities for Phases grown in the Ti-Al-Nb-O-N System

Table C.1 α-Al_2O_3 peak positions from PDF card #42-1468

Field Intensity (%)	h k l	2θ Value (°)	Notes
100	**1 1 3**	**43.363**	
97	1 0 4	35.151	
82	1 1 6	57.504	
70	0 1 2	25.577	
45	3 0 0	68.209	
42	1 1 0	37.785	
42	0 2 4	52.559	
30	2 1 4	66.522	
16	4 1 6	136.101	outside of the range scanned in the study
13	1 0 10	76.882	outside of the range scanned in the study

bold - Primary peak used for phase identification

Table C.2 α-TiO_2 peak positions from PDF card #21-1276

Field Intensity (%)	h k l	2θ Value (°)	Notes
100	**1 1 0**	**27.447**	
60	2 1 1	54.323	
50	1 0 1	36.086	
25	1 1 1	41.226	
20	3 0 1	69.010	
20	2 2 0	56.642	
12	5 2 1	140.052	outside of the range scanned in the study
12	1 1 2	69.790	
10	3 1 0	64.040	
10	2 1 0	44.052	
10	0 0 2	56.642	

bold - Primary peak used for phase identification

Table C.3 Al_2TiO_5 peak positions from PDF card #41-258

Field Intensity (%)	h k l	2θ Value (°)	Notes
100	**1 0 1**	**26.524**	
68	**2 3 0**	**33.725**	
66	2 0 0	18.801	outside of the range scanned in study
31	4 3 0	47.774	
29	2 2 0	26.399	
27	0 0 2	50.796	
19	2 4 0	42.048	
19	5 3 1	62.588	
18	4 2 0	42.629	
18	3 4 1	54.272	
17	2 3 2	62.348	
15	0 2 0	18.394	outside of the range scanned in study
15	3 3 1	47.668	

bold - Primary peaks used for phase identification

Table C.4 Nb_2O_5 peak positions from PDF card #27-1003

Field Intensity (%)	h k l	2θ Value (°)	Notes
100	**1 8 0**	**28.309**	
90	**0 0 1**	**22.607**	
50	1 8 1	36.496	
45	2 0 0	22.607	
25	3 8 0	50.886	
25	0 0 2	46.060	
25	1 8 2	54.972	
20	2 0 1	36.994	
20	2 0 2	55.332	
20	1 17 0	55.296	

bold - Primary peaks used for phase identification

Table C.5 $AlNbO_4$ peak positions from PDF card #41-347

Field Intensity (%)	h k l	2θ Value (°)	Notes
100	**1 1 0**	**25.030**	
65	0 0 2	28.850	
38	2 0 -1	17.500	
35	3 1 -1	33.440	
30	2 0 1	24.000	
29	4 0 -1	29.810	
24	-7 1 1	58.610	
23	4 0 0	30.830	
22	0 0 1	14.300	outside of the range scanned in the study
22	4 2 -1	58.190	
22	0 2 0	48.720	

bold - Primary peak used for phase identification

Table C.6 $Al_{27}O_{39}N$ peak positions from PDF card #26-33

Field Intensity (%)	h k l	2θ Value (°)	Notes
100	**-2 2 0**	**37.490**	
100	**3 2 1**	**45.571**	
100	**3 0 4**	**46.459**	
100	**-6 0 5**	**66.441**	
100	**-3 1 8**	**66.763**	
100	**-3 3 5**	**67.632**	
80	-3 0 3	33.627	
80	-5 2 0	60.502	
80	0 0 5	37.801	
80	0 2 3	39.170	

bold - Primary peaks used for phase identification

Table C.7 $CaCO_3$ peak positions from PDF card #5-586

Field Intensity (%)	**h k l**	**2θ Value** (°)	**Notes**
100	**1 0 4**	**29.406**	
18	1 1 3	39.402	
18	2 0 2	43.146	
17	0 1 8	47.490	
17	1 1 6	48.513	
14	1 1 0	31.418	

bold - Primary peak used for phase identification

Appendix D - X-Ray Energy Dispersive Spectroscopy Peaks

Table D.1 Characteristic energies in keV for elements found in this study from Goldstein et al (1981).

Element	Atomic Number	$K_{\alpha 1}$	$K_{\alpha 2}$	$K_{\beta 1}$	$K_{\beta 2}$	L_1	L_n	$L_{\alpha 1}$	$L_{\beta 1}$
N	7	0.392	0.392						
O	8	0.523	0.523						
Al	13	1.487	1.486	1.553					
Ti	22	4.510	4.504	4.931		0.395	0.401	0.452	0.458
Nb	41	16.614	16.520	18.621	18.951	1.902	1.996	2.166	2.257
Impurities									
Ta	73	57.524	56.270	65.210	66.999				
Cu	29	8.047	8.027	8.904	8.976				
Fe	26	6.403	6.390	7.057					
Si	14	1.740	1.739	1.832					

References

Ashley, S. (1991). "Titanium Aluminides: Tough Materials for Tomorrow's Engines." Mechanical Engineering (December 1991): 49-52.

Asta, M., A. Ormeci, J. M. Wills and R. C. Albers (1995). "First-Principles Study of Intermetallic Phase Stability in the Ternary Ti-Al-Nb Alloy System." Material Research Society Symposium Proceedings, **364**: 157-162.

Balsone, S. J. (1989). "The Effect of Elevated Temperature Exposure on the Tensile and Creep Properties of Ti-24Al-11Nb.", in *Oxidation of High-Temperature Intermetallics (Conf. Proc.)*, eds. T. Grobstein and J. Doychak, The Minerals, Metals & Materials Society, Warrendale, PA. p. 219-234.

Bannykh, O. G., E. N. Sheftel, G. S. Usmanova and A. A. Sharapov (1995). "Hot Oxidation Resistance of an Intermetallic Nb-Ti-Al Alloy." Materials Research Society Symposium Proceedings, **364**: 969-974.

Becker, S., A. Rahmel, M. Schorr and M. Schütze (1992). "Mechanism of Isothermal Oxidation of the Intermetallic TiAl and of TiAl Alloys." Oxidation of Metals **38**(5/6): 425-464.

Becker, S., M. Schuetze and A. Rahmel (1993). "Cyclic-Oxidation Behavior of TiAl and of TiAl Alloys." Oxidation of Metals **39**(1/2): 93-106.

Beddoes, J. C., W. Wallace and M.C. de Malherbe (1992). "The Technology of Titanium Aluminides for Aerospace Applications." Materials & Manufacturing Processes **7**(4): 527-559.

Bennett, M. J. (1992). "Real Time Studies of Scale Development and Failure." in *High Temperature Corrosion of Advance Materials and Protective Coatings (Conf. Proc.)*, eds. Y. Saito, B. Onay and T. Maruyama, Elsevier Science Publishers B.V., p. 51-60.

Berztiss, D. A., F. S. Pettit and G. H. Meier (1995). "Anomalous Oxidation of Intermetallics." Materials Research Society Symposium Proceedings **364**: 1285-1290.

Beye, R. W. and R. Gronsky (1994). "Novel Phases in the Oxidation of Gamma-Titanium Aluminum." Acta Metallurgica et Materialia **42**(4): 1373-1381.

Blank-Bewersdorff, M. and J. A. Peters (1994). "Effect of Different Atmospheres on the Microstructure of Super Alpha-2 Titanium Aluminide Foils." Scripta Metallurgica et Materialia **31**(7): 945-950.

Brady, M. P., R. J. Hanrahan Jr., S. P. Elder Randall and E. D. Verink Jr. (1993). "On the Transition to Protective Alumina Formation at High Temperature in Nb-Ti-Al Alloys." Scripta Metallurgica et Materialia **28**: 115-120.

Brady, M. P., J. L. Smialek and D. L. Humphrey (1995). "Microstructure /Oxidation/Microhardness Correlations in γ-Based and τ-based Al-Ti-Cr Alloys." Materials Research Society Symposium Proceedings, **364**: 1309-1314.

Brady, M. P., W. J. Brindley, J. L. Smialek and I. E. Locci (1996). "The Oxidation and Protection of Gamma Titanium Aluminides." Journal of Metals **48** (11): 46-50.

Brick, R. M., A. W. Pense and R. B. Gordon (1977). *Structure and Properties of Engineering Materials*, McGraw-Hill Publishing Company, New York.

Busso, E. P. and F. A. McClintock (1993). "Thermal Fatigue Degradation of An Overlay Coating." Materials Science & Engineering A, **A161**(2): 165-179.

Chaze, A. M., C. Coddet and G. Beranger (1982). "Influence de l'Aluminium sur la Tenue à l'Oxydation." Journal of the Less Common Metals **83**: 49-70.

Chen, G., Z. Sun and X. Zhou (1992). "Oxidation of Intermetallic Alloys in the Ti-Al-Nb Ternary System." Corrosion **48**(11): 939-946.

Chen, G., Z. Sun and X. Zhou (1992). "Oxidation and Mechanical Behavior of Intermetallic Alloys in the Ti-Nb-Al Ternary System." Materials Science and Engineering A **A153**: 597-601.

Chen, Z., F. Simca and M. T. Cope (1992). "Microstructure and Tensile Properties of Aged Superalpha 2 Intermetallic Compound." Materials Science and Technology **8**: 729-738.

Chinmulgund, M., R. B. Inturi and J. A. Barnard (1995). "Effect of Ar Gas Pressure on Growth, Structure, and Mechanical Properties of Sputtered Ti, Al, TiAl and Ti_3Al Films." Thin Solid Films **270**: 260-263.

Christodoulou, L. (1990). "Titanium Aluminides." in *Encyclopedia of Materials Science and Engineering Supplementary Vol. 2*, eds. R. W. Cahn and M. B. Bever, MIT Press, Cambridge, MA. p. 1347-1354.

Cockeram, B. V., H. J. Schmutzler, J. Shyue, K. Hoshino, S. Meng, R. Wheeler and H. L. Fraser (1995). The High-Temperature Oxidation of Nb-40Ti-15Al and the Effect of Cr Alloy and Silicide Diffusion Coatings. Materials Research Society Symposium Proceedings, **364**: 1327-1332.

Cullity, B. D. (1978) *Elements of X-Ray Diffraction*, Addison-Wesley, Reading, MA, pp. 139 & p. 523-4.

Cunnington, G. R., and J. C. Robinson and R. K. Clark (1991). Chemical Vapor Deposition Coatings for Oxidation Protection of Titanium Alloys. in *Damage and Oxidation Protection in High Temperature Composites (Proc. Conf.),* ASME, New York. Vol. 1, p. 1-8.

Dary, F.-C., and T. M. Pollock (1996). "Effects Of High Temperature Air and Vacuum Exposures on the Room Temperature Tensile Behavior of the (O+B2) Titanium Aluminide Ti-22Al-23Nb." Materials Science and Engineering A **A208**: 188-202.

Dettenwanger, F., E. Schumann, M. Rühle, J. Rakowski and G. H. Meier (1995). "The Effect of Nitrogen on the Oxidation of TiAl." Materials Research Society Symposium Proceedings, **364**: 981-986.

Dettenwanger, F., E. Schumann, J. Rakowski, G. H. Meier and M. Rühle (1996). "Investigation of the Oxidation of TiAl Using TEM." *Microscopy of Oxidation III*, The Institute of Materials, Cambridge, UK, p. 277-286.

Dowling, W. E. Jr., W. T. Donlon and J. E. Allison (1995). "Development of TiAl-Based Automotive Engine Valves." Materials Research Society Symposium Proceedings, **364**: 757-768.

Duncan, J. C., (1994) "Simultaneous Oxidation/Sulfidation of Cr-Nb Alloys", Massachusetts Institute of Technology S.M. Thesis.

Figge, U., W. J. Quadakkers, H. Schuster and F. Schubert (1992). "The Effect of Chromium, Niobium and Yttrium Additions on the Growth Phenomena of Oxide Scales on TiAl-Based Intermetallic Compounds." in *Proceedings 12th Scandinavian Corrosion Congress & Eurocorr '92, Espoo, Finland, 31 May - 4 June 1992*, ed. P. J. Tunturi, The Corrosion Society of Finland. p. 591-599.

Figge, U., A. Elschner, N. Zheng, H. Schuster and W. J. Quadakkers (1993). "Surface Analytical Investigation on the Oxidation Behaviour of TiAl-based Intermetallics." Fresenius Journal of Analytical Chemistry **346**: 75-78.

Froes, F. H., C. Suryanarayana and D. Eliezer (1992). "Review: Synthesis, Properties and Applications of Titanium Aluminides." Journal of Materials Science **27**: 5113-5140.

Gama, S. (1993) Aluminum-Niobium-Titanium System in *Ternary Alloys: A Compendium of Evaluated Constitutional Data and Phase Diagrams*, eds. G. Petzow and G. Effenberg, VCH Publishers, New York. Vol. 7, p. 382-398.

Gauer, L., S. Alperine, P. Steinmetz and A. Vassel (1994). "Influence of Niobium Additions of High Temperature Oxidation Behavior of Ti_3Al Alloys and Coatings." Oxidation of Metals **42**(1/2): 49-74.

George, E. P. and C. T. Liu (1995). "Review of Environmental Effects in Intermetallics." Materials Research Society Symposium Proceedings, **364**: 1131-1146.

Gil, A., H. Hoven, E. Wallura and W. J. Quadakkers (1993). "The Effect of Microstructure on the Oxidation Behaviour of TiAl-based Intermetallics." Corrosion Science **34**(4): 615-630.

Gil, A., B. Rajchel, W. J. Quadakkers and H. Nickel (1995). "The Influence of Implanted Chromium and Yttrium on the Oxidation Behaviour of TiAl-based Intermetallics." Journal of Materials Science **30**(22): 5793-5798.

Gill, S. C., J. A. Peters, P. Blatter, J. C. Jaquet and M. A. Morris (1996). "Production of Low Oxygen Contamination Orthorhombic Ti-Al-Nb Intermetallic Foil." Scripta Materialia **35**(2): 175-180.

Goldstein, J. I., D. E. Newbury, P. Echlin, D. C. Joy, C. E. Fiori and E. Lifshin (1981) "Scanning Electron Microscopy and X-Ray Microanalysis." Plenum Press, New York, NY.

Guilherme de Aragao, B. J., and F. Ebrahimi (1996). "High Temperature Deformation of Nb-Ti-Al Alloys with (sigma + gamma) $\sigma + \gamma$ Microstructure." Materials Science and Engineering A **A208**: 37-46.

Hebsur, M., J. R. Stephens, J. L. Smialek, C. A. Barrett and D. S. Fox (1989). "Influence of Alloying Elements on the Oxidation Behavior of $NbAl_3$." in *Oxidation of High-Temperature Intermetallics (Conf. Proc.)*, eds. T. Grobstein and J. Doychak, The Minerals, Metals & Materials Society, Warrendale, PA. p. 171-183.

Hennessey, T. P. and J. E. Morral (1992). "Oxidation and Nitridation of Niobium in Air Above 1150°C." Oxidation of Metals **38**(1/2): 163-187.

Hobbs. L. W. (1996), lecture notes for the course "Oxidation and Corrosion of Materials at High Temperature" at MIT, Boston, MA.

Holmes, J. W. and F. A. McClintock (1990). "The Chemical and Mechanical Processes of Thermal Fatigue Degradation of an Aluminide Coating." Metallurgical Transactions A **21A**: 1209-1222.

Inouye, H. (1960) in *Columbian Metallurgy*, eds. D. L. Douglass and F. W. Kunz, Interscience, New York.

Jackson, M. R., R. G. Rowe and D. W. Skelly (1995). "Oxidation of Some Intermetallic Compounds and Intermetallic Matrix Composites." Materials Research Society Symposium Proceedings, **364**: 1339-1346.

Kameda, J., C. R. Gold, E. S. Lee, T. E. Bloomer and M. Yamaguchi (1995). "Localized Oxidation Near Cracks and Lamellar Boundaries in a Gamma Titanium Aluminide Alloy." Materials Research Society Symposium Proceedings, **364**: 1297-1302.

Kekare, S. A. and P. B. Aswarth (1997). "Oxidation of TiAl-based Intermetallics." Journal of Materials Science **32**(9): 2485-2499.

Kim, Y.-W. (1989). "Intermetallic Alloys Based on Gamma Titanium Aluminide." Journal of Metals **41**(7): 24-30.

Kim, Y.-W. and F. B. Froes (1989). "Physical Metallurgy of Titanium Aluminides." in *High Temperature Aluminides and Intermetallics (Conf. Proc.)*, eds. S. H. Wang, C. T. Liu, D. P. Pope and J. D. Stiegler, The Minerals, Metals and Materials Society, Warrendale, PA. p. 465-492.

Kim, Y.-W. and D.M. Dimiduk (1991). "Progress in the Understanding of Gamma Titanium Aluminides." Journal of Metals **43**(8): 40-47.

Kim, Y.-W. (1994). "Ordered Intermetallic Alloys, Part III: Gamma Titanium Aluminides." Journal of Metals **46**(7): 30-39.

Kim, B. G., G. M. Kim and C. J. Kim (1995). "Oxidation Behavior of TiAl-X (X=Cr, V, Si, Mo or Nb) Intermetallics at Elevated Temperature." Scripta Metallurgia et Materialia **33**(7): 1117-1125.

Kim, Y.-W. (1995). "Conference Review: Gamma Titanium Aluminides." Journal of Metals **47**(7): 38 (single page).

Kim, Y.-W. (1995). "Overview: Gamma Titanium Aluminides: Their Status and Future." Journal of Metals **47**(7): 39-41.

P. Kofstad (1988) *High Temperature Corrosion*, Elsevier Applied Science, New York.

Koo, C. H., J. W. Evans, K. Y. Song and T. H. Yu (1994). "High-Temperature Oxidation of Ti3Al-Nb Alloys." Oxidation of Metals **42**(5/6): 529-544.

Kröger, F. A. and H. J. Vink (1956). "Relations Between the Concentrations of Imperfections in Crystalline Solids." in *Solid State Physics: Advances in Research and Applications*, eds. F Seitz and D Turnbull, Academic Press, New York. Vol. 3, p 307-435.

Kumari, S. V., P. M. Rogers and J. A. Little (1996). "Oxidation Characteristics of Ti-22.8%Al, 11.5%Nb Alloy." in *Microscopy of Oxidation III (Conf. Proc.)*, eds. S. B. Newcomb and J. A. Little, The Institute of Metals, London. p. 297-306.

LaBranche, M. H. (1985). "The Oxidation of Chromium at Low and High Oxygen Partial Pressures, (Part I). The Oxidation/Sulfidation of Chromium in H_2-H_20-H_2S Gas Mixtures, (Part II).", Massachusetts Institute of Technology Ph.D. Thesis.

Lang, C. and M. Schuetze (1996). "The Initial Stages in the Oxidation of TiAl." submitted to Materials and Corrosion.

Lang, C. and M. Schuetze (1996). "TEM Studies of the Mechanisms in the Early Stages of TiAl Oxidation." in *Microscopy of Oxidation III (Conf. Proc.)*, eds. S. B. Newcomb and J. A. Little, The Institute of Metals, London. p. 265-276.

Lang, C. and M. Schuetze (1996). "TEM Investigations of the Early Stages of TiAl Oxidation." Oxidation of Metals **46**(3/4): 255-285.

Lide chief editor (1991), CRC Handbook of Physics and Chemistry, CRC Press, Boston, MA.

Ma, J. C., J. E. Benci and T. P. Feist (1995). "Effects of Processing on the Mechanical Properties and Oxidation Behavior of Al_2Ti." Materials Research Society Symposium Proceedings, **364**: 1303-1308.

Majumdar, B. S., C. Boehlert, A. K. Rai and D. B. Miracle (1995). "Structure-Property Relationships and Deformation Mechanisms in an Orthorhombic Based Ti-25Al-17Nb Alloy." Materials Research Society Symposium Proceedings, **364**: 1259-1264.

Maki, K., M. Shioda, M. Sayashi, T. Shimizu and S. Isobe (1992). "Effect of Silicon and Niobium on Oxidation Resistance of TiAl Intermetallics." Materials Science and Engineering A **A153**: 591-596.

Massalski, T. B. (1990). *Binary Alloy Phase Diagrams* . ASM International, Materials Park, Ohio.

McCollough, C., J. J. Valencia, C. G. Levi and R. Mehrabian (1989). "Phase Equilibria and Solidification in Ti-Al Alloys." Acta Metallurgica, **37**: 1321-1336.

McKee, D. W. and S. C. Huang (1991). "Oxidation Behavior of Gamma-Titanium Aluminide Alloys." Materials Research Society Symposium, **213**: 939-943.

McKee, D. W. and S. C. Huang (1992). "The Oxidation Behavior of Gamma-Titanium Aluminide Alloys under Thermal Cycling Conditions." Corrosion Science **33**(12): 1899-1914.

Meier, G. H., D. Appalonia, R. A. Perkins and K. T. Chiang (1989). "Oxidation of Ti-Base Alloys." in *Oxidation of High-Temperature Intermetallics (Conf. Proc.)*, eds. T. Grobstein and J. Doychak, The Minerals, Metals & Materials Society, Warrendale, PA. p. 185-193.

Meier, G. H. and F. S. Pettit (1992). "The Oxidation Behavior of Intermetallic Compounds." Materials Science and Engineering A **A153**: 548-560.

Meier, G. H., N. F. Birks, F. S. Pettit, R. A. Perkins and H. J. Grabke (1993). "Environmental Behavior of Intermetallic Materials." in *First International Symposium on Structural Intermetallics (Conf. Proc.)*, eds. R. Darolia, J. J. Lewandowski, C. T. Liu, P. L. Martin, D. B. Miracle and M. V. Nathal, The Minerals, Metals & Materials Society, Warrendale, PA. p. 861-877.

Meier, G. H. (1994). *Oxidation of Intermetallic Compounds*. Seminar given at Max Planck Institut für Metallforschung, Stuttgart, Germany.

Moore, J. B. (1988). in *Application of Advanced Materials for Turbomachinery & Rocket Propulsion- Proceedings of Propulsion and Energetics Panel 72nd Specialists Meeting, Bath, UK*, NATO Advisory Group for Aerospace Research and Development, AGARD, Neuilly sur Seine, France. p. 1-1 to 1-5.

Mozer B., L. A. Bendersky, W. T. Boeltinger and R. G. Rowe (1990) "Neutron Powder Diffraction Study of the Orthorhombic Ti_2AlNb Phase." Scripta Metallurgica et Materialia **24**:(12) 2363-2368.

Muraleedharan, K., S. V. Nagender Naidu and D. Banerjee (1990). "Orthorhombic Distortions of the α_2 Phase in Ti_3Al-Nb Alloys: Artifacts and Facts." Scripta Metallurgica et Materialia **24**: 27-32.

Nakamura, H., M. Takeyama, Y. Yamabe, and M. Kikuchi (1993). "Phase Equilibria in TiAl Alloys containing 10 and 20 at.% Nb at 1473 K." Scripta Metallurgica et Materialia **28**: 997-1002.

Nickel, H., N. Zheng, A. Elschner and W. J. Quadakkers (1995). "The Oxidation Behaviour of Niobium Containing γ-TiAl Based Intermetallics in Air and Argon/Oxygen." Mikrochimica Acta **119**: 23-29.

Niu, Y., F. Gesmundo and F. Viani (1996) "The Corrosion of Pure Niobium in Oxidizing, Sulfidizing, and Oxidizing-Sulfidizing Gas Mixtures at 600-800°C." Oxidation of Metals **46** (13/4): 287-297.

Oishi, Y. and W. D. Kingery (1960). *"Oxygen Diffusion in Periclase Crystals."* Journal of Chemical Physics **33**: 905-906.

Perkins, R., K. T. Chiang, G. H. Meier and R. Miller (1989). "Formation of Alumina on Niobium and Titanium Base Alloys." in *Oxidation of High-Temperature Intermetallics (Conf. Proc.)*, eds. T. Grobstein and J. Doychak, The Minerals, Metals & Materials Society, Warrendale, PA. p. 157-169.

Perkins, R. A. and G. H. Meier (1990). "The Oxidation Behavior and Protection of Niobium." Journal of Metals **42**(August): 17-21.

Peters, M. and H. Buhl (1992). "Titanium Alloys and Aluminides." in *Advanced Aerospace Materials*, ed. H. Buhl, Springer-Verlag, New York. p. 58-83.

Pint, B. A. (1992). "The Effect of Reactive Elements on the Growth of Al_2O_3 Scales.", Massachusetts Institute of Technology Ph.D. Thesis.

Pope, D. P. and R. Darolia (1996). "High-Temperature Applications of Intermetallic Compounds." MRS Bulletin **21**(5): 30-36.

Popille, F. and J. Douin (1996). "Comparison of the Deformation Microstructures at Room Temperature in O and B2 Phases of a Ti_2AlNb Alloy." Journal De Physique IV, Colloque 2, suplement au Journal de Physique III 6(mars 1996): C2-211-216.

Proske, G., G. Luetjering, J. Albrecht, D. Helm and M. Daeubler (1992). "The Microstructure and Mechanical Properties of the Intermetallic Compound Super Alpha 2." Materials Science and Engineering A **A152**: 310-316.

Qiu, G., J. Wu, L. Zhang and D. (T. L.) Lin (1995). "Oxidation Behavior of Ti_3Al Alloyed with Niobium and Silicon." Scripta Metallurgia et Materialia **33**(2): 213-217.

Quadakkers, W. J., A. Elschner, N. Zheng and H. Nickel (1993). "SNMS Studies on the Oxidation Behaviour of Titanium Aluminides." Corrosion Control for Low-Cost Reliability, 12th International Corrosion Congress, Houston, Texas, NACE International.

Quadakkers, W. J., A. Elschner, N. Zheng, H. Schuster and H. Nickel (1993). "SNMS Investigations Concerning the Effect of Niobium Additions on the Oxidation Behaviour of Titanium Aluminides." Microscopy of Oxidation - 2, Selwyn College, University of Cambridge, UK, The Institute of Materials.

Rahmel, A., W. J. Quadakkers and M. Schuetze (1995). "Fundamentals of TiAl oxidation - A Critical Review." Materials and Corrosion **46**: 271-285.

Retallick, W. B., M. P. Brady and D. L. Humphrey (1997). "A Phosphoric Acid Surface Treatment for Improved Oxidation Resistance of Gamma Titanium Aluminides." short communication submitted to Intermetallics.

Roth, R. S. and L. W. Coughanour (1955). "Phase Equilibrium Relations in the Systems Titania-Niobia and Zirconia-Niobia." Journal of Research of the National Bureau of Standards **55**(4): 209-213.

Rowe, R. G. (. (1992). "Ti_2AlNb-based Alloys Outperform Conventional Titanium Aluminides." Advanced Materials and Processes **3**: 33-35.

Saffarian, H. M., Q. Gan, R. Hadkar and G. W. Warren (1996). "Corrosion Behavior of Binary Titanium-Aluminide Intermetallics." Corrosion Science **52**(8): 626-633.

Sawhill, H. T. (1985) "Study of the Ni/NiO Interface Region in High-Temperature Oxidation of Nickel." Massachusetts Institute of Technology Ph.D. Thesis.

Schaeffer, J. C. (1993). "Isothermal Oxidation Behavior of Alpha-2 Titanium Aluminide Alloys." Scripta Metallurgica et Materialia **28**: 91-796.

Shanabarger, M. R. (1992). "The Initial Oxidation of α_2 (Ti_3Al) and γ (TiAl) Titanium Aluminide Alloys." Materials Science and Engineering A **A153**: 608-612.

Shida, Y. and H. Anada (1993). "Oxidation Behavior of Binary Ti-Al Alloys in High Temperature Air Environment." Materials Transactions, JIM (Journal of the Japan Institute of Metals) **34**(3): 236-242.

Shida, Y. and H. Anada (1994). "Role of W, Mo, Nb and Si on Oxidation of TiAl in Air at High Temperatures." Materials Transactions, JIM (Journal of the Japan Institute of Metals) **35**(9): 623-631.

Shida, Y. and H. Anada (1996). "The Effect of Various Ternary Additives on the Oxidation Behavior of TiAl in High-Temperature Air." Oxidation of Metals **45**(1/2): 197-219.

Shimizu, T., T. Iikubo and S. Isobe (1992). "Cyclic Oxidation Resistance of an Intermetallic Compound TiAl." Materials Science and Engineering A **A153**: 602-607.

Sims, C. T. (1981). "A Perspective of Niobium in Superalloys." in *Niobium, Proceedings of the International Symposium.*, ed. H. Stuart, The Minerals, Metals & Materials Society, Warrendale, PA. p. 1169-1220.

Singh, P. N., B. K. Singh, C. Ramachandra and V. Singh (1996). "Room Temperature Low Cycle Fatigue Behaviour of Titanium Aluminide Ti-26.23Al-15.2Nb-0.4Mo." Scripta Metallurgica et Materialia **34**(11): 1791-1796.

Smialek, J. L. (1993). "Oxidation Behaviour of $TiAl_3$ Coatings and Alloys." Corrosion Science **35**(5-8): 1199-1208.

Smialek, J. L., J. A. Nesbitt, W. J. Brindley, M. P. Brady, J. Doychak, R. M. Dickerson and D. R. Hull (1995). "Service Limitations for Oxidation Resistant Intermetallic Compounds." Materials Research Society Symposium Proceedings, **364**: 1273-1284.

Stiegler, J. O. and C. T. Liu (1988). "Aluminides for Structural Use." in *Encyclopedia of Materials Science and Engineering Supplementary Vol. 3*, eds. R. W. Cahn and M. B. Bever, MIT Press, Cambridge, MA. p. 3-9.

Stroosnijder, M. F., N. Zheng, W. J. Quadakkers, R. Hofman, A. Gil, and F. Lanza (1996). "The Effect of Niobium Ion Implantation on the Oxidation Behaviour of a γ-TiAl- Based Intermetallic." Oxidation of Metals **46**(1/2): 19-35.

Sunderkötter, J. D., V. A. C. Haanappel and M. F. Stroosnijder (1996). "The Influence of Niobium on the High Temperature Oxidation Behaviour of Near Gamma Ti-48Al-2Cr." in *Microscopy of Oxidation III (Conf. Proc.)*, eds. S. B. Newcomb and J. A. Little, The Institute of Metals, London. p. 287-296.

Takasaki, A., K. Ojima, Y. Taneda, T. Hoshiya and A. Mitsuhashi (1992). "High Temperature Oxidation of Two-Phase (Ti_3Al + TiAl) Intermetallic Compounds." Scripta Metallurgica et Materialia **27**: 401-405.

Takeyama, M. and C. T. Liu (1992). "Elevated-Temperature Environmental Embrittlement and Alloy Design of $L1_2$ Ordered Intermetallics." Materials Science and Engineering A **A153**: 538-547.

Tallan, N. M. (1988). in *Application of Advanced Materials for Turbomachinery & Rocket Propulsion- Proceedings of Propulsion and Energetics Panel 72nd Specialists Meeting, Bath, UK*, NATO Advisory Group for Aerospace Research and Development, AGARD, Neuilly sur Seine, France. p. ix - xix.

Tanaguchi, S., T. Shibata, A. Murakami and K. Chihara (1994). "Improvement in the Oxidation Resistance of TiAl by Preoxidation in a TiO_2-Powder Pack." Oxidation of Metals **42**(1/2): 17-29.

Taniguchi, S., T. Shibata, A. Murakami and K. Chihara (1994). "Improvement in the Oxidation Resistance of TiAl by Preoxidation in a Cr_2O_3 Powder Pack." Materials Transactions, JIM **35**(9): 616-622.

Taniguchi, S. (1994). "Coatings for TiAl." MRS Bulletin **19**(10): 31-34.

Taniguchi, S., T. Shibata and S. Sakon (1995). "Oxidation Resistance of TiAl Significantly Improved by Combination of Preoxidation and Hf addition." Materials Science and Engineering A **A198**: 85-90.

Taniguchi, S., T. Shibata, T. Saeki, H. Zhang and X. Liu (1996). "Effect of Nb-Ion Implantation on the Oxidation Resistance of TiAl." Materials Transactions, JIM **37**(5): 998-1003.

Taniguchi, S., H. Juso and T. Shibata (1996). "Improvement in High-Temperature Oxidation Resistance of TiAl by Addition of 0.2 mass% Zr." Materials Transactions, JIM **37**(3): 245-251.

Taylor, T. N. and M. T. Paffett (1992). "Oxide Properties of a γ-TiAl: A Surface Science Study." Materials Science and Engineering A **A153**: 584-590.

Thompson, A. W. (1992). "Effects of Hydrogen in Titanium Aluminide Alloys." Materials Science and Engineering A **A153**: 578-583.

Tomasi, A., S. Gialanella, P. G. Orsini, and M. Nazmy (1995). "Oxidation Behaviour of Intermetallic Compounds Based on Ti-Al System." Materials Research Society Symposium Proceedings, **364**: 999-1004.

Touryan, L.A., (1993). unpublished research.

Tsuyama, S., S. Mitao and K. N. Minakawa (1992). "Alloy Modification of γ-Base Titanium Aluminide for Improved Oxidation Resistance, Creep Strength and Fracture Toughness." Materials Science and Engineering A **A153**: 451-456.

Unnam, J., R. N. Shenoy and R. K. Clark (1986). Oxidation of Metals **26**: 231.

Vasudevan, V., J. Yang and A. P. Woodfield (1996). "On the β to B2 ordering Temperature in a Ti-22Al-26Nb Orthorhombic Titanium Aluminide." Scripta Metallurgica et Materialia **35**(9): 1033-1039.

Venkkatu, D. L. and L. E. Poteat (1969). Materials Science and Engineering **5**: 258.

Verma, S. K., G. M. Raynaud, and R. A. Rapp (1981). "Hot-Stage Scanning Electron Microscope for High-Temperature In-Situ Oxidation Studies." Oxidation of Metals **15**(5/6): 471-483.

Welsch, G. and A. I. Kahveci (1989). "Oxidation Behavior of Titanium Aluminide Alloys." in *Oxidation of High-Temperature Intermetallics (Conf. Proc.)*, eds. T. Grobstein and J. Doychak, The Minerals, Metals & Materials Society, Warrendale, PA. p. 207-218.

Wiedeman, K. E., S. N. Sankaran, R. K. Clark and T. A. Wallace (1989). :"Static and Dynamic Oxidation of Ti-14Al-21Nb." in *Oxidation of High-Temperature Intermetallics*

(Conf. Proc.), eds. T. Grobstein and J. Doychak, The Minerals, Metals & Materials Society, Warrendale, PA. p. 195-206.

Williams, J. C. and G. W. Kuhlman (1989). "Titanium Alloys." Treatise on Materials Science and Technology. Academic Press. 651-661.

Wolf, W., R. Podloucky and P. Rogl (1995). "First Principles Studies of Gamma-TiAl Based Ternary Alloys." Materials Research Society Symposium Proceedings, **364**: 1005-1010.

Yamaguchi, M., H. Inui, K. Kishida, M. Matsumoro and Y. Shirai (1995). "Gamma Titanium Aluminide Alloys." Materials Research Society Symposium Proceedings, **364**: 3-16.

Yamaguchi, M., H. Inui, S. Yokoshima, K. Kishida and D. R. Johnson (1996). "Recent Progress in Our Understanding of Deformation and Fracture of Two-Phase and Single-Phase TiAl Alloys." Materials Science and Engineering A **A213**: 25-31.

Yolton, C. F. and J. P. Beckman (1995). "Powder Metallurgy Processing and Properties of the Ordered Orthorhombic Alloy Ti-22at.%Al-23at.%Nb." Materials Science and Engineering A **A192**: 597-603.

Yoshihara, M., R. Tanaka, T. Suzuki, M. Shimizu (1991). "Development of Surface Treatment Techniques to Improve Oxidation Resistance of Titanium Aluminide." Materials Research Society Symposium Proceedings, **213**: 975-980.

Yoshihara, M., T. Suzuki and R. Tanaka (1991). "Improvement of Oxidation Resistance for TiAl by Surface Treatment Under a Low Partial Pressure Oxygen Atmosphere and Aluminum Diffusion Coating." ISIJ International **31**(10): 1201-1206.

Zheng, N., W. Fischer, H. Grubmeier, V. Shemet, and W. J. Quadakkers (1995). "The Significance of Subsurface Depletion Layer Composition for the Oxidation Behaviour of Gamma-Titanium Aluminides." Scripta Metallurgica et Materialia **33**(1): 47-53.

Zheng, N., W. J. Quadakkers, A. Gil, H. Nickel (1995). "Studies Concerning the Effect of Nitrogen on the Oxidation Behaviour of TiAl-based Intermetallics at 900°C." Oxidation of Metals **44**(5/6): 477-499.